The Development of Novel Coating Solutions for the Improvement of Pre/Post Heat Treatment Performance Properties of Carbon Steel Conveyance Tubes

Submission of Engineering Doctorate

James David Grant

December 2022

Declaration

I, James David Grant, hereby certify that this thesis and all attributed work has been composed by myself and that it is a record of my own research from the period of October 2017 to October 2021. Except where specific reference is made to other sources or collaborators, the work presented in this thesis is the original work of the author. It has not been submitted, in whole or in part, for any other degree.

Acknowledgements

I would like to thank Swansea University and TATA Steel for funding this Engineering Doctorate project. In particular, Dr Chris Owen for supporting me during industrial visits and providing access to the production mill at Corby. In Swansea, my supervisor Dr Amit Das has given me great guidance and I thoroughly enjoyed working together on the undergraduate engineering projects. I am hugely grateful to SPECIFIC, WCPC and AIM for the equipment I have utilised throughout the project as well as their assistance. I would like to offer sincere gratitude to Reda Felfel and the University of Nottingham, whose collaboration has been highly successful. I'd also like to thank my senior technicians Leighton and Gareth who have been enormously helpful in preparing experiments and providing me with essential knowledge. Finally, I would wholeheartedly like to thank my parents and my fiancé Sophie, whose support, and guidance have enabled this endeavour to be possible.

Abstract

Due to the normalisation process at the SR2 Mill in TATA Steel Corby, low carbon steel conveyance tubes generate an unwanted surface oxidation called scale. This is both detrimental to the yield loss and surface cosmetic appearance of the conveyance product. To inhibit this, a coating was designed to be applied prior to the normalisation stage to protect the steel surface. The construction and use of a purpose-built controlled atmosphere furnace allowed coating trials to experience the 9% O_2 in the SR2 mill. Samples were heat treated using a pre-set thermal cycle and metallurgically prepared for optical microscope and SEM analysis. After a wide scope of coatings trials, two solutions were determined to be effective in scale prevention and were optimised by observing the oxidation kinetics, thermomechanical and phase properties. The first coating, utilised $Na_5P_3O_{10}$ in combination with an acrylic addition to produce an impermeable phosphate coating through sol-gel application. This solution reduced oxidation by 82.1% and surface roughness improved by 41.1%. Using Laser Flash Analysis and Differential Scanning Calorimetry, it was determined that the thermal conductivity of this coating was between 0.6-1.0W/mK which may affect thermal transfer. The second coating was a silicate-based solution which was a mullite material reinforced with $Zr O_2$ for improved porosity traits. This solution reduced oxidation by 94.9% but increased surface roughness by 14.7%. An initial investigation of the untreated steel found that there was a clear point at 650°C where wüstite domination was prominent and that furnace atmospheres with <6% O_2 caused the wüstite – magnetite ratio to reduce from 94% to 88%.

Contents

List of Abbreviations and Sample Nomenclature

BSD   Back Scatter Diffraction

C_p Specific Heat Capacity

dH_20 Distilled Water

DSC   Differential Scanning Calorimetry

EDS   Energy Dispersive Spectroscopy

EDF   Extended Depth of Field

FTIR   Fourier Transformed Infrared Spectroscopy

HAZ   Heat Affected Zone

HexChi   Hexanoic Chitosan

HFI   High Frequency Induction

HRc   Highly Fine Recycled Glass

k Thermal Conductivity

LFA   Laser Flash Technique

MLI   Mean Line Intercept Method

PMRC   Pilot Manufacturing Research Centre

SEM   Scanning Electron Microscopy

Pt   Surface Porosity

PVA   Poly(vinyl alcohol)

PVB   Polyvinyl butyral

Ra   Surface Roughness Average

Rz   Surface Roughness Point Height of Irregularities

SOPAC   Sodium Polyphosphate with Acrylic Addition

SR2   Stretch Reduction Two (TATA Corby)

STA   Simultaneous Thermal Analysis

STCA1   Standard Thermal Cycle Atmosphere 1

STCG1   Standard Thermal Cycle Gas Composition 1

Tc   Crystallisation Temperature

Tg   Glass Transition Temperature

TGA   Thermal Gravimetric Analysis

UE1/24/41   Uncoated Steel Grade E1/E24/E41

VOC   Volatile Organic Compounds

WLI   White Light Interferometry

XRD   X- Ray Diffraction

α Thermal Diffusivity

ϱ Density

Chapter 1

Introduction

Carbon Steel tubes are a mainstay for many construction projects around the world and feature prominently in some of the UK's most well-known landmarks such as Wembley Stadium, the London Eye, and the Millennium Stadium. TATA Tubes, a division of TATA Steel based in Corby, Northamptonshire, produces a premium 'Install' carbon steel conveyance tube product range primarily for the building and services industry. Conveying water or air, the tubes are manufactured in accordance with BS EN 10255 and typically are implemented into Heating Ventilation Air Conditioning (HVAC) applications, high-pressure systems, or industrial pipework conveyance. Due to the service life expectations for tube products in this industry, TATA Steels' Install 235, Install 235+ and Inline 265 products must comply with performance standards in high temperature resistance, low corrosion susceptibility and elevated pressure tolerance. To achieve this, TATA employs a 'hot-finished' manufacturing process which provides significant advantages over alternative cold-formed commodity tubes. The term 'Hot finished' refers to a furnace treatment which occurs after the High-Frequency Induction (HFI) welding stage during manufacture and the production process is described in Figure 1.1.

The furnace treatment is beneficial for three key reasons. Firstly, the higher temperatures ensure the parent hollow is made malleable for the ensuing strength reduction process for products which require a different shaping or reduced outer diameter. Secondly, the internal stresses within the bulk

material, which are induced during forming and rolling, are alleviated by achieving grain structure homogeneity. Thirdly, and most importantly, the normalization removes a 'heat affected zone', an area of weakness around the weld line which is generated when shaping the steel into the tube profile and is explained in section 1.1.
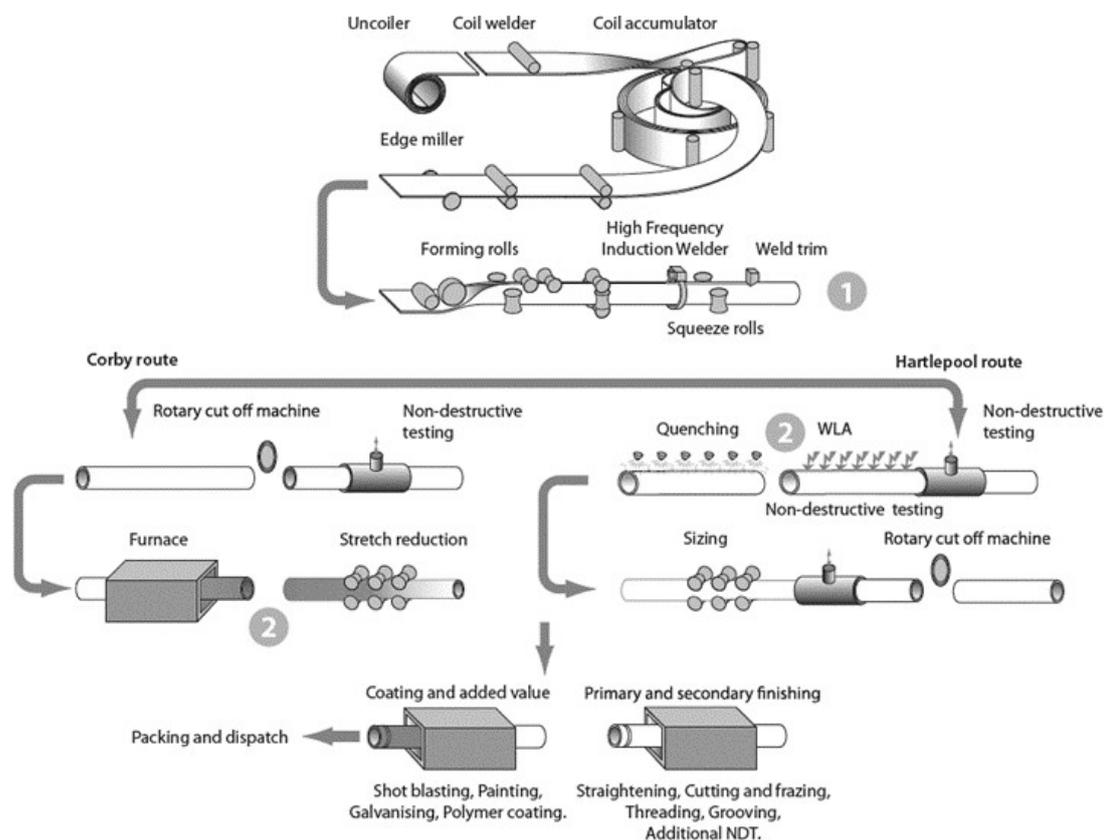
Figure 1.1 [1]: Carbon Steel Conveyance Tube manufacturing process utilised by TATA Steel. TATA in Corby employs a normalisation route to produce their 'Hot finished' products.

1.1 High Frequency Induction Welding Process

The most common electrical resistance welding technique used in industry is the High-Frequency Induction (HFI) process which is the preferred method TATA Steel employ to produce their conveyance products. Figure 1.2 illustrates the HFI induction welding mechanism. Alternate tube manufacturing techniques, such as the rotary pierced process, offer a seamless option by forcing a heated single billet around a moulding plug which eliminates any need for subsequent welding. However, rotary piercing

often leads to inconsistent wall thickness and poor roundness in the tube profile as well as difficulty in achieving consistent tube lengths.

The HFI process begins with the passage of an uncoiled carbon steel sheet through a series of accumulators and bent into a tube profile using forming rolls. The two inner edges of the steel converge together and are surface heated using an induction coil. This is achieved via the application of a high-frequency alternating current through the coil resulting in the production of an electromagnetic field which subsequently induces a current in the conductive steel material [2]. Due to the high resistivity characteristics of the steel, the energy lost due to its resistivity is converted into heat; a process known as eddy current heating or joule heating [3]. The welding creates a small amount of protruding material over the weld centerline; known as the flash. For the stretch reduction production mill, this flash is removed prior to the heat treatment via a weld trim.
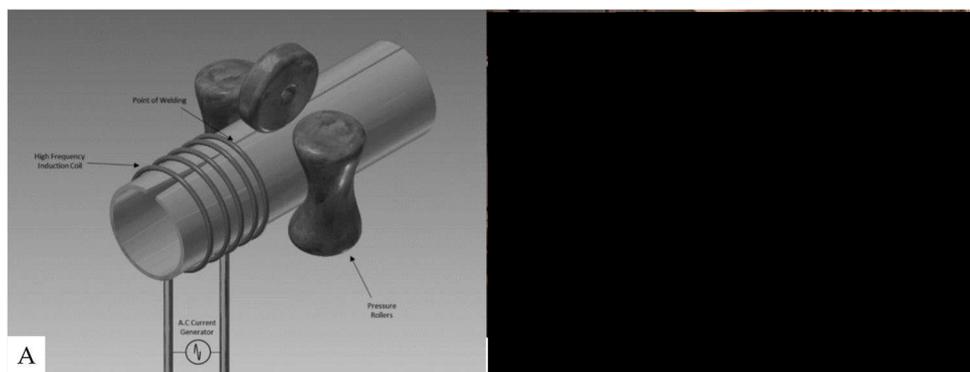
Figure 1.2 A) Illustration of the HFI welding process. B) Example of a HFI welder at HVAC applications mill.

The use of HFI Welding introduces an undesirable Heat Affected Zone (HAZ), formed due to the application of high temperatures along the weld line and causing a solid-state transformation of the microstructure [4]. The HAZ spans from the area of peak temperature along the weld fusion centerline; known as the 'Fusion Zone' and ends at the region with no

observed microstructural change; known as the unaffected base material [5].
Figure 1.3 illustrates this HAZ typically found in steel conveyance tubes. Low
carbon steel has a ferrite-pearlite structure in which the pearlite regions
transform into austenite above the eutectoid temperature before cooling to
form mostly ferrite in a variety of forms, such as acicular ferrite nucleations,
with a mixture of remnant austenite and martensite present within the
microstructure [6][7]. The grain size and uniformity of the HAZ material in
the weld are distinctively different to that of the unaffected base material.
Specifically, the austenite grains become coarser and finer in size due to a
more severe deformation in the fully austenised region, a process known as
dynamic recrystallisation [8].
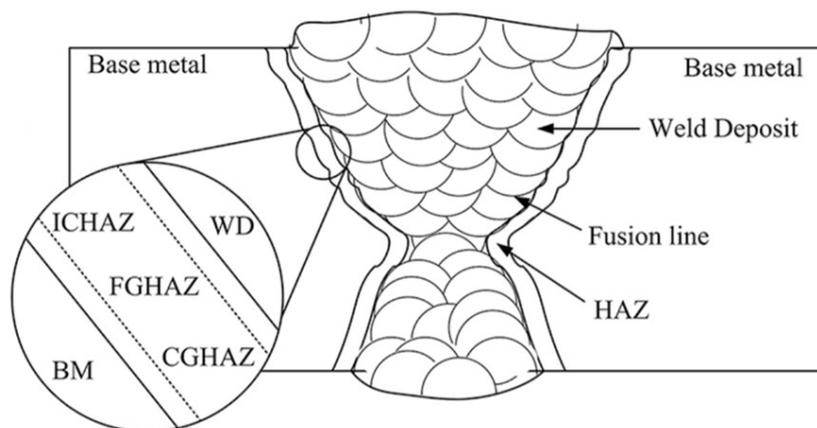
Figure 1.3: Heat Affect Zone and Fusion Zone in the weld centreline. The grain structure
and mechanical properties of these zones differ greatly from the bordering unaffected bulk
material [9]. The figure also depicts the granular variation of HAZs, namely the
Intercritical (ICHAZ), Fine Grain (FGHAZ) and Course-Grained Heat Affected Zones
(CGHAZ).

This variation in grain structure results in weaker and more brittle
material, leading to a reduction in toughness and overall pressure
integrity. More significantly, the grain structures of the HAZ differ from
those of the base metal because it has been heated to a temperature just below
the material's melting point and then cooled rapidly, unlike the adjacent base

metal. Figure 1.4 depicts a Smartzoom micrograph of the HAZ region in a cold-formed conveyance product without subsequent normalisation. In addition, research has shown the HAZ region can decarburize by as much as 30% due to the rapid heat transfer of HFI welding, which produces an area of low carbon content [10].
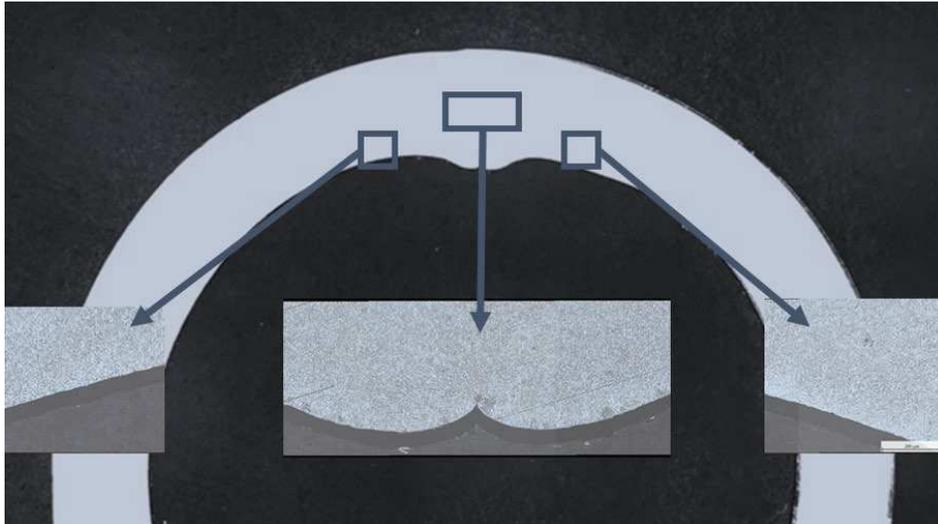
Figure 1.4: Smartzoom 5X micrograph stitch of the tube profile at the weld line area of a cold-formed conveyance product. Observer images at a higher magnification indicate the grain structure at the HAZ differs greatly from the bulk material of the tube profile.

This section of the tube will be weaker, more corrosion susceptible, and likelier to split due to the reduction in strength and hardness characteristics of the steel and the poor grain size homogeneity with the surrounding parent material. This variation in the microstructure of the HAZ is due to the difference in maximum temperature and cooling rate experienced away from the weld line and its mechanical properties are dependent on the thermal cycle experienced during the heating [11]. Removal of this HAZ, therefore, is highly beneficial by providing significant market advantages due to products being able to withstand higher pressure tolerances and exhibit superior service life compared to cold-formed tubes. Normalisation is the most suitable process for HAZ elimination in this application and TATA tubes

utilize a mixture of furnace treatments during mill production as explained in section 1.2.

1.2 Normalisation and Stretch Reduction Processes

Normalisation is a heat treatment process in which a steel structure is taken above its austenising temperature to change the microstructural characteristics of the material [12][13]. TATA Steel employ this method by setting the parent hollow on a conveyor or walking beam, the speed of which is determined by the length of the heat treatment and leaves the resulting tube to cool gradually in air at room temperature. This is in contrast to some alternative steel making processes like annealing, whereby the material is subjected to controlled cooling or 'quenching', in which the steel is cooled rapidly in water. By heating above austenizing temperature but below melting temperature, the residual stresses present within the material are alleviated due to the recovery, recrystallisation and growth of the grain structure in the austenitic phase. Furthermore, the HAZ's distorted, mis-orientated, and non-homogenous grains are also recrystallised and resemble a granular structure far closer to that of the encompassing bulk material; effectively removing the HAZ from the tube profile [7][14].
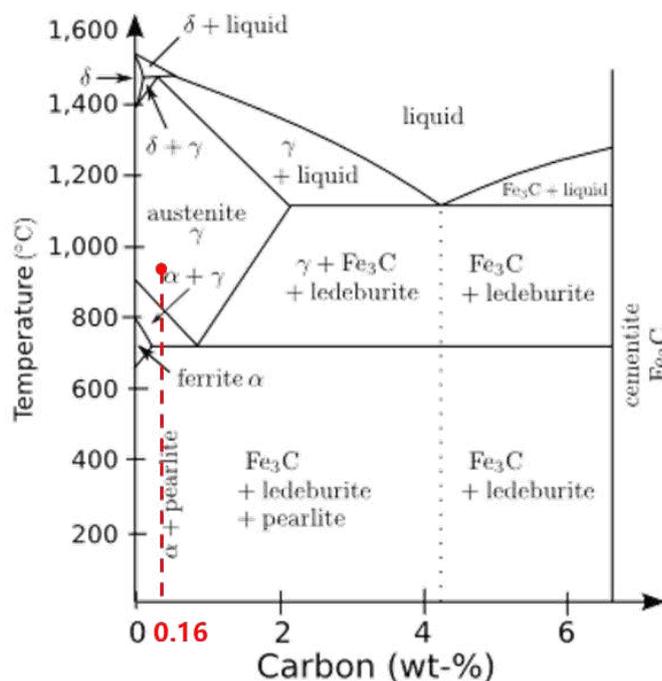
Figure 1.5: Iron Carbon Phase diagram, a hypoeutectic steel grade (0.16% carbon) is taken to the austenitic phase during normalisation. Improved hardness, tensile strength and pressure ratings are achieved due to the recovery and recrystallisation of the parent hollow [15].

In addition, normalisation is typically utilized in carbon steels after casting or hot rolling due to the inconsistencies within the steel such as the large grains of unwanted carbides or bainite. The result is a fine-grain microstructure with good uniformity and mechanical properties. In the case of hypo-eutectoid steel, a grain refinement occurs during the austenitic transformation producing a uniform microstructure of ferrite and pearlite [16]. During air cooling, the grain refinement is further enhanced by the formation of pearlite due to the initial separation of the ferrite and austenite grains. This resulting microstructure is far improved from the coarse grain size that is caused during hot working, which is a symptom of exceeding a homogenising temperature range, typically between 1000°C-1200°C, resulting in an excessive austenitic grain size. In theory, compared with the controlled slower cooling of annealing, normalisation denies the carbon

atoms time to move through the lattice structure and form larger carbides. This results in a high hardness material explained by the formation of a finer pearlite and ferrite microstructure [17]. For the stretch reduction mill at Corby, the parent hollow is transferred to the Priest furnace, a long gas barrel system which conveys the tube during a ███████ normalisation using a fuel mixture of ███████████████. The Priest furnace extends over 100 meters along the mill allowing an isothermally stable region at ███████ █████ which is shown in Figure 1.6. the tubes then enter a Raydyne induction "top up" furnace at █████████████████████, though this soak temperature is largely dependent on the NB and product specification.
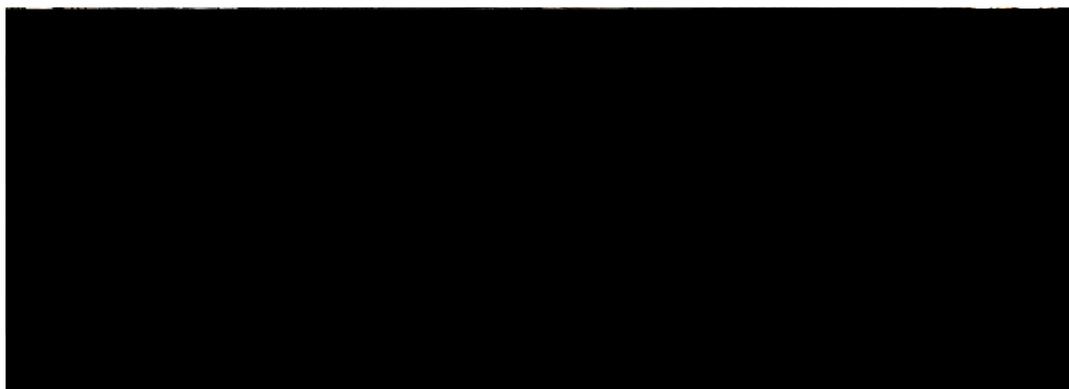
Figure 1.6: A) Entrance to the SR2 Gas Barrel Furnace. Parent hollow sections from the transfer table are subjected to 30–40-minute heat treatment at 800°C-850°C after HFI welding. B) Image depicting the Gas Barrel full length. Raydyne induction furnaces "top-up" heat treatment at 950°C prior to descaling and stretch reduction.

Once normalised, the products are sent through a descaling box, which acts unintentionally as a partial cooling mechanism, reducing the steel temperature to approximately ██████ At these elevated temperatures, the tube material is naturally more ductile and malleable and so the parent hollow is subsequently transferred through the stretch reduction sizer to achieve a pre-determined wall thickness and diameter for the tube. Rolling stands in series act as a stencil matrix to determine the Nominal Bore and

overall shape (circular hollow sections are often formed into a construction standard rectangular hollow sections) of the product. This process and the aforementioned descaling box are shown in Figure 1.7. By adopting the 'hot finished' approach to tube making, the Install 235 products gain a significant market advantage over cold-formed tubes. Namely, the internal stresses and inconsistent microstructure present in cold-formed alternatives are instead replaced with a homogeneous crystal structure able to perform at much higher-pressure integrities as shown in Table 1.1.

Table 1.1: Mechanical Properties and performance characteristics of Hot Finished vs Cold Formed Tube products. Due to normalisation, Hot Finished tubes outperform commodity alternatives in tensile strength parameters, temperature tolerances and elongation limits [18].

Production Method	Tensile Strength Range	Tensile Ratio	Operational Temperatures	Elongation lon. (min)
Hot Finished Product	441MPa- 531MPa	1.20	-30°C to 300°C	27%
Cold-Formed Alternatives	511MPa-551MPa	1.08	-20°C to 250°C	22%

In addition, the poor mechanical properties due to the residual HAZ in cold-formed tubes leads to issues in fabrication, installation, and service life, increasing the risk and cost for construction projects. 'Hot finished' carbon steel conveyance tubes are priced as a premium product against cold-formed due to consistency in achieving BS EN10255 standards, improved corrosion performance and a greater ability to be threaded, grooved, and bent to tight radii without splitting or creasing. However, normalising the product exposes the raw unprotected steel to unfavorable conditions such as high oxidising gases, elevated normalising temperatures and considerable soak time. These allow the parent hollow to generate significant amounts of high temperature surface oxidation during normalisation. This surface oxide is called scale and jeopardises the marketability advantage of Install products against cold-formed alternatives as explained in section 1.3.

1.3 The Challenge of Scale Oxide

Scale oxide is a by-product of most industrial steel making processes due to insufficient protection at high temperatures and the availability of free oxygen during combustion in gas furnaces. Scale, a dark brittle compound, is generated due to the reaction of Fe cations with the free O anions and thus contains a significant amount of grade quality steel, around 55%. The shorter thermal cycles at Corby produce between 50μm-200μm thick scale in the walking beam and stretch reduction processes while the Hot Mill process at Port Talbot, which sustains the slabs over 1000°C for 2-3 hours can produce well over 1000μm in scale thickness. The oxide is removed via water or hydraulic descaling after normalisation, and this prevents the factor of 'rolled in scale' which is highly detrimental for surface cosmetics and in the application further added value coatings. Figure 1.7 depicts the collection of the scale oxide garnered from the stretch reduction descaler. The crucible contains tons of grade-quality steel that could have been used to produce premium tube product.

Figure 1.7: Oxide crucible collection of the by-product scale. Estimates of yield loss in tube production range from 1-3%. The oxide is reprocessed back to Port Talbot to recover quality-grade steel in the Blast Furnace.

Estimates of the cost of oxide growth project between a 1.5%-3% yield loss which increases further when costs administered by surface defects are accounted for [19]. Directly, poor surface quality with remnant surface oxide hampers the service life and performance of Install Tube products, reducing their value and incurring rebates for affected customers due to failure. This is attributed to the fact that a poorly adhered scale layer will spallate after the application of added value finish and such coatings, like a corrosion-inhibiting paint, will be absent in areas of the tube. Indirectly, and more importantly, the marketability of the Install 235 product is deeply affected by a poor surface cosmetic aesthetic as shown in Figure 1.8.

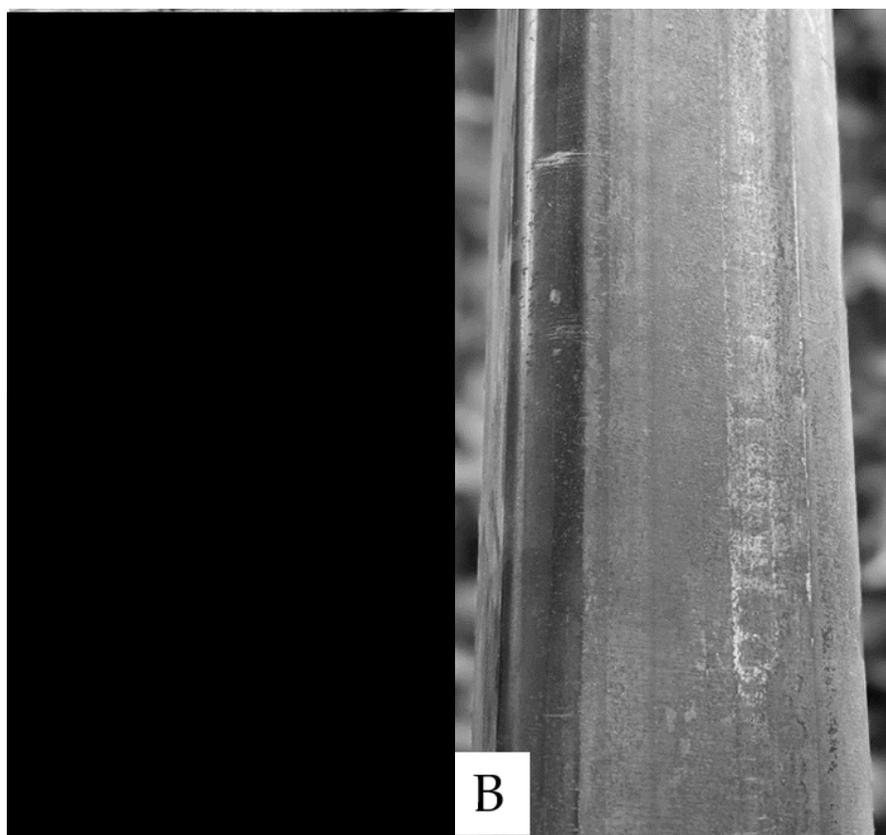**Figure 1.8:** A) Premium 'Hot-Finished' Install product prior to shot blasting and added value coating application. Surface defects and rolled-in scale present on the tube surface are amplified further after the application of the red paint finish or galvanisation. B) Cheaper Cold Formed commodity tube. Lack of normalisation provides little surface oxide, leaving a low surface roughness and consistent finish.

In addition, wider TATA business ventures see amplified scale-related detrimental effects due to an emissivity issue at higher gauges of scale thickness. Due to oxide attributing a poorer thermal transfer conductivity of ~1.7 $Wm^{-1}K^{-1}$ and higher emissivity at 1000°C-1100°C when compared with grade steel, 50 $Wm^{-1}K^{-1}$ [20], the heat energy ingress by furnace systems is greatly reduced. For the Port Talbot hot mill, as an example, this decreases energy efficiency in elevating the slab steel to 1200 C and effectively reduces the strip line speed in the reheat furnace prior to coiling. Despite the vastly improved mechanical performance properties of the Install 235, customers will prefer a cold-formed alternative due to superior cosmetic characteristics. This is especially evident in projects with products installed in open visible spaces. TATA Tubes' strategy is to produce market-leading conveyance tubes, complete with full traceability of the steel used in production, a technical specification package and support through service life not provided by imported alternatives. The cosmetic issue undermines the market advantage gained by hot finishing and provides a challenge to educate customers on why Install products are superior to the cold-formed alternatives. If the surface quality of the Install conveyance tube can be enhanced, the perceived market gap between the competing products will increase, allowing TATA a better marketability position to ask for a premium price for its hot-finished product range. To achieve this, and to reduce the yield loss incurred due to oxide growth, TATA Tubes aim for this project to develop a novel coating solution which will protect the raw steel during normalisation and prevent the growth of the detrimental scale prevalent on the tube profile substrate as explained in section 1.4.

1.4   Project Aims and Objectives

Previously, SR2 utilized an atmospheric controlled furnace which initiated a low oxygen atmosphere during normalisation to inhibit oxidation. Due to costimplications, the system was removed in favour of the aforementioned gas-barrel priest furnaces. However, this desired oxide prevention could potentially be replicated by the application of an inhibition coating to the tube product and thus provides a low-cost, added-value engineering solution to the production process.The novel coating was designed to be applied after HFI welding and prior to the priest gas barrel furnace entrance as shown in Figure 1.9.
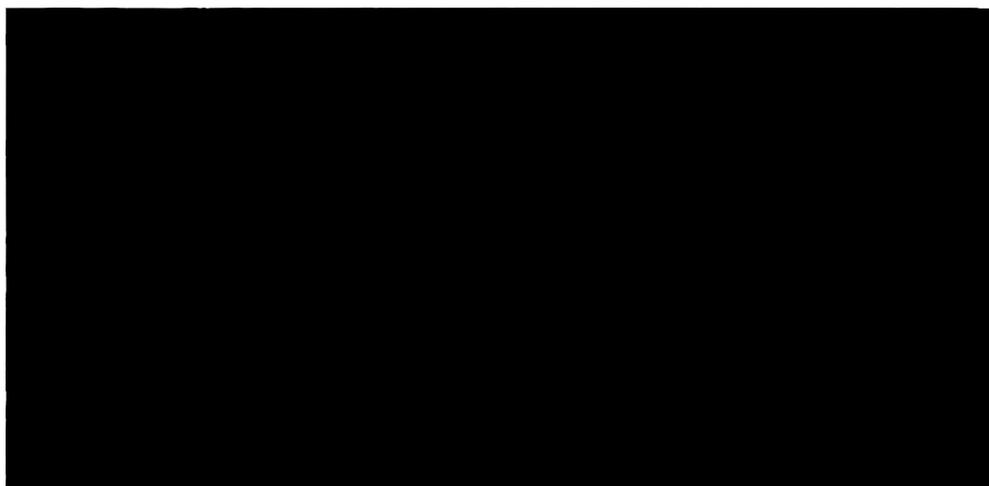
Figure 1.9: Proposed positions for the induction priming oven and air spray ring system on the SR2 Mill.

To be a viable option for installation at TATA Corby, the coating must pertain to certain characteristics both in synthesis and operation. These include:

1. Inhibition of high temperature oxidation through sacrificial active action or passive barrier protection. The coating ideally will form a uniform, non–porous barrier which prevents permeation of oxygen to the steel surface denying the diffusion of O_2 anions to react with Fe cations at the boundary interface. The novel coating

may aim to reproduce the effects observed on the scale under low oxidising atmospheres, whereby fluctuating levels of CO_2, CO, N, and excess air have a significant impact on the ratio between interstitial phases. This is key, as magnetite phases are characteristically known to act as a spallable or stringy phase [21].

2. A high adhesion coefficient between the coating and steel substrate. During normalisation, the coating must not degrade at elevated temperatures, nor spallate due to vibrations from the walking beam mechanism. Afterwards, the coating should revert to a low adhesion during cooling in preparation for the descaler. Remnant coating is undesirable for surface cosmetics as the material will be rolled into the substrate during stretch-reduction and leaves behind an unwanted substance on the tube product. Therefore, the coating must be able to spallate away during descaling and additionally adhere to any remaining oxide present thereby delaminating it from the tube profile and thus providing a low Ra, consistent and aesthetically desirable finish.

3. The total budget of the coating per tonne must not surpass the value of the quality grade lost due to oxidation per tonne. Operation costs in consideration are material costs, synthesis costs, application expenses, equipment purchase and installation, failure rates, maintenance costs, energy usage and labour. This will be counterbalanced by the Net Profit Value achieved by the coating by increased yield and added value due to price enhancement from cosmetic improvements. This will be simulated using an economic appraisal model.

4. The coating must not release any harmful VOC during application or operation. TATA engineers operate in close proximity to the transfer

table in an open workstation area and the emission of harmful levels of CO_2 CO, SO_x, NOx, HF or any other toxic gases is strictly prohibited as they present an immediate health hazard to workers on the mill.

5. A low R_a and R_z value after descaling. Surface roughness improvements will provide a better finish for subsequent added-value coatings and increase the marketability advantage of the Hot Finished Install products.

6. Suitable wettability and surface tension characteristics for application. The favoured application method of a spray ring system requires suitable contact angle and viscosity values in addition to a high curing rate. Furthermore, the coating must form without pinhole defects, non-uniformity, or conglomeration.

The aim of this project therefore is to research, develop and synthesise the required coating, and the objectives of this work can be categorized into three key areas:

- Investigate and understand the oxidation kinetics of the E1, E41, and E24 mill-grade steel and analyse the phase morphology due to its normalising conditions. This includes the development of a novel furnace methodology to control thermal properties and atmospheric conditions.

- Explore viable coating candidates from mainly phosphate-based or silicate-based technology. Assess the performance of the coatings through mill simulations, evaluating their ability to reduce oxidation and improve surface cosmetics.

- Determine the feasibility of implementation for promising candidates. Partly through application testing, but mostly in economic appraisal

testing and VOC emissions reports.

The following Chapter 2 performs an in-depth literature review covering the mechanism of high-temperature oxidation, its attributing factors, and the types of inhibition coating technology available to prevent scale formation. Chapter 3 focuses on the materials and methods employed to evaluate the topics while Chapter 4 investigates the oxidation properties of the subject steel and its dependency on atmosphere and temperature. Chapter 5 presents and discusses the synthesis, application, and performance of phosphate-based coatings. While Chapter 6 further continues coating research by observing the performance and suitability of silicate-based coatings. Finally, Chapter 7 summarises these coatings' characteristics and compares the feasibility of both against the requirements of the SR2 mill and includes their economic impact.

Chapter 2

Literature Review

2.1 Scale oxide formation and growth

Exposure of raw steel to high soaking temperatures in the reheating furnace leads to the rapid growth of iron (II), iron (III), and iron (II, III) oxide mixture formation, more commonly known as mill scale [22]. Oxidation is a chemical reaction in which the interaction of oxygen anions and metal cations form an oxide phase [23]. While oxide growth occurs naturally, the reaction between a metal and oxygen is often very slow but can be enhanced by exciting the atoms with external energy, such as the high thermal energy introduced by the reheating furnace. The process begins with the adsorption of the gas onto the metal surface before the dissolution of oxygen ions into the material causes oxide nucleation to occur at the metal-atmosphere boundary, forming oxide nuclei [24][25]. The growth of these nuclei produces the formation of a thin oxide film across the surface of the metal which continues to expand with oxygen diffusion. This expansion may lead to a porous oxide layer consistent with microcracks and cavities as shown by Figure 2.1. The increase of the oxidation temperature directly promotes scale expansion due to faster diffusion of the iron and oxygen ions [26], [27].
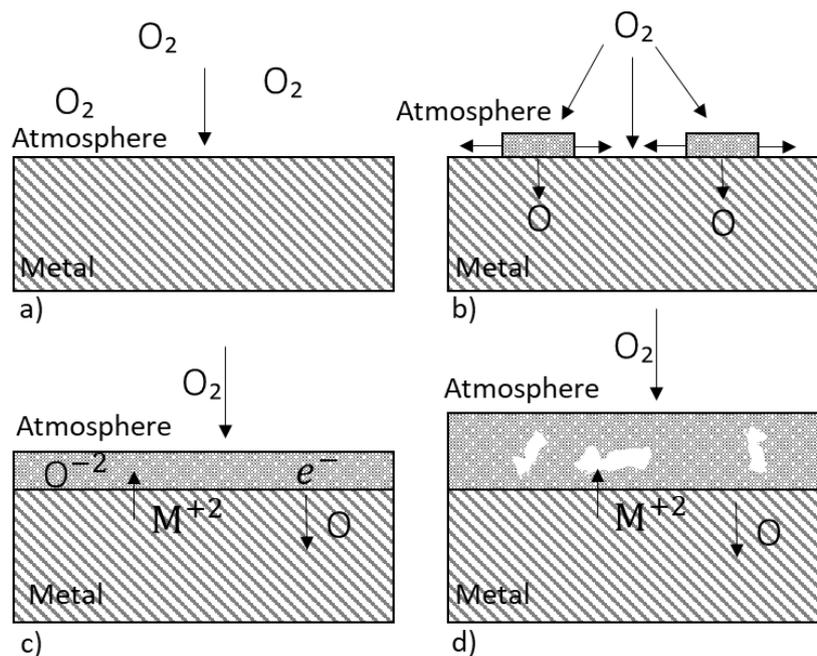
Figure 2.1: Illustration of oxide scale formation on pure metal substrate a) Oxygen absorption at the surface; b) formation of nuclei c) lateral growth of nuclei d) growth of the oxide scale and emergence of microcavities or cavities in the porous layer [28].

When considered as a chemical reaction, the metal ions and electrons migrate to the oxide-gas boundary via iron vacancies and electron holes respectively. The cationic diffusion of a metal will cause the initially formed oxide to drift towards the metal causing oxide growth at the oxide-gas interface, while anionic diffusion leads to oxidation at the metal-oxide interface. Once the lateral growth of the oxide concludes, the newly formed thin film provides desirable protection against further oxidation such as corrosion due to possessing enhanced oxidation resistance compared with the metal below. This oxidation phenomenon can be described by equation 1.1, where M is the metal and n is the number of electrons diffusing to the substrate boundary [29].

$$M \rightarrow M^{n+} + ne^- \ (1.1)$$
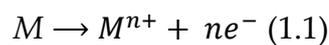
The rate of oxidation occurring is largely dependent on the amount of free oxygen available and the accessibility of iron to the oxidising gas through a thin gas boundary layer at the reaction surface [23]. Initially, oxygen adsorption into a scale is slow and linear, regardless of temperature, and the only rate limiting step

in oxygen transport is the concentration of oxygen in the gas mixture [15]. Once the oxide layer acquires a certain thickness, the oxidation follows a parabolic rate due to the cationic diffusion of iron through the oxide layer. This parabolic rate is mainly dependent on the oxidation time as expressed by equations 1.2 and 1.3.

$$dx/dt = k_p/x \quad (1.2)$$

Where x is the thickness of the oxide, k_p is the parabolic rate constant and t is the oxidation time [30].

$$\therefore x^2 = k_p t \quad (1.3)$$

The rate constant for a metal is dependent on the kinetics of the reaction and can be expressed as a function of reaction temperature as shown in equation 1.4 [31]. This is also known as the Arrhenius equation, where k_0 is a constant, ΔE is the activation energy of the diffusion process, R is the universal gas constant and T is the absolute temperature.

$$k_p = k_0 e^{\Delta E/RT} \quad (1.4)$$

The activation energy of the material, steel in this case, is particularly reliant on the alloying elements in the metal [32] and indicates the minimum temperature requirements for high temperature oxidation to occur. For low carbon steels, activation energies vary between 40-500KJmol^{-1} [13][14] with attributing factors such as recrystallisation and grain recovery incurring modulations in due to individual rates of deformation in the bulk material. Additionally, the partial pressure of oxygen has an important role in the kinetics of scale oxidation during reheating. The rate of impingement of oxygen molecules dominates the oxidation rate at low pressures of oxygen, essentially making the reaction rate directly proportional to oxygen pressure. However, at elevated temperatures at the metal-atmosphere interface, this relationship develops from P to $P_{O_2}{}^{1/2}$.

In steel oxidation, scale oxide creates additional challenges in most steel making processes due to differentials in thermodynamic, dielectric, and mechanical

properties between the base metal and the grown oxide. The main theoretical detriment of these differentials is that the scale acts effectively as heat resistant layer during cooling and prevents heat ingress to the slab during annealing. Endo et al. explored the relationship between oxide thickness in hot rolled strip steel and its respective values in thermal effusivity, thermal conductivity and thermal diffusivity and the key findings from this investigation are shown in Table 2.1.

Table 2.1 – Thermophysical properties of oxide scale investigated by Endo et al. on hot rolled strip steel. Half-life analysis with Laser flash technique was used to determine thermal diffusivity, while thermal conductivity was calculated as a function of heat capacity (C_p), density (ρ) and thermal diffusivity (α) [20].

Oxidation time/s	Thickness/mm			Thermal diffusivity/10^{-6} m^2s^{-1}		Thermal conductivity/ $Wm^{-1}K^{-1}$
	Total, d_s	Oxide scale, d_{oxide}	Steel, d_{steel}	Sample, α_s	Oxide scale, $\alpha_{oxide,m}$	Oxide scale, $\lambda_{oxide,m}$
770	1.099	0.0978	0.903	6.97	0.478	1.74
1 650	1.131	0.133	0.865	4.56	0.450	1.69
3 600	1.204	0.206	0.792	2.14	0.376	1.55

The research revealed a 69.3% reduction in the overall thermal diffusivity of the steel sample due to oxidation and a further 11.1% drop in thermal conductivity in the oxide scale; all of which were magnitudes lower than a standard ultra-low carbon steel conductivity of $71.1 Wm^{-1}K^{-1}$. The study also indicated a lower effusivity for oxide scales, ~2.52 $KJs^{1/2}m^2K$, when compared with a typical hot rolled low carbon steel effusivity, ~16.04 $KJs^{1/2}m^2K$ [35], which theoretically greatly reduces the ability of a bulk material to absorb thermal energy. The reason for the comparatively low thermal conductivities in scale is attributed to the air voids within the film thereby acting as an insulation barrier.

In addition, most oxide scales possess a thermal expansion coefficient higher than that of Fe at 800°C (~14.6 x $10^{-6}/C°$) the scale of which is dependent on the phases present within the oxide [36]. The thermal stress induced by the

differential in thermal expansion coefficient causes scale cracking and spallation between the boundary of the inner-most layer of oxide and the parent material underneath. This delamination in the normalisation process will occur for three reasons. Firstly, the contraction differential between the steel and the oxide is able to overcome the electrostatic interactions and van der Waals forces at the interface boundary. Secondly, the epitaxial stresses induces an interfacial stress at the material surface and finally, even during isothermal development of the steel-oxide system, growth stresses occur [37]. In the 1970's, efforts through the EPRI (Electric Power Research Institute) led to the development of the Armitt diagram, a theoretical model predicting the adherence failure of an oxide based on the compressive or tensile forces acting on an oxide as a function of its thickness [38]. The diagram depicts the regions of expected oxide integrity and delamination dependent on the failure mechanism and is illustrated in Figure 2.2.
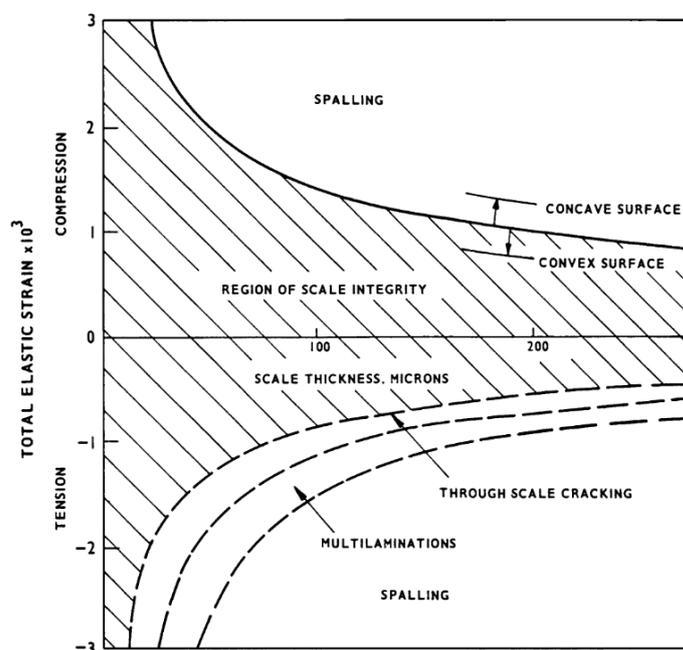

Figure 2.2 – Armitt Diagram describing oxide scale failure. Later developed diagrams incorporated attributing factors into the failure strain, such as young's modulus, defect size, interface roughness and fracture toughness [21].

Industry will and will not desire an oxide scale prevalent on the steel surface depending on the application of the product. Full and proper descaling occurs

after most reheating processes through either acid bath pickling or water jet descaling, as cold rolling embedded scale leads to surface cosmetic issues [39]. As such, the magnitude of the adhesive performance of an oxide can be quantified by observing its ability to withstand a mechanical force. Kim et al conducted this experimentally through scratch adhesion testing shown in Figure 2.3 [40].
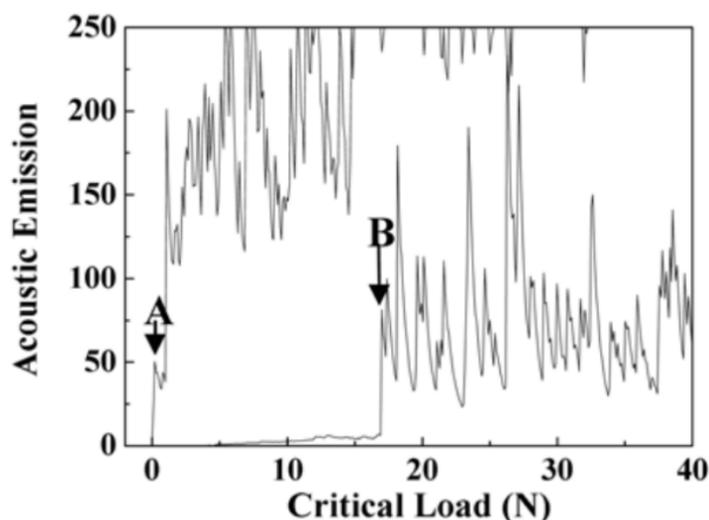

Figure 2.3 – Scratch Adhesion Testing of low carbon steel by Kim et al. The oxide grown at 1250°C clearly shows adherence failure at A (outer scale) and B (inner scale).

Typical outer oxides grown above 1000°C have negligible adherence after any considerable soak time and are highly prone to spallation. While inner scales are able to withstand some mechanical stress, the removal of the encompassing outer oxide enables nucleation of many oxide crystallites with a characteristic whisker formation on the stressed inner scale surface. Schütze et al explored the critical oxide stress, a ratio determining the plastic region of an oxide and critical temperatures at which damage and spallation would likely occur. The study indicated a dependency of critical strains on the physical size of defects within the oxide and young's modulus of the oxide [38]. The behaviour of outer and inner scales can vary dependent on the phases present within in each layer; outer oxides typically obtain a finer grain compared to nearly equiaxed coarser grain

sizes for outer scales. Section 2.2 explores the oxide phases present within high temperature scale and their thermophysical properties under different conditions.

2.2 Oxide Phases and their variation due to Stoichiometry

The oxide structure of scale is highly complex however they can generally be characterised into a three-layer model [26]. Wüstite (FeO), the innermost layer and making direct contact to the steel substrate, is a NaCl type face centred cubic lattice structure with the richest iron content and a p-type semiconductor mechanism allowing high mobility of cations and electrons [15]. The intermediate layer, Magnetite (Fe_3O_4), has an inverse spinel matrix indicating Fe^{2+} occupation of octahedral sites and half of the Fe^{3+} ions occupying tetrahedral sites. Unless at high temperatures, this phase is similar to its stoichiometry and expectedly, contains an intermediate level of oxygen [19][27]. The outer most phase, Haematite (Fe_2O_3), typically presents in two forms, α-Fe_2O_3 which has rhombohedral structure, and a cubic γ-Fe_2O_3. Only α-Fe_2O_3 is present at high temperature due to the oxidisation of magnetite. This phase is the richest in oxygen content with ions in a hexagonal close packed structure and the Fe^{3+} ions occupying around two thirds of the octahedral sites. As a oxide film, Wüstite, Magnetite and Haematite typically display a 95:4:1 thickness ratio at room temperature after high temperature oxidation [41]. The basis for this proportionality is the fact that the diffusion coefficient for Wüstite is greater than that of magnetite and haematite, both of which have slow iron and oxygen coefficients [42].

This ratio and mechanism of oxide growth for each of the phase layers depends significantly on the free oxygen availability and the reheating temperature. Figure 2.4 depicts the iron-oxygen phase diagram, indicating that, during Fe oxidation, Wüstite fails to form below 570ºC and presents a two-phase layer of

Fe_2O_3 and Fe_3O_4 at the metal-oxide interface. The key reason for this behaviour, is the eutectoid decomposition of FeO to α-Fe and Fe_3O_4 but metastable Wüstite can be maintained when sufficient undercooling occurs [43].
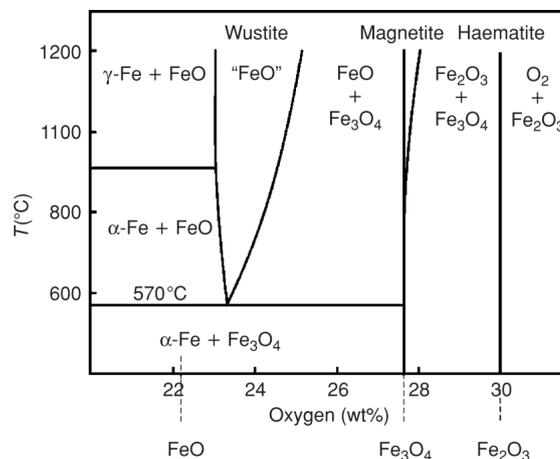

Figure 2.4 – Iron-Oxygen phase diagram describing the phase compositions present within an iron oxide film during reheating [15].

As an example, Chen at al found evidence of a metastable Wüstite structure between 400ºC-500ºC due to finger and flake formation during the reduction of pure haematite [44]. Above 570ºC however, Wüstite is stable and has a rapid reaction rate, causing accelerated growth in this phase and thereby domination in the overall oxide layer. In 1983, Birks and Meier suggested a model detailing the mechanism of oxide growth which underpins the reasons for this accelerated growth and reveals the reactions associated with the multi-layer model [15][29]. At the iron-Wüstite boundary ionisation occurs due to the following reaction:

$$Fe \longrightarrow Fe^{2+} + 2e^- \text{ (1.5)}$$
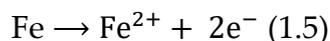
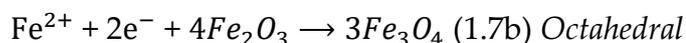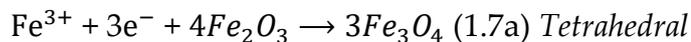Migration of the iron ions and electrons through the Wüstite layer, via vacancies and holes respectively, causes a reaction with Magnetite at the Magnetite-Wüstite interface as shown by equation 1.6:

$$Fe^{2+} + 2e^- + Fe_3O_4 \longrightarrow 4FeO \text{ (1.6)}$$
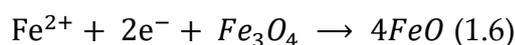
Excess iron ions and electrons from this reaction migrate outward through the magnetite phase over ion vacancies in the octahedral and tetrahedral sites and at

the Haematite-Magnetite boundary. The following reaction, as shown in equation 1.7, occurs to form Magnetite:

$$Fe^{3+} + 3e^- + 4Fe_2O_3 \longrightarrow 3Fe_3O_4 \text{ (1.7a) } \textit{Tetrahedral}$$

$$Fe^{2+} + 2e^- + 4Fe_2O_3 \longrightarrow 3Fe_3O_4 \text{ (1.7b) } \textit{Octahedral}$$

If mobile iron ions are present in the Haematite, new Fe_2O_3 is formed due to the migration of the iron ions over the Haematite layer via ion vacancies together with electrons. The reaction is shown in equation 1.8 and occurs at the atmosphere-Haematite interface:

$$2Fe^{3+} + 6e^- + \frac{3}{2}O_2 \longrightarrow Fe_2O_3 (1.8)$$
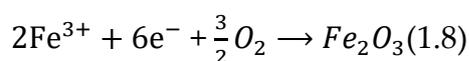
If surplus oxygen ions, when considering the reactions of Magnetite and Haematite, migrate inward in the Fe_2O_3 layer, a reaction will occur with the oxygen ions transported by oxygen vacancies and will form additional Haematite as shown in equation 1.9:

$$2Fe^{3+} + 3O_2{}^{2-} \longrightarrow Fe_2O_3 \text{ (1.9)}$$
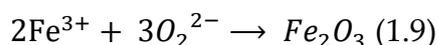
Due to the dominance of Wüstite in scale layers, the growth of this phase mainly determines the overall rate of oxidation. Sun et al found the immediate initial oxidation was extreme for predominantly Wüstite high temperature systems, before falling to a parabolic law after a short time period [22]. The three-layer model identifies the core phases present within an iron oxide, however, in reality, scale structures present a much more complex system. XRD and SEM highlight typical composite phase layers as shown in the work by Raman et al in Figure 2.5 [45].
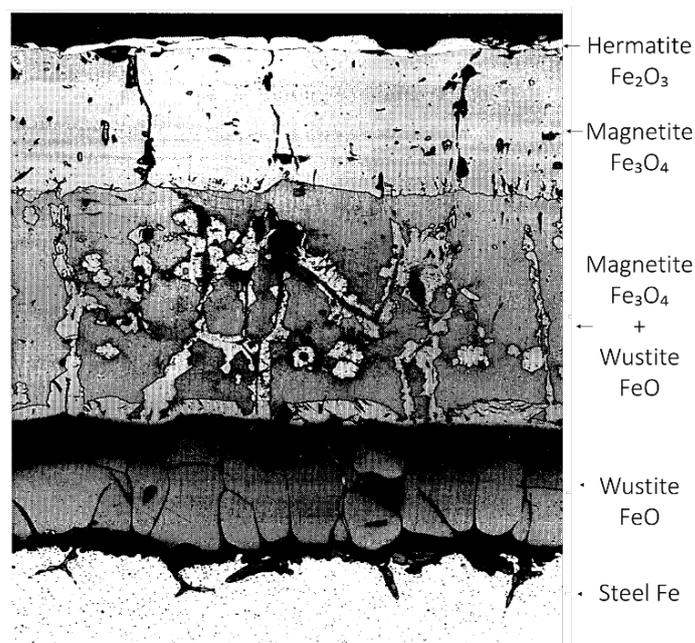
Figure 2.5-Cross section of mild steel revealing the phases of scale oxidised at 1200°C. The Magnetite and Wüstite combine to form an intermediate layer due to the precipitation of the magnetite during cooling [45].

Gas fired furnaces, such as Corby's Gas Barrell SR2 Priest furnaces, produce varying stoichiometric conditions by introducing gas species generated from the fuel mixture. These compounds can include water vapour, carbon monoxide, carbon dioxide and other fuel burn-off products. The presence of these gases, plus the ratio of excess air-gas fuel, significantly alters the growth and phase structure of the oxide [46]. Kofstad indicated that, above 750°C, most steels will oxidise faster in the presence of water vapour when compared with dry air. Furthermore, Rahmel and Tobolski estimated a scaling rate increase of 1.2 and 1.6 at 850°C and 950°C respectively under an atmosphere with water vapour [47][31]. Environments rich in H_2O under a low-oxygen atmosphere, such a 1% O_2-N_2, observed an enhanced parabolic rate constant compared to their dry counterparts and display improved steel-scale adherence with greater scale plasticity. Furthermore, the water vapour plays a key role in preventing a line of large porosities, parallel to the steel-scale boundary, by providing Wüstite an additional free source of oxygen and triggering a growth in the slow growing

grains which are often depleted of oxygen and so typically form deep cavities in the scale layer boundary [46]. Carbon dioxide has a similar but smaller scaling effect on oxide growth with Schmeltzer observing a change from linear to parabolic growth with the introduction of a higher carbon dioxide content. In addition, Sachs and Tuck indicated CO_2 atmospheres develop a crystalline scale with an irregular outer surface, which is attributed to growth of idiomorphic crystals. These crystals form due to surface reactions acting as the primary rate controlling mechanism, therefore preferential planes at the oxygen atom would incur a faster adsorption rate during initial oxidation [29]. Fuel-generated Carbon Monoxide (CO) affects scale growth through blister gas inflation, in which a stress induced blister containing CO, CO_2 and N_2, forms during scale formation [48]. Commonly, CO reacts with iron oxide in a reduction process to form Fe and CO_2 and so is utilised in the greater steel making processes [43]. The rate of this reduction is largely dependent on the Wüstite formation temperatures with reduction being most easy and fastest at the lowest temperature of Wüstite growth.

Reducing agents like CO and H_2, incur significant variations in oxidation kinetics and reaction rate to the interstitial phases present within scale. As an example, Fe_3O_4 is rate limited to solid state diffusion in a H_2 induced atmosphere and causes reduction rate within the oxide to increase with higher increments of temperature [49]. Other studies have indicated FeO instead rate limits to the phase boundary reaction under H_2 and the reduction kinetics follow a sigmoid shape curve between 238ºC - 417ºC [50]. Bonalde et al discovered that Fe_2O_3 ,while also displaying phase boundary limitation, has a dependency on porosity and particle size when determining its reduction rate and found that H_2 the most effective reduction agent compared with carbon dioxide [51]. Additionally, the stoichiometric gas composition during reheating will cause a change in the ratio between phases within an oxide scale. Depending on the temperature, higher free

oxygen contents shift the classical 95:4:1 phase ratio to a more magnetite/haematite heavy composition as shown in the work by Mancheno as shown in Figure 2.6. His investigation centred on tracking the molar concentrations of FeO, Fe_3O_4 and Fe_2O_3 under variations of H_2O, O_2, CO_2, N_2, temperature and oxidation time.
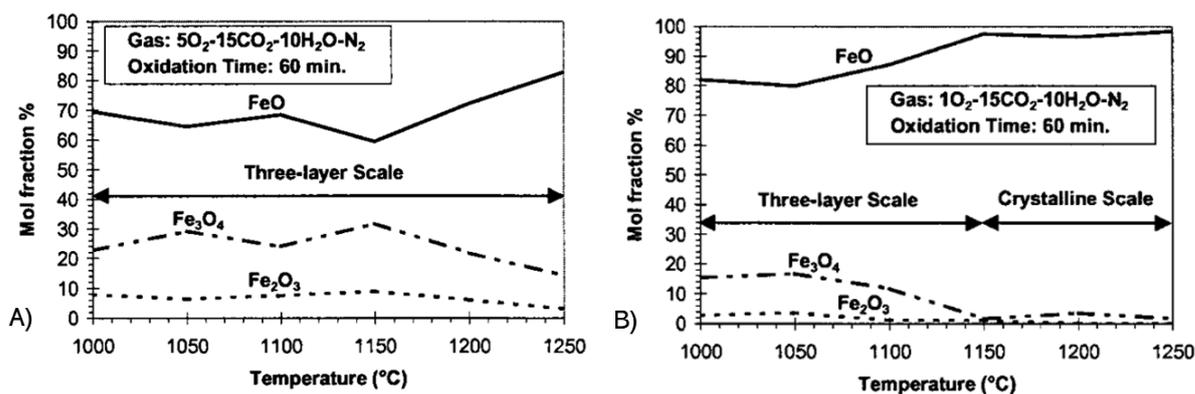

Figure 2.6 – Effect of free oxygen and temperature variation on FeO, Fe_3O_4 and Fe_2O_3 mole fractions for 60 min oxidation time in A) $5O_2$-$15CO_2$- $10H_2O$-N_2 and B) $1O2$-$15CO_2$-IOH_2O-N_2. The investigation also noted the shift between crystalline scales, a Wüstite dominated irregular outer surface with minimal magnetite, and a classical three-later scale [29].

The research also observed changes in phase composition due to carbon dioxide was small at 1100ºC and negligible at 1250ºC. Interestingly, it was found that diluted atmospheres (high ratio of N_2) allow increased magnetite and haematite ratios under increasing oxidation time parameters. This phenomenon was also observed for vapour-free atmospheres, with Wüstite phase decreasing due to gaps forming at the steel-scale interface which significantly reduced the ability of Fe ions to diffuse to the scale layer.

2.3 Surface Cosmetics

Failure of oxide scales is a key challenge to the product quality of steel products due to it causing poor cosmetic appearance and a discontinuous surface uniformity. Often, spallated scale is rolled-in by subsequent steel making processes and produces an increased surface roughness on the substrate, which

is highlighted through added value coatings, a highly detrimental feature if the product is intended to be installed in an open visible area [52].

The mechanical failure of oxides can be categorised into two modes: tensile strain failure and compression stress failure. Fracture in tension occurs when a defect is present within the oxide and the critical scale strain value, ε_c, is reached due to decohesion caused by a differential in thermal contraction coefficient during cooling [37]. This through-scale cracking is dependent on the thickness of the oxide, the Young's modulus of the oxide, the length of defect and the cohesive fracture energy density and an illustration of this mode is shown in Figure 2.7.
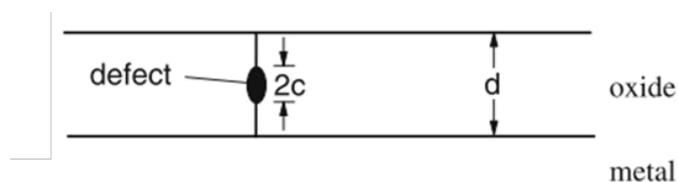

Figure 2.7 – *Through-scale cracking* – A tension fracture due to tensile forces during reheating initiated by a defect in the oxide scale layer. Where *c* is the length of the defect and *d* is the thickness of the oxide scale [21].

This failure is also associated with a delamination occurrence in which crack deflection along a phase boundary interface, such between haematite and magnetite, is induced by the through cracking mechanism. This type of failure typically occurs when the cohesive fracture energy exceeds the relevant interfacial fracture energy. Compression fractures, such as spalling, buckling, crack deflection and interfacial crack growth, transpire due to the external forces acting upon the substrate and the bulking nature of the oxide when undergoing rapid growth. Again, this biaxial compression occurs from cooling and can be initiated through pre-existing defects within the oxide as shown in Figure 2.8; which displays the types of compression failures [53].
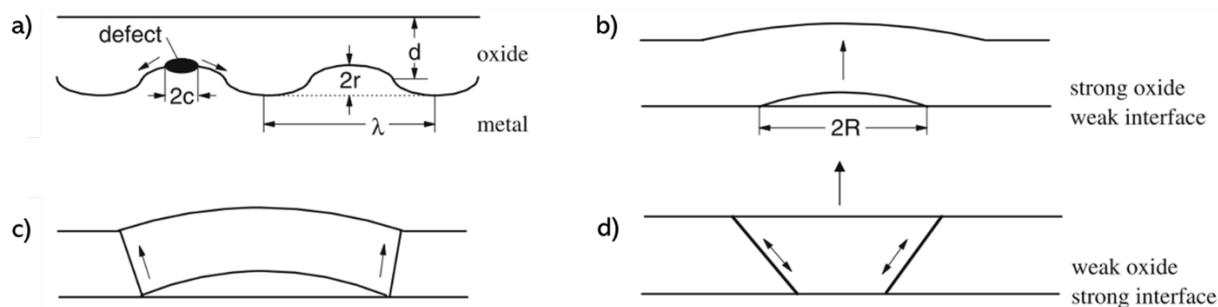
Figure 2.8 – Compressive stress failures types; a) interfacial crack growth, b) buckling, c) crack deflection towards surface, d) spalling [21].

Numerically described by Evans et al, interfacial crack growth is possible due to an existing defect and is related to the amplitude of the interfacial roughness, potentially caused by machining marks, as well the wavelength λ of the rough substrate. Buckling is a result of local delamination and an undulating oxide layer whereby the adhesion strength of the scale-steel boundary is low, forcing the film to buckle under a compression force. Conversely, spalling occurs through a high adhesion interface between the oxide film and the steel substrate. A weak oxide layer will instead shear crack via a wedge mechanism in which an oxide crack will propagate toward the surface and isolate a thickness under the region of decohesion before delaminating a portion of scale upward away from the substrate [54].

Scale blistering, a swollen surface oxidation phenomenon due to gas release at the steel-scale interface, is encouraged by the aforementioned stresses during scale formation. Whilst mainly associated with high carbon content steels, blisters primarily form above 850°C and result in a spotty, irregular and pockmark shaped appearance on the substrate surface at room temperature as shown in Figure 2.9. Alloying elements, chemical composition and heating temperature are all determinants in the onset of blistering but most importantly, it is well understood that sufficient inert gases, like N_2, must be present for the formation to occur [55]. This is due to the partial pressure of these gases preventing the collapse of the blister structure shown in Figure 2.10, but this dependency has

been disputed by Matsuno, who's study indicated that blistering is possible in vacuum environments with a pure non-alloyed iron [56].
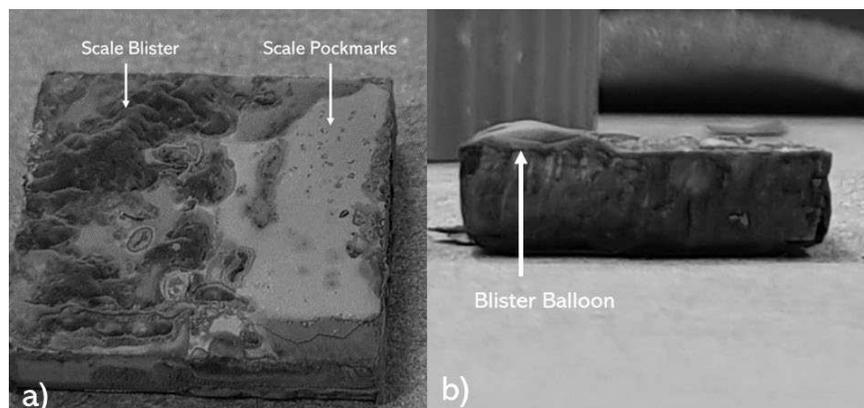

Figure 2.9 – a) Cosmetically unappealing surface of an oxidised low-carbon steel. At room temperature, a mixture of fully formed and punctured blisters appears, as well as pockmarks from nucleation. b) Sideview of a blistered steel sample. Blisters 'balloon' once formed due to the inert gases expanding within the cavity between the scale and substrate.

When observing blisters cross-sectionally, they arch outward over cavities between the steel substrate and the scale. Blisters do not form when a Wüstite monolayer is prevalent in the oxide layer and will only nucleate upon conversion to a three-layer scale [57]. Therefore, the thin scale layer is primarily comprised of magnetite and haematite due to the blistered region terminating iron supply as a consequence of scale delamination from the surface, thus converting the initially formed Wüstite into the favourably oxygen-rich phases. Nucleation, growth, coalescence, shrinkage and collapse are the main five stages of a blister during reheating whereby initial blister formation occurs due to two main mechanisms [48].
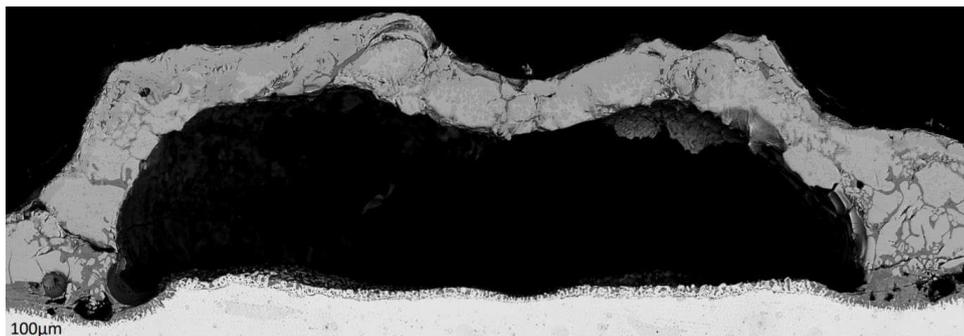
Figure 2.10 – Dewfall's BSD image of an intact scale blister. The arch-like structure is comprised of a magnetite-haematite composition and internal oxidation of the steel substrate is inhibited due to the presence of inert N_2 [58].

Firstly, the gas generations present within raydyne furnaces like CO, CO_2, and N_2 are trapped in the arch-like blisters during reheating before subsequently being released at the steel-scale interface. Alternatively, deformation of the mill scale occurs due to the stress generated during formation. Kondo et al studied the blister formation of scale and proposed a further model of blister nucleation. They concluded that carbon is enriched at the steel surface and leads to an increase in carbon activity, which acts as a catalyst to increase the partial pressure of CO and CO_2 through enhanced reactivity. The scale separates when the pressure exceeds the limit of scale adhesion. Because the oxidation reaction is stopped by scale detachment, carbon begins to diffuse into the bulk steel reversing the carbon reactions and reducing the pressure of CO and CO_2. As N_2 is uninvolved in the reactions, it remains to maintain the blister and provides, along with scale growth stress, a reason for the subsequent growth of the blister in that N_2 gas escapes from the cavity prior to coalescence and rupture. The process is described in Figure 2.11.
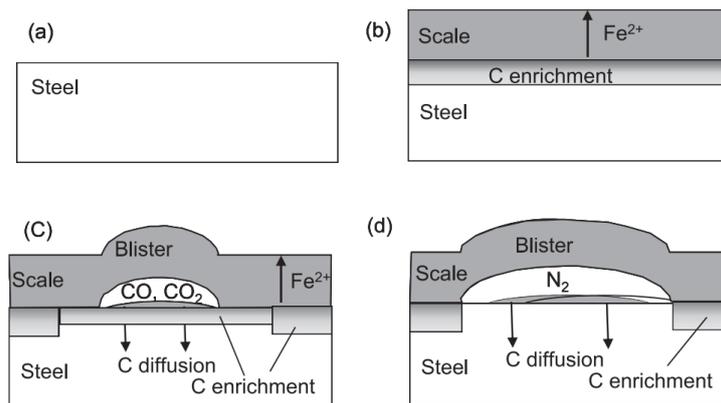
Figure 2.11 – Blister nucleation due to carbon enrichment. The increased partial pressure of inert gases, CO and CO_2 expand the blister outward until equilibrium is reached within nitrogen remaining until the growth stage [48].

The influence of blistered oxide scale and processing conditions on surface quality are largely variable on the manufacturing processes in operation. Hot rolling, where cosmetic appearance is significant, can produce smooth products with surface scale as it achieves high ductility through sufficiently high temperatures and deforms with the underlying bulk material. However, if the oxide does not achieve the required temperature, the ability to flow plastically is removed. Thus, the scale layer cracks and fractures, leaving regions of exposed worked steel to protrude out during hot rolling and make unintended contact with the tool. This causes extrusions and undulations in the slab surface, and subsequent descaling reveals a bumpy or rough surface on the steel sheet. In addition, the presence of alloying elements, like Ni or Si to the steel material for high-strength applications often invokes further cosmetic damage due to the promotion of black stripes on the hot rolled surface.

These phenomena apply to tube-making processes whereby carbon steel tubes expect to produce an absolute surface roughness between 1-10mm. This figure, however, is dependent on the process implemented and Bidmus et al explored how the surface roughness of pipe products varies from the differing main manufacturing routes like HFIW (High-Frequency Induction Welding) or DSAW

(Double Submerged Arc Welded). They found the Cold Drawn process induces the lowest roughness on a pipe product, while conversely, the Hot Rolled process produced the highest surface roughness as detailed in Table 2.2

Table 2.2 - Mean roughness values of pipe products by manufacturing process. Bidmus et al sampled pipe products from numerous sources and evaluated the surface quality using a Mitutoyo SJ-201 surface roughness gauge [59].

Manufacturing Method	Absolute Roughness Range (mm)	Average Absolute Roughness (mm)
Hot Rolled	3.9- 26.0	12.5
Welded DSAW	6.1-14.9	10.7
Hot Expanded	1.7-10.6	5.8
Cold Drawn, then Hot Expanded	2.5-6.3	4.5
Welded HFIW	1.4-9.0	4.3
Cold Pilgering	2.4-4.8	3.5
Cold Drawn	1.0-14.6	3.4
Stainless Steel	1.0-2.1	1.4

Furthermore, the study also evaluated the effect of heat treatment and post-processing treatments of a hot expanded pipe on surface roughness. They concluded that products treated at very high temperatures were far more likely to develop enhanced surface roughness with a 920ºC heat treatment incurring a 370% increase in average absolute roughness. Additionally, chemically treated, and sandblasted pipes in post-processing caused roughness to increase by 34% and 39% respectively.

2.4 Protective Coating Solutions for Oxidation Inhibition

Protective coatings in the application of high-temperature oxidation prevention are well known and recently, high-temperature steel coatings have been divided into three main types of category [60]. The first, active coatings, possess a highly reactive material which acts to prevent solid-state M^{2+} ion diffusion by filling any vacancies within the bulk with alkaline earth such as Ca or Mg. The second category, semi–active coatings, are designed to be a less reactive coating. However, they do react with the existing scale, acting to avoid O_2 diffusion and reducing adhesion to the steel surface. Finally, passive coatings, are designed to avoid any recombination of M^{2+} and O_2 ions by preventing O_2 adsorption to the

surface. These coatings technologies are optimised in formulation to combine both; network builder elements (semi-active or passive materials such as Si or Al) and flux type elements (like chemically active B, Na or K) to enhance oxidation prevention and decarburisation reduction.
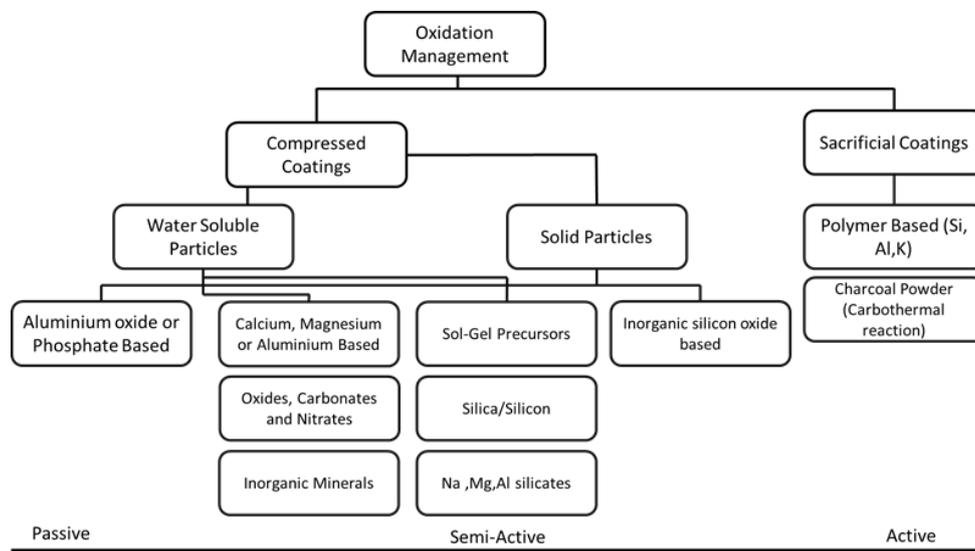

Figure 2.12 – Range of potential coatings for high-temperature oxidation protection screened by Farrugia for Oxmapro [60]. The materials were outlined based on their reactivity characteristics with both scale and steel. In addition, the coatings were categorised by the level of sacrificial design, the intention of the coating's degradation through a thermal cycle.

Elevated temperature protection coatings have been utilised for many years. In the 1960's, the first types of oxidation inhibition in the aerospace turbine application were developed. Largely based on monoaluminides, the coatings were produced through diffusion with substrate alloys and significantly improved sulfidation and oxidation resistance for refractory metals and super alloys operating at 1200ºC. Further researched coatings were outlined into four main categories, intermetallic compounds that formed glassy compact oxides, alloys reacting to form oxide layers, refractory oxides which prevent oxygen penetration and noble metals that resist oxidation [61]. This classification is a similar construct to the categorisation shown in Figure 2.12 and successful coatings of any type must adhere to five key principles. Prospective coatings must; exhibit low growth rate of its protective oxide layer, be resistant to

cracking, show relatively low levels of evaporation, be able to self-repair during reheating and display low rates of reactivity between the coating and the substrate.

For an oxide layer to form an impermeable barrier, it must resist the transport of Metal and O_2 ions and display low intrinsic diffusivity. In addition, the composite must remain close to stoichiometric and exhibits low lattice defect properties. Logically, thicker oxide coatings should offer better protection due to greater displacement for ion and vacancy transport between the steel and the oxidising environment and this mostly agrees with experimental findings in literature [62]. However, beyond a critical thickness, cracking is induced within the material network and the reduction effect is reversed. While localized and small cracks have a negligible effect on oxidation protection, at high temperatures the cracks propagate through the coating film, causing delamination. Any increase in oxidation is likely to be proportional to the region of steel exposed from excessive cracking. As such, porosity is a key characteristic in synthesising an effective coating whereby a highly porous material will allow undesired precipitation of oxygen gas through the film to react with steel surface. In addition, a denser coating usually results in an increased thermal conductivity rating but some porosity is required to tolerate strains and stresses induced during thermal cycling [63]. Scrivani et al reported a 21%-29% porosity within their thermal barrier coatings which was able to relieve the internal stresses within the film and lead to a longer lifetime during reheating [63].

Sections 2.5 and 2.6 outline the literature pertaining to the two main coating technologies researched by this project but a variety of coating types were considered. One example is an active coating system developed by a previous EngD student, Jon Richards. The coating included a coal reaction solution combined with a polyether compound and an activated charcoal powder which would act as a scavenging agent. Theoretically, the O_2 in the atmosphere of the

furnace would be depleted by a carbothermal reaction while also reacting with present mill scale on the steel surface. This technology can be applied using a binding agent such as Polyethylene Glycol (PEG) which will wet the coal powder to the steel surface and is highly viable due to its solubility in water and its relatively inexpensive nature. Further to this, water soluble solutions such as Ca, Ti or Mg are highly effective active coatings, which prevent diffusion and act in two main functions. Through decomposition to carbonates or oxides, the active chemical reaction of Ca to CO_3 or Mg to MgO in the coating layer limited the diffusion of Fe^{2+} and thus inhibited iron oxidation by impacting scale kinetics. Secondly, coatings such as Ti, Si and B mixed with alkaline oxides may act to change the microstructure by adapting the structure, thickness, and composition of the lower secondary scale thickness by forming a physical barrier. ARSA evaluated the efficiency of these soluble coatings on mild steel through an 800ºC thermal treatment and found the most effective solution was $Ca(NO_3)_2$ in water which provided a 70% reduction in scale after 1 minute.

Semi-active solutions such as Aluminium oxide, offer promising scale reduction characteristics alongside favourable mechanical properties such as very high hardness and chemical inertness. Badaruddin et al investigated the application of hot dipped-Al films on low-carbon steels in C_2H_6O-H_2-H_2O atmospheres during long high-temperature thermal cycles. The aluminide layer was designed to form a protective Al_2O_3 by preventing oxygen permeation to the steel surface and they reported a 62% reduction in scale reduction compared with bare steel.
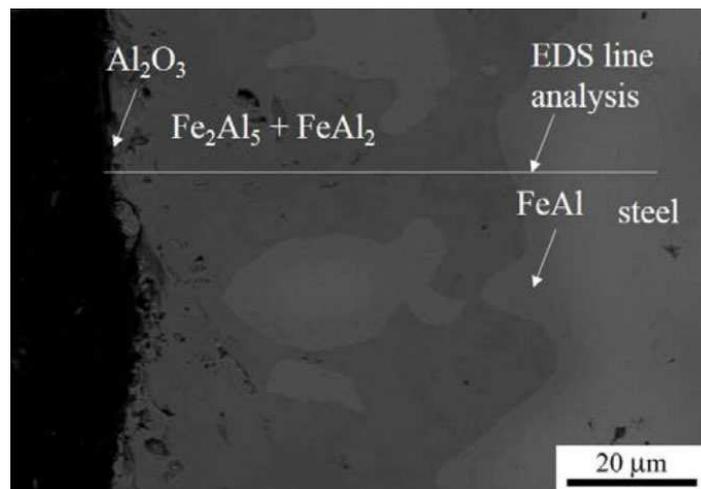
Figure 2.13 – Cross-sectional SEM image of an aluminide coating on low-carbon steel by Badaruddin et al. Morphology of the intermetallic layers and XRD analysis indicate the presence Fe_2Al_5, Al_2O_3 and FeAl [64].

The aluminide coating's effectiveness was achieved through two main mechanisms. The outward diffusion of Al generated a thin but impermeable Al_2O_3 layer at the oxide-atmosphere boundary and is essential in the inhibition of hydrogen and water vapour precipitation into the scale layer. This is significant, as hydrogen permeation is a well-known accelerator of high temperature oxidation because of both increased O_2 permeability and dissolved H_2 causing a loose porous outer oxide which facilitates the transfer of O_2 in toward the metal. Secondly, the intermetallic compounds shown in Figure 2.13 indicate the inward diffusion of Al to react with Fe ions, acting as a kinetic inhibitor and reducing the overall diffusion of Fe to the steel interface.

However, α-Al_2O_3 is the only phase stable phase among Al oxides, which leads to most application methods, such as plasma spray, causing microcracks during coating formation. This is a result of initially present γ- Al_2O_3 and δ-Al_2O_3 phases, transforming to α-Al_2O_3 during reheating, initiating a 15% change in volume which fractures the oxide film. Consequently, Al_2O_3 alone remains an unviable candidate for high-temperature protection but when combined as an addition to other solutions, it provides crucial mechanical properties, like hardness, to enhance thermal life cycling and increase oxidation resistance, as proven in Yttria

stabilized zirconia solutions [65]. Furthermore, the addition of alumina to silicate solutions is a well-understood technology and is detailed in section 2.5.

2.5 Silicate Based Solutions

Recently, silicon-based high-temperature corrosion coatings have been widely researched as a single or multiphase nanostructured ceramic. In addition to possessing a high melting point and good chemical stability, SiO_2 coatings have been reported to provide an excellent barrier to oxidation for substrates such as stainless steels. By preparation of Sol-Gel synthesis, layers of SiO_2 are also reported to offer effective protection against thermal oxidation up to $800^\circ C$ due to their low oxygen diffusivity and active inhibitor release [66]. Aegerter et al investigated inorganic SiO_2 films in the application of corrosion resistance for 316L stainless steel by the application of a thin sonocatalyzed sol oxide via dip coating. They reported greatly improved high-temperature protection but indicated delamination of the film due to the growth of Cr_2O_3 single crystals at the metal interface [67]. In addition, Gugliemi et al investigated the oxidation protection of SiO_2-B_2O_3 coatings by observing differentials in % weight gain of mild steels during a set thermal cycle. They concluded the borosilicate films significantly delayed the onset of oxidation at $550°C$ when compared to bare steel as shown in Figure 2.14, while coating adhesion integrity was mainly dependent on film thickness and formulation composition.
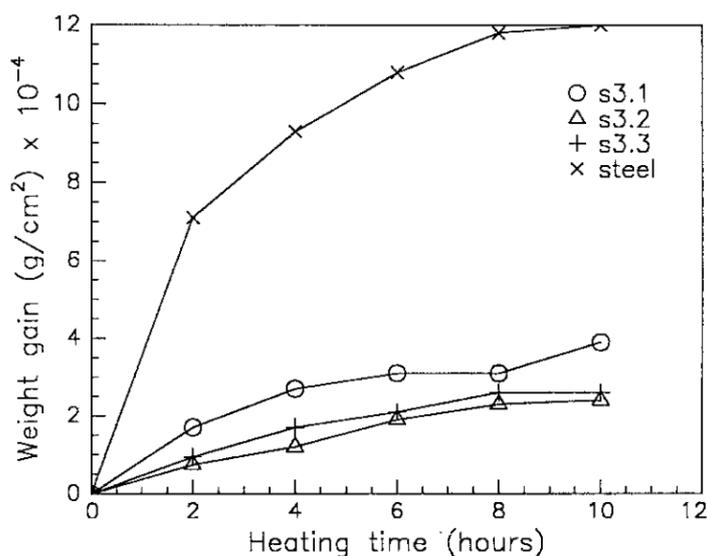
Figure 2.14 – Thermogravimetric analysis of mild steels with dip coated SiO_2-B_2O_3 films (s3.1-s3.2-s3.3) treated at 550ºC in air by Gugliemi et al [68].

SiO_2 composites with other stable oxides, such as TiO_2 and ZrO_2, have shown promising results in the inhibition of oxidation at high temperatures. Due to high chemical resistance to acids, ZrO_2-SiO_2 systems are typically utilised for corrosion inhibition, $ZrSiO_4$, also known as Zircon, is an excellent obstacle to high temperature oxidation and has a favourably low thermal expansion coefficient as well as a high thermal conductivity (3.46 W $m^{-1}K^{-1}$). The barrier protection is due to disassociation during spraying providing a highly stable crystalline ZrO_2 phase in a coating mixture with SiO_2. Karthik et al reported similar zirconium silicate thermal coatings, after elevated heat treatments (800ºC, 900ºC, 1000ºC), exhibited low volume change, a crack-free surface and a pore size distribution which improved microstructure surface stability [69]. Meanwhile, TiO_2-SiO_2 composites are known alkali diffusion inhibitors and increase the protection against air corrosion above 800°C [67]. These films act as geometric blockers; an inert barrier for the steel surface to the atmosphere and cause a reduction in reaction rates consistent with the proportion of surface coverage.

However, one of the most viable and effective ceramic combinations for high-temperature applications is SiO_2-Al_2O_3, also known as Mullite. Previous research

into oxidation inhibiting SiO_2 composites with alumina-based additions mainly centred around materials designed to prevent scale during the reheating of cast slabs. Mullite is one of the most promising Al-based silicates due to being thermally stable up to 1800°C as well as having a high chemical resistance, low density, and low thermal expansion coefficient relative to alumina. In principle, the coating is composed of SiO_2, a refractory powder (chamotte), Al powder, synthetic mica and a dispersion agent [70]. During reheating, the Al converts the mullite within the chamotte, $3Al_2O_3 \cdot 2SiO_2$, into separate components, Al_2O_3 and SiO_2 and forms a metallic silicon by enhanced decomposition of the SiO_2. This metallic silicon oxidises in atmospheric conditions and forms an impermeable SiO_2 film which prevents the diffusion of O^{2-} ions. Additionally, the aluminium is oxidized to form an Al_2O_3 film and a $FeO \cdot 3Al_2O_3$ layer which have the ability to protect against oxidation. However, above 1200°C, this barrier begins to drop in oxidation inhibition due to the formation of fayalite. Fayalite, Fe_2SiO_4, preferentially reacts with the aluminium to form $FeO\text{-}Al_2O_3$ thereby exchanging the SiO_2 to Si and reducing the diffusion barrier [70],[71].

In addition, Torkar et al investigated a similar scale protective coating consisting of SiO_2, $FeO \cdot Al_2O_2$ and $\alpha\text{-} Al_2O_2$ which are impermeable to oxygen. These are formed by an exothermic reaction of chamotte flour and Al powder, degrading and melting respectively between 600-700°C to form the protective films. They concluded the highly prospective not only reduces the scale thickness by 30-60% but also creates a reducing atmosphere by lowering the oxygen content within the furnace. While optimal use is between 1000-1200°C, the coating also exhibits decarburization characteristics at these temperatures, although these findings were conducted for the hot rolling application rather than reheating chambers [72]. Mullite is the only stable phase in the alumina-silica system and the only chemical compound produced by the reaction of $\alpha\text{-}Al_2O_3$ and SiO_2 as shown by the alumina-silica phase diagram in Figure 2.15.
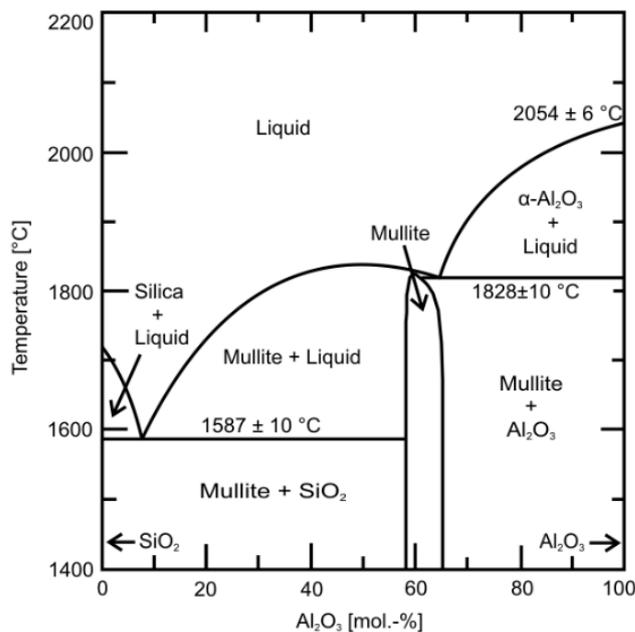
Figure 2.15 – Alumina-Silica Phase Diagram by Aramaki and Roy [73].

These investigations, however, disagree on the congruent nature of melting in Mullite systems and phase formation. Davis and Pask observed incongruent melting at 1890°C and boundary shift of solid mullite solutions to a higher alumina content beyond 1600°C [74]. While Toropov and Galakhov have confirmed findings of congruent melting behaviour in thin fused SiO_2-Al_2O_3 rods made from ammonia alum and crystal quartz above 1890°C [75]. The thermal conductivity of Mullite is reported to range between 5 $Wm^{-1}k^{-1}$ to 7 $Wm^{-1}k^{-1}$ at room temperature dependent on the synthesis route utilised and is independent to temperature up to 800°C. However, a sharp decrease occurs above 1000°C and one study observed a 35% drop in conductivity which is mainly attributed to the highly conductive α-alumina content in the mixture [76]. Conversely, the linear thermal expansion coefficient remains between 4.5 x 10^{-6} K^{-1} to 6 x 10^{-6} K^{-1} for temperatures ranging from 200°C-1000°C which is attributed to the impact grain boundary phases and porosity changes during reheating.

It has been theorised the flattened liquidus curve from 5.5% Al_2O_3 eutectic to the alumina side is caused by silica evaporation. The considerable volatilization of

SiO_2 from the melts of the aluminosilicate allows the mixture to be enriched with Al_2O_3 [77]. With a density of ~ 3.1gm^{-3}, Mullite's crystal structure is similar to that of an orthorhombic aluminosilicate system; sillimanite, whereby the two ceramics have edge sharing AlO_6 octahedra forming chains that run parallel to the crystallographic c-axis. However, spinel or amorphous phases may form due to precursor heterogeneity and depend on the hydrolysis and sintering rates during synthesis. Additionally, Hou et al observed a tetragonal structure with an outer layer of columnar grains from chemically vapour-deposited mullite coatings as shown in Figure 2.16. A secondary interfacial layer below was analysed to be a vitreous $SiO2$-based matrix embedded with Al_2O_3 crystallites.
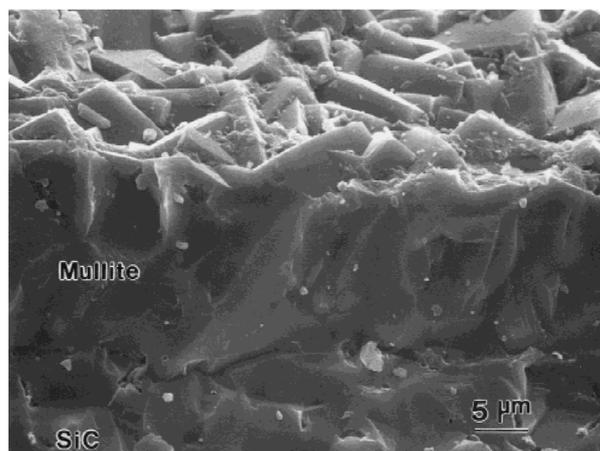

Figure 2.16 – SEM cross-sectional image of a mullite coating deposited onto a SiC substrate by Hou et al [78]. The columnar grains present on the top layer are a result of the chemical vapour deposition process.

Although a promising candidate, plain Mullite presents limitations due to its low fracture toughness, high fabrication temperatures and inability to sustain thermal and mechanical activities once exposed to continuous residual stresses [79]. The absence of a reinforcement phase within the ceramic matrix causes poor stress tolerance and leads to material failure in excessive heating or cooling rates. Therefore, extensive development of reinforced mullite has been conducted; whereby a material is added to the ceramic matrices to provide enhanced mechanical properties during reheating. Natural reinforcement introduces

Mullite fibres, platelets and whiskers to the material matrix and Takada et al reported enhanced strength characteristics such as a 490MPa fracture strength, compared to plain mullite [80].

As one example of a composite reinforcement, Metal inclusions in the Mullite matrix, such as $3Al_2O_3 \cdot 2SiO_2$ – Mo, reduce the growth of cracks and lower the stress intensity at fracture edges by bridging the gap between separated grains. While typically used as an insulation element, molybdenum is a suitable composite material for Mullite due to its highly similar thermal expansion coefficient of approximately 5.8×10^{-6} K^{-1}. As an alternative example, utilising a continuous ceramic matrix, Alumina reinforced mullite is reported to possess very high flexural strength as well as improved hardness and enhanced fracture toughness. Marple et al reported a 75% increase in fracture toughness of alumina infiltrated $3Al_2O_3 \cdot 2SiO_2$ compared with plain mullite as shown in Figure 2.17 [81]. They additionally reported a 35% enhancement in biaxial flexure strength for once 4h-infiltrated mullite-alumina and a 65% improvement in twice 4h-infiltrated mullite-alumina compared with plain alumina. During sintering, a glassy aluminosilicate phase due to alumina inclusions is well known to form due to incomplete crystallization from small amounts of additives in the batch composition and contributes to remarkable mechanical properties when compared with pure mullite. Theoretically because of the thermal expansion coefficient differential of alumina (8.2×10^{-6} K^{-1}) and mullite (4.5×10^{-6} K^{-1}), the wear resistance, crack propagation susceptibility and thermal shock resistance are all improved in an alumina-mullite composite with a high glassy phase content.
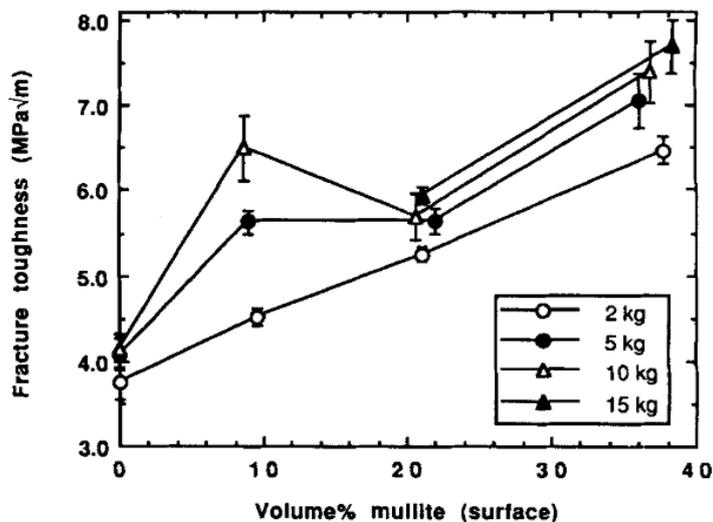
Figure 2.17- Fracture Toughness variation with Volume% mullite in alumina/mullite composites using indentation crack length measurements by Marple et al [81]. Increasing indentation load dependency suggests the presence of residual surface compression.

Kubong manufactured alumina-core/mullite-shell ceramics to investigate the reinforcement impact of alumina on the microstructure and thermophysical properties of mullite. Utilising the sol-gel method with a colloidal silica precursor and alumina powder, Kubong observed the growth of a glassy layer in the matrix and the mechanical performance of the composite was dependent on the phase amount of both amorphous and crystalline phases present. When comparing two silica precursors, he reported that tetraethyl orthosilicate produced a higher porosity compared to colloidal silica, which could accommodate more thermomechanical stress but also noted a poorer thermal shock resistance. Furthermore, samples with enhanced alumina contents contributed to a higher skeletal density of 3.7 gcm^{-3} and may have increased the flexural strength of the material [79]. This is in agreement with Medvedovski, who concluded that $3Al_2O_3 \cdot 2SiO_2$ systems with earth-alkali–alumino-silicate glassy phases were low in brittleness (4.08x10^{-6} B/m) and, achieved a uniform microcrystalline structure and exhibited excellent wear resistance. However, alumina-mullite systems with a higher glassy phase content and lower hardness were indicated to have a poorer wear resistance [82].

Further ZrO_2 additions to mullite systems are well known for their densification attributes. Namely, the mechanical improvements are due to liquid phase sintering achieved by a glassy phase on $ZrSiO_4$ dissociating into ZrO_2 and SiO_2 [83]. Wahsh et al reported excellent thermal shock resistance in $66.8Al_2O_3$-$30.5ZrO_2$-$2.69MgO$ composites, citing a cold crushing strength of 550MPa and a 187% improvement in fracture toughness when doubling the concentration of zirconia in solution [84]. Similarly, Yuen et al found flexural strength and fracture toughness improvements of 15%-30% of mullite composites due to 10%-20% ZrO_2 additions. Zirconia is a representation of a phase transformation toughening mechanism whereby research has shown that the formation of microcracks during cooling improves the fracture toughness of the mullite due to the change of monoclinic crystal phase to a tetragonal crystal, which absorbs stress energy under cooling. In addition, mullite grains are inhibited from further growth because of large ZrO_2 particles pinning at grain boundaries which improves the hardness, sinterability and fracture strength of the material [85]. Abdallah et al confirmed the densification effect through zirconia additions and noted a thermal expansion coefficient increase of 32.2% with increasing ZrO_2 content and enhanced bending strength from 60.66MPa to 83.3MPa in mullite-zirconia sol-gels [86]. MgO additives have been proven to stabilise the cubic and tetragonal phase in ZrO_2-$3Al_2O_3$·$2SiO_2$ composites, as well as rapidly increasing zircon disassociation and acting as a sintering catalyst for cross-linked mullite grains. However, MgO has also been trialled as a reinforcement agent for mullite itself, proving to limit exaggerated grain growth and be vital in forming a close-packed structure. However, Marple et al prepared $0.05MgO$-$0.95Al_2O_3$ powders for mullite synthesis to observe changes in mechanical properties but concluded no discernible change in strength or toughness due to MgO bodies aside from a smaller and more uniform microstructure. MgO presence in the mullite matrix, like zirconia, produces a liquid phase capable of improving sinterability and

enhances the shrinkage of doped mullite bodies, a highly beneficial trait in industrial applications [87].

2.6 Phosphate Based Solutions

Phosphate coatings are typically utilised as a degreasing or passivation mechanism in cleaning applications for cold-rolled metal products. However, due to their porosity, simple synthesis and inexpensive nature, phosphate-based solutions offer a suitable and viable candidature in the search for oxidation-preventative coatings. In particular, water-based polyphosphate solutions, when used as an alkali addition, can be used in small concentrations, are non-toxic and protect against corrosion and scale deposition [88]. Conventionally, phosphate coatings are synthesised by immersing a metal into a bath with dissolved phosphate additions and a high pH acid. Acting as a form of metal pre-treating, the acid reacts with the metal to increase the pH of the bath in the immediate substrate region, which in turn leads to the phosphate being insoluble and crystallizes to a deposited impermeable film on the metal surface [89]. Additionally, the reaction produces a local iron phosphate which also deposits material at the bath-metal interface and this phosphating process is illustrated in Figure 2.18. The concentration of the accelerators introduced has a direct impact on coating fabrication properties such as morphology and crystal size as well as establishing a required temperature equilibrium. Asadi et al investigated thin film phosphate barrier coatings on carbon steel substrates in 3.5 wt. % NaCl solutions for the corrosion resistance application. They concluded that zinc phosphating reduced corrosion current density and that achieving enhanced polarization was possible when coatings were synthesised at 45°C and with a high immersion time thus providing the film with excellent continuity and compactness [90].
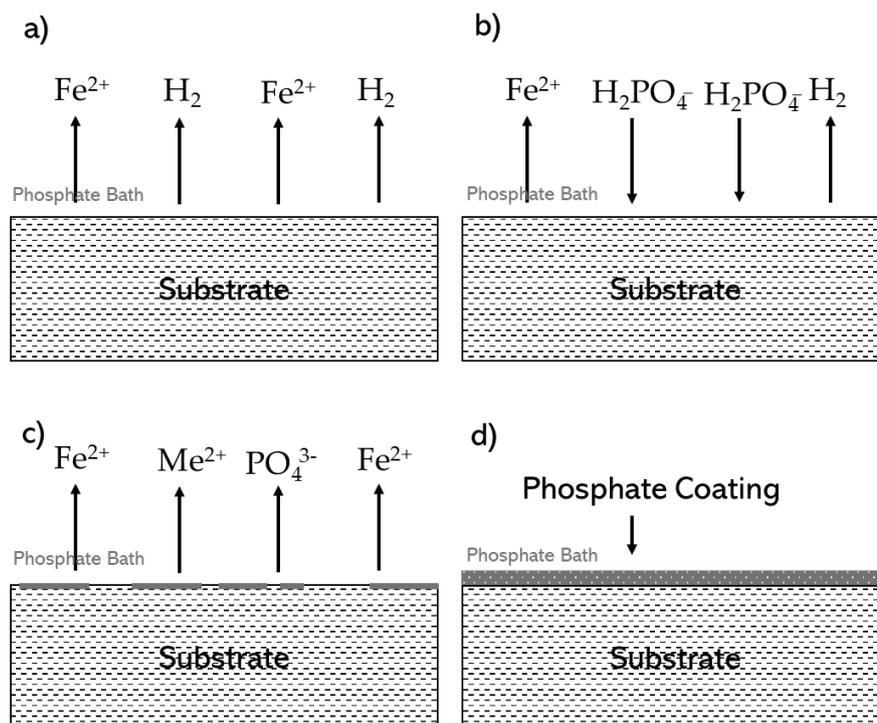
Figure 2.18 – The conventional phosphating process for coating metal substrates. Phosphate material is formed through crystallisation on the surface by a chemical reaction [89].

Recently, research has shown that by introducing cross-linking additions to a phosphating bath, such as a high molecular weight Polyacrylic Acid (PAA), the topcoat adherence and corrosion inhibition performance can be enhanced. Furthermore, the film ductility is improved due to the reduction of crystallite size and the incorporation of PAA segments into the surface structure providing additional adhesive bonding to the coating-substrate interface [91].

Sodium Tripolyphosphate, $Na_5P_3O_{10}$, is an inorganic compound which has been utilised in many applications such as modification in cleaning product ingredients to enhance the ability to penetrate fibres of clothes. Additionally, $Na_5P_3O_{10}$ has been used as a pH buffer to soften acidic water or as a food additive, in which the water-holding capacity of meats and fish is improved, and spoilage is slowed down. It's particularly appealing for industrial purposes due to its very high solubility,14.5 g/100mL at 25°C, and its non-toxicity in low concentration as reported by an FDA categorisation which stated the compound was "generally

recognised as safe to consume". For this application of a feasible protective coating, the benefit of utilising sodium tripolyphosphate is the nature of the compound to hydrolyse into a phosphate in straightforward synthesis conditions which forms a dense microcrystalline structure with low porosity, an ideal characteristic in barrier protection.

Wear resistance is an additional property which can be imparted to carbon steel substrates through phosphate coatings. Useful to reduce surface defects and pockmarks, manganese phosphate coatings are able to withhold oily material, which improves the anti-friction characteristics and enhances corrosion resistance. This barrier protection may be made deficient when the coating is damaged through mechanical, chemical, or thermal stress. However, phosphate coatings possess an advantageous self-healing effect which occurs when soluble phosphates leach from the bulk coating material and precipitate to defective sites for repair.

Similarly, phosphate-based glasses possess useful physical characteristics which have been commercialised for a number of applications in recent years. Namely, the regeneration of skeletal muscle as a reinforcing material or a cell guide when combined with Al_2O_3 and FeO_3. Further, due to their enhanced chemical durability, iron phosphate glasses have been used in the vitrification of high-level nuclear waste. Phosphate-based glasses are built from the phosphate tetrahedra which link to form polymer-like chains in a three-dimensional network. As an example, a P_2O_5 glass network is shown as an illustration in Figure 2.19 where PO_4 tetrahedra are connected through P-O-P chains.
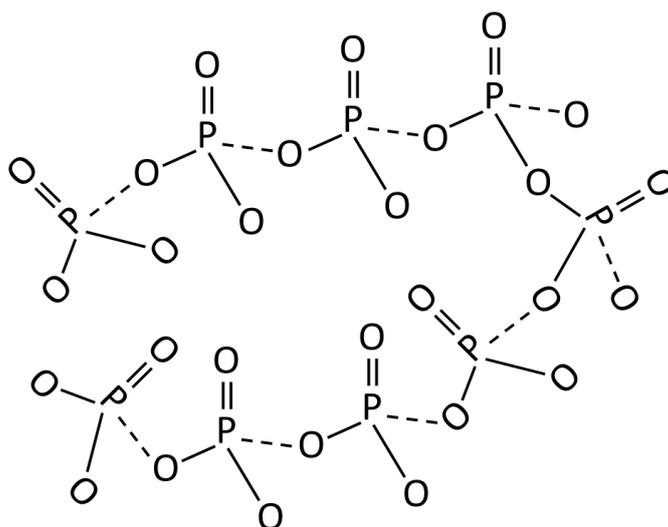
Figure 2.19 – Neighbouring groups of PO$_4$ tetrahedra connected with P-O-P chains. Three of the oxygens on each phosphorous are bonded to nearby P atoms with one oxygen being double bonded to phosphorus [92]. The glass forming substrate in phosphate glass is P$_2$O$_5$ rather than SiO$_2$ in silicates glasses.

This network can be cross-linked by metal cations through non-bridging oxygens which allows for their straightforward synthesis into fibres from a melt due to their polymeric nature. The drawing direction of the phosphate glass fibres is dependent on the alignment of the phosphate chain's axes [93][94]. Unmodified P$_2$O$_5$ has a relatively low melting point of 340°C, a specific heat of 0.170 cal g^{-1}°C^{-1} and possesses poor durability against chemical or aqueous corrosion. Typically, phosphate glasses have been utilised as an immobilizing agent for Na waste through Na-Al$_2$O$_3$ additions due to their enhanced chemical durability. The optimum ratio of Na-P is between 1.0 and 1.3 for moderate melting temperatures (850°C-950°C) but this can be increased along with an elevated 40% alumina content for high temperature applications. Poluektov et al exhibited the glass forming regions in Na$_2$O-Al$_2$O3-P$_2$O$_5$ systems as shown in figure 2.20a and also reported the content of alumina present as a function of the Na/P ratio in figure 2.20b.
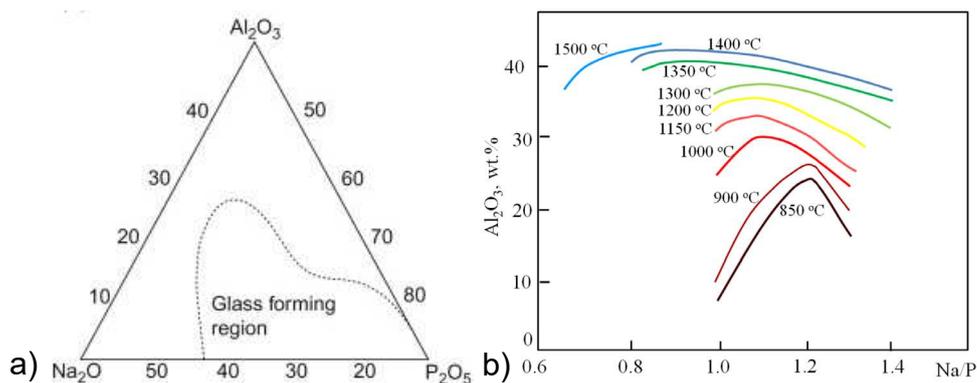
Figure 2.20 - a) Glass forming regions in Na_2O-Al_2O_3-P_2O_5 systems b) Solubility of alumina as function of the Na/P ratio at various constant temperatures [95].

The dissolution of a phosphate-based glass into an aqueous medium is a well-known phenomenon which was first reported by Bunker et al who described a two-part mechanism to depolymerise the structure. The base-catalysation hydration of the phosphate glass network causes the uniform dissolution and a breaking of the P-O-P linkage. Their research aimed to provide chemically durable phosphate glasses superior to silicate counterparts by improving aqueous corrosion resistance. They observed the first stage of corrosion was controlled by surface hydration in Na-CaO-P_2O_5 metaphosphate glasses with weight loss being dependent on the square root of time elapsed ($t^{1/2}$) [96]. However, this is contested by Delahaye et al who proposed the $t^{1/2}$ relationship was in fact due to the increase in electrostatic interactions between the polyphosphate chains caused by an increase in the strength of the leaching solution from reduced dissolution rates [97]. The second mechanism involves the intact polyphosphate chains dictating a linear relationship between time and weight loss during hydration of the glass surface. These hydrolysis reactions can be accelerated in acids whereby dissolved phosphate anions facilitate protonation and the P-O-P linkage is severed. The literature has also indicated that after this hydration, modifier ions such as Na+ or Li+ exchange as protonated species, causing further breakage to P-O-P chains at the glass layer and dissolution of the material. Given the appropriate P_2O_5 content in the

composition, phosphate-based glasses and their fibres are therefore very susceptible to dissolution by aqueous media which proves a highly beneficial property for any coating which is required to be absent after its processing application.

Applications in low temperature sealing glasses have revealed key thermal characteristics of phosphates such as thermal expansion behaviour and glass transition temperature. High thermal expansion properties are prominent in glasses with lower transition temperatures, especially when compared with silicates, and are linked to the degree of polymerization in the network. T_g can be further reduced due to trace amounts of water dissolved into the glass or through the addition of an alkali oxide at 20 mol% [92]. Modifier cations may also increase the thermal expansion coefficient with additions like Zinc and Lead to the glass composition although the most effective formulation contains alumina, as the enhancement of chemical stability is complemented by a reduction in crystallization tendency. A similar observation was made by Szumera et al when investigating the influence of Mn ions on P2O5–SiO2–K2O–CaO–MgO glass systems. They also reported that during crystallization, manganese ions were preferentially incorporated into the phosphate structure ahead of SiO_2 which was associated with an observed reduction in the transition temperature of the glass [98]. Less is known about the stability and crystallization behaviour of phosphate glasses at high temperatures. While devitrification usually occurs above the transition temperature, the glass' ability to resist crystallisation is theoretically dependent on the composition, surface quality, and atmospheric conditions during processing. Li explored this dependency by observing the structural form of glass networks using high-performance liquid chromatography. They concluded that improved thermal stability of a Fe-Na-P glass can be instigated by the presence of stable crystalline compounds. Also, sodium-containing

phosphates generally performed poorer than sodium-free phosphates for crystallization resistance and decreased with the oxygen-phosphorus ratio in the range of 3.04-3.36 [94].

Iron components in phosphate glasses offer promising candidate as a materials selection for numerous applications due to their ability to improve chemical stability and display a melting temperature around 100-200K lower than borosilicate glasses. When an iron phosphate composite is heated to melting temperature and quenched to a glass, it contains a combination of Fe^{3+} and Fe^{2+} ions, the fraction of which is determined by the melting time, atmospheric conditions, and glass composition. Goj et al stated that increasing Na content in iron phosphate glasses causes depolarization of the iron which improves the ΔC_P by 292.3% and decreases the crystallization temperature by 4.6% [99]. While Stoch et al explored why iron phosphate glasses perform favourably as capacity storage for radioactive waste and concluded this was due to exhibited structural expansion, as well as molar volume, increases when exposed to thermal environments [100]. Fe-Na-P glass systems have shown remarkable resistance to aqueous corrosion in recent studies. Yu et al researched the compositional limits of Fe_2O_3 additions in various sodium phosphate glasses and discovered that the more chemically durable P-O-Fe(II) or P-O-Fe(III) bonds replaced the P-O-P bonds connecting the tetrahedra with increased Fe_2O_3 content [101]. These stronger P-O-Fe bonds reduced the aforementioned structural expansion characteristic through a lower thermal expansion coefficient and in glasses with over 30 mol% Fe_2O_3, the dissolution rate significantly reduced to levels normally associated with window glasses. Along with Fe_2O_3, other modifier oxides such as TiO_2 and CaO can also exhibit greater hydration resistance because of their cross-linking effect from network strengthening. As an example, Ahmed et al evaluated the biocompatibility and dissolution rates of $CaO-Na_2O-Fe_2O3-P_2O_5$

systems using XRPD and found that increased CaO mol% content reduced dissolution rates of iron phosphate fibres. Furthermore, the T_g of the composites were tuneable through the content of modifiers as shown in Figure 2.21.
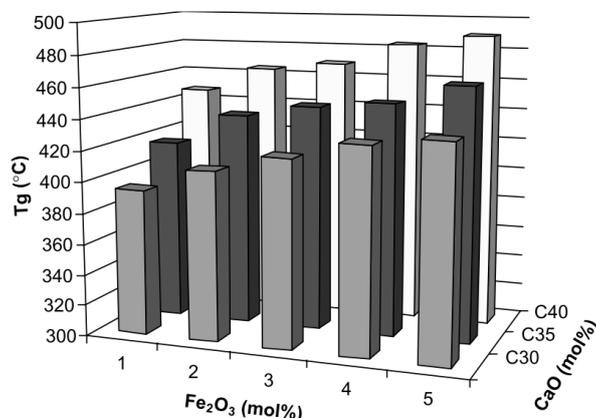

Figure 2.21- 3D Graph depicting the T_g modification through additions of 1-5 mol% Fe_2O_3 and 30-40 mol% CaO [102].

However, it was reported that few of the composites correlated their T_c or T_m with the content increases of the modifier oxides which was expected considering the substitution of Na2O with Fe_2O_3 in this investigation.

2.7 Mechanical Properties variation due to normalisation and thermal properties of adhered layers.

Once a coating is applied, whether phosphate or silicate-based, the impact of the coating's thermal properties may be significant enough to improve or worsen the normalisation process. This section reviews the effect of coatings on ingression thermal energy and the mechanical properties affected by application.

As mentioned in section 1.3, scale oxide poses a challenge to the heat flow from the induction furnace to the underlying bulk steel due to its poorer thermal characteristics. By effectively replacing the scale with a coating during normalisation, an opportunity presents itself to improve the heat transfer coefficient at the surface and increase the ingression of heat energy into the steel. For scale oxide, Hu et al examined the interfacial heat transfer coefficient (IHTCα)

variation due to film thickness as shown in Figure 2.22 and concluded that the average IHTCα dropped by 2461 W/(m²°C) for a 2128.56% increase in scale thickness.

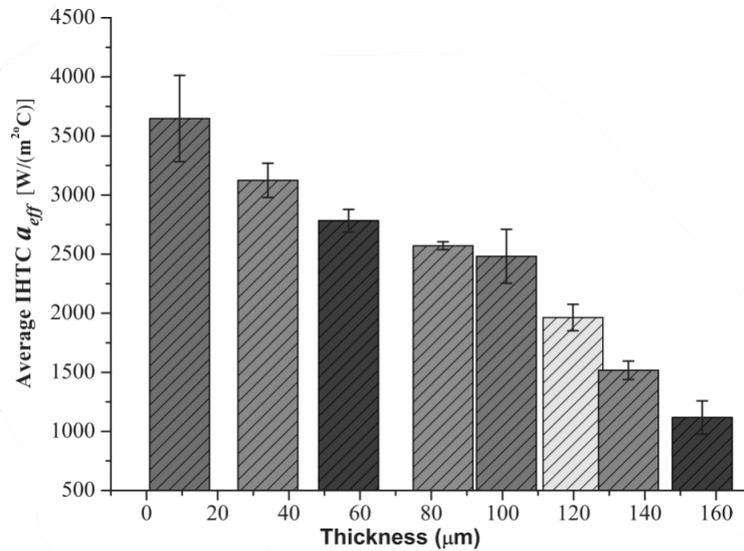**Figure 2.22** – Effect of different scale thicknesses on average effective Heat Transfer, IHTCα, in the hot stamping application by Hu et al [103].

Further, Yukawa et al calculated the IHTC of each of the interstitial phases within the oxide layer by measuring the thermal resistance between the interface and $FeO/Fe_2O_3/Fe_3O_4$ [104]. However, the model and experimental results were based on pre-existing thermal conductivities, λ_i, of the phases and only determined the overall coefficient by considering the thickness as a 3-layer system as opposed to measuring an individual phase structure for its heat transfer properties.

For the low-carbon steel to reach the required temperatures for normalisation, a constant influx of heat energy is provided by both gas barrel and induction furnaces. Clearly, there is a temperature differential between the oxide surface temperature T_P, and the steel surface temperature T_s as shown in Figure 2.23.
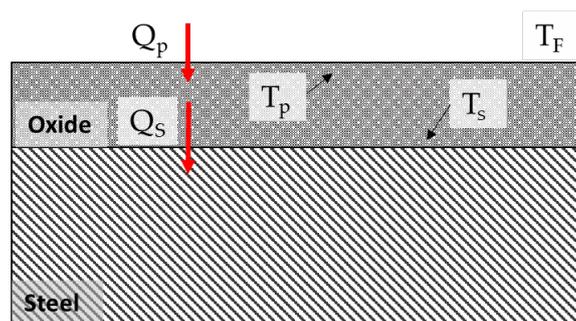
Figure 2.23 – Illustration of the heat flux from the atmosphere of the furnace to the oxide scale. The differential between the heat flux, Q_s and Q_s, is related to the thermal conductivity, thickness, and HTC of the oxide.

The dependence between these factors is shown in equation 2.3, where T_F is the temperature of the furnace, λ is the thermal conductivity of the oxide, δ is the thickness of the scale and HTC is the heat transfer coefficient.

$$T_s = T_p + \frac{HTC\ \delta\ (T_p - T_F)}{\lambda} \quad (2.3)$$

The relative emissivity, ε, of any film layer atop the steel surface is a key property in heat transfer efficiency, as a perfect blackbody radiator would be able to absorb and emit 100% of the ingressional thermal radiation incident upon it. Emissivity is the ratio between the radiant exitance of a material and the exitance of a black body at the same temperature. Therefore, an applied coating should aim for an emissivity close to 1 so as to radiate as much of the absorbed heat energy into the bulk material across the entire surface area of the interface. In the temperature region 500°C - 1200°C, oxide scale possesses an emissivity of *0.85-0.89 which is significantly higher than rolled sheet steel's emissivity of *0.660 due to the oxides' dielectric properties. It is well understood that surface roughness is intrinsically linked to emissivity as a greater interface contact with incident light reduces reflectivity and increases absorption. Sridharan et al investigated the spectral emissivity variation of SA508 steel due to surface oxidation [105]. Initially, the very thin native oxide suggests the optical properties of the material were attributed mainly to the base metal surface causing a low refractive index. Using the Lorentz model for metals, as oxide thickness increases, the proportion of free

electrons decreases which reduces optical constant values and widens the range of wavelengths absorbed by the dielectric scale. Therefore, increased surface roughness and oxide thickness results in a higher emissivity due to the enhancement of penetration depth in the scale layer.

For the previously discussed coatings, the emissivity of mullite fibres is reported to be between 0.8-0.85 while common glasses range between 0.67 to 0.95 depending on the finish and composition [106]. However little research has been conducted on the emissivity value variation with formulation or synthesis factors. Shao et al reported porosity as a key influence on emissivity for MoSi2-TaSi2-borosilicate glass coatings. They observed an emissivity of 0.87 in the lower range of porosity, 0.3-2.5μm, and 0.88 in the higher range, 2.5-15μm [107].

Current anti-oxidation coatings, such as ESPON, also are engineered to prevent decarburisation during normalisation and achieve a uniform surface hardness. While claiming to avoid heat transfer interference, the coating has been reported to provide retention of heat energy in the bulk material after reheating. If achievable, this would be highly advantageous as, along with decarburization prevention, the differential in grain size between the central and surface regions across the steel cross-section can be reduced and ensure microstructure uniformity during cooling [108].

2.8 Synthesis Methods, Application Technologies, and Feasibility Constraints in Industrial Settings

While implementation costs and size are significant factors in selecting a synthesis and application method, ultimately the means to applying the coating will be decided by the characteristics of the material mixture. These factors include viscosity, volatility, adherence to the tube substrate as well as ease of fabrication on the mill. This section will identify the suitable synthesis routes for a potential coating and the compatible methods of application available for the Hot-Finished Corby Mill.

Sol-Gel fabrication is a highly advantageous method Combined with a metal oxide, Sol-Gel coatings share similar characteristics to ceramics, such as oxidation resistance [62], but they do so to a lesser extent and so are not classed as a "classical ceramic". A Sol-Gel commences as a Sol; a polymer network due to colloidal monomers, and then converts into a Gel; a semisolid colloidal mixture suspended in a liquid. Creation of a sol-gel comprises of a solution of coating precursors (alkoxides and polymers) in an alcohol to form a sol. The sol then undergoes a two-step inorganic polymerisation that includes hydrolysis to form a metal hydroxide solution and a condensation reaction producing a three-dimensional gel which is subsequently dried into a hard, thin film [109] [66]. This process is explained in Figure 2.24.
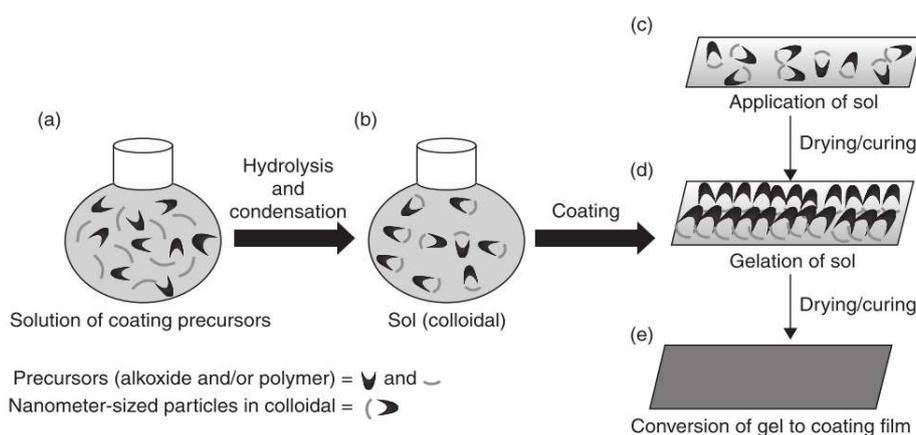

Figure 2.24-Sol-Gel Coating Fabrication [110]. (a) Preparation of solution of coating precursors (b) Creation of sol through hydrolysis and condensation reactions of precursors. (c) Application of sol onto a substrate. (d) Three-dimensional gel formation throughout the medium due to gelation of sol. (e) Conversion of gel into solid coating film after drying/curing.

Sol-gel coatings have largely been used in industry so far to actively manipulate the growth of thin iron oxide films, including research which used iron nitrate and iron chloride solutions to form only the haematite layer during thermal treatments [111]. Other sol-gel coatings include zirconia coatings (ZrO_2) which are advantageous due to possessing similar expansion coefficients of steel. These have been found to reduce oxidation by a factor of 6.5 although for mild steels at a lower temperature range of 450°C to 550°C [112]. Other Sol-Gel investigations

include forming a SiO_2 coating using nanoparticulate SiO_2 sols which, at 800°C, show excellent oxidation protection [113]. This, however, was performed on a stainless steel and may be dependent on if the steel is passivated; both characteristics of which are irrelevant.

Sol-gel synthesis is also effective in forming bioactive glass derivative ceramics which, due to low-temperature processing environments, obtain high purity, intrinsic porosity, and high homogeneity. Traditionally, the alternative melt-quenching method is employed, in which oxide precursors are processed above 1000°C before being rapidly cooled by quenching, fusing one or more of the precursors. The suppression of nucleation and crystal growth due to the high cooling rate causes the melt's disordered state to reduce to an amorphous solid state [93]. However, highly uniform, and thin film coatings are realistically only achievable through sol-gel synthesis routes because of the tunability of microstructural features of the ceramics via the chemical approach. In addition, the sol-gel method is more energy efficient and can produce a wide range of morphologies when compared with melt quenching.

Spray coating offers the most viable application method due to the geometry of the tube products, the uniformity of the film that could be applied and the straightforward implementation of a spray ring into the production line. The coating deposited will be influenced by three key factors: the droplet size and distribution, the spray nozzle angle, and the spray distribution pattern.

Spray coating is described as a pre-metered process in that the average final coating thickness is dictated by the feed rate of the liquid. The technique holds many advantages over other potential coating methods for the following reasons.

- Spraying is typically reliable and requires very few moving parts, therefore reducing the opportunity for maintenance suspensions or user intervention.

- Wholly non-contact applicator, removing any surface defects or inconsistencies that may occur in a brush or roller coating.

- The spray rig can be easily tailored to fit varying tube sizes (from 6″ to 20″ mills) and is able to comprehensively surround the tube geometry in the form of a ring.

- Variable droplet sizes are available between coatings for any viscosity or surface tension.

The mechanism implemented in spray production is critical to coating deposition and is highly dependent on the nozzle selected to generate droplets from the liquid feed. Pressure nozzles offer the simplest option; the liquid feed is forced through a small orifice and breaks up the liquid stream as it passes through into the air. Similarly, turbulence nozzles accelerate the liquid in a rotary manner to form a conical shape as it exits the orifice. Impact nozzles utilise a stationary atomizing surface which breaks up the liquid into droplets when a high-velocity stream of material is directed towards it. The most popular nozzle type is an air-assisted nozzle, illustrated in Figure 2.25, which through the acceleration of high-pressure air, draws liquid material from a reservoir and forms droplets in the low-pressure region, these are subsequently propelled toward the surface through the pressurised air [114].
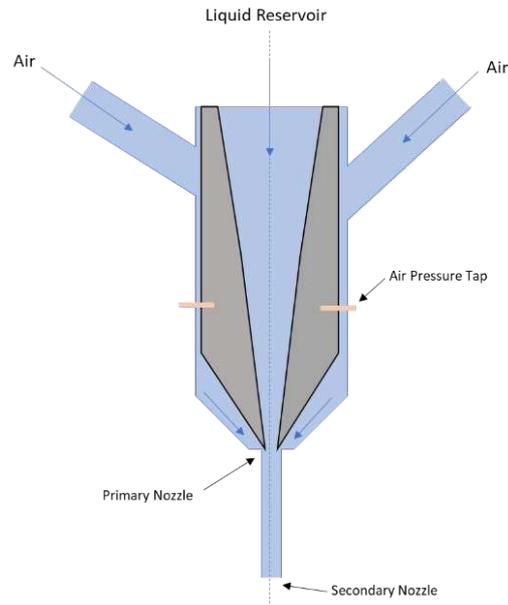
Figure 2.25-Schematic Representation of an Air-Assisted Nozzle. Droplets formed in the low-pressure zone are forced outward from the nozzle due to highly pressurised air.

Depending on the viscosity, particle size and surface tension of the material tested, the feed rate and nozzle type may need to be adjusted accordingly to achieve a uniform coating of the aimed thickness. Moreover, spray coating emits droplets and particles of the material into the atmosphere so health and safety requirements must be considered when deciding if a potentially hazardous material is suitable for such an application method.

The advantage of variable droplet sizes is attributed to correlations in the viscosity and surface tension when compared with water droplets. These correlations are stated in Equations 2.0 and 2.1.

$$D_i = D_w \mu^{0.2} \qquad (2.0)$$
$$D_i = D_w (\sigma/73)^{0.5} \quad (2.1)$$

Equation 2.0 states the droplet size acquired with changes in viscosity, where D_i is the droplet size material being examined, D_w is the droplet size of water of a specific nozzle type and μ is the viscosity of the liquid material in centipoise. Equation 2.1 states the droplet size acquired with changes in surface tension, where σ is the surface tension in dynes per cm^2 of the liquid material.

A potential alternative application method which is suitable for mill implementation is the roller coating technique. These consist of multiple rotating cylinders which transfer material from a reservoir to the substrate via a number of consecutive rollers. However, devising a roller system which could uniformly coat to a tube's cylindrical geometry is a challenge and so the application would occur prior to the HFI welding stage allowing materials transfer onto the flat uncoiled steel substrate.

Additionally, the complexity of the rheological relationship between rollers is enhanced in multi-roll systems leading to undesirable variations in coating thickness. Therefore, a single roll coating design which integrates an air knife following a single roller application may provide the required coating uniformity. The air knife blasts pressurised air at the substrate to remove excess coating material to obtain a constant film thickness [115] as shown in Figure 2.26.
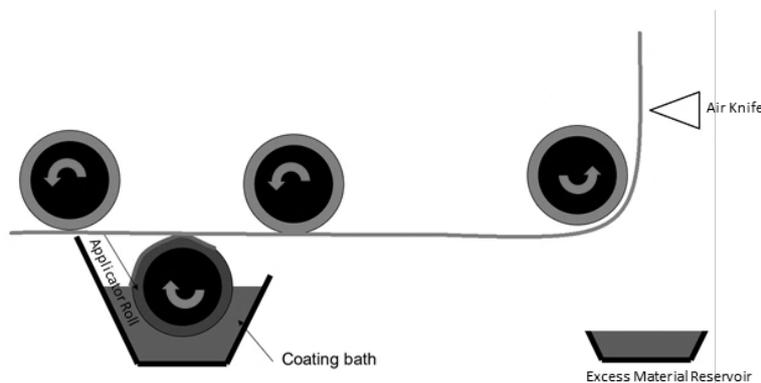

Figure 2.26-Air knife roller coating technique. The air knife provides a film thickness dependent on the air pressure directed toward the substrate. Removed excess is collected via a reservoir and can be recycled back into the coating bath.

The final film thickness in this case is dictated by the factors associated with the air knife; the angle at which the air impinges the coating, the air velocity, the blade opening orifice and the position of the air knife relative to the steel substrate. While air knives provide a non-contact and simple method to alter the coating thickness, improper set-up can lead to irregularities in the coating thickness as well as mottling if the air knife is too aggressive in impinging the

material. Challengingly, the coating must retain its scale inhibition characteristics after adhering to a surface which will undergo high stress rolling and HFI welding and also must not interrupt the fusion of the converging steel sheet edges.

Several other industrial application methods were investigated while conducting this literature review but were deemed highly unviable. These methods were ultimately not considered further for testing due to the nature of their deposition and are listed below.

- **Dip Coatings:** The tube profile must be immersed in a reservoir bath to coat all areas of the product. Not only is the logistical challenge of displacing a sizeable section of tube from the mill and into a coating bath a major difficulty but would also activate the unwanted inhibition of oxidation on the inner surface of the tube. The scale grown on the inside of the tube products is advantageous during its service life, as it provides enhanced corrosion resistance, particularly in the water conveyance application.

- **Electrodeposition:** Similarly, the technique will coat the inner surface of the tube and suffer from the additional shortfall of being integrated between the cutting stage and the heat treatment stage. The tubes are well over 50m in length at this point and an electrolytic bath of such size will be required with a mechanical system integrated to immerse and reintegrate the tube.

- **Physical Vapor Deposition:** The requirement of this technique would involve a vacuum chamber in which a gaseous material, a vaporised polymer for example, is condensed to form a film on the steel substrate. This technique would be between the cutting stage and heat treatment stage and is highly unfeasible due to the significant challenge of creating

a large-scale vacuum chamber and the identical issue of coating all sections of the tube with an antioxidant.

- **Addition to the coolant:** The production mills run several lines of coolant which is applied at the HFI welding stage and throughout the process to cool the CSCT material as it forms the final product. If a liquid material was researched to have sufficient anti-oxidation properties and matched the viscosity of the coolant, the material could be integrated into the coolant as it covers the entirety of the tube before the reheating furnace. Additionally, the mill has an incorporated recycling system to feed the used coolant back into the lines.

The drawback to using this application technique is the limitations imparted on the material to be selected. The materials can't have any volatile solvents nor contain hazardous material due to the locations of coolant deposition (due to H&S considerations) and must not degrade over time as the majority of the material will be circulated through before any implementation into the reheating stage. Furthermore, the coating may alter the coolant chemistry through reaction and cause an equipment blockage due to an increase in the viscosity of the fluid or by deposition of the material within the transporting medium.

Summary of the Literature Review

This Literature Review highlights 5 key topics of interest in discovering a suitable coating for the Install 235 products as summarised below. These consider the current knowledge base and the unexplored scientific understanding associated with high temperature normalisation and its resulting scale.

1. Scale growth is directly influenced by higher oxidation temperatures due to the faster diffusion of oxygen and iron ions. This oxidation rate is highly dependent on the atmospheric composition during reheating, specifically the free oxygen availability and accessibility of iron to the oxidising gas. As this relationship is non-linear above a certain oxide thickness, the only accurate determination of the oxidation kinetics of a system is by mimicking its atmospheric and thermal properties.

2. Surface cosmetic issues attributed to normalisation are caused by scale blistering and mechanical failure of the oxide scale. While much is known about blister formation and its influential factors, like inert gas presence or alloying elements, there are very few examples of bespoke coatings designed to enhance surface cosmetics while also reducing oxidation at the steel surface.

3. Passive coatings are successful in preventing high temperature oxidation by preventing the recombination of metal and oxygen ions. Silicate-based solutions are well-known for effective oxidation protection up to 800°C however are primarily researched for corrosion prevention. These silicate solutions are greatly enhanced with thermally stable additions, like TiO_2 or ZrO_2, but their effectiveness is largely dependent on the synthesis and formulation makeup of the mullite. This is logical, as undetermined sintering temperatures or poor particle size selection could generate non-uniform densification during reheating and subsequent coating failure.

This suggests any mullite solution must first be tailored to the heating rate and thermal properties of its substrate.

4. Phosphate coatings offer promising results in the prevention of oxidation and are an attractive option due to their non-toxicity and affordability. Due to its impermeable microcrystalline layer, oxygen is unable to access the steel surface and phosphates also possess a self-healing attribute which is beneficial for this heavy engineering application. However, its coating properties are strongly linked to the concentration of accelerators and cross-linking attributes. Therefore, the dissolution mechanism of phosphates has not been extensively researched against its impact on the crystallisation behaviour at high temperatures.

5. Scale oxide's poor thermal transfer characteristics create issues for the ingress heat flow to the bulk material during reheating. These thermal properties also directly affect surface quality due to differences in thermal expansion and thermal conductivity between scale and steel. A suitable coating has the potential to enhance the efficiency of heat transfer and reduce troublesome spallation, but only if the thermal characteristics of the coating are well understood - including its interaction with the steel substrate during specific thermal cycles.

Chapter 3

Materials and Methodology

The following section outlines the materials and methodology utilised to perform the oxidation and coating investigations in Chapter 4. In particular, it will detail the standard approach in the determination of oxide thickness as well as the qualitative techniques used to evaluate phase morphology and coating composition. Additionally, details of coating application are explored as well as apparatus or processes generated for experimentation.

3.1 Atmospheric Furnace Construction and its Thermal Cycles

From the temperature specification of the SR2 Mill described in section 1.2, the Nabertherm N 41/H furnace was selected due to its ability to achieve the maximum isothermal temperatures of the Raydyne Induction furnace and flow a custom atmosphere through the heated system. Furnace normalisation treatments were performed within an atmospheric box; a custom-built accessory made for the Nabertherm N 41/H which supplied a constant flow of desired stoichiometry over the sample area as shown in Figure 3.1.1.
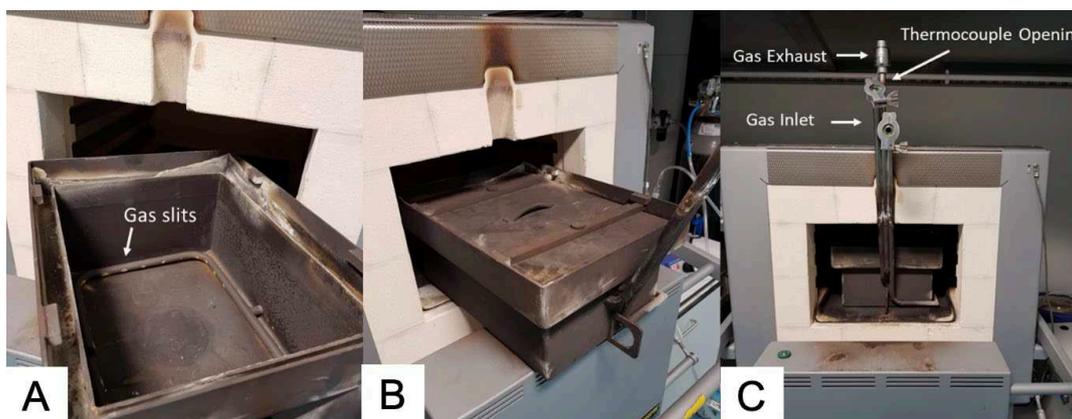

Figure 3.1.1 – Custom Built Atmospheric Furnace Box for the Nabertherm 3000 capable of flowing a desired atmosphere through the sample chamber. A) Open Furnace Box B) Closed Furnace Box C) Fully Inserted Furnace Box with Inlets + Exhausts.

Atmospheric composition was achieved through a novel gas mixing system constructed for the project. The mixing system incorporated volumetric rotameters which regulated the flow of 4 gases utilised for experimentation: CO_2, Ar, N_2 and compressed air. Once a volumetric flow was set, a design of three overlapping inlet pipes, as shown in Figure 3.1.2a, was employed to vortex the gases within the mixing chamber. This was encased in a configuration compromising two stainless-steel domes and a hollow stainless-steel cylinder with a 6-bar pressure release valve as illustrated by Figure 3.1.2b.
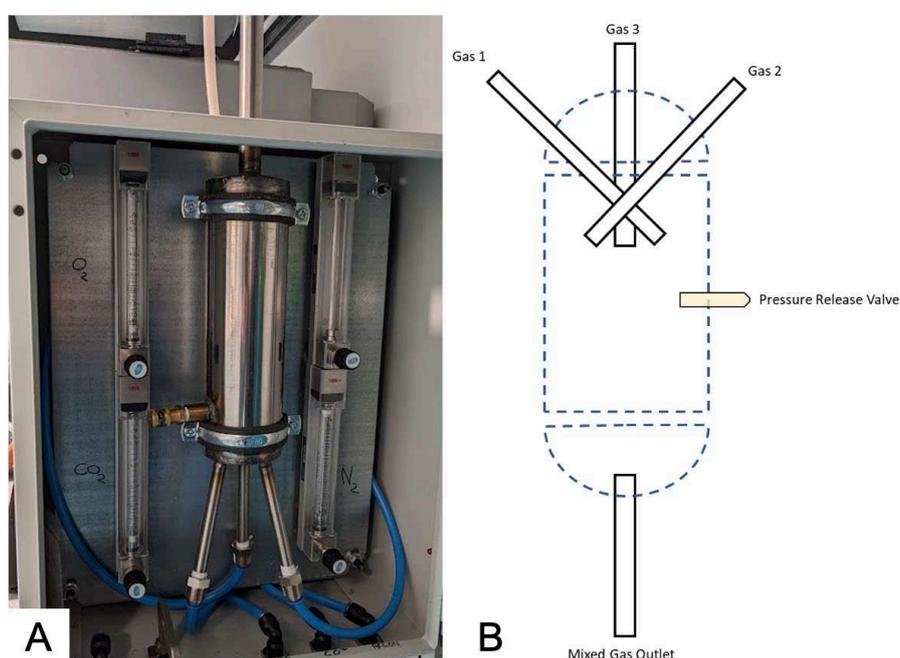
Figure 3.1.2 – a) Fabricated gas vortex mixing system fed by calibrated rotameters b) diagram depicting the design of the vortex mixing system.

To mimic the atmosphere of the gas-barrel furnaces, around 8-12% O_2, a standard flow from the outlet of 12.5L/min was set for all methodologies and the rotameters were adjusted to meet this standard depending on the gas composition required for each experiment. Calibration of the gas chemistry exiting the gas mixing system was performed using a Testo 300 LL flue gas analyser. The analyser examined O_2 concentration in situ and using Dalton's law of partial pressures [116] the required flow rate of CO_2 and N was calculated to

achieve the desired stoichiometry %. An example of a gas calibration used for a partial pressure calculation is shown in Figure 3.1.3.
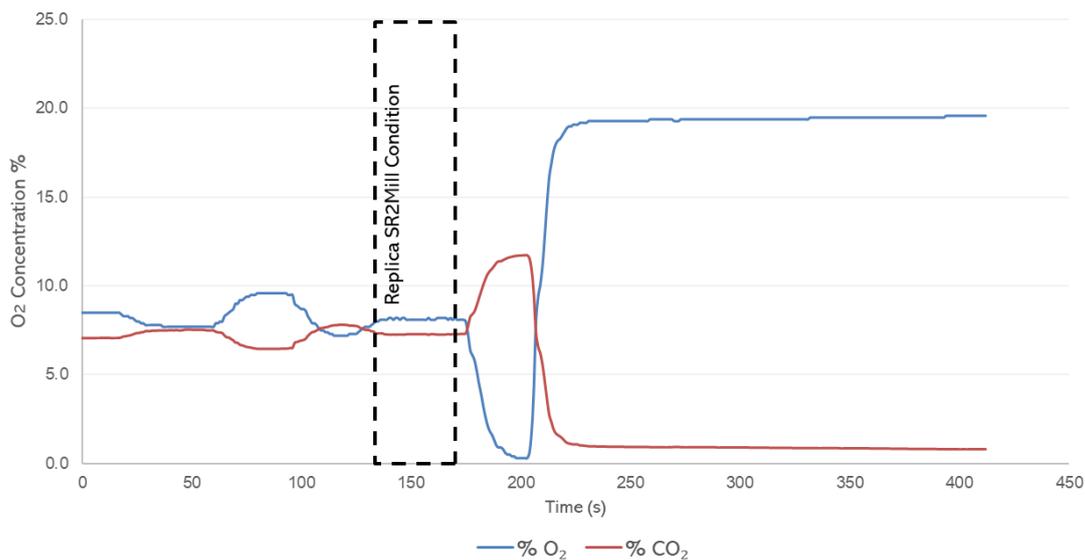

Figure 3.1.3 – Testo 300 LL flue gas analysis of exhaust gas. The highlighted area outlines the achieved % desired for analysis wherein the flow rate was recorded on each rotameter.

RS Pro 1mm type K thermocouples were utilised to measure the sample temperature. The junction end of the thermocouple was welded to a reference steel sample and readings were recorded by a Tenma 72-7715 thermometer. Data acquisition occurred every second by Tenma software and was converted to a CSV. As shown in Figure 3.1.4, the Testo 300 was additionally utilised to record exhaust gases during a thermal cycle, however, due to a gas leakage in the furnace box, this was highly inaccurate.

Figure 3.1.4 – Overview of the Atmospheric Furnace rig in PMRC. The rig consists of gas bottles, mixing mechanism, probe apparatus and a box furnace.

Programmed thermal cycles were designed dependent on the atmospheric composition required and coating investigation. Before each thermal cycle, the furnace was pre-heated to 1000°C so as to return to the desired isothermal temperature (950°C) in a short period of time and reduce heating rate differentials between cycles. In addition, the sample chamber was flushed with argon up until the end of the "Ramp up" Zone to hasten the reducing furnace to its desired O_2 level. Figure 3.1.5 describes the standard programmed thermal cycle (STCA1) and depicts the critical time points when gas flows were turned on/off during the cycle. An argon flush at 15L/min was conducted after the 30min isothermal period had ended to prevent further oxidation.
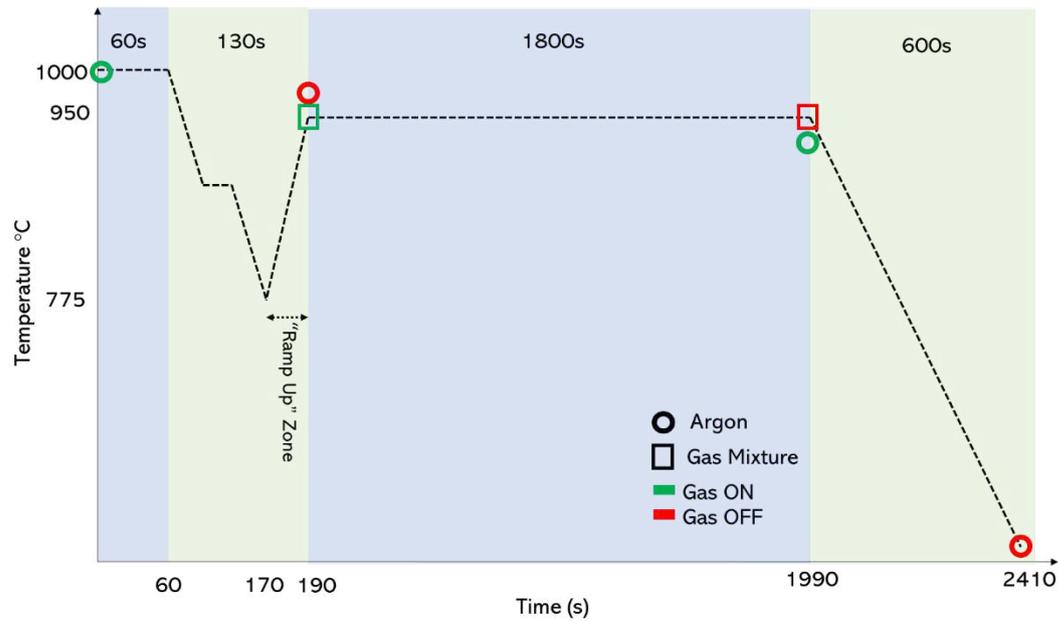
Figure 3.1.5 – Standard Thermal Cycle (STCA1) programmed temperatures as a function of reheating time with gas flow on/off switch points**.**

Close replication of thermal cycles conducted by the SR2 mill in Corby was the aim for the majority of the cycles utilised by the project. The requirement for achieving both the atmospheric composition and isothermal temperature of mill conditions was set out and the current SR2 mill's furnace characteristics were determined through a data acquisition during a work placement. Table 3.1 sets out these conditions and the standard thermal cycles used during experimentation.

Table 3.1 – Thermal Cycles associated with the SR2 Mill and generated standards utilised by this project for experimentation.
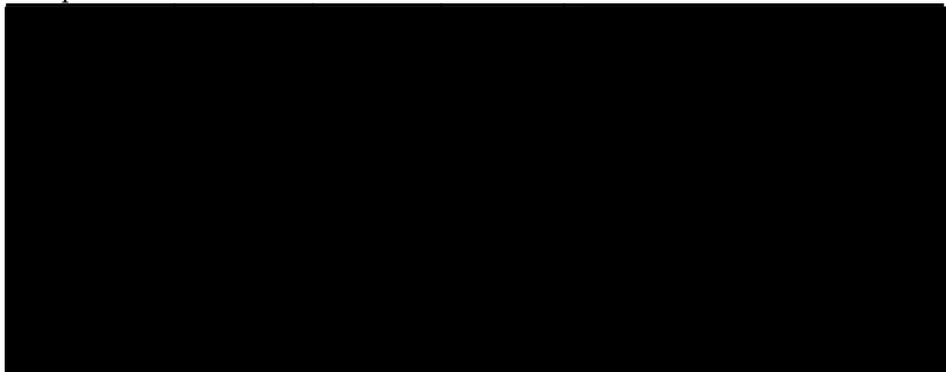
While the presence of NOx and CO is well known and recorded within the SR2 Priest Barrel Furnaces, it was not feasible to bring in and safely flow these gases in the open shared lab at PMRC and so were not considered for experimentation.

3.2 Metallurgical Preparation

Depending on the product specification, three main grades of steel are utilised in TATA Steel Corby to produce the hot-finished carbon steel tubes. For Install Plus 235 products, S235GT or S195T grades sourced directly from Port Talbot are employed for the manufacture of tubes for general industrial conveyance applications. For Inline 265 products, however, P265GH/TC1 grades are utilised to produce higher nominal bore tubes for specialist building and engineering services [117]. Internally, these grades are known as E1, E41 and E24 respectively and were obtained directly from the SR2 Mill prior to the forming stage shown in Figure 1.1 for all oxidation and coating analysis.

Initially sourced as large, 0.8cm gauge, steel plates cut by the QA team in Corby. The grades were subsequently machined into small steel coupons of 3.5cmx3.5cm through water jet milling at PMRC. Prior to any normalisation testing, the coupons had their mill scale removed via a course P120 grit griding paper followed by a fine wet grinding sequence on both sides with P240, P400, P800 and P1200 grit papers. Next, samples were polished to 1-9μm with a monocrystalline diamond suspension, prior to an acetone wash. Steel samples prepared purely for oxidation investigations were polished close to 1μm as shown by Figure 3.2.1a while samples readied for coatings were given a rougher surface or "key" to provide an adequate adhesion for material application. The samples were normalised with the pre-set thermal cycles shown in Figure 3.1.5 and were dependent on each investigation. A 950°C thermal cycle with the Nabertherm 300 is exhibited in Figure 3.2.1b.
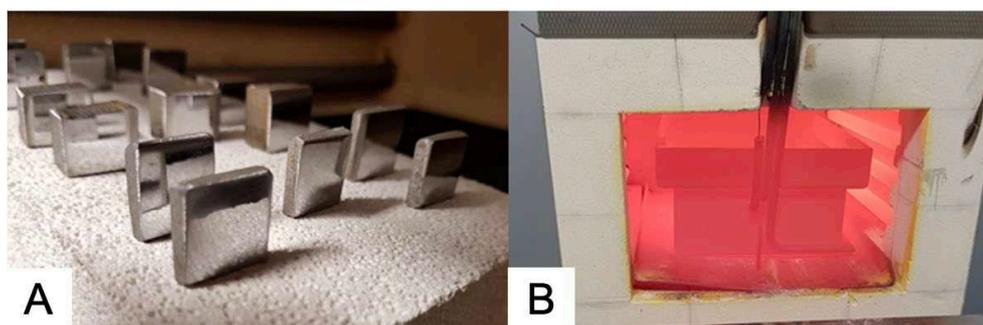
Figure 3.2.1 – a) E1, E41 and E24 steel samples polished to 1µm prior to a 950°C thermal cycle in air. b) Nabertherm 300 and atmospheric furnace box during a 950°C thermal cycle.

After reheating, the steel samples were removed to cool in air outside the furnace box. Then, the coupons were bisected in half via an abrasive cut-off wheel and mounted in Bakelite to reveal a key area of interest, the cross-sectional surface layer. The samples were then ground with sequential grit papers and polished on Chem Cloth to 1µm with a CloreanTech DiaTwin polycrystalline diamond suspension and colloidal silica in accordance with ASTM E3-11(2017) and from techniques described in literature [64]. Figure 3.2.2a and Figure 3.2.2b illustrates the cross-sectional area of interest and the cut-off wheel utilised for bisection. This technique may affect the likelihood of scale adhesion after preparation, however very few samples experienced delamination which ensured the samples did not need to switch to a cold-mounted solution.
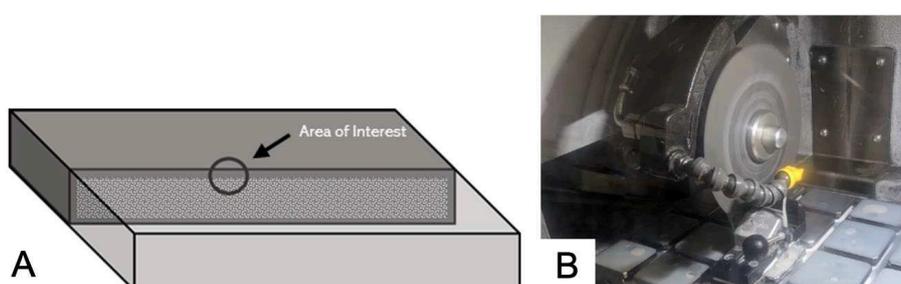

Figure 3.2.2 – a) Illustration of steel sample bisection after oxidation and the area of interest for microscopy investigation. b) Fly Cut-Off Wheel utilised to bisect the samples.

A 20s etch in a $5HNO_3$ - 95 C_2H_6O solution was performed for samples which required determination of the steel sample's grain structure or oxide morphology. Samples prepared for SEM analysis were given an additional step

of a plasma clean. The metallurgical preparation of cutting, mounting and polishing oxidised steel coupons was carried out for all samples which required the light microscopy measurement methodology detailed in section 3.3.

3.3 Oxide Layer Measurement and High Depth of Field Microscopy

As detailed in section 4.2, measurement of the oxide thickness of the scale layer, OxT, was the metric determined to evaluate the performance of the coatings ability to inhibit oxidation during normalisation. The Zeiss Axio Observer microscope was employed as the primary tool to perform these measurements. Capable of Extended Depth of Field (EDF) measurements, high-resolution composite image stitching and auto focus, as well as many post-processing features, the Observer is the ideal choice to record the scale gauge and take macroscopic examinations of the surface layer of sample substrates. EDF was beneficial due to its capability to quickly capture a target with large variations in its surface and retains its transversal resolution during measurement [118]. In accordance with ASTM B 487 – 2007, the layer thickness measurement programme was configured to build a standard procedure for automatically detecting layer boundaries and provide an accurate measurement of the oxide thickness. Images of sample cross-sections were taken at 200X magnification as shown by Figure 3.3.1 which revealed the interstitial layer of oxide residing atop the steel substrate and the Bakelite resin encapsulating the sample.
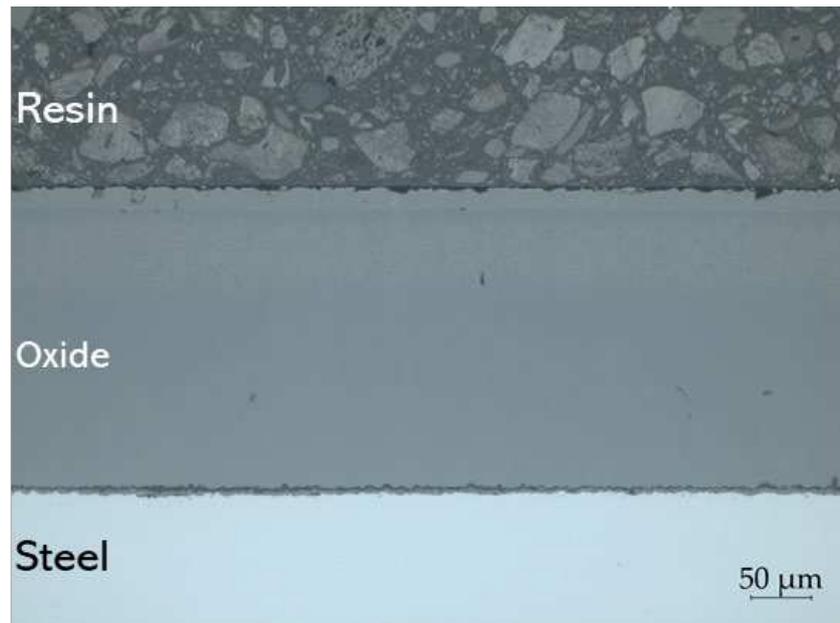
Figure 3.3.1 – Cross-sectional micrograph of an oxidised steel sample at 200X magnification.

The integrated Zeiss image processing software, ZenCore, detected the clear interface boundaries between these layers and distributed vertically parallel measurement chords to determine an average gauge for each sample oxide layer. Figure 3.3.2 displays the original micrograph, the ZenCore measurement chord overlay and the statistical analysis performed with the chords to determine average layer thickness.
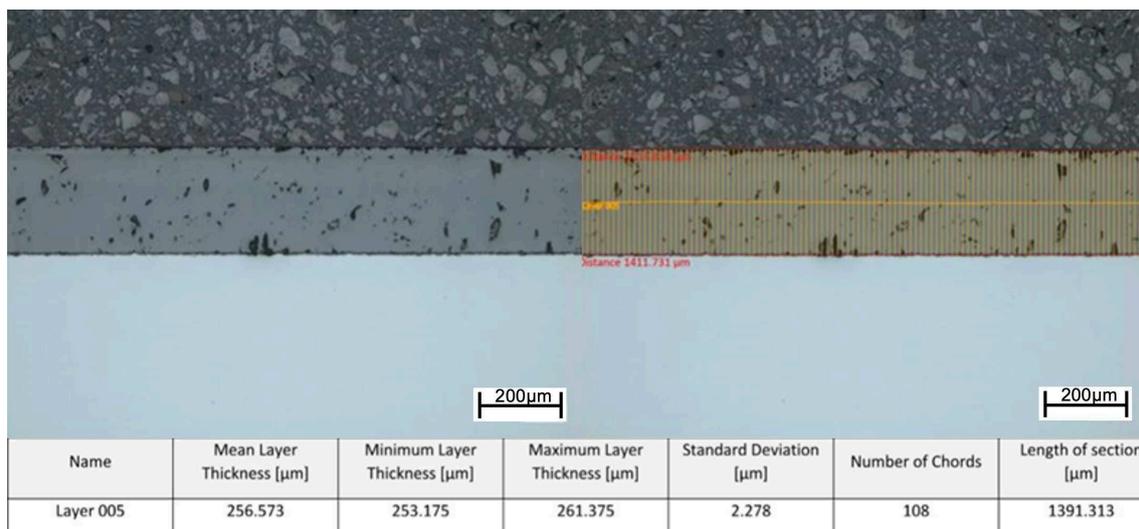

Name	Mean Layer Thickness [μm]	Minimum Layer Thickness [μm]	Maximum Layer Thickness [μm]	Standard Deviation [μm]	Number of Chords	Length of section [μm]
Layer 005	256.573	253.175	261.375	2.278	108	1391.313

Figure 3.3.2 – ZenCore layer measurement software in determination of oxide thickness. The distributed measurement chords are the same gauge as the layer and are averaged to determine the overall thickness.

Unless stated otherwise, the investigations into oxidation kinetics and coating inhibition utilised between 3-10 samples for O_xT analysis and took 5 micrograph measurements from each sample substrate in determination of a final overall oxidation value. In addition, the high-resolution imaging of the Observer allowed the detection of the Wüstite-Magnetite boundary within the bulk oxide by observing the cross-section of the two phases. Phase morphology ratios were determined using the interactive boundary layer method in ZenCore and Figure 3.3.3 displays an example of the measurement chords allocated to the FeO and Fe_3O_4 phases and the associated statistical analysis performed.

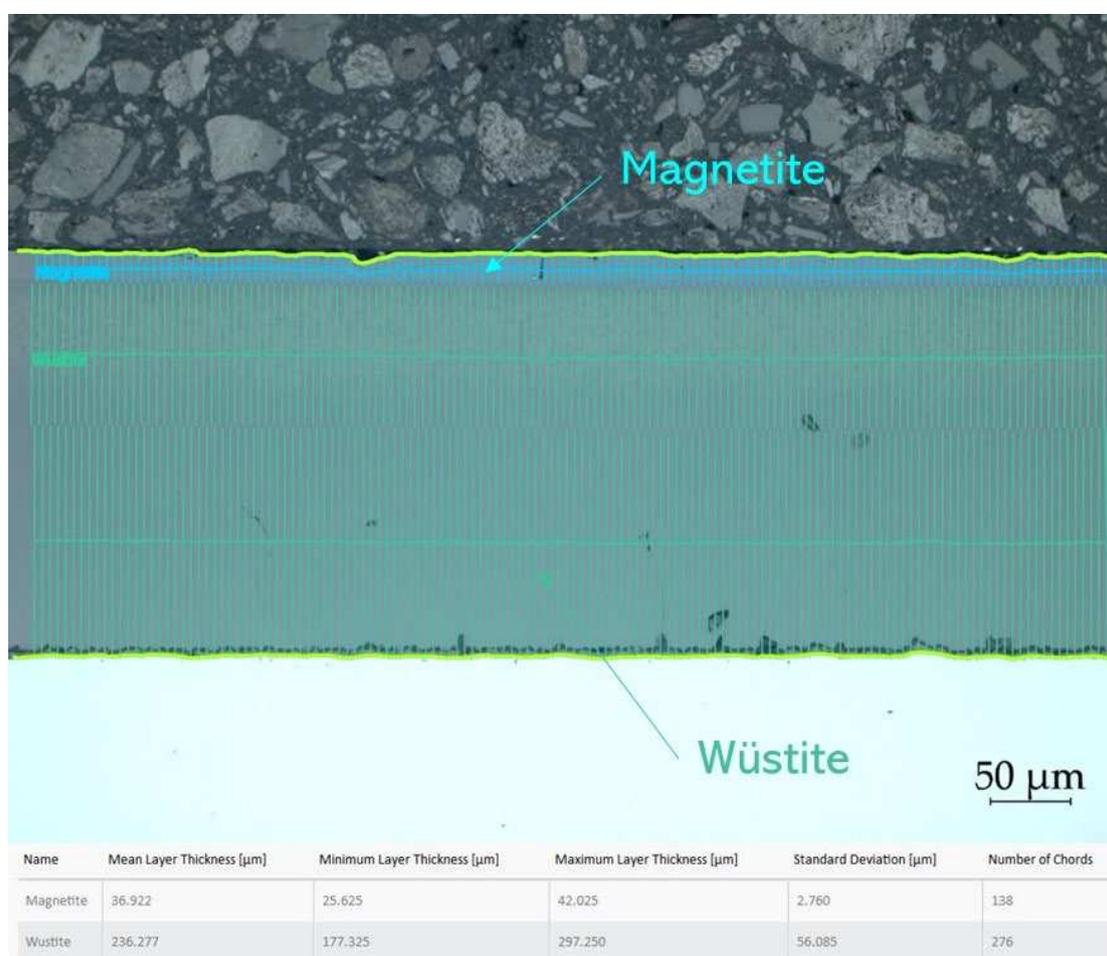| Name	Mean Layer Thickness [μm]	Minimum Layer Thickness [μm]	Maximum Layer Thickness [μm]	Standard Deviation [μm]	Number of Chords
Magnetite	36.922	25.625	42.025	2.760	138
Wustite	236.277	177.325	297.250	56.085	276

Figure 3.3.3 - ZenCore layer chord measurement of an oxidised steel sample in the determination of its Wüstite - Magnetite phase ratio.

Further light microscopy was conducted for coated solutions using the Zeiss Smartzoom 5. The Smartzoom produced high-resolution, high depth of field

images over large areas through image stitching and coaxial illumination with EDF. Additionally, the automated height adjustment and autofocus for each focal point in the image allowed the software to determine a depth profile and could thereby generate a 3D visualisation of the surface topography. Useful as a macroscopic view of surface roughness, Figure 3.3.4 displays a topographical map of a coated solution (Sopac20) generated through EDF processing and can detect differences in surface geometry within the µm-mm scales.
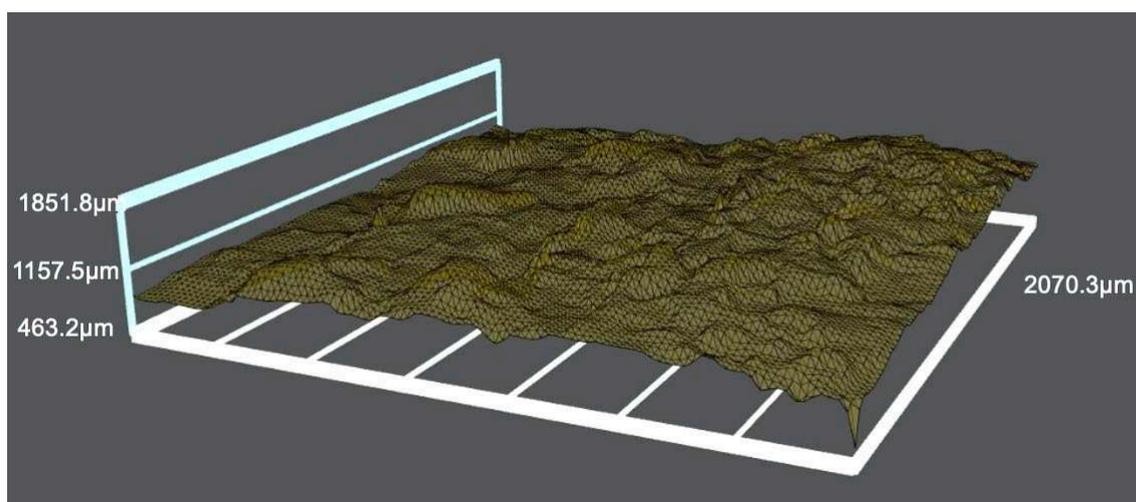
Figure 3.3.4 – Smartzoom topography map of a Sopac20 solution generated through EDF imaging. Depth profiles are associated with the focal heights of each pixel during acquisition.

Other light microscopy techniques in this project included the ZenCore grain size analysis programme and ImageJ software which was utilised for various mechanical tests as described in section 3.4.

3.4 Mechanical Testing Methods

For standardised testing of the steel samples and in the evaluation of the impact of an applied coating on their thermal transfer characteristics, two mechanical tests were employed. Firstly, a determination of the cross-sectional variation in samples' grain size after normalisation, and also a parallel investigation into the cross-sectional variation in material hardness.

In grain size evaluation, BS EN ISO 643:2020 was employed through the Observer's grain size measurement programme. The standard utilised the mean line intercept method (MLI) to provide an accurate 2D depiction of average grain size distribution [119]. Equation 3.4 explains how an average grain size diameter ($\acute{l}$) is calculated from the total length of lines (L_T), the magnification of the micrograph (M) and the number of intercept points (N).

$$\acute{l} = \frac{L_T}{PM} \qquad\qquad (3.4.)$$

The Abrams three-circle procedure was used for MLI analysis by ZenCore software as shown in Figure 3.4.1 in which N is recorded for every intersection with a circle.
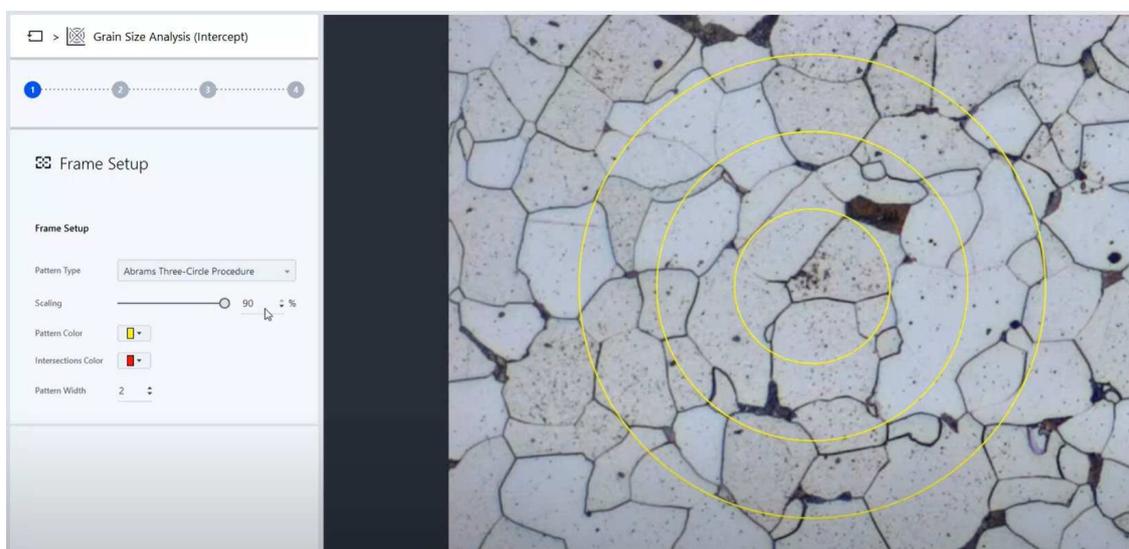

Figure 3.4.1 – ZenCore grain size programme implementing the MLI Abrams three-circle procedure to determine average grain size diameter.

To observe the variation in grain size throughout the cross-section, a continuous vertical stich at 200X magnification was generated and multiple MLI analyses performed across the width of the steel substrate as shown by examples in Figures 3.4.2

Figure 3.4.2 –Cross-sectional Vertical Stitch at 200X magnification for a Grain Size analysis of Sopac20 coated E1 Steel.

Similarly, hardness testing was observed along the substrate cross-section, whereby the steel grades were subjected to a standard Vickers test with 1Kg load and 10s dwell time using an Innovatest Nexus 4303. The equipment impresses a diamond indentation into the material, from which the Nexus software analyses the edge of the profile in order to evaluate a value for hardness as shown in Figure 3.4.3
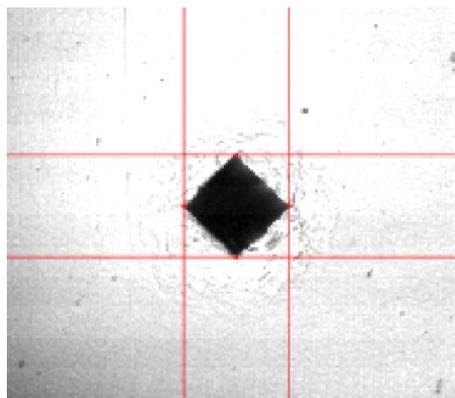

Figure 3.4.3-Indentation of E1 surface from a 1Kg load 10s dwell time with software analysis of an uncoated steel sample.

The measurements were taken in fixed intervals along the cross section of the substrate to determine the variation in hardness as displayed by Figure 4.1. The central hardness variation is a direct indicator of ingressional thermal energy into the bulk material [2]. Hardness acquisition intervals were at least 0.3mm apart to avoid case hardening. A representation of the automated hardness acquisitions made by the Innovotest is shown in Figure 3.4.4.
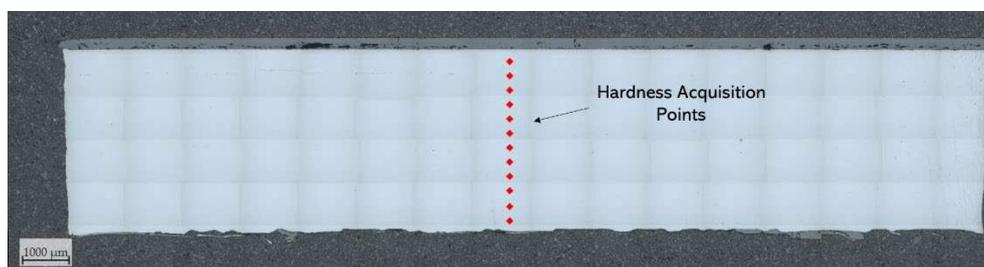

Figure 3.4.4 – 20X magnification stitched overview of an uncoated E1 steel after reheating. Hardness indentations were made along the cross-section of the substrate.

Adhesion properties of coating materials were tested using the Cross Hatch pull-off testing method under ASTM d3359-22. The standard involves cutting the

coated surface with a sharp edge into a square grid and applying a scotch tape over the marked area. After smoothing to remove remnant air bubbles, the tape is removed rapidly, and the grid area is inspected for material flaking and delamination. Figure 3.4.5 details the classifications attributed by ASTM d3359-22 for the levels of material removal after pull-off [120].
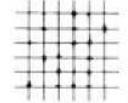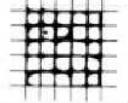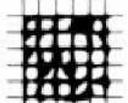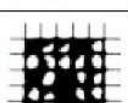
Description	Performance	Class(ASTM)
The edges of the cuts are completely smooth; none of the squares of the lattice is detached		5B
Detachment of small flakes of the coating at the intersections of cuts. A cross-cut area not significantly greater than 5% is affected		4B
The coating has flaked along the edges and/or at the intersections of the cuts. A cut area significantly greater than 5%, but not significantly greater than 15% is affected		3B
The coating has flaked along the edges of the cuts partly or wholly in large ribbons, and or it has flaked partly or wholly on different parts of the squares. A cross cut area significant greater than 35% is affected		2B
The coating has flaked along the edges of the cuts in large ribbons and/or same square have detached parity or wholly. A cross-cut area significantly greater than 35%, but not significantly greater than 60% is affected		1B
Any degree of flaking that cannot even be classified		0B

Figure 3.4.5 – ASTM d3359-22 classification of Cross Hatch adhesion testing. 5B indicates a very high level of adhesion associated with a coating while 0B indicates a very poor adhesion with near total delamination [121].

In addition, the surface porosity, P_t, of coated samples was calculated through ImageJ post-processing of either a SEM or light micrograph. As the metric determines the fraction of pores to total surface area, as shown by equation 3.5, the porosity indicated the permeability of the coatings during reheating [122].

$$P_t = \frac{Surface\ Area\ of\ Pores}{Total\ Surface\ Area} \tag{3.5}$$

To evaluate the surface area of pores for a coating material, ImageJ generated an overlay mask which traced the edges of the pores in the micrograph. The porosity mask shown in Figure 3.4.6b allows ImageJ to calculate the ratio of black-white surface area to determine P_t.
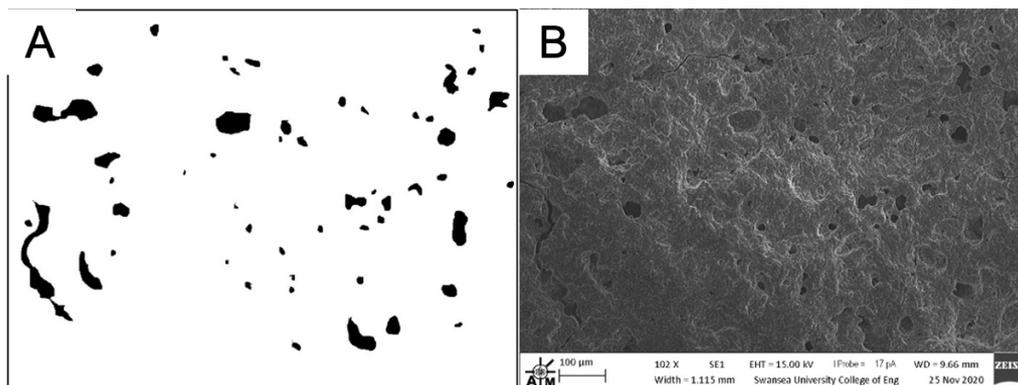
Figure 3.4.6 – a) Surface SEM image of Sopac20 coating b) Porosity mask generated by ImageJ post-processing.

Determination of the steel grades' chemical composition in section 4.1 was performed through Optical Emission Spectroscopy (OES). The technique utilises a high voltage source through an electrode, which generates a discharge due to a high potential difference between the sample surface and the counter-electrode. This produces an electrical arc, vaporising atoms of the surface material which emits a characteristic spectral pattern which can be detected for elemental analysis [123].

3.5 Scanning Electron Microscopy

Scanning Electron Microscopy (SEM) is a specialist instrument that uses focused electron beams to analyse and image a sample. The signals that are generated from the interactions of the high energy electrons and the sample reveal information about the material's morphology, composition, orientation, and crystal structure. The high-resolution topographical images convey the signal electrons surface interactions with the specimen for around a 1µm depth and conventional techniques can magnify from between 20X to 30,000X with a spatial resolution of between 5-10nm [55] [56]. Combined with optical microscopy, the measurement of the thickness of the scale phases by observing the cross-section of normalised samples has been achieved with SEM [57]. The SEM functions by accelerating electrons from an electron gun source at 1-30 keV as described Figure 3.5a. The electron beam is then shaped into the form of a condenser lens by the

anode before direction into a condensing lens by the magnetic lens. The scanning coils impart a magnetic field over the electron beam to deflect the beam in the horizontal and vertical directions in order to achieve a raster scan over an area of the sample surface. The SEM utilised for this project was the Zeiss Evo LS25, as shown in figure 3.5.1b, and images were processed using Evo 18 software.
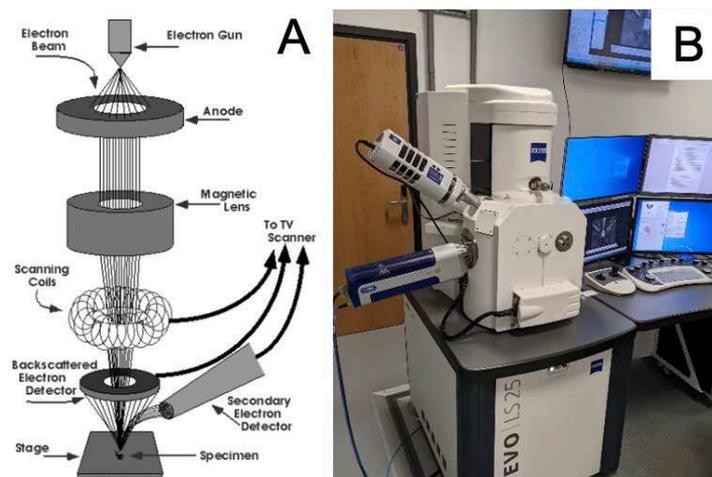

Figure 3.5.1-a) Schematic of the operation of a Scanning Electron Microscope [124]. The secondary electron detector gives an output exhibiting the topography of the sample through Electron Back Scatter Diffraction b) Image of the Zeiss Evo LS25 at Swansea University Bay Campus.

The secondary electron detector provides an output exhibiting the topography of the sample through Electron Back Scatter Diffraction (BSD). This is highly relevant for scale research as BSD has been indicated in recent years to be a powerful tool in characterizing the phases within scale [27] [29], particularly for low carbon steel. With such a technique, additional information about the grain size, phase boundaries and morphology of the material can be identified [7]. Significant improvement in the resolution of SEMs has been possible due to enhanced accelerating voltages (and therefore velocity) thus reducing the wavelength of the electron.

$$\lambda = \frac{h}{mv} \tag{3.6}$$

This can be explained by the de Broglie wavelength, λ, in equation 3.6 which dictates that the velocity of the electron, v, has an inversely proportional relationship to the source wavelength. Figure 3.5.2 displays the advantage of BSD when trying to understand phase morphology and grain structure for oxide analysis.
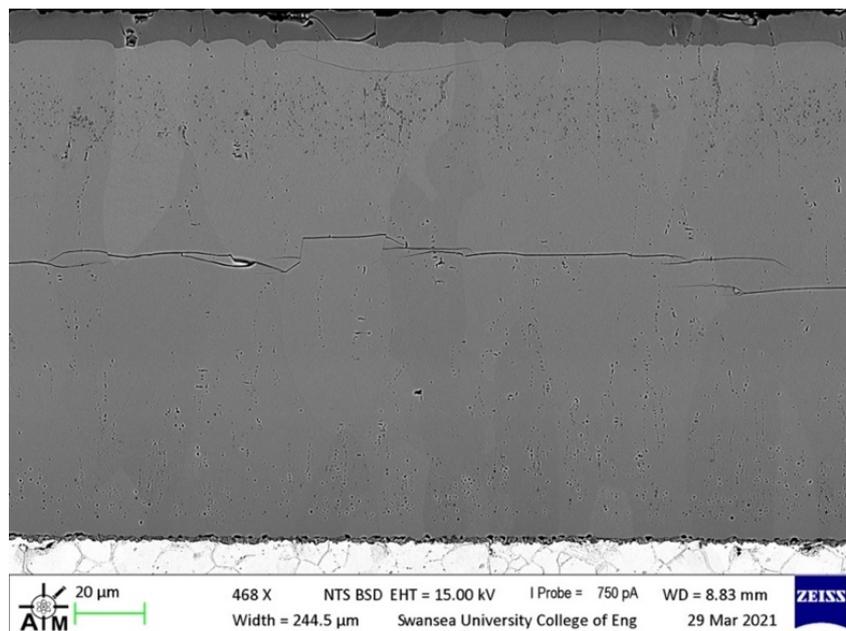

Figure 3.5.2 – Cross sectional SEM Micrograph captured through BSD to highlight oxide grain structure alignment and phase boundaries.

3.6 Energy Dispersive Spectroscopy

Energy dispersive spectroscopy is a method of indicating the presence of certain elements at the surface of a substrate such as an oxide film or coating layer. The technique works in-situ with SEM by utilising a detector which absorbs x-ray spectra incident from the sample and analysing the energy spectrum obtained [125]. Samples examined by SEM in Chapter 4 were also analysed with either a map or line scan at 15kV, 750pA and at a working distance 8.00mm. Generally, most scans operated between 10,000 - 100,000 counts with a deadtime of 30-50%. EDS generally produces lower than SEM-level resolution due to an inability to low primary beam voltages. In addition, poor sensitivity for lighter elements

means analysis can only be performed on materials with an atomic number greater than 4.

3.7 X – Ray Diffraction

X-Ray Powder Diffraction (XRD) is a non-destructive technique used to measure crystalline compounds and determining phase compositions of materials. XRD achieves this by generating x-ray photons and observing the diffraction pattern caused by the interaction of the x-rays with the crystalline phase of the material [52]. These diffraction effects are the result of the wavelength of light and the periodicity of the crystal having the same magnitude and the direction of these diffractions depend on the orientation of the crystal lattice structure. Diffracted X-rays which are in phase with one another after diffraction from the crystal lattice are said to have constructively interfered, and constitute the peaks found on an XRD graph. Destructively interfering x-rays have scattered in all directions and appear as the background on an XRD graph [53]. This is explained by the Bragg condition, which states that if the angle of an incident x-ray wave is equal to its diffracted wave, peaks of scattered intensity will be observed. This is described in Equation 3.7

$$2dsin(\theta) = n\lambda \qquad (3.7)$$

The detector for the XRD is rotated through a series of varying (2θ) angles and the peaks of intensity found by the detector correspond to the crystallographic planes of the material. These planes are quantified as miller indices (h,k,l) [54] which have an inversely proportional relationship to the interplanar spacing between atoms. Divergent XRD was utilised with a Goebel mirror and with default Da Vinci settings. Most samples were analysed as a fine powder through grinding with a pestle and mortar, however some were determined as a continuous structure after reheating, as shown in Figure 3.7.
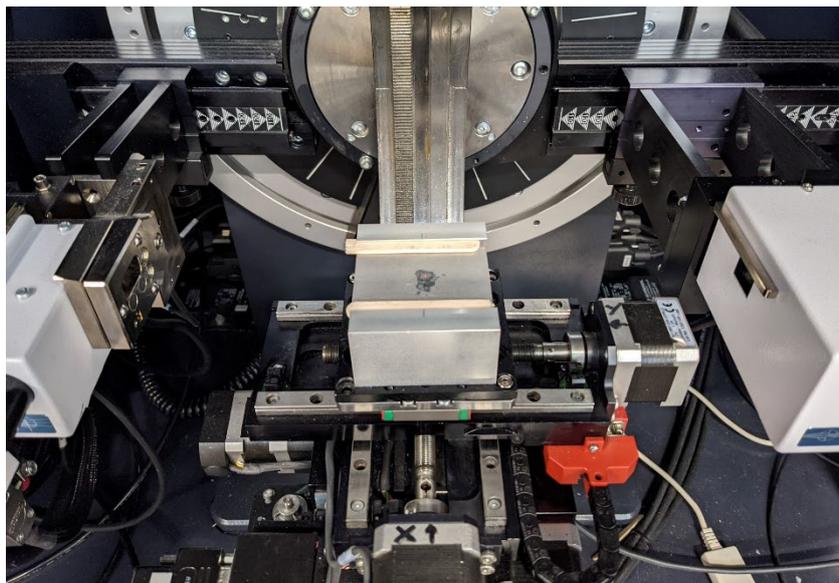
Figure 3.7 – Axial Divergent XRD on an 89μm thick scale layer after reheating. The height of the sample platform was calibrated for each sample in preparation for their Z-scan.

After a height adjustment through a Z-Scan, a 2Θ scan was performed and the resulting X-ray diffraction pattern was analysed using the Reitweld technique with Profex V5 software. The primary slit collimator size for all experiments for 0.6mm and using 2Θ angles between 10° and 80° in a diffractometer, each sample was analysed using Co kα radiation (40 kV, 40mA) with a scan speed of 0.03°/s. The diffraction pattern was characterised using Reitweld technique and displayed 2Θ peaks consistent with oxide phases as reported in literature when considering the expected surface morphology from each scan.

3.8 Raman Spectroscopy

Raman spectroscopy performed bulk phase analysis for the oxides and composites generated by the project. Raman spectroscopy uses the variation in frequency of light when interacting with a molecule to generate a shift pattern caused by an element's atom. Due to this shift in frequency being instigated by the crystal lattice of the material, it is possible to identify the phase of the sample by its Raman shift of scattered light. Specifically, Rayleigh scattering occurs as the main elastic electromagnetic interaction between the photon and the molecule, where emitted photons travel at the same wavelength as the incident

photons [45]. While Raman scattering is an inelastic interaction in which photons scatter with a different wavelength to that of the incident photon as shown in Figure 3.8.
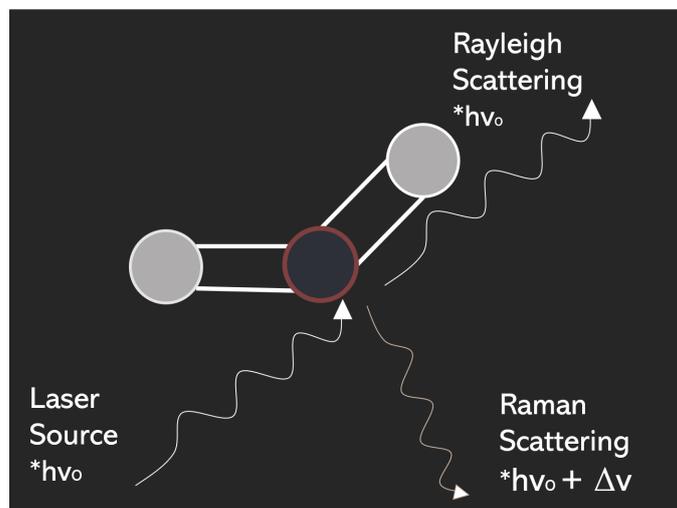

Figure 3.8 – Laser source interaction with a molecule results in either Rayleigh or Raman scattering. Shifts in wavelength in Raman scattered light can be measured to determine phase compositions.

Samples were either analysed as a metallurgically mounted and polished cross-section (as seen in Figure 4.12) or as a continuous detached layer of coating or oxide. Most analysis was performed with a 531nm laser at 0.013mW for 1 second exposure time. The apparatus used for analysis was the Renishaw Qontor InVia confocal microscope located at Swansea Bay Campus.

3.9 Simultaneous Thermal Analysis

Simultaneous Thermal Analysis (STA) is an instrument which performs both Differential Scanning Calorimetry (DSC) and Thermogravimetric Analysis (TGA) in unison. DSC is a technique used to measure the heat flow of a sample and determine the temperature of phase transition in the steel [47] as well as being able to determine the melting behaviours and thermal stability of a material. This is primarily achieved by measuring the amount of energy absorbed (endothermic reaction) or released (exothermic reaction) while the sample is heated or cooled [48]. TGA is another thermoanalytical technique which is able

to determine the oxidation rate by observing the mass change of the sample as a function of temperature [49] [50]. TGA measures this mass change with time which usually shows an increase due to the absorption of the atmosphere during the thermal cycle, thereby analysing the sample reaction with the air. A mass loss can be observed if a volatile component is present within the material and such an observation allows the determination of evaporation rates and volatile emissions of liquid mixtures. In addition, the analysis can be undertaken within a controlled atmosphere of variable gases and vacuums as well as isothermally or with increasing temperature gradients. By combining STA and TGA, the system eliminates any discrepancy in sample preparation or ramp time due to the measurements being taken simultaneously. Moreover, the STA can be combined with Fourier-Transform Infrared Spectroscopy (F-TIR) and Gas Chromatography-Mass Chromatography (GC-MS) to provide information of gas evolution to evaluate the specific gas emissions of the material during the heating cycle [51]. TGA is able to measure the scale oxide growth in-situ which would be unobtainable or limited through measuring oxide growth with microscopy techniques. In addition, TGA is capable of performing experimentation with reduced O_2 content and a mix of inert gases. This is highly useful for this application due to the ability to reproduce the gas mix present due to reheating with the gas barrel furnaces. This technique is not suitable for coated samples and determination of their oxidation prevention due to the considerable weight added to the sample and differentiation between the mass loss of the coating and oxide growth of the steel during reheating would be challenging.

For oxidation kinetics investigations, the STA 449 F3 Jupiter was utilized, as shown in Figure 3.9.1, and required 3x3x3mm cubic coupons to generate consistent and comparable gravimetric curves. The steel grades were cut to

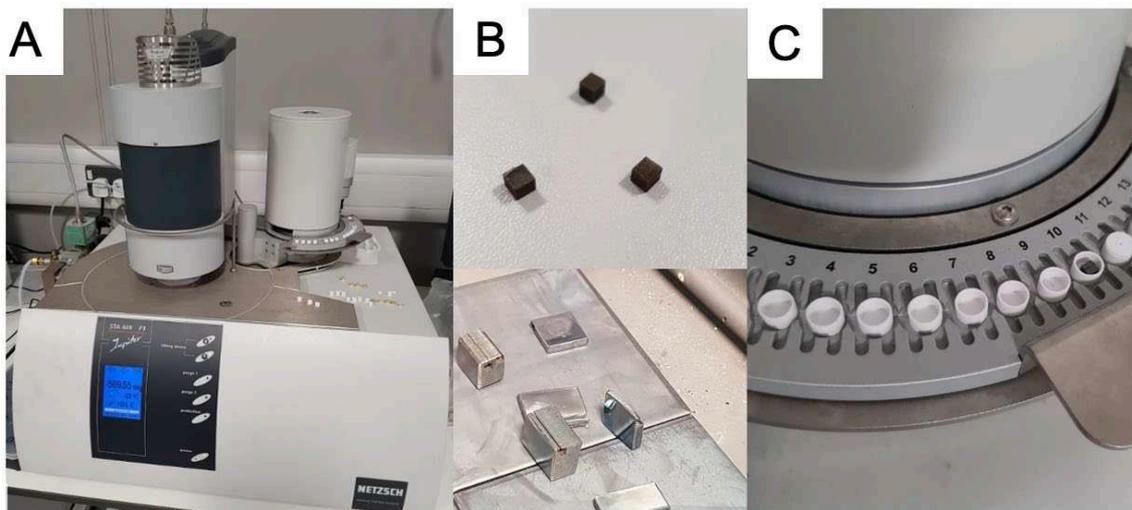dimension using a wire EDM method to ensure a minimal discrepancy between the cubes prior to analysis.

Figure 3.9.1-a) STA 449 F3 Jupiter b) Cubic steel coupons cut using wire EDM c) Al_2O_3 crucibles used for sequential analysis.

The cubes were placed into Al_2O_3 crucibles which possessed high thermal conductivity and inert behaviour under high temperatures. These in turn were loaded into a sequential automatic sample chamber which inserted the crucibles into the STA for measurement one at a time for heat treatment. The thermal cycles programmed for the investigation are shown in Figure 3.9.2 and were generated to correspond to the oxide investigation in section 4.2.
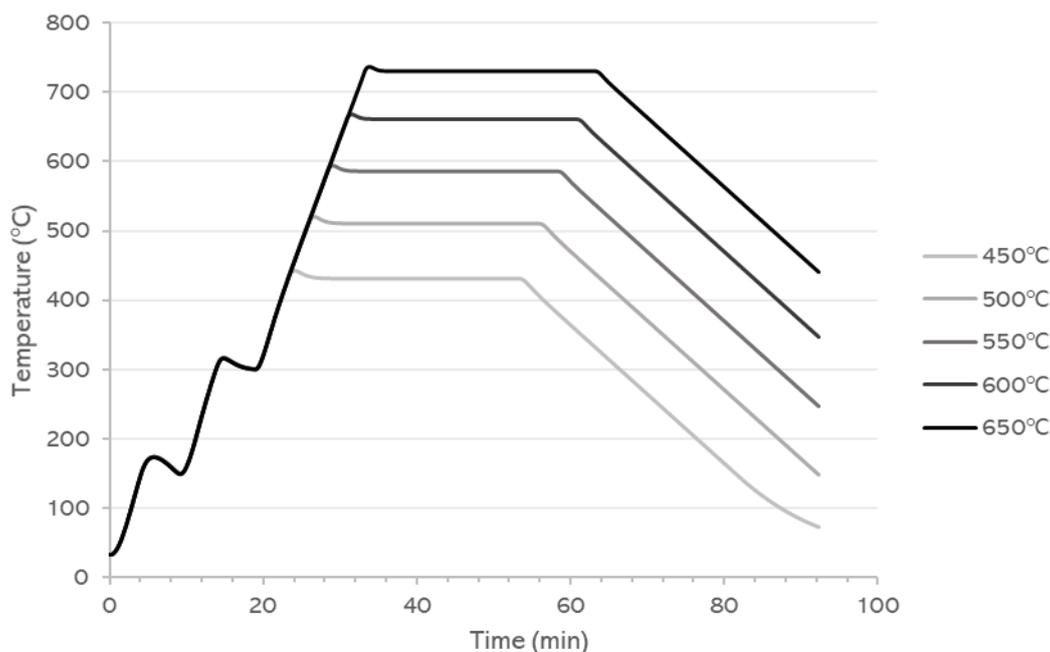
Figure 3.9.2 – STA Thermal Cycles for oxidation kinetics investigations. Data from the reference thermocouple measures the temperature as a function of time.

A custom BOC bottle of 90Na-10O$_2$ supplied the STA for all measurements. This fixed 10% O$_2$ gas supply was flowed through the system at 10ml/min to ensure there was no variation in atmospheric conditions during reheating. For coated samples STA was utilised in combination with Laser Flash Analysis (LFA) to determine thermomechanical properties as described in Chapter 5 and Chapter 6. LFA determines the thermal diffusivity, α, of a sample by heating the top side of a parallel sample and measuring the rear side temperature as a function of time. This factor can be combined with the density, ρ, and the specific heat, C_p, to determine thermal conductivity, κ, as described in equation 3.9 [126].

$$\alpha = \frac{\kappa}{\rho C_p} \quad (3.9)$$

While DSC material preparation was similar to the steel samples, LFA analysis required a 12mm diameter disk with gauge 3.5mm to determine the diffusivity and Figure 3.9.3 exhibits one such sample, Sopac20-HRc-Bo, as prepared for LFA analysis.

Figure 3.9.3 – Sopac20-HRc-Bo 12mm disk prepared for LFA analysis. The coating disk was prepared specifically for this technique and was machined using a Dremel 3000 rotary tool.

3.10 White Light Interferometry

White light interferometry (WLI) is a well-established non-contact technique to determine the surface topography of materials and evaluate a high-level understanding of the surface roughness over large areas. The main mechanism of this technique analyses the interference pattern of two or more waves of the same frequency in superposition and measures the differential in phase caused by either constructive or destructive interference. The optical configuration utilises a collimated light source in the µm range which is split into a measurement beam and reference beam by a beam splitter. The reference beam is directed to a mirror and the measurement beam strikes to either be reflected or scattered by the test sample as shown by Figure 3.10.
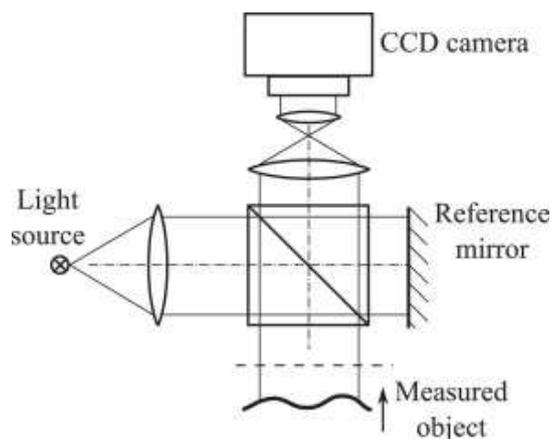
Figure 3.10 – Optical configuration of WLI by Pavliček [127].

Once the two beams recombine, they are focused onto a CCD camera. For optical paths which are different, constructive interference occurs, resulting in a low intensity camera pixel. Conversely, if the surface height is such that the optical paths are the same, the intensity will be at its highest for those points and forms an interference pattern. A record of all these points is displayed in a topographical image through a CCD element, which measures the surface asperity due to unequal path lengths and generates a roughness map [128]. Unless stated otherwise, the Veeco NT9800 optical profiling system was utilised for all white light interferometry in this project parameters were set-up to use a sampling resolution of 640 x 480 at a sampling length of 3.65μm. One of the first oxides tested in this project for surface roughness, was detached E41 scale taken directly from the SR2 mill in Corby after normalisation. Those samples were given the nomenclature MSR1-10.

Chapter 4

Material Analysis and its Oxidation

Introduction

The results here present the oxidation characteristics of TATA's grade steel from the SR2 mill and 6″ stordy mill as well as the performance of novel inhibition coatings designed to inhibit this scale growth. The availability of a viable, low-cost coating for use in mill production had been highly limited until now, and a suitable candidate would signify improved yield performance and enhanced cosmetic properties for the Install 235 products.

The following Chapter 4 assesses the steel grades' mechanical properties to generate standards to which the coated solutions can be compared. The section also investigates the oxidation kinetics of the grades to understand the impact of furnace conditions on scale growth and phase morphology. Finally, a comprehensive review of the phases present within the mill scale from the SR2 Mill and the replica oxide generated by the atmospheric furnace system built in PMRC. While the primary objective of this work, as stated in section 1.4, was to develop a coating solution to enhance the overall tube product during reheating, initially the uncoated grade steel was comprehensively tested for its mechanical and metallurgical properties. Clearly, researching the variation of these traits during normalisation is highly beneficial for TATA Steel, however the main reason for this pre-coated testing is to establish standards at which a comparison of the novel coating solutions' performance could be made

Therefore, Section 4.1 has evaluated the E1, E41 and E24 grade steels for their composition and mechanical attributes. In addition, the R_a and R_z values for typical tube substrates will be addressed under certain processing parameters. The effects of temperature and gas composition on oxidation kinetics will be

observed in Section 4.2 by subjecting grade material to reducing atmospheres. While the phase structure of the oxides has been qualitatively computed in Section 4.3 and provides analysis of scale directly extracted from the Mill. For each section, the reproducibility and resulting standards from each process is also stated.

4.1 Initial Mechanical Properties of Mill Grade Steel and its metallographic variation due to normalisation

All steel grades investigated, as revealed in methodology, are displayed in Table 4.1, and were analysed via OES to determine their elemental composition and carbon content. Compositions varied within error of the target alloying elements stated in TATA's Install 235 technical package. Testing confirmed the hypoeutectic composition of the steel alloys and indicated an elevated █████ content for E24. In addition to the compositions shown Table 4.1, Trace elements of █████████████ detected in E1 and E41, while trace amounts ████████ were also observed in E24.

Table 4.1 – Elemental analysis of TATA Steel Corby's Mill Steel Grades. Spark testing was conducted by the TATA R&D Harbourside facility using Optical Electrical Spectroscopy.
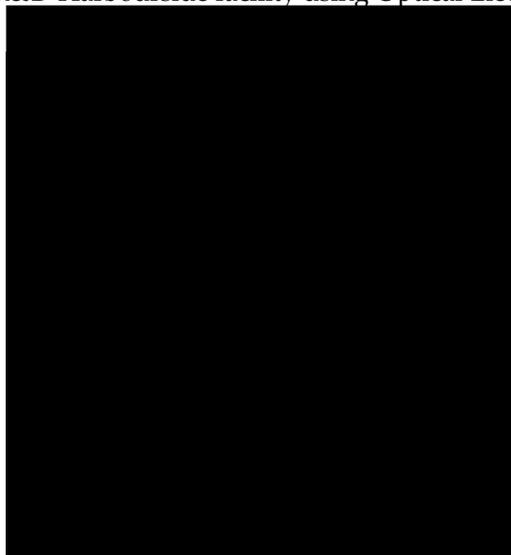
The following investigation adopted metallurgical preparation as stated in section 3.2 and hardness and grain size testing as stated in section 3.4. Initially,

the cross-sectional mechanical properties of the grades were evaluated where the positional distance along the cross-section increases as a figurative percentage from 0 to 100. First, the hardness variation across the length of the cross-section was analysed for 15 steel coupons according to ASTM-E92-17-3-01. The sample groups; UE1, UE24 and UE41 (UE1-UE41) were subjected to thermal cycle STC1 under a normal atmosphere. UE1-UE41 all observed a 12-14% drop in hardness throughout the mid-cross section as shown in Figure 4.1 and UE1-UE41 all exhibited a 6-10 HV/1 differential between top and base substrates. In addition, E24 observed a ~6% overall hardness increase over E1 and E41. Additional less macroscopic observations of the 40-60% regions failed to produce consistent results due to case-hardening effects of the diamond load indentation.
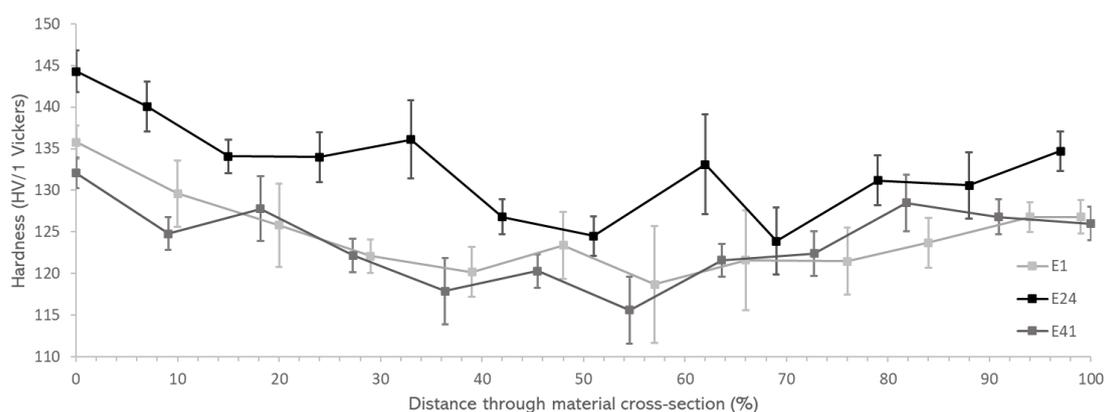

Figure 4.1 – Vickers Hardness (HV/1) variation in TATA Steel Mill grades across the material cross-section. Diamond indentation was applied with a 1Kg load for 10s. Repeat sample hardness increased in variation between the 30-70% region in the cross-section.

In further exploration of the grade steel's mechanical properties, grain size cross sectional analysis of UE1-UE41 was conducted through measurements in accordance with BS EN ISO 643:2020. The results are shown in Figure 4.2 and the full-length stitches used for grain size analysis were similar to those measured in Figure 3.4.2. The measurements observed expected poor grain size homogeneity across the material cross section for all UE1-UE41 samples and revealed a ~20-25% drop in grain diameter in the 40-60% region compared to the surface

boundary grain sizes. However, no discernible variation in grain size was detected between top and base substrates.
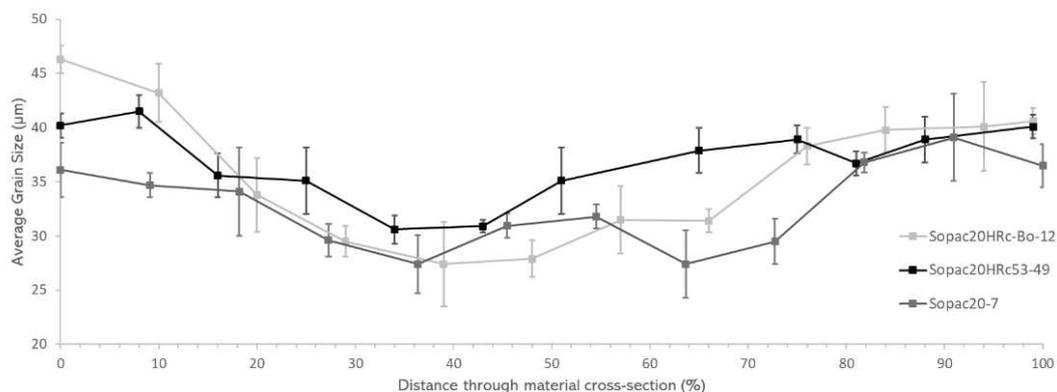

Figure 4.2 – Grain Size (µm) variation in TATA Steel Mill grades using the mean line intercept method. Calculation of the grain size diameter, 650µm lines were drawn diagonally across intermittent micrographs spaced apart as a function of the total cross-section distance.

Next, the surface roughness parameters were determined by estimating Ra and Rz values for SR2/6" Stordy products (MSI1-MSR2), in addition to UE1-UE41 samples. White light interferometry (WLI) was conducted at 5.1X magnification in VSI Mode with processing times dependent on height calibration. WLI analysis indicated the Ra for MSR1 was found to be between 13.0µm-15.5µm and the Rz to be between 105 µm-140 µm. Further analysis evaluated the Ra and Rz of steel coupons normalized in replica mill conditions to provide a quantitative standard at which the coated samples could be compared. The results indicated UE1-UE41 samples produced lower surface roughness values than MSR1 products with Ra and Rz ranging between 6.1µm-8.8µm and 46.6µm-85.6 µm respectively. Figures 4.3a and 4.3b exhibit examples of the WLI maps utilised to evaluate these estimations of surface roughness. Due to the microscopic nature of the Veeco NT9800, the uniformity of these surface roughness values across entire samples was assumed to be within the ranges stated.
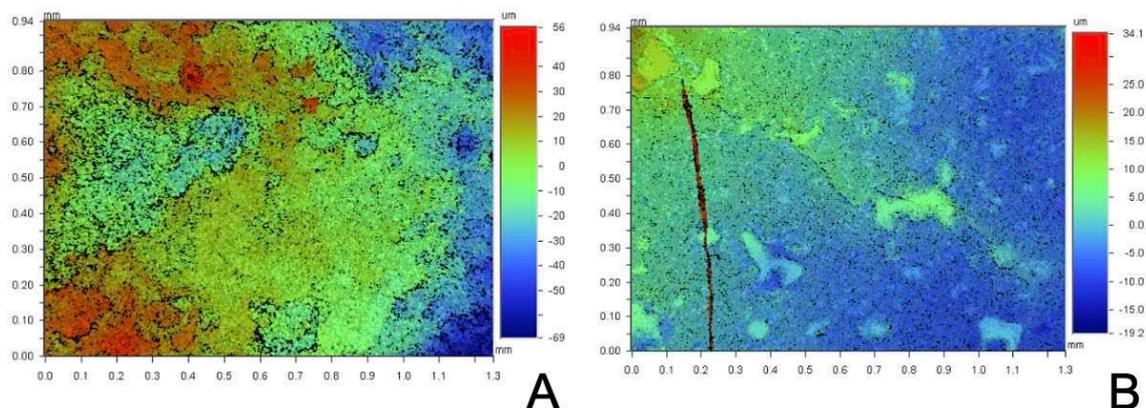
Figure 4.3 - a) Surface profile of a MSR1 product normalised on site at the SR2/6″ stordy b) Surface profile of a A2UE1-A2UE41 replica sample normalised at PMRC with the atmospheric furnace using STC2.

Finally, the thermal characteristics of the UE1-UE41 control samples were evaluated using DSC and LFA measurements. For LFA Analysis, UE1-UE41's thermal conductivity was determined using equation 3.9 where measurements of thermal diffusivity, density and specific heat capacity were input. Figure 4.4 exhibits both the specific heat capacity measured and the predicted thermal conductivity during heating.
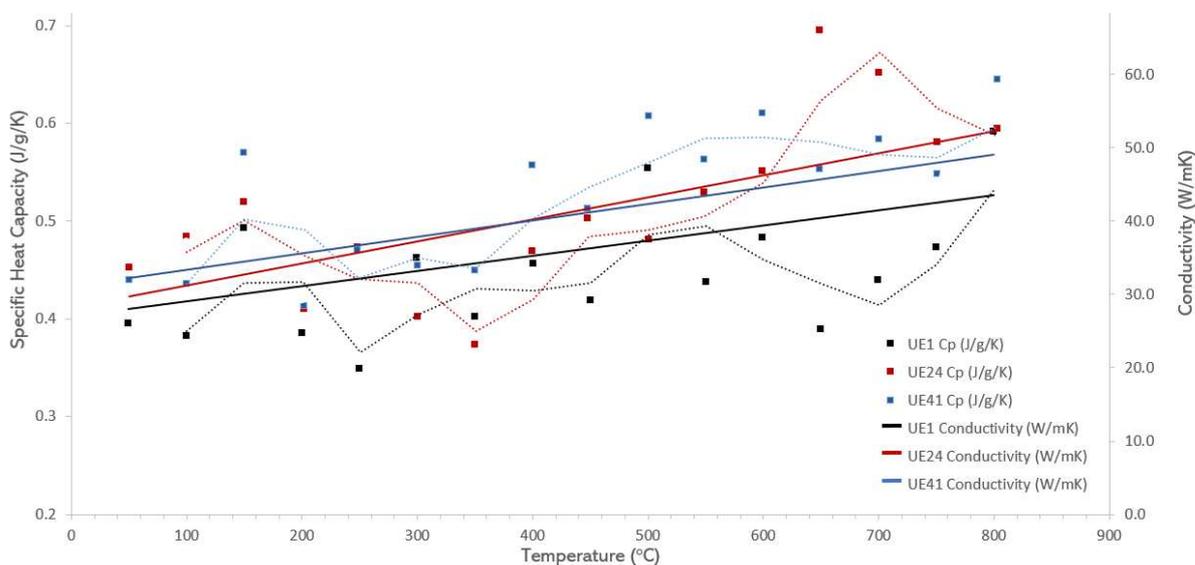

Figure 4.4 – Thermal Property variation with temperature for UE1-UE41 samples using LFA Analysis. Conductivity was calculated from equation 3.9 and Cp values were evaluated through the well-known Laser Flash comparison method.

UE1 displayed low conductivity values of 31.2W/mK at room temperature and ~45W/mK at 800°C. UE24 and UE41 exhibited similar thermal properties of

~36W/mK and ~51W/mK at 800°C. In validation, DSC Cp values also were determined through observing the heat flow and mass of the sample as explained by equation 3.9. The standards set in this section were considered benchmark values at which to compare the effective thermal transfer characteristics of the coatings outlined in Section 4.2 and Section 4.3.

Figure 4.4 exhibits sizeable fluctuations in thermal conductivity and specific heat capacity across the thermal spectrum. There are two reasons why this behaviour could be observed in a combined LFA-DSC determination. First, the batches or cuts of samples used for LFA-DSC may differ greatly in terms of grain size and are likely to have differences in electron mobility and phonon scattering, a fundamental factor in thermal conductivity during temperature changes. Second, LFA and DSC are highly sensitive techniques. Achieving sample preparation or surface roughness consistency and good thermal contact for multiple samples is difficult and often affects the determined results.

4.2 Oxidation Behaviour in Simulated Furnace Conditions

Initially, a numerical appraisal was conducted to calibrate the atmospheric furnace's STCA1-STCA2 cycle methods due to an inability to perform exact replica thermal cycles for each sample testing. This is evident from variations in "Ramp-Up" periods, as explained in section 3.1, between many thermal cycles which, theoretically, should be identical due to the programmed ramp rates and isothermal settings. These variations are likely due to imperfect PID settings which take into account the thermal mass of samples and supporting crucibles when imparting heat into the furnace system. Figure 4.5 exhibits an assortment of STCA1 cycles which were programmed identically as displayed in section 3.1 but produced some variation in ramp up rates, furnace door temperature drops and maximum isothermal temperature.
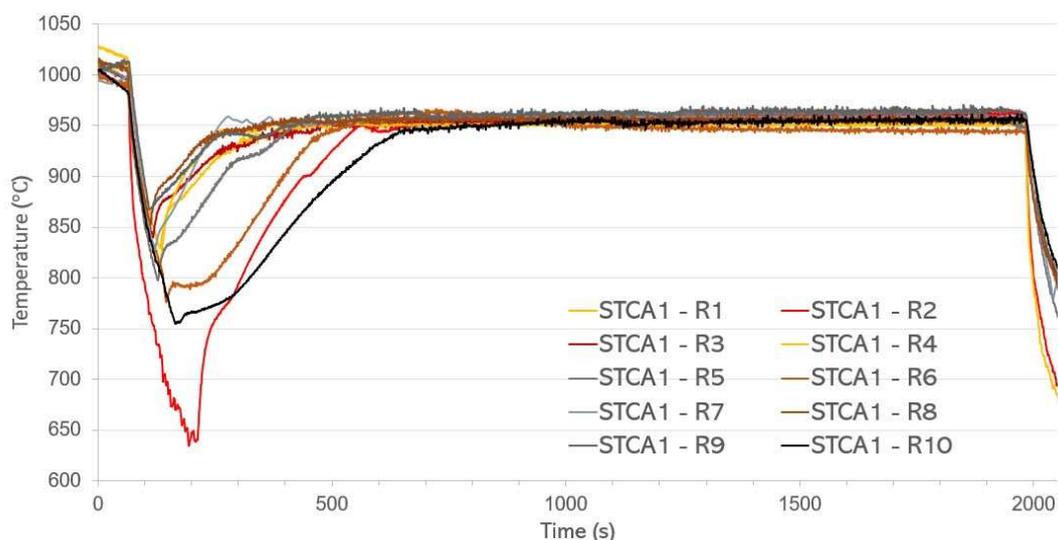
Figure 4.5 – Examples of STCA1 thermal cycles with dissimilar ramp rates after furnace opening and varied isothermal temperatures. Each thermal cycle was programmed to the settings shown in Figure 3.1.5.

To account for this variation, reference sample data of oxide thickness from coating formulation trials and kinetic investigations was extracted to determine calibration factors based on temperature variations in STCA1-STCA3 thermal cycles. The raw oxide values were calibrated according to their maximum isothermal temperature using equation 1.3 and the standard variation in thickness is illustrated in Figure 4.6.
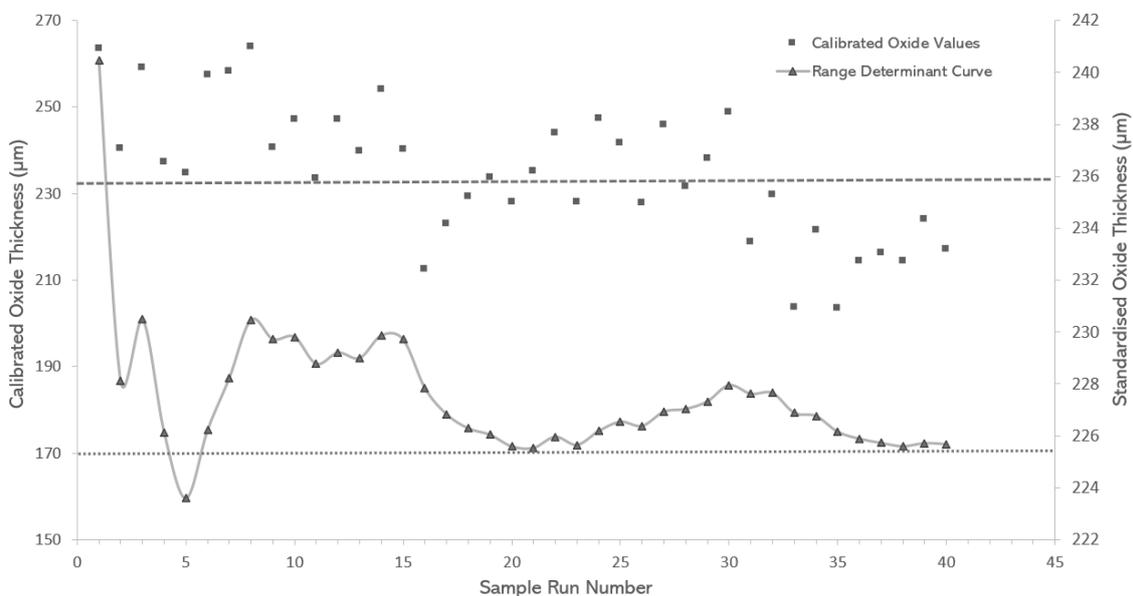

Figure 4.6 – Calibration of Oxide Values due to fluctuations in the set isothermal temperature standard during STCA1-STCA3 cycles. Further coating investigations were corrected with reference to their maximum isothermal temperature but were conditioned to fall within the pre-set standardised range (234.4µm ± 9.0µm).

The Range Determinant Curve presented below determines the range (9.0μm) of the standard by calibrating the raw results from the oxide measurements against the variations in maximum furnace temperature. This determines a suitable variability against a baseline which is approximated when the variations stabilise to an average value. Utilisation of the calibration was persistent throughout all oxide investigations and Table 4.3 exhibits examples of oxide thickness correction due to isothermal temperature fluctuation. Usefully, 234+9.5μm is the same order of magnitude found in most SR2 mill scale thicknesses, making it an ideal benchmark to analyse coating performance although there are exceptions depending on the product type, steel grade and furnace thermal cycle.

Table 4.3 – Examples of calibration of reference samples during oxide or coated examinations. An oxide thickness benchmark of 234 ± 9.5μm was determined. Samples with reference oxides outside this benchmark were discounted from the main coating analysis.

Sample Name	Reference $Ox\ T$ (μm)	Max T (°C)	τ	$Ox\ cT$ (μm)	Range Boolean
UE41	248.1	928	0.970	240.6	True
SOPAC20 5SiO2-B$_2$O$_3$	225.6	890	1.011	228.13	True
Mul-Zir 15	253.1	922	0.976	247.1	False

The 6″ stordy scale, however, varies between a lower 10μm-50μm thickness range, as shown in Figure 4.7. Therefore, performing accurate oxide reduction analysis is unfeasible when setting Ox T benchmarks using these thinner scales and so the benchmark Ox T was kept uniform for all coating investigations.
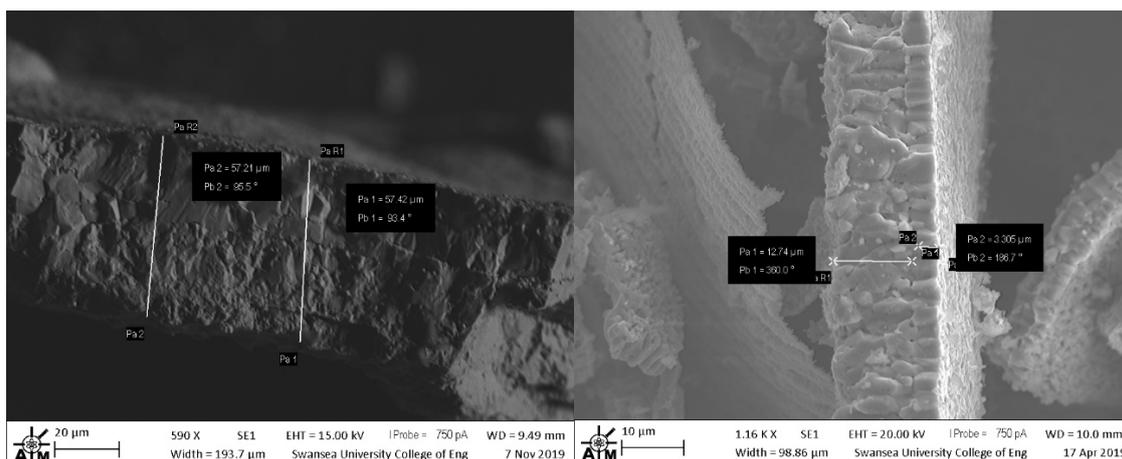
Figure 4.7 – 6" Stordy oxide thicknesses from TATA Corby mill. Typical scale thickness varies from 10μm-50μm dependent on applied processing conditions.

Next, the oxidation kinetics of UE1-UE41 was measured using STCA1-STCA3 thermal cycles at varying isothermal hold temperatures. The consequences of parameter variations of temperature, atmospheric composition and flow rate on oxide thickness and phase composition were investigated. Adherence and kinetic behaviours were also observed for oxides generated with water vapour induced atmospheres. Initially, oxidation growth was determined in the temperature range 400°C – 800°C using STCA3 and the kinetics by maximum isothermal temperature is illustrated in Figure 4.8.
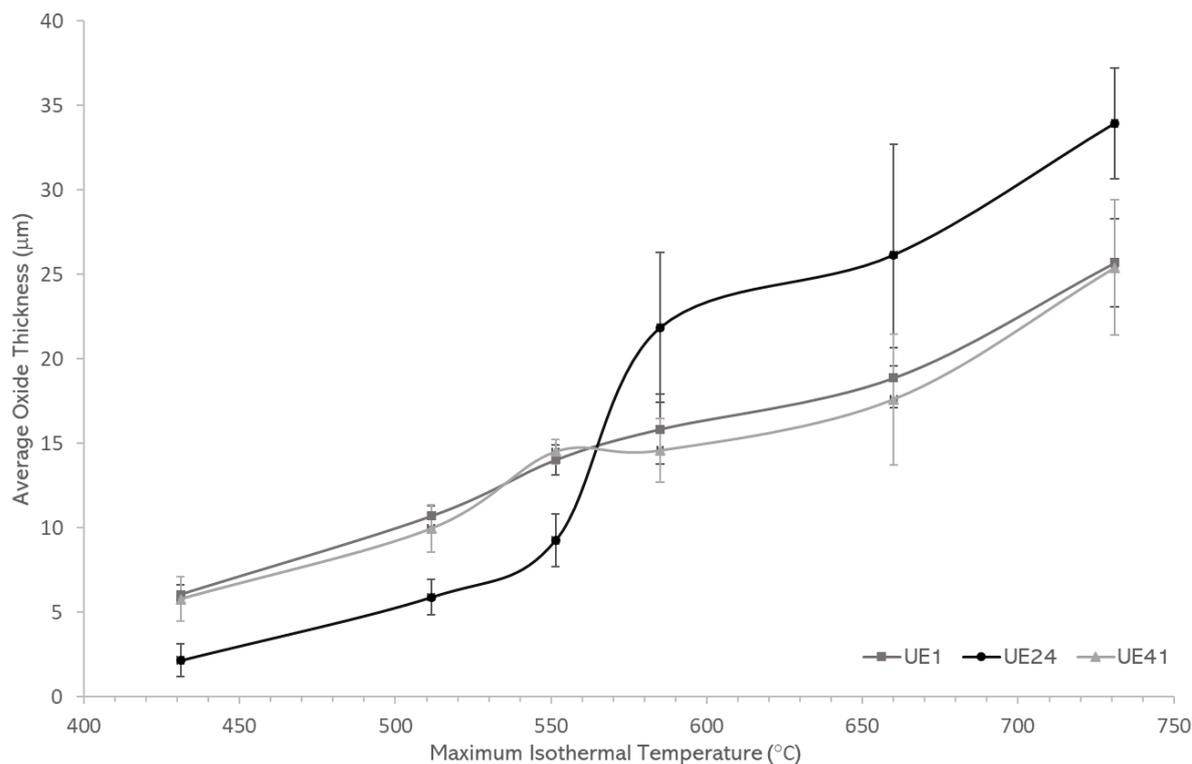
Figure 4.8 – Variation in oxide thickness due to maximum isothermal temperatures for UE1-UE41 in STCA3 thermal cycles.

Kinetic investigations indicated that an increase in k_p was most prevalent in UE24 above 550°C. Wüstite domination was identified as the cause for the increase in parabolic rate constant during reheating.

Further research of UE1-UE41 kinetics was conducted through utilisation of STA analysis. As set out in methodology, the mass of the mill grade steels was measured using TGA for varying maximum temperatures. To validate the findings of the previous kinetic investigation and to focus on the increased k_p region, a temperature range of 450°C- 650°C was selected. Figure 4.9 shows the results from the TGA analysis where sample weight % was evaluated as a function of time from initial sample weight. The gas composition mix for analysis was 10%O_2-90%N_2. A flow rate of 100ml/min was implemented to initially purge the STA chamber with Ar and a protective flow of 60ml/min was utilised during acquisition. Using a pre-programmed thermal cycle with the STA software, a

ramp rate of 30K/min was programmed in for non-isothermal regions plus an isothermal soak of 30 min at the desired maximum temperature.
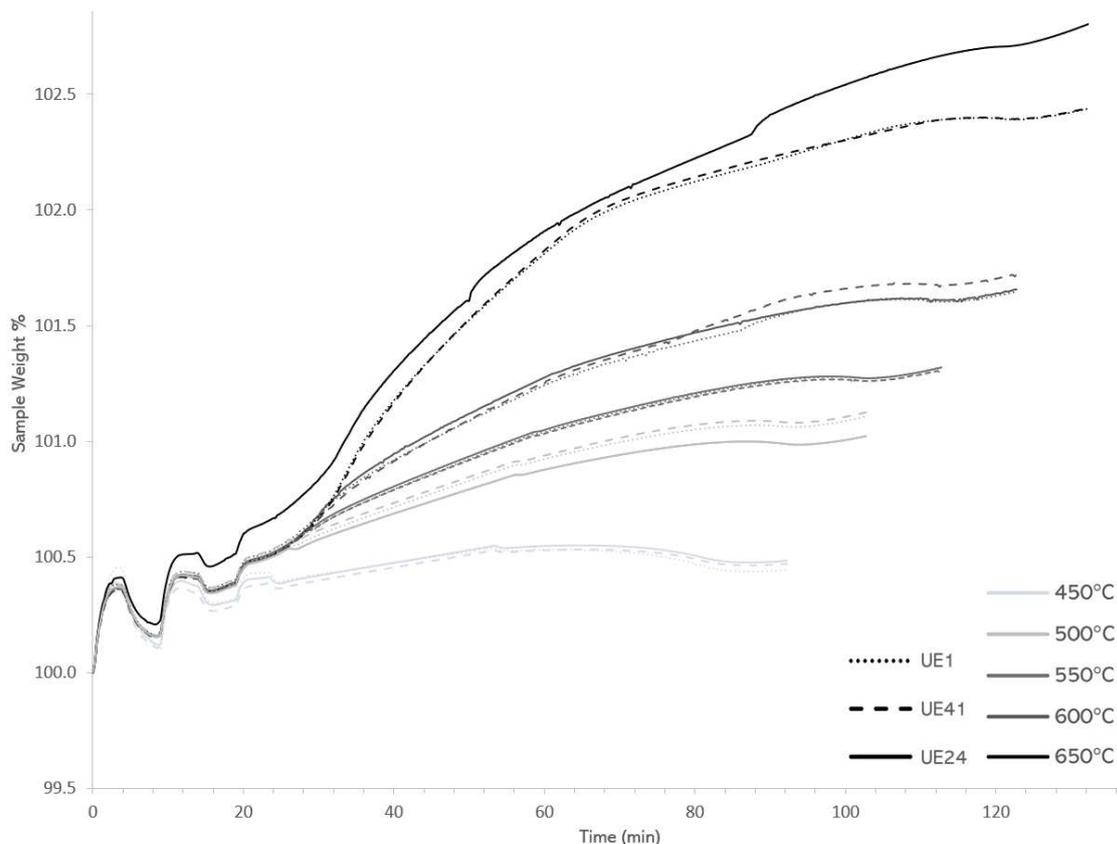

Figure 4.9 – STA Analysis of UE1-UE41 for 450°C, 500°C, 550°C, 600°C, and 650°C thermal cycles (max temp). Sample weight variation was measured as a % of starting weight.

While processing conditions had been extensively investigated for factors involving temperature, little is known about the impact of atmosphere composition on the kinetics of UE1-U41 steel. Therefore, as set out by methodology in section 3.3, the Ox T was measured as a function of the free oxygen available during normalisation. The quoted accuracy for the implemented rotameters was around ±1.5% and so in trying to achieve a 2% increase in O_2 content, there was likely to be high error and variance between thermal cycles. STCG1 was utilised as a thermal cycle and a flow rate of 250ml/min was set for the ingressional gas mixture. The resulting micrographs were examined for both the overall Ox T and Wüstite-Magnetite ratio variation. The results from the evaluation of overall oxide thickness are displayed in Figure

4.10 while examples of the STCG1 thermal cycles used for experimentation are displayed in Figure 4.5. The initial impact on oxidation kinetics commenced between 18% - 15% O_2 in which overall scale thickness dropped by 94.4μm in the reducing atmospheres. Absolute oxidation inhibition was not achieved at $100N_2$ as remnant O_2 presence after the argon purge caused between 15μm-25μm of oxidation. This is likely caused by leakage in the furnace box system from an inconsistent frit application or from an inability to remove all free oxygen in the system using the flow rates available. Figure 4.10 also highlights the absolute oxide thickness of the UE1-U41 steel under different oxygen contents within this experimental system.
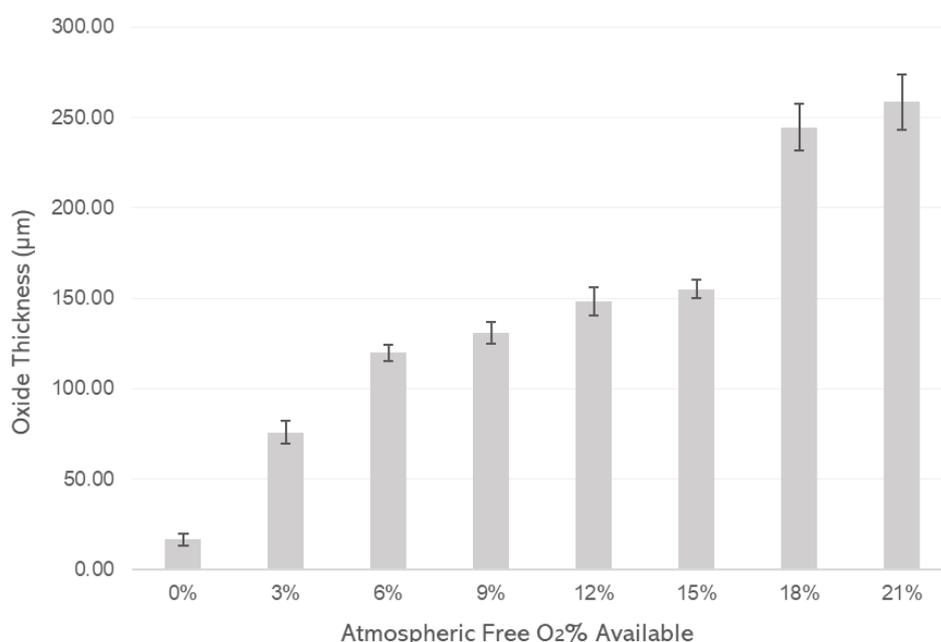
Figure 4.10 – Variation of Oxide thickness due to free oxygen availability of UE1 using STCG1 thermal cycles.

Sample micrograph analysis continued in the identification of the Wüstite-Magnetite boundary and their relative ratio as a function of thickness was calculated as shown in Figure 4.11. The Wüstite-Magnetite ratio was observed to reduce by ~6% in the lowest oxygen environment set by STCG1. This behaviour is somewhat counterintuitive, as lower oxygen levels typically favour FeO formation because less O_2 is required to form an iron (II) oxide. Plus, with more

oxygen available, there is an expectation that the iron would oxidize further to form magnetite and haematite. There are a couple of reasons why this phenomenon may have occurred in this instance. First, the very high temperatures enable the oxidation of iron through different pathways, and sudden increases in the oxygen partial pressure permit the formation of subsequent Wüstite growth from iron directly. Secondly, the Wustite phase is potentially more stable than previously thought for this material at elevated temperatures and the FeO layer is acting as a kinetic barrier for the growth of magnetite with slow diffusion rates. This could be down to phase changes or the presence of certain impurities within the Wüstite layer.
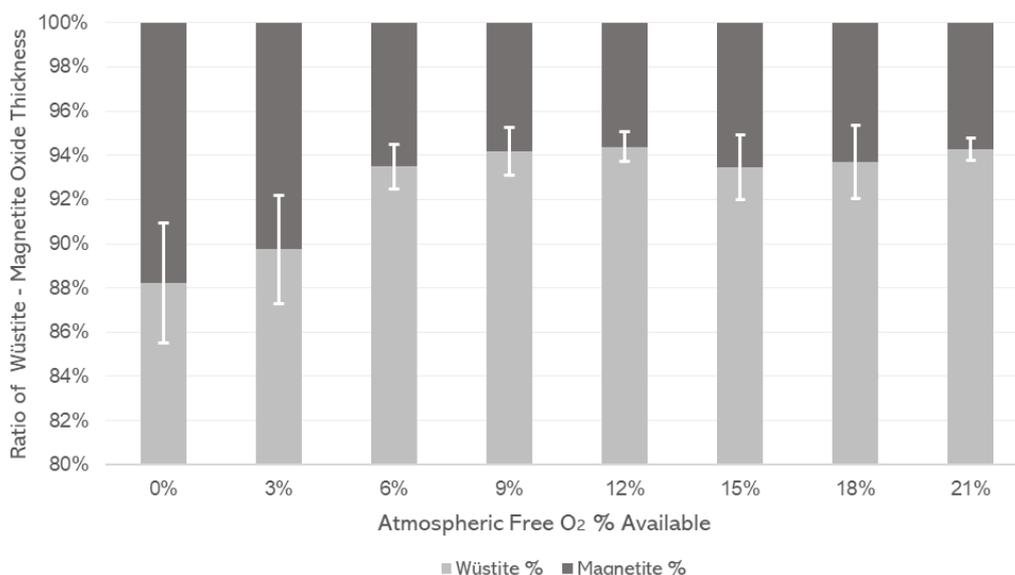

Figure 4.11 – Ratio of FeO-Fe3O$_4$ phases in UE1 oxides as a function of free oxygen availability. Wüstite-Magnetite boundaries were detected using Zeiss Observer layer analysis.

The experiment attempted a 0% free O$_2$ state within the atmospheric chamber, however, Figure 4.10 and Figure 4.11 indicate that some oxidation still occurred. The most likely explanation is the residual O$_2$ absorbed by the furnace material and the success rate of absolute oxygen removal during the argon purge being low. Less likely but plausible occurrences could be the presence of other oxidizing agents within the chamber (such as H$_2$O and CO$_2$) and the possibility that the steel contains some non-metallic inclusions which decompose at high

temperatures, releasing oxygen from those compounds leading to solid-state oxidation.

Quantitative analysis in this investigation was determined by correctly identifying interstitial boundaries between oxide phases. As well as depicting these phase ratios, Section 4.3 outlines the research performed to validate the phase identification using SEM, XRD and Raman spectroscopy and further understand the crystal morphology of the oxide scale after normalisation.

4.3 Phase Characterisation of mill scale and its replicated furnace scale

Initial characterisation was performed using SEM-EDS techniques as outlined in section 3.5 and 3.6. Oxide extracts were delaminated from low carbon steel products at the Corby 6″ mill and were observed for their crystal structure at their opposite and exterior surfaces. Figure 4.12a shows an SEM micrograph of fragmented E41 oxide from the stordy furnace in which a portion of the intermediate layer had been detached from the innermost Wüstite. The scale was found to possess consistent modes of inverse spinel Fe_3O_4 atop a cubic FeO matrix, the structures of these phases are demonstrated in Figure 4.12b.
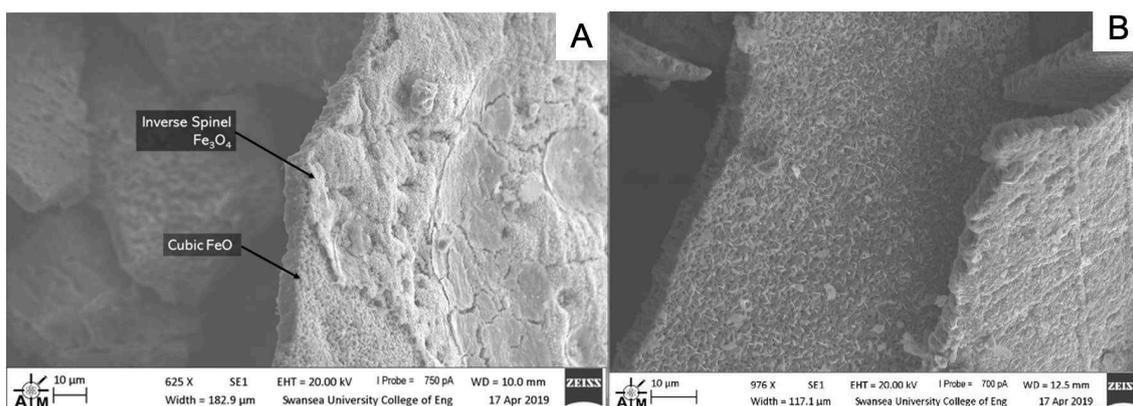

Figure 4.12 – a) SEM Micrograph of detached E41 stordy oxide revealed FeO matrix underneath delaminated Fe_3O_4. **b)** Visual discrepancy in oxide morphology and crystal structure between FeO and Fe_3O_4 phase layers.

Detection of rhombohedral α-Fe_2O_3 or cubic γ-Fe_2O_3 was not possible through SEM imaging alone. Therefore, EDS was utilised in combination to detect

haematite in scale grown on UE41 with an STCG1 thermal cycle which was metallographically prepared afterwards for cross sectional analysis. Initial EDS mapping of the uppermost oxide layer confirmed increased O_2^- content and unexpected increased Fe content in oxide layers closest to the atmospheric interface as shown in Figure 4.13. The two-layer system shown in the associated SEM image indicated an $FeO \cdot Fe_3O_4$ composite below a pure magnetite region. Further detection of additional layers at the atmosphere-oxide interface was incompatible with the resolution of conventional EDS mapping and so linescan or points scan analysis was subsequently utilised. Trace detection of steel elements such as manganese indicated low precipitation of the alloying material into the oxide layers. Negligible detection of silicon ruled out the possibility of fayalite presence within the overall scale.
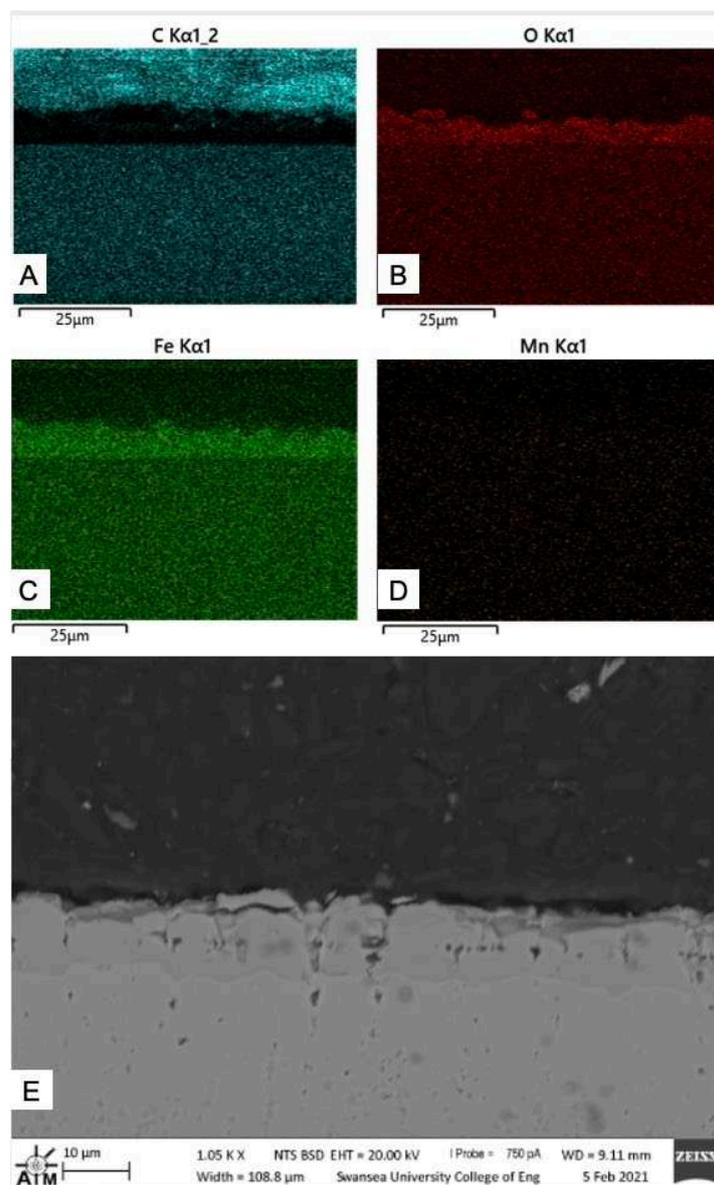
Figure 4.13 – EDS mapping of counts of a) Carbon b) Oxygen c) Iron d) Manganese - of an uppermost two-layer magnetite system. A FeO · Fe_3O_4 composite was attributed to the intermediate layer under the Fe_3O_4 phase.

The counterintuitive nature of a seemingly higher Fe content in the magnetite layer is mostly linked to the disadvantage of the EDS technique in determining the phase identity of oxide layers. On a Molar level, FeO has an iron content of 50%, while Fe_3O_4 has an iron content of 43%. However, the number of X-rays detected is not just affected by the molar ratio of the compound being measured but also some materialistic factors as well. These include the beam interaction volume which is attributed to the microstructures of the samples and the fact that

magnetite is crystallographically denser than Wüstite, leading to stronger signals of Fe as magnetite would contain more iron atoms in the same volume. Identification of α-Fe_2O_3 was achieved through a cross-sectional line-scan of the suspected haematite-magnetite boundary where impoverished Fe detection and an oxygen rich tertiary layer indicated the presence of haematite. The linescan is shown in combination with a quantitative graph of counts per second of each element against the distance along the cross section in Figure 4.14.
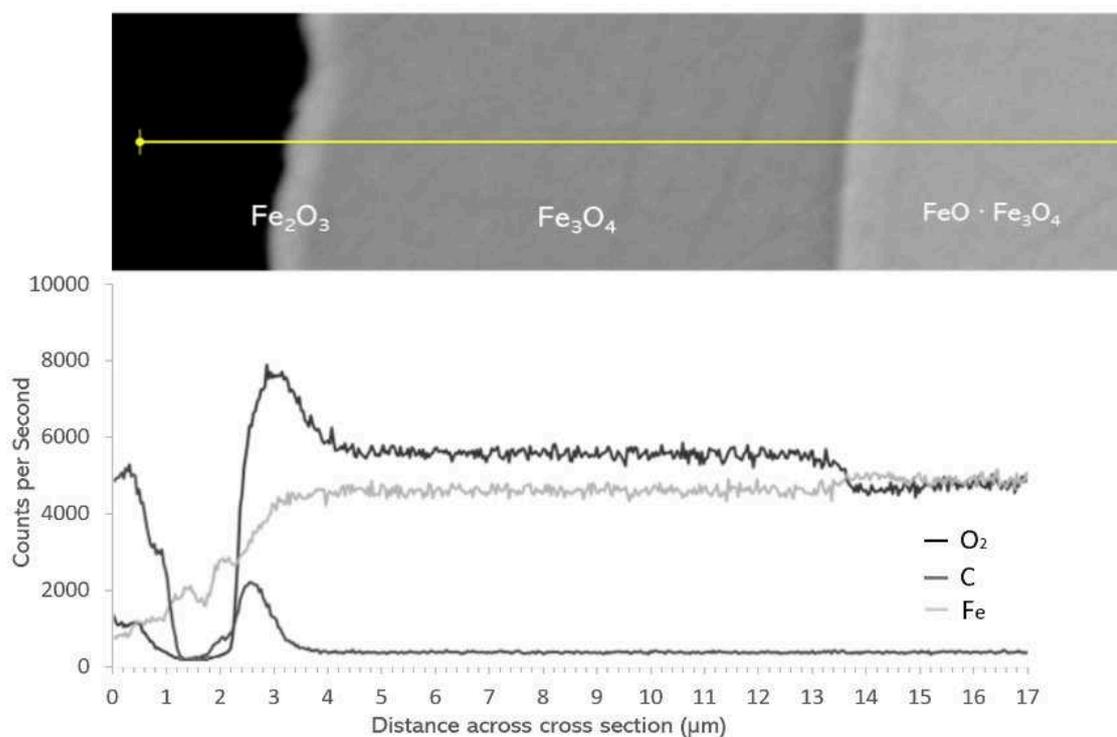
Figure 4.14 – EDS linescan elemental analysis of O_2, C and Fe across upper most phase boundaries of an UE41 oxide layer. Haematite detection was suspected due to an in O_2 rich region at the oxide-resin interface.

Then, Raman spectroscopy was utilised as a validatory method in determination of interstitial phase composition. The resolution spot size of 10μm for Raman limited the ability to analyse the outer-most layer shown in Figure 4.13 and so two main spectra were taken along the cross-section for the inner and outer oxide layer of the prepared UE41 samples as shown in Figure 4.15.
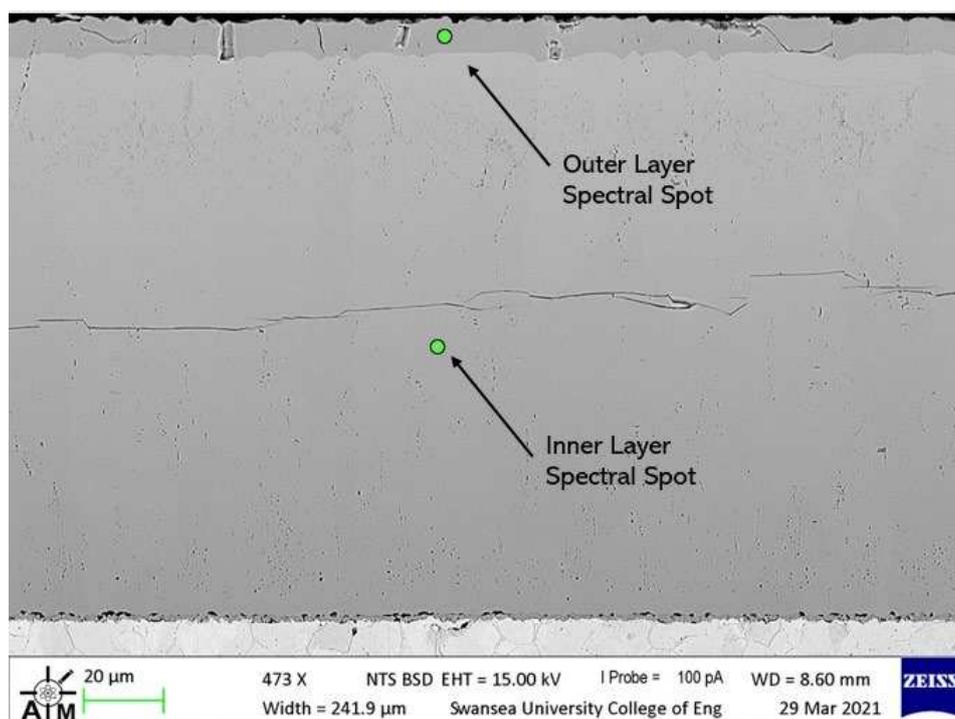
Figure 4.15 – SEM image at 470x magnification with annotations showing the two spectral areas utilised during Raman spectroscopy.

An initial point scan, centrally, in the bulk oxide was performed at 0.013mW for 1s using a 531nm radiation. The resulting spectra is shown in Figure 4.16 in which Savitzky–Golay smoothing of a second order polynomial, was performed to remove accidental peaks and reduce noise. Similarly, a spectrum was taken of the Outer oxide layer which utilised a 531nm radiation at 0.013mW for 5s and is shown in Figure 4.17 with the aforementioned processing.

Figure 4.16 – Raman spectra of central inner oxide layer from UE41 steel. Savitzky–Golay smoothing was applied of the second order polynomial.

Figure 4.17 - Raman spectra of the Outer oxide layer from UE41 steel. Savitzky–Golay smoothing was applied of the second order polynomial.

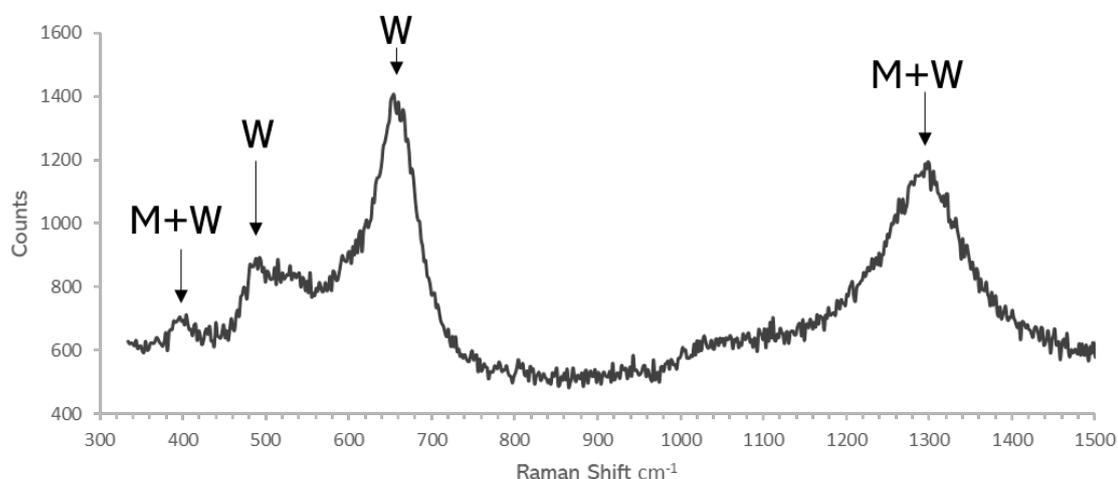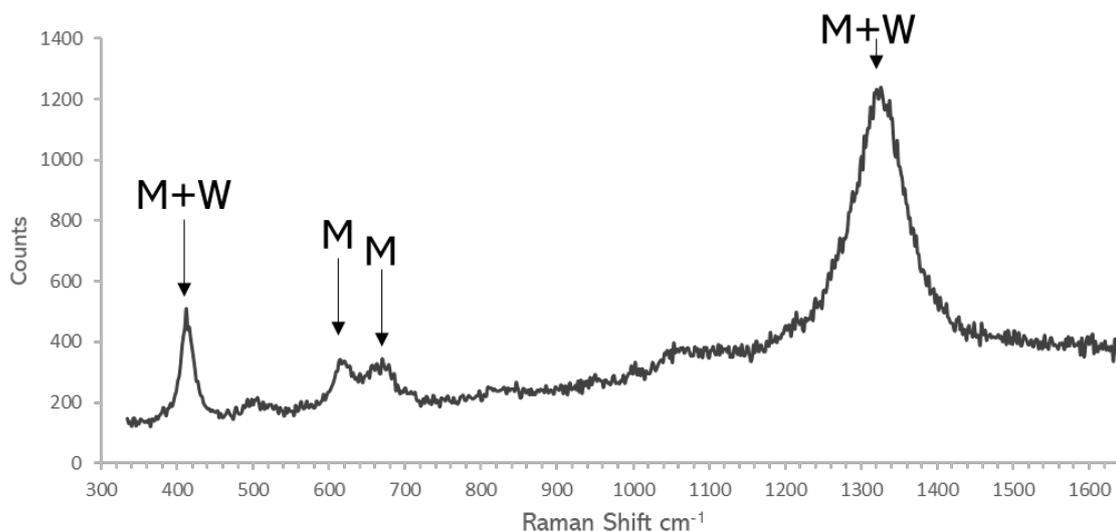The results indicate that the main bulk oxide is primarily made up of a Wüstite crystal structure with precipitants of magnetite present throughout the layer. This can be concluded from the largely consistent placement of the Wüstite peaks, such as 500cm^{-1}, 650cm$^{-1,}$ and 1290cm^{-1}, when compared with spectra taken from literature.   Agreement with magnetite peaks was also found with previously conducted research in literature. Most notably, the characteristic 'double peak' between 600-700cm^{-1} is a strong indication that the layer has an Fe$_3$O$_4$ phase matrix. Due to the overlapping nature of oxide peaks in complex scale systems in Raman spectroscopy, understanding the presence of precipitates within each oxide layer was observed through XRD.

Next, samples of pre-oxidised UE41 were prepared for High Resolution X-ray diffraction (HRXRD) analysis to get a qualitative understanding the Fe$_2$O$_3$, FeO and Fe$_3$O$_4$ make up in each interstitial layer and the levels of precipitation occurring due to the diffusion of O$_2^-$ down into the bulk oxide layer. With this spot size being larger than the cross-sectional areas of pre-prepared UE41 samples in a hot mount, the x-ray diffraction was performed on non-

metallographically prepared powdered extracts of delaminated 220µm thick scale grown using STCG1. Outer oxide layers were associated with secondary detached scale as shown in Figure 4.7 and inner or intermediate oxide layers typically were partially adhered primary oxides closest to the steel substrate. The diffraction pattern of the Outer and Intermediate scale is displayed in Figure 4.18 with analysed crystal structures. XRD confirmed the main presence of Wüstite in the intermediate inner oxide layer with small peaks of magnetite indicating low levels of Fe_3O_4 precipitation into the bulk FeO layer during reheating. In the outer oxide layer, Magnetite was a dominating crystal structure with peaks at 30.3°, 36.3° and 57.0° however trace detection of FeO and Fe_6O_3 also indicated the existence of haematite within the outer layer and a composite a $FeO \cdot Fe_3O_4$ layer formation preceding the thin oxide-atmosphere interface shown in Figure 4.15.
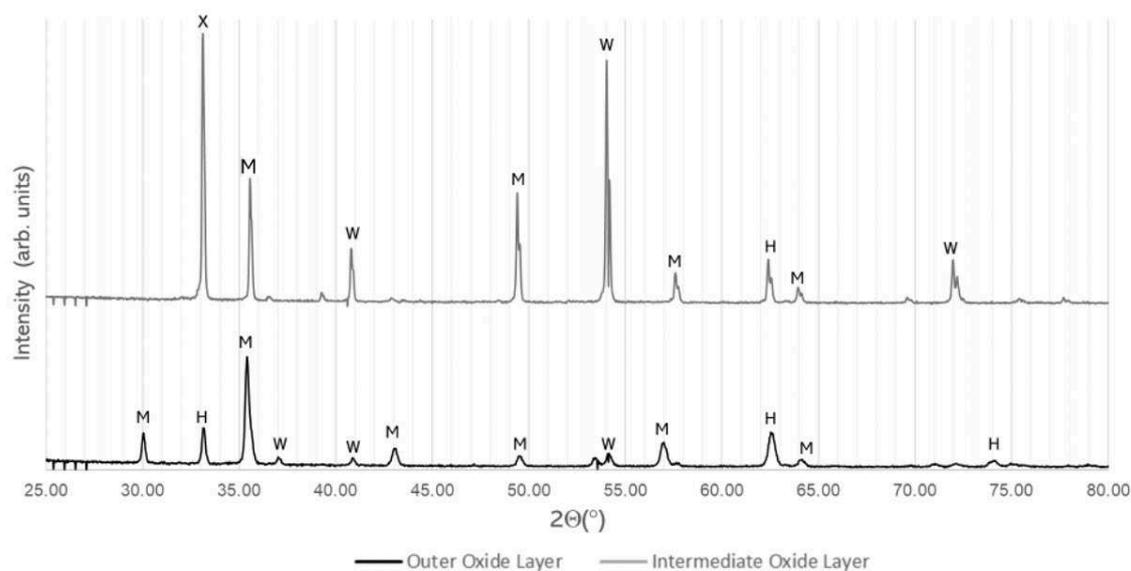
Figure 4.18 – XRD powder scan (2Θ) of the Outer and Intermediate Oxide layer of UE41 steel and Reitweld refinement conducted to determine crystal structure present within the oxide layers.

This qualitative analysis established a standard of phase morphology that would be expected in future oxide growth, even with fluctuations in isothermal temperatures for the STCG1 cycles or variation in atmospheres when investigating coating performance. The standard allowed for direct comparison with previously coated oxides to determine if a compound has made an impact

on the phase make-up of the scale due to its inhibition technique. Furthermore, the discovery of very few or no external elements in the oxide signifies any qualitative detection of well-known complex oxide compounds, such as Fe_2SiO_4, with XRD, EDS or Raman must be attributed to a reaction with the coating material.

With 6″ and SR2 steel grades fully tested for their mechanical properties, oxidation behaviour and phase morphology, and a dedicated standard established for each of these parameters, work on inhibition coatings could be conducted. As such, the results of the following chapters either reference or compare the findings from this section.

Conclusion

Chapter 4 has determined key standards which permitted the evaluation of inhibition performance for the coatings investigated in Chapter 5 and Chapter 6. Additionally, it discovered essential characteristics of the oxide grown from UE1-UE41 samples.

- The standard oxide growth for an STCA1 thermal cycle was set at 234.4μm ± 9.0μm. The ratio between FeO and Fe_3O_4 remained constant for free O_2 concentrations above 6% and the oxide growth for this metal had a marked increase at around 550°C, signifying the temperature region of interest for coating solutions.

- A standard of hardness reduction and grain size reduction was set at 12%-14% and 20%-25% respectively for the UE1-UE41 steel samples. This is conjuncture with average readings for surface roughness through WLI – which indicated typical uncoated samples displayed Ra values ranging from 13.0μm to 15.5μm. These are the baselines which future coating mechanical performance could be compared against.

- SEM-EDS, Raman spectroscopy, and XRD were leveraged to ascertain that the inner layers of the oxide scale were predominantly Wüstite. While Magnetite dominated the outermost layer albeit followed by a $FeO \cdot Fe_3O_4$ composite. This phase understanding is crucial, as it will identify how the coatings affect the phase morphology during reheating and how they could be optimised in mitigating the undesired side effects from normalisation, such as delamination.

Chapter 5

Phosphate Based Coating Solutions

Introduction

Next, Chapter 5 outlines all experimental work conducted to evaluate potential phosphate-based solutions prior to formulation optimisation to enhance oxidation inhibition characteristics. Key glass additives were explored before investigations into the composite materials established during reheating trials and their indirect impact on thermal transfer.

This chapter also reviews the first branch of coating type investigated for the EngD project; phosphate-based inhibitors. Section 5.1 will evaluate coating synthesis trials and application attempts as well as experimentation performed to optimise the most successful formulations. Also, this section provides the first quantitative indication of oxidation reduction. Next, evaluation of successful coatings' thermomechanical properties and processing compatibility will be conducted. In addition, section 5.2 will assess the suitability of the coatings with regard to their impact on cosmetic appearance of the Install 235 tube product and ability to delaminate after reheating.

The oxidation prevention performance is further detailed in section 5.2 including an economical appraisal of its impact to the wider TATA Steel business. Finally, section 5.3 evaluates the evolved coating composites due to reheating as well as glass transitions, crystallographic phase changes and thermal glass stability.

5.1 Initial phosphate formulation trials, their synthesis, application, and normalisation

In this section, the phosphate-based glass coatings produced were based on P_2O_5 tetrahedral networks and the coatings were prepared using the sol-gel method outlined in section 2.8. Initially, $Na_5P_3O_{10}$ solutions were trialled with a number

of cross-linking agents to create a sol-gel. As dissolved sodium polyphosphate possesses a P-O-P linkage, chemical cross linking will enable the physical alteration of a polymer to a more rigid and well-defined shape. As an example, linkage of CH_2-$CHCO_2H$ cross linked polymers through a polymerisation of dissolved $Na_5P_3O_{10}$ permitted the synthesis of a metalalkaline solution (sol). Due to the hydrolysis of the P-O-P chains during dissolution, the exchange of Na^+ ions and H^+ ions resulted in a hydrated layer between the metal surface and the glass layer. Once a sol was generated through hydrolysis, application to the substrate was followed by evaporation of solvent to leave behind xerogel film which was subsequently heated to form a coating film.

Initially, however, trialled coatings were categorised into three synthesis groups, CaP suspended in various media, dissolved P_2O_5 with additions for cross-linked polymerisation and glass or mineral scaffolds dispersed in phosphating systems. Formulations were synthesised in line with the target compositions detailed in Table 5.1 and the weight% of each precursor was weighed manually and mixed with a magnetic stirrer. In this case, preprepared $Na_5P_3O_{10}$ from Sigma Aldrich was dissolved in 100ml of dH_2O at 90°C prior to a predetermined % of CH_2-$CHCO_2H$ acting as a cross-linking agent as shown in Table 5.1. Compositions varied by a maximum of 2.5 mol% from intended targets as set out in methodology and viscosity modifiers additions were determined by the relative contact angle required to achieve desired coating thicknesses between 10-50µm. Between 5-10 samples of each coating type were trialled and were subjected to an STCA1 thermal cycle if film adhesion was sufficient. Visual inspection was performed to decide which formulations were to be further researched as well as ImageJ analysis in determination of coating coverage. Over 150 coated samples were utilised and analysed from material selection up to final optimisation in the determination of a feasible formulation for Install product application.

Table 5.1 – Initially trialled coatings with formulation details, application technique and adhesion proficiency.

Sample Name	Formula Mol %	Coating Material	Glass/mineral Addition	Viscosity Modifier	Application Method	Curing Time	Adhesion Success Boolean
HexChi PP25	25.9 $C_{56}H_{103}N_9O_{39}$ – 70.2 $Ca_{10}(PO_4)_6(OH)_2$ – 3.9 $C_6H_{12}O_2$	25 Micron Phosphate Powder	N/A	Hexanoic Chitosan	Bar	1-2 hours	NO
AceChi PP25	3.6 $C_{56}H_{103}N_9O_{39}$ – 18.1 PO $Ca_{10}(PO_4)_6(OH)_2$ – 1.5 $C_2H_4O_2$	25 Micron Phosphate Powder	N/A	Acetic Chitosan	Bar	1-2 hours	NO
SOPAC10	88.0 $Na_5P_3O_{10}$ – 5.1 C_2F_4 - CH_2 – 14.9 $CHCO_2H$	Sodium Polyphosphate	N/A	Teflon	Pipette	45 mins	NO
PVAPP25	97.0 $C_{56}H_{103}N_9O_{39}$ – 3.0 C_2H_4O	25 Micron Phosphate Powder	N/A	PVA	Bar	3-4 hours	YES
POPAC10	82.5 KH_2PO_4 - 17.5 $CHCO_2H$	Potassium Phosphate	N/A	N/A	Pipette + Spin	45 mins	YES
SOPAC10	82.3 $Na_5P_3O_{10}$ – 17.7 $CHCO_2H$	Sodium Polyphosphate	N/A	N/A	Pipette + Spin	45 mins	YES
SOPAC10 -HSi	80.2 $Na_5P_3O_{10}$ – 14.7 $CHCO_2H$ - 5.1 SiO_2	Sodium Polyphosphate	Silica Gel	PVA	Pipette	50 mins	YES
SOPAC20 -HRc	80.5 $Na_5P_3O_{10}$ – 14.4 $CHCO_2H$ – 5.1 N/A	Sodium Polyphosphate	Recycled Glass	PVA	Pipette + Spin	45 Mins	YES
SoVer10	79.9 $Na_5P_3O_{10}$ – 14.7 $CHCO_2H$ - 5.4 $(Mg,Fe^{2+},Fe^{3+})_3[(Al,Si)_4O_{10}](OH)_2 \cdot 4H_2O$	Sodium Phosphate	Vermiculite	N/A	Dip + Cure	1 hour	YES
SOPAC 20 – HSLo	80.1 $Na_5P_3O_{10}$ – 14.9 $CHCO_2H$ – 5.0 $CaO \cdot 6SiO_2$	Sodium Polyphosphate	Soda Lime Glass	N/A	Pipette	45 Mins	YES
SOPAC 20 –HBo	80.5 $Na_5P_3O_{10}$ – 14.3 $CHCO_2H$ – 5.2 N/A	Sodium Polyphosphate	Borosilicate Glass	N/A	Pipette	45 Mins	YES
SOPAC 20 –HBa	79.4 $Na_5P_3O_{10}$ – 15.6 $CHCO_2H$ – 5.0 CaO $SiO_2P_2O_5MgOK_2ONa_2O$	Sodium Polyphosphate	BioActive Glass	N/A	Pipette	45 Mins	NO
SoPer10	80.0 $Na_5P_3O_{10}$ – 14.8 $CHCO_2H$ – 5.2 $Al_2CaFe_2K_2MgNa_2O_{12}Si$	Sodium Phosphate	Pearlite	N/A	Dip or Bar	1 hour	NO

The adhesion to the substrate and protective ability were the two dependency factors in deciding upon a coating application for formulations while some coatings, such as PVAPP25 & AceChiPP25, displayed a high viscosity of around 5MPa·S which prevented the utilisation of pipette or spin coated techniques. Defects in the form of bubbling, blistering and poor coverage were attributed to the bar coated technique with the aqueous SOPAC solutions and therefore either a dip-coated or spin coated techniques was adopted for further trials. The pipette

and spin technique proved the most effective coating technique displaying enhanced coverage and low defects provided pipette material deposition volume and spin speed were optimised as shown in Figure 5.1. HexChiPP25 and AceChiPP25 were discounted from further research due to agglomeration of phosphate particulates clumping within the chitosan suspension and this phenomenon was also prevalent in Teflon additives to SOPAC solutions.
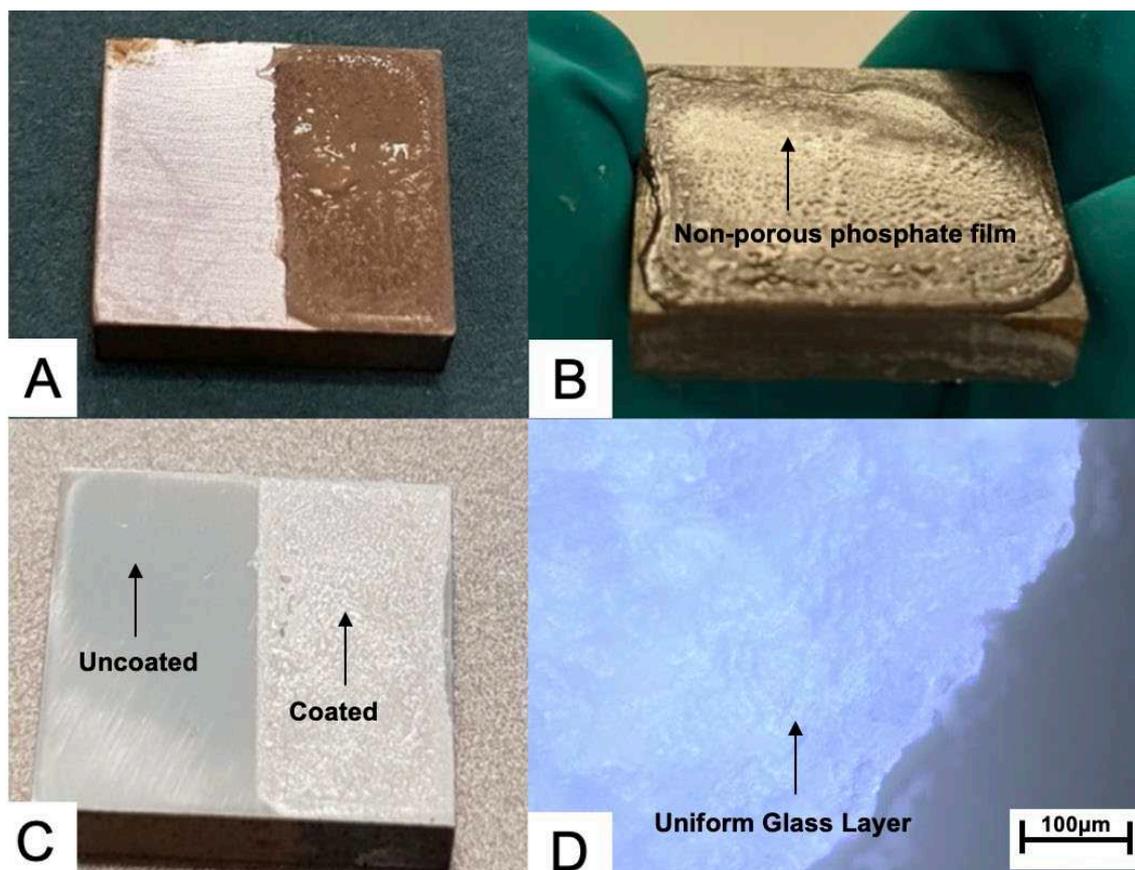

Figure 5.1 –a) 1μm polished E1 Steel with a spin coated 45μm $Na_5P_3O_{10}$ coating.
b) SOPAC10 with ~ 91% coverage c) Optimised Sopac10 application with > 99% coverage d) Smartzoom optical image of non-adhered Sopac 20 coating.

Similarly, coating samples suspended with Polyvinyl alcohol (PVA) were not proceeded with as high levels of cracking and stress peel occurred after curing. In addition, PVA proved an ineffective viscosity modifier for glass or vermiculite formulations due to inconsistent uniformity in the distribution of particulates. This was confirmed in subsequent oxidation trials using STAC1 in which protection only covered around 30% of the sample area whereby significant

clustering occurred during reheating as shown in Figure 5.2. Perlite additions to Sopac10 were discounted from further investigation due to the inability to suspend consistently within the media and displayed low adhesion to the steel surface.
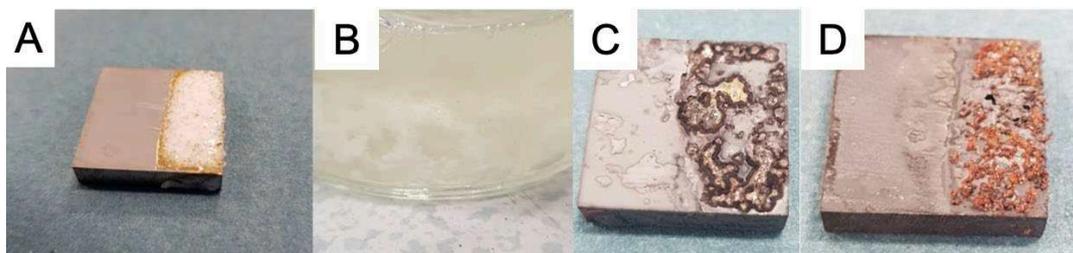

Figure 5.2 – a) Non-uniform distribution of silica gel particulates in Sopac10-HSi in PVA b) AceChiPP25 clumping of 25-micron phosphate powder in chitosan c) Post-normalised Sopac20-Hrc d) Post-normalised SoVer10.

Visual inspection of the trialled samples concluded that $Na_5P_3O_{10}$ coating technology provided the most consistent, uniform, and effective protection coverage against high temperature oxidation compared with the alternative solutions. In addition, in accordance with ASTM D3359-22, scotch-hatch adhesion tests exhibited an adhesion score of 3 or 4 for Sopac10 solutions while alternative solutions such as PP25PVA scored between 1-2. STAC1 oxidation of Sopac solutions indicated high levels of scale inhibition however blistering, checking, and cratering (small bowl shaped $3\mu m$- $5\mu m$ depressions in the film) were observed in some repeat samples as shown in Figure 5.3 which suggested inadequate formulation.
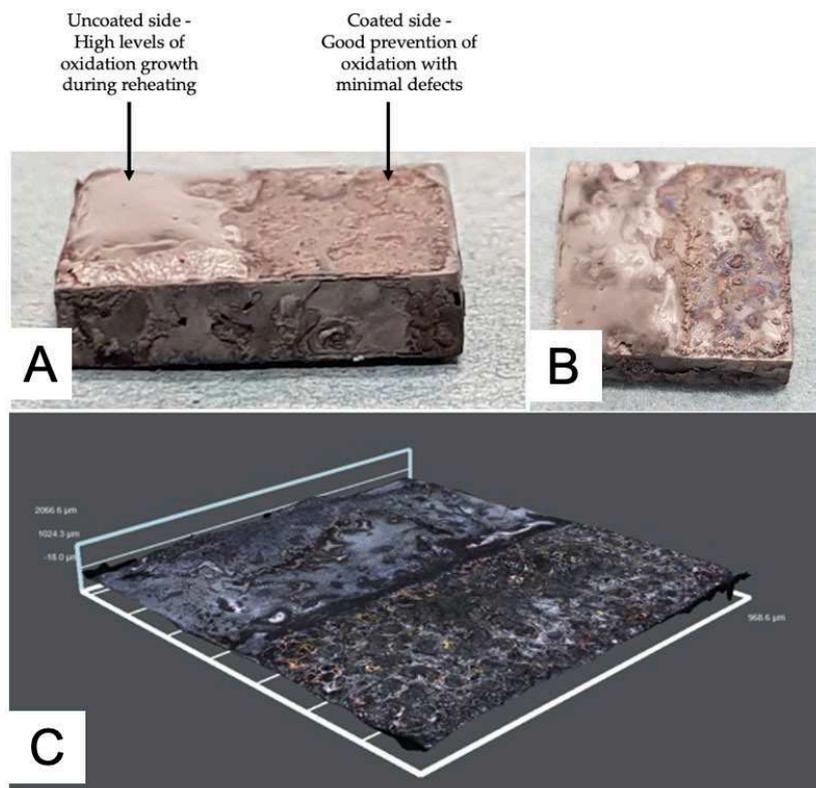
Figure 5.3 – a) Sopac10 sample exhibiting high oxidation inhibition with few defects b) Repeat Sopac10 sample with cratering defects c) Repeat Sopac10 sample with blistering defects that infiltrated into the non-coated area as shown by a Smartzoom micrograph.

To further improve the surface cosmetics of underlying surface after normalisation and reduce defects occurring frequently, a formulation optimisation of the $Na_5P_3O_{10}$ solutions was performed. Primarily focussing on coating concentration, specific weight and film thickness, the optimisation also investigated varying compounds (including monobasic or dibasic salts) such as K_3PO_4 or pyrophosphates as an alternative to sodium tripolyphosphate.

The superior performance of Sopac10 solutions against phosphate alternatives was somewhat expected as the coated layer displayed in Figure 5.1B and Figure 5.1D exhibited 3 key coating characteristics outlined in Chapter 2 for phosphate glasses. First, Sopac 10 achieved a glassesous state layer which adhered well to the steel preventing oxygen and other reactants from permeating to the surface. Next, the self-healing nature of Sopac10 delayed the degradation of the coating at high temperatures. Upon heating, the viscosity of the sodium polyphosphate

decreases, allowing it to flow into any damaged areas. As the material flows, it fills in the cracks or scratches and re-solidifies, thereby restoring the integrity of the protective layer. This flow and re-solidification occur without additional material, driven purely by the localized thermal events at the site of damage. Finally, the viscoelastic properties of Sopac10 appear to be favourable to high-temperature applications. Party due to the adaptability of the coating to changes to the thermal dynamics of the substrate, but mostly the flexibility or thermal expansion coherence (to steel), Sopac10 avoided extensive cracking during reheating thus maintaining barrier integrity.

5.2 Sodium Polyphosphate Concentration Trials

Initially, the effect of weight% change in $Na_5P_3O_{10}$ for SOPAC solutions on oxidation was investigated using STCA1 thermal cycles. 20-25μm thick Sodium Tripolyphosphate coatings formulated with concentrations of 5%, 7.5% 10%, 15%, 17.5%, 20% and 25% with 3% $CHCO_2$ were trialled, and their corresponding oxide thicknesses were measured as shown in Figure 5.4.

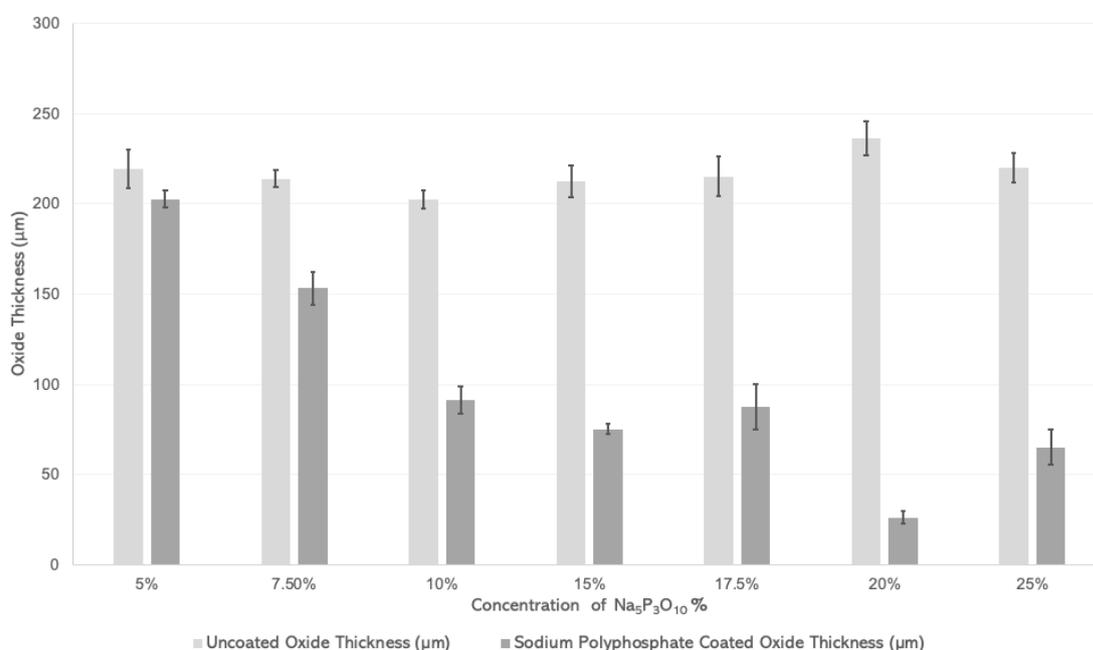**Figure 5.4** – Variation of Oxide thickness due to % of $Na_5P_3O_{10}$ concentration during Sopac formulation. Uncoated reference samples were subsequently calibrated relative to each STCA1 isothermal temperature to determine if samples referenced were within standard benchmark.

Randomly forming oxidation blisters were distributed on 5%-7.5% concentrated samples as well as significant surface roughening. Craters from oxide spallation occurred in scales ranging between 300μm -500μm and no remnant coating material was detected post-normalisation suggesting complete thermal degradation. While 10-17.5% $Na_5P_3O_{10}$ samples exhibited improved oxidation resistance of around 55%-60% compared to uncoated samples, defect characteristics of cracking, cratering and high porosity upon drying were still prominent in some areas of the post-normalised film. More specifically, surface porosities of 0.15, 0.19 and 0.16 were attributed to the 10%,15% and 17.5% concentrations respectively and cohesive remnant coating material was visually detected in many of the samples as shown in the SEM image in Figure 5.6. Coating adhesion was found to be unaffected by % concentration, with ASTM d3359-22 tests either reporting 2 or 3. The most promising coating evaluated was the 20% $Na_5P_3O_{10}$ formulation with a near 89% reduction in oxide growth compared to its uncoated counterpart and greatly superior surface cosmetics.
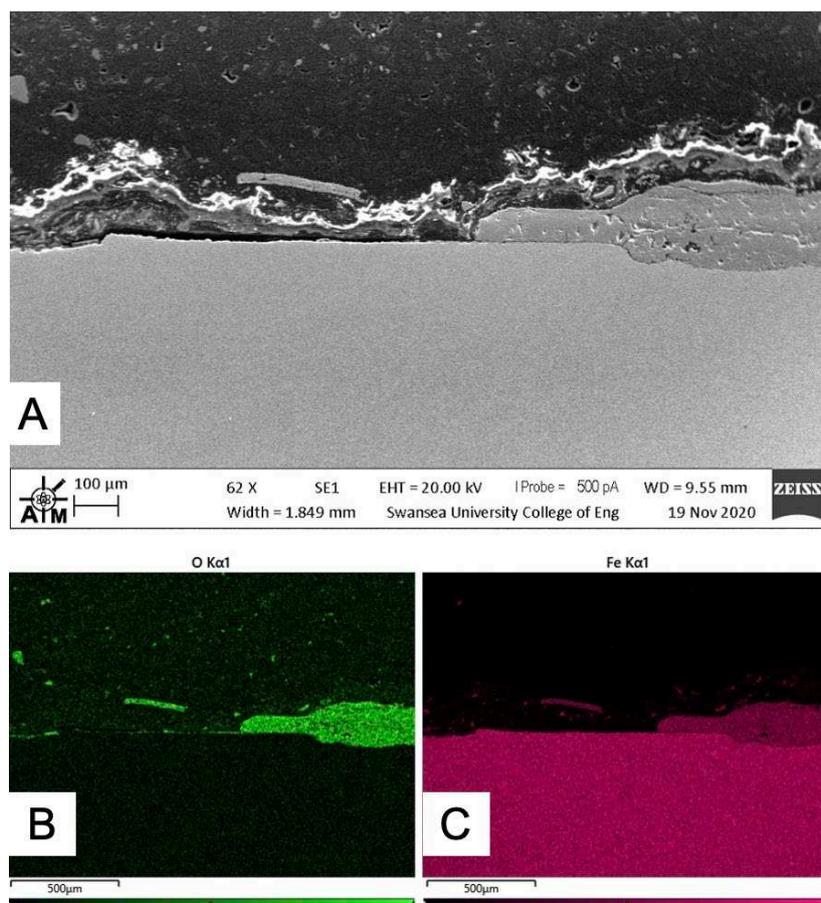
Figure 5.6 – Sopac10-3 sample a) 60x SEM image with a 50μm coating at both adhered (left) and non-adhered (right) regions b) O_2 EDS map c) Fe EDS map.

Further to this, Figure 5.7 provides Smartzoom and WLI maps of the improved surface roughness due to 20% $Na_5P_3O_{10}$ concentrations or "Sopac20" against 5% $Na_5P_3O_{10}$ concentrations. The results indicate that the higher % $Na_5P_3O_{10}$ provided enhanced surface cosmetic performance compared to the lower %. Chemical stability in phosphate solutions at high temperatures are generally more likely with higher concentrations, ensuring little decomposition and maintaining its barrier-like properties. In addition, high concentrations of sodium polyphosphate in the coating can result in denser and more uniform coverage. If the surface is uniformly covered, there are fewer weak points where oxidation can initiate thus leaving the surface less prone to blistering.
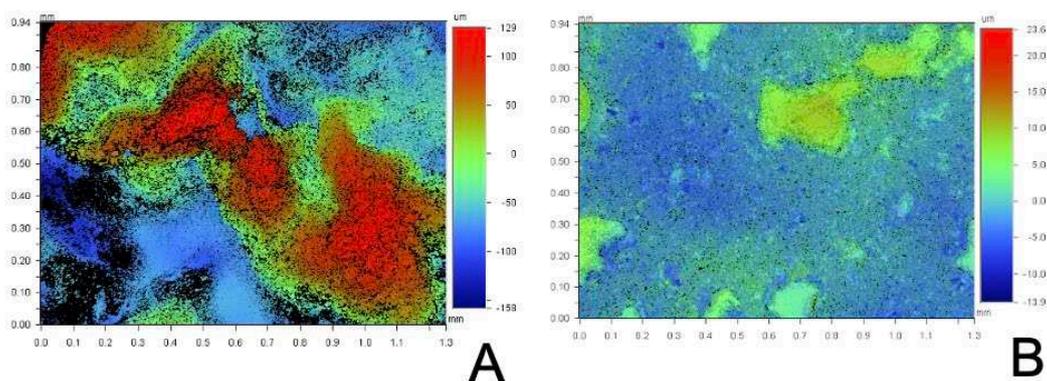
Figure 5.7 – Surface Roughness analysis of a) WLI surface map of 5% $Na_5P_3O_{10}$ b) WLI surface map of 20% $Na_5P_3O_{10}$.

In regions where no failure in coating adhesion had occurred, the oxidation inhibition was reduced by >99% however permeation of oxygen clearly was still achievable as indicated by the oxidation in Figure 5.8. This coating performance was additionally validated by Figure 5.9c, which annotates areas of the steel cross section which were preserved due to oxidation inhibition when compared with the unprotected side. Remnant oxide layers of 10µm remained however, as some cavity issues persisted for even highly concentrated Sopac solutions, with Sopac20 displaying a surface porosity of 0.08.
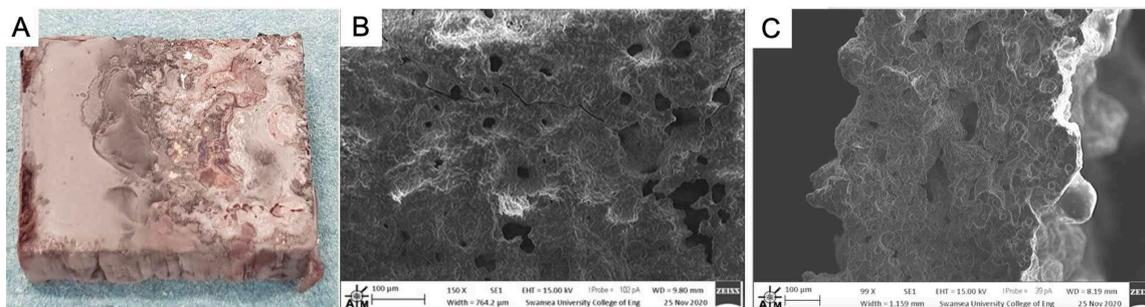
Figure 5.8 – a) Prevalent oxide blistering in 5-7.5% $Na_5P_3O_{10}$ concentrations b) SEM image of 10% $Na_5P_3O_{10}$ displaying 0.15 surface porosity and cracking c) SEM image of 20% $Na_5P_3O_{10}$ exhibiting 0.08 surface porosity.

Figure 5.9 depicts the differential of surface heights due to oxidation prevention. As this difference was around 84.5µm, the measured 2-dimensional surface area of steel preserved due to coating protection was calculated to be 1.94mm^2 which is 1.61% of the overall bulk material in the coated zone.

Figure 5.9 – a) Sopac20-4 after a STCA1 thermal cycle b) Sopac20-4 mounted and polished to 1µm, 200X cross-sectional view. The micrograph displays the coated-uncoated boundary after a STCA1 thermal cycle c) Cross-sectional view of d) Sopac 20-2 overview 200X stich across the length of a Sopac20 sample with high delamination occurrence.
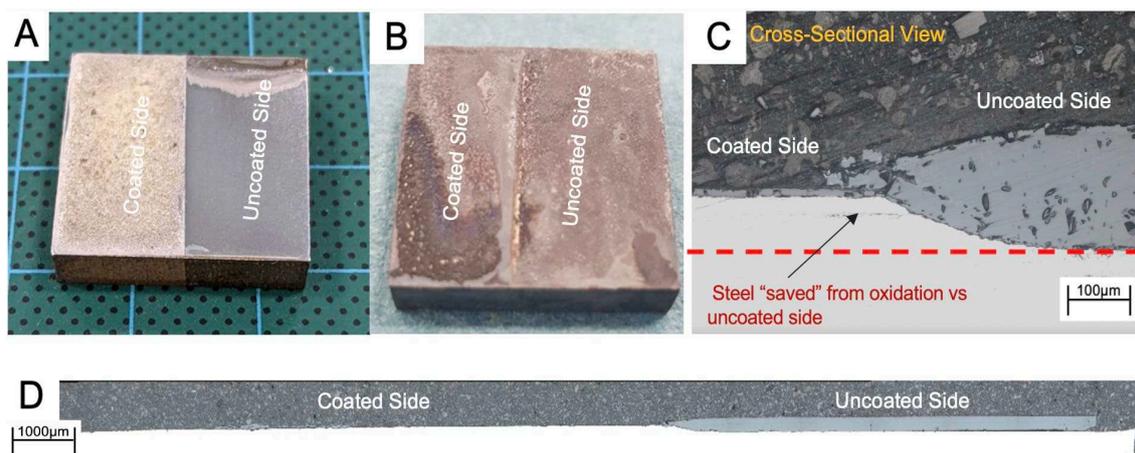
Previously, coating failure in lower concentration Sopac solutions had been attributed to high temperature degradation at, but 15-25% formulations failures suggested ingress O_2 permeating through pores of the spongy $Na_5P_3O_{10}$ matrix and oxidising the Fe below the coating surface, causing delamination. This phenomenon is shown in Figure 5.6 and consequently, the optimisation then focussed on the reduction of porosity within $Na_5P_3O_{10}$ solutions. To achieve this, glass additives were introduced to act as a support network that sintered together at its rubbery state at temperatures between 600°C-800°C to form a cohesive $Na_5P_3O_{10}$ glass composite.

5.3 Introduction and Optimisation of Glass Additives to Sopac20 Solutions

Initially, Sopac20-HRc was investigated in relation to the average particle size of the recycled glass powder so as to reduce overall coating porosity and produce an impermeable barrier for oxygen delivery to the steel substrate. Grind fineness was determined using ASTM D1210-05 and Sopac20-Hrc composites with <100µm, >100µm, >78µm, >53µm, >39µm, and >20µm were synthesised. The composites were subjected to a STCA2 thermal cycle with an attenuated ramp

rate as described in section 3.1 and the oxidation inhibition performance is shown in Figure 5.10.
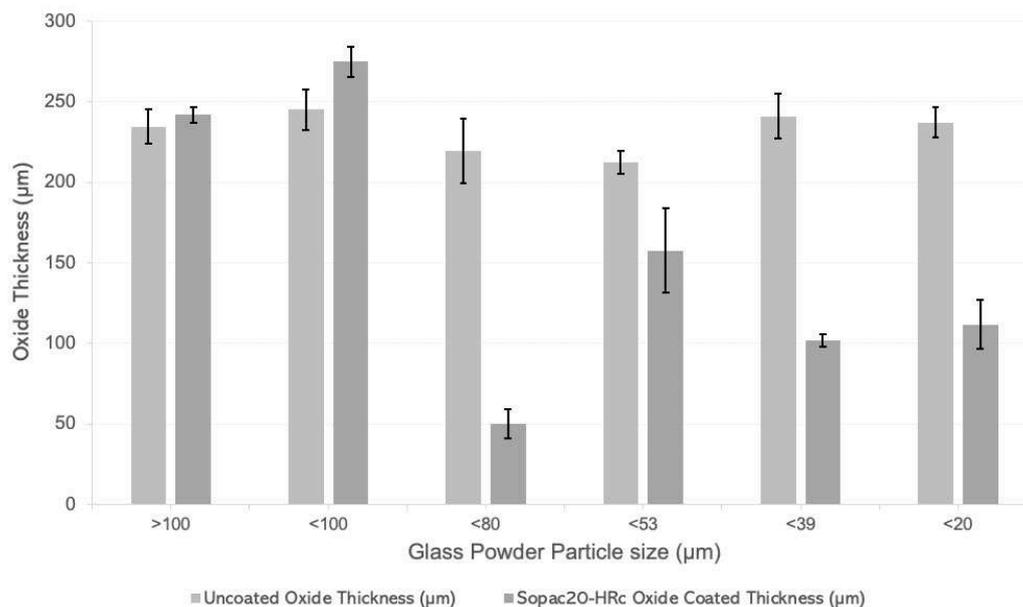
Figure 5.10 – Variation in oxide thickness due to glass powder particle size (μm) for Sopac20-HRc samples.

Generation of a consistently uniform glasseous layer with Sopac20-HRc was achieved with particles sizes between 53μm - 80μm. While some low size grind samples, such as Sopac20-HRc-17 were observed to possess low coverage of 68% after normalisation, the delaminated coating area still possessed a reduced oxide thickness between 75μm and 100μm suggesting partial protection prior to removal during STCA2. The surface roughness was inversely impacted by delamination occurrences with a reported decrease in Ra of 78.8% from <100μm to <20μm as shown by the WLI maps in Figure 5.11.
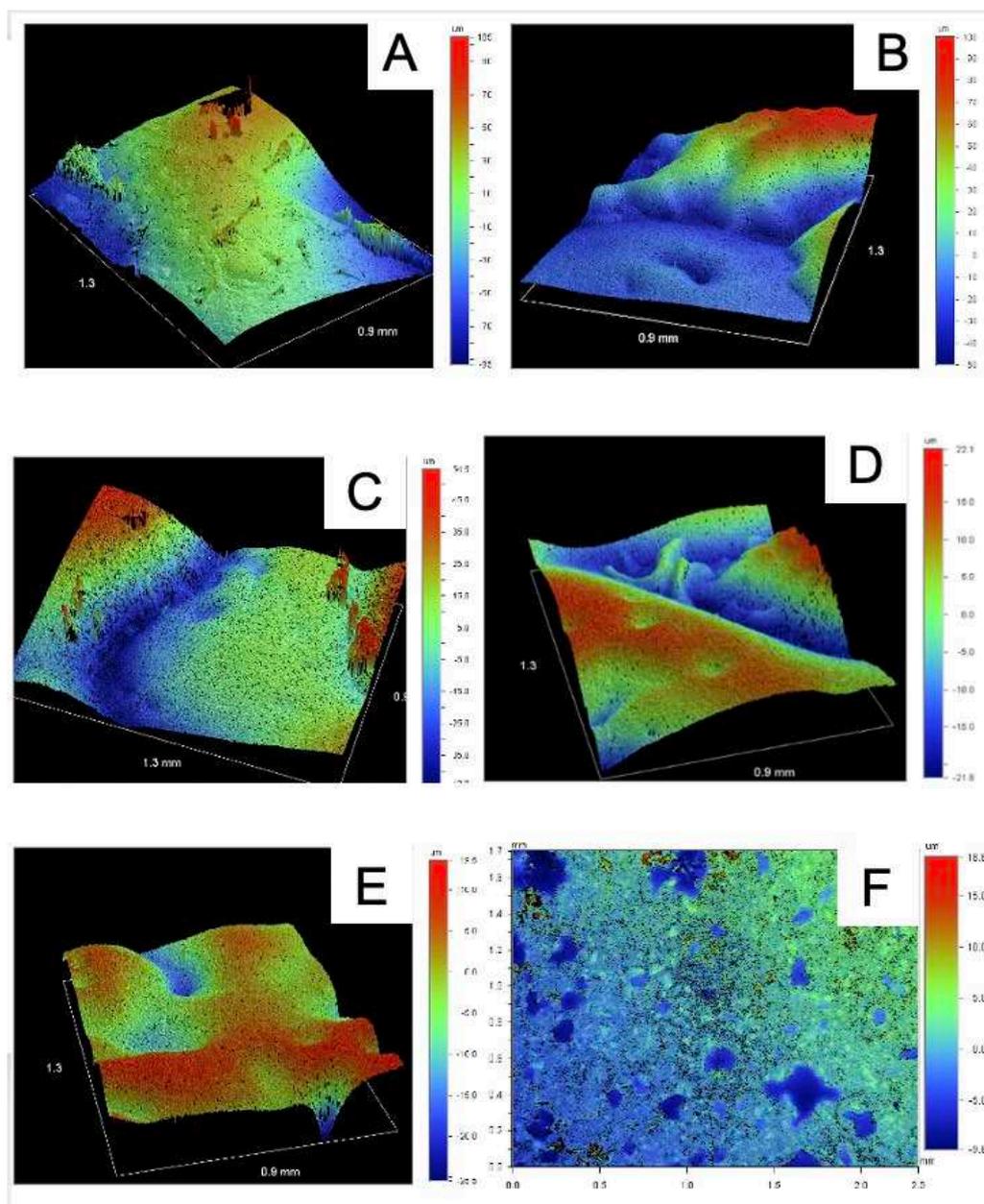
Figure 5.11- WLI surface roughness maps examples of a) >100μm particle size; Sopac-HRc-23 b) <100 μm particle size; Sopac-HRc-27 c) <80μm particle size; Sopac-HRc-34 d) <53μm particle size; Sopac-HRc-36 e) <39μm particle size; Sopac-HRc-41 f) <20 particle size; Sopac-HRc- 48.

Initial optimisation of the promising Sopac20-Hrc coating revealed the most consistent formulation parameter to utilise in the generation of a high-performing phosphate-based inhibitor. Namely, a hydrolysed xerogel film produced from an aqueous solution of 20% $Na_5P_3O_{10}$, cross-linked with a 5% CH_2-$CHCO_2H$ agent and $SiO_2 \cdot CaO \cdot Na_2O$ (recycled) glass additive. This glassesous layer is depicted as a detached layer away from the steel surface in Figure 5.12,

indicating successful sintering and composite formation of the $Na_5P_3O_{10}$ matrix and the $SiO_2 \cdot CaO \cdot Na_2O$ film.
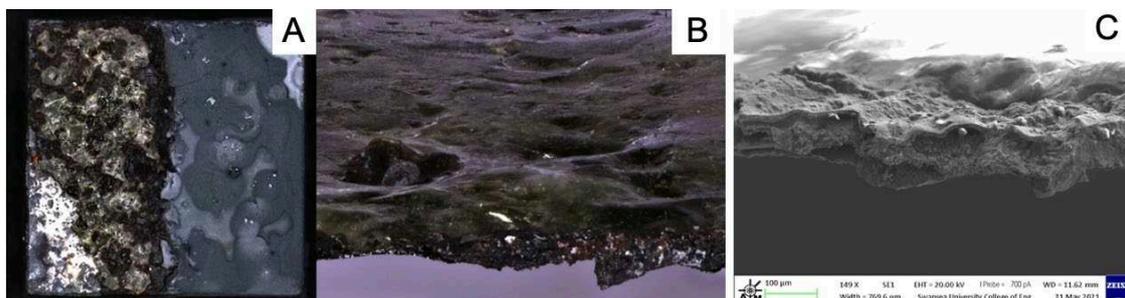
Figure 5.12 – Sopac20-HRc-17 a) Smartzoom 10x overview image. b) Smartzoom EDF view of a delaminated glasseous layer after normalisation. C) SEM 140x image with an indicative view of the $Na_5P_3O_{10}$ base matrix below the $CaO \cdot Na_2O$ glass layer.

Figure 5.13 displays the 87% oxidation inhibition achieved in highly adhered regions after STCA1 normalisation and SEM analysis of the composite morphology.
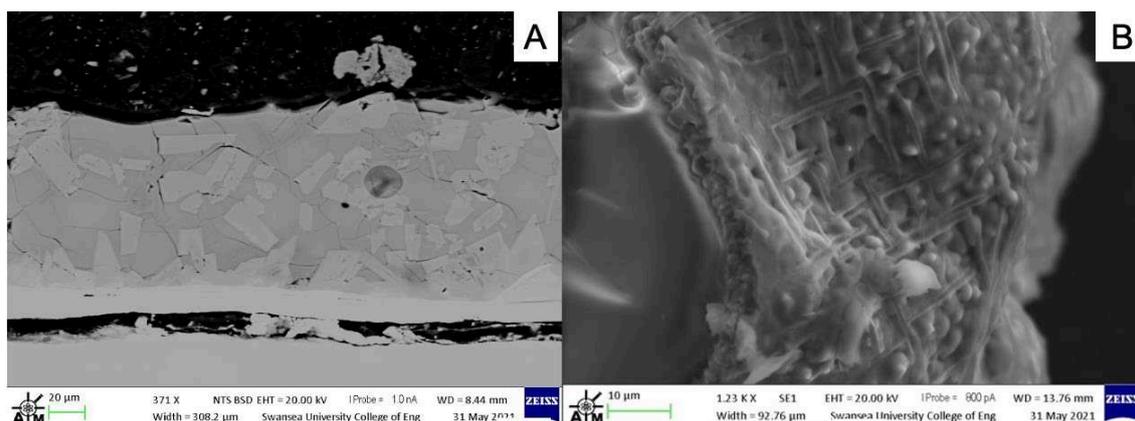
Figure 5.13 - Sopac20-HRc-15 a) 370x magnification SEM image of Sopac20-HRc layer atop the grown oxide layer and steel substrate. b) SEM image 1200x of $Na_5P_3O_{10} - SiO_2 \cdot CaO \cdot Na_2O$ composite matrix from delamination coating material.

The optimisation proceeded further with a variation in coating gauge investigation, in which evaluations of oxidation inhibition was coupled with tests for adhesion performance for the different film thicknesses. Through the dip coated method outlined in methodology, 5-10 steel samples of each coating gauge were subjected to a STCA1 thermal cycle, and their oxide layer thickness recorded as detailed by section 3.3. The results of this coating weight optimisation are shown in Figure 5.14.
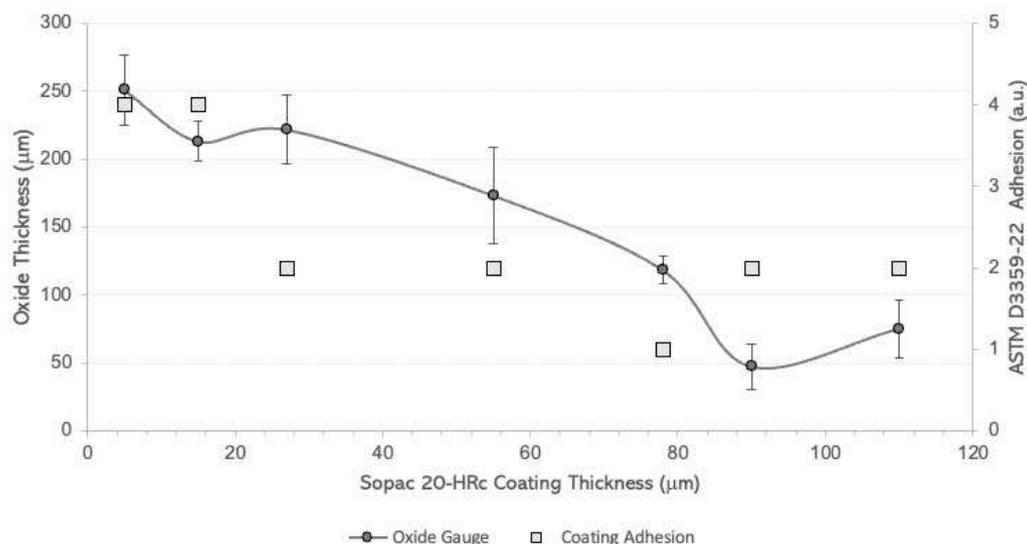
Figure 5.14 – Variation in oxide thickness for Sopac20-HRc53 samples due to applied coating thickness. Elcometer readings taken from 5 predetermined points on the coating substrate prior to normalisation. ASTM D3359 Adhesion was concurrently recorded for each coating gauge.

Clearly, samples with a higher thickness gauge outperformed those with a thinner protective film. While there are many reasons this could be the case, the most pertinent is the ability for the coating to accommodate for stresses (σ) during reheating by possessing more volume than previous solutions. Energy from these σ is enabled to be dissipated across a 2-3 times greater area, significantly reducing the risk of cracking during reheating. Also, the obvious extension of a physical barrier between the atmosphere and the steel substrate means the transport of oxygen ions through the film is greatly limited. This effect is amplified at high temperatures when reaction kinetics are accelerated from increased heat energy input.

Samples with increased coating gauges, such as Sopac20-HRc53-49 with its 44µm film, experienced regions of fragmented oxide splinters amongst the cohesive phosphate coating as shown in Figure 5.15. The surface morphology of these samples was analysed with Energy dispersive spectroscopy as described in methodology section 3.6.
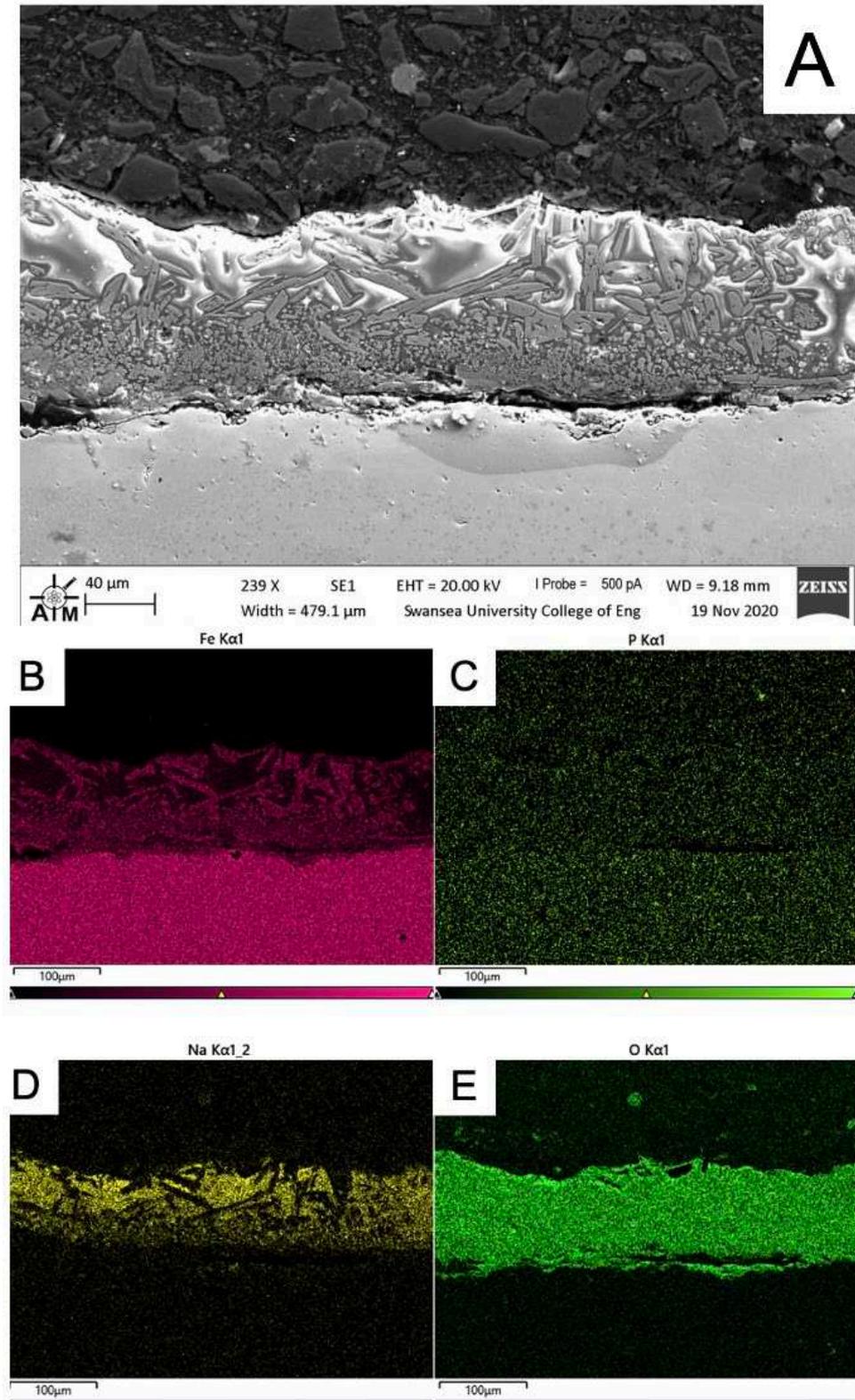
Figure 5.15 - Sopac20-HRc53-49 a) SEM image at 240x Image b) Fe EDS Spectral Map c) Phosphate EDS Spectral map d) Sodium EDS Spectral Map e) Oxygen EDS Spectral Map.

Other phosphate-based materials were trialled as an alternative to sodium tripolyphosphate, the most notable of which were Sodium Pyrophosphate and Potassium phosphate solutions. Initially, 10 samples of Popac10 and 85.1 $Na_4P_2O_7$ - 14.9 $CHCO_2$ (NaPyro10) were prepared with an average coating gauge of 47.8μm and surface coverage of 91%. Both sets of samples were subjected to a STCA2 thermal cycle but displayed high levels of thermal stress degradation and delamination as shown by Figure 5.16. Additionally, the post-normalised surface roughness was evaluated to have a Ra value between 29.7μm-35.1μm for Popac10-4 and exhibited only a 9.3% reduction in oxide thickness. These poor characteristics, when compared with Sopac20, combined with no discernible improvement in coating application or coverage meant that no further investigation of $Na_5P_3O_{10}$ alternatives.
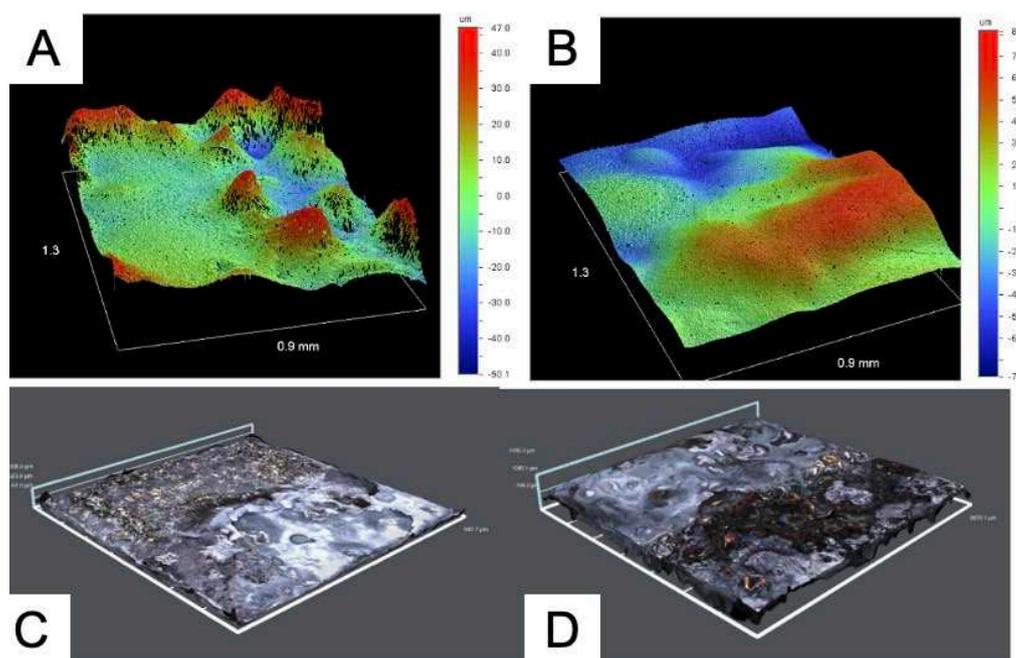
Figure 5.16 – a) Popac10-4 sample after STCA2 thermal cycle b) NaPyro10-2 sample after STCA2 thermal cycle c) WLI surface roughness map of Popac10-3 d) WLI surface roughness map of NaPyro10-1 samples.

After investigations of alternative phosphate bases to be cross-linked with $CHCO_2$, additional research was undertaken to compose a suitable and optimised glass additive blend in combination with Sopac20. Initially, Sopac20-

HSLo which uses a soda lime glass, Sopac20-HBo which uses a borosilicate glass, and Sopac20-HBa which uses a BioActive glass samples were synthesised and subjected to STCA2 thermal cycle. As Sopac20-HBa displayed poor adhesion and coverage characteristics during application and severe delamination was observed for Sopac20-HSLo after 700°C during reheating, only Sopac20-HBo was pursued further in the investigation.

Therefore, 15 samples with the most promising alternative glass additive, borosilicate glass, were synthesised and an additional 15 steel samples were coated with a blend of two glass types to enable modification of glass transition temperatures of Sopac20-HRc to a desired set value. The samples used ranged between 40-60µm in coating thickness and were prepared in accordance with methodology section 3.2. The blended investigation samples were subjected to STCA2 cycles, and the oxidation inhibition and surface cosmetic results are recorded in Table 5.3.

Table 5.3 – Sopac20 formulations and results for combined Borosilicate/Recycled Glass blends as a glass additive. Includes <80µm, <53µm, and <39µm particle size 100% borosilicate glass additive coatings trials.

Sample Name	Glass Additives	Average Coating Thickness (µm)	Average Oxidation Reduction	ASTM D3359-22 Adhesion	Surface Coverage	Average Surface Roughness Ra (µm)
Sopac20-Bo-(1-5)	100% Borosilicate Glass (<80µm particle size)	38.2	70.6%	4	96.8%	32.6
Sopac20-Bo-(6-10)	100% Borosilicate Glass (<53µm particle size)	67.4	88.9%	5	99.5%	21.5
Sopac20-Bo-(11-15)	100% Borosilicate Glass (<39µm particle size)	64.3	72.0%	5	98.1%	17.7
Sopac20-HRc-Bo-(1-3)	80% Borosilicate Glass 20% Recycled Glass	46.8	79.5%	3	97.7%	28.3
Sopac20-HRc-Bo-(4-6)	60% Borosilicate Glass 40% Recycled Glass	55.1	49.1%*	3	57.9%	15.9
Sopac20-HRc-Bo-(7-9)	40% Borosilicate Glass 60% Recycled Glass	49.0	66.0%*	3	61.2%	26.4
Sopac20-HRc-Bo-(10-12)	20% Borosilicate Glass 80% Recycled Glass	51.6	82.8%	4	97.9%	11.4
Sopac20-HRc-Bo-(13-15)	0% Borosilicate Glass 100% Recycled Glass	61.7	73.4%	3	98.6%	13.5

*High levels of delamination occurred during cooling

No tenable link between glass additive blends of borosilicate and recycled glass was found in % oxidation reduction or average surface roughness Ra for the

coated steel samples. Majority replacement of the glass additive with a borosilicate powder did lead to a 4.8% increase in surface coverage when compared with Sopac20-HRc. ASTM D3359-22 tests consistently reported adhesion scores of 4 or 5 and this high level of adhesion and coverage is apparent after visual inspection post-normalisation as shown in Figure 5.17.
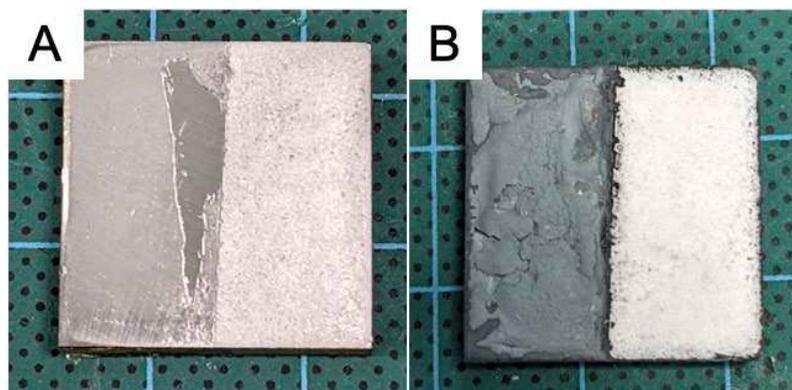
Figure 5.17 – Sopac20-Bo-14 a) before STCA2 thermal cycle b) after STCA2 thermal cycle.

Furthermore, DSC and TGA analysis were performed in accordance with methodology section 3.9 on the coating materials synthesised in Table 5.3. Initially, Sopac20-HRc-Bo-15 was analysed to define T_c and T_g regions for this coating and with a STCA3 thermal cycle, the DSC and TGA curves were determined up to 800°C as shown by Figure 5.18. STCA3 was chosen as it was essential to determine the behaviour of the coating at various isothermal temperatures for a holding period as opposed to a fixed temperature.
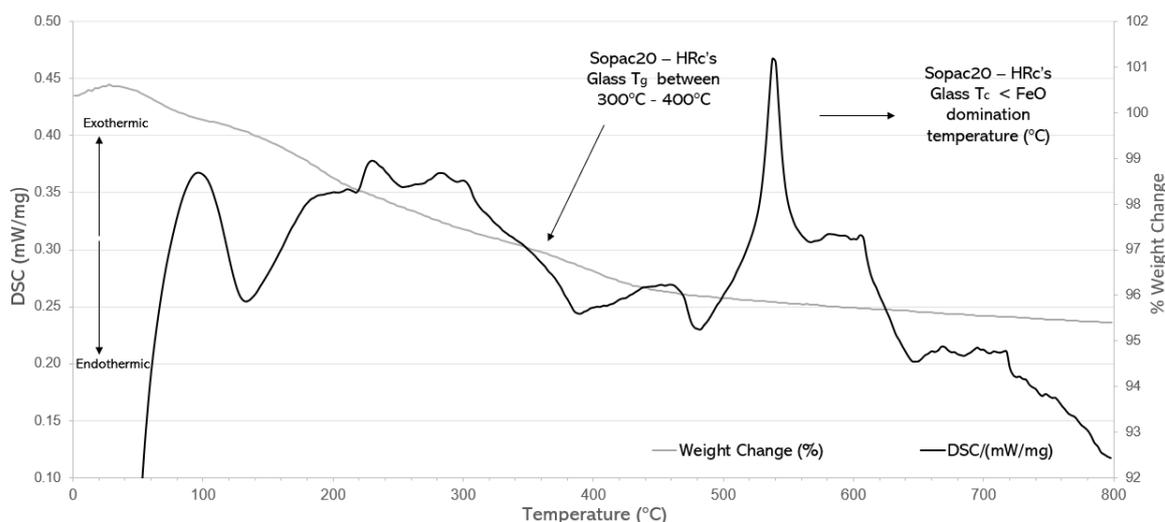
Figure 5.18 – DSC and TGA Curves for Sopac20-HRc-Bo-15 using an STCA3 Thermal Cycle. T_c and T_g are indicated by characteristic drops and peaks in heat flow.

Samples with increased weight % of borosilicate, like Sopac20-HRc-1 was designed to shift the T_g and T_c zones toward the Wüstite dominating temperature region from purely recycled glass additives. The DSC curve clearly indicates a broad endothermic change in the region of 300°C - 400°C and this is typical for a glass transition range where the material transitions from a hard and relatively brittle state into a more viscous or rubbery state. In addition, exothermic reactions are probably occurring after T_g indicating cross-linking or a crystallization of the constituent parts in Sopac20-HRc-Bo-15. This is likely, as discussed in Chapter 2, because amorphous materials tend to crystallize upon heating due to being in an initial metastable state which releases energy. This appears as an exothermic peak in Figure 5.18 and suggests the coating is undergoing significant changes to its mechanical properties as it transitions into a crystalline state.

Observation of their DSC curves however, provided no tangible evidence of this shift as shown in Figure 5.19 and further research into the phenomena was not conducted. Therefore, the optimisation was solely determined by oxidation properties and surface cosmetic performance determined in Table 5.3 and the Sopac20-HRc-Bo (10-12) formulation was deemed to provide the most promising

characteristics for a prospective coating to be applied to the Install235 products. Specifically, a 60μm film of Sopac20-HRc-Bo with a recycled glass 80:20 borosilicate blend at a 53μm powder particle size.
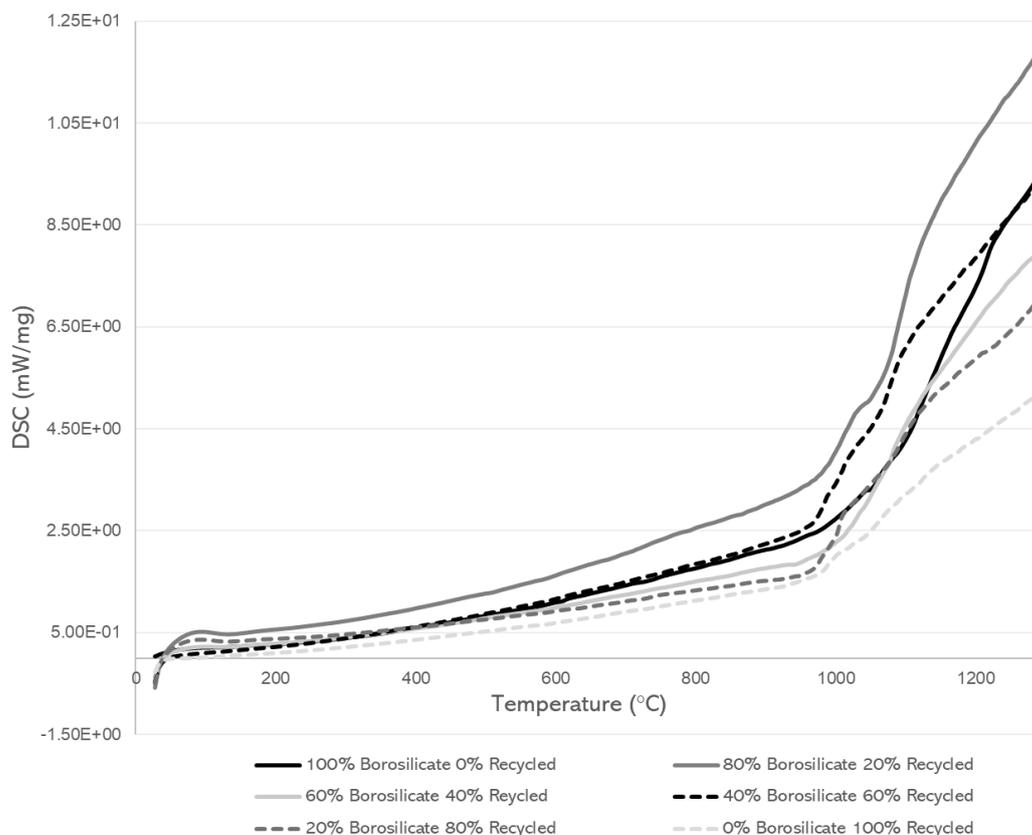
Figure 5.19 – DSC and TGA analysis curves of glass blends from Table 5.3 which combined borosilicate additives to Sopac20-HRc solutions. T_g and T_c were undefined and suggested no reaction occurred within the temperature range.

When compared against purely Sopac20 coatings, introductions of glass additives were found to improve overall oxidation growth by 17.7% and reduce surface roughness by 64.5% for Sopac20-HRc-Bo. In addition, ImageJ optical inspection of the coating observed a change in surface porosity from 0.08 to 0.01 and this improved porosity characteristic is exhibited by the SEM image of Sopac20-HRc-Bo shown in Figure 5.20a. The figure also highlights the high surface coverage of the coating prior to normalisation (<99.9%) and after normalisation (97.9%). ASTM D3359-22 adhesion for Sopac20-HRc-Bo was typically between 3 and 4. During delamination, the coating detached as a

complete structure, leaving no remnant material on the underlying steel substrate as shown in Figure 5.20b.
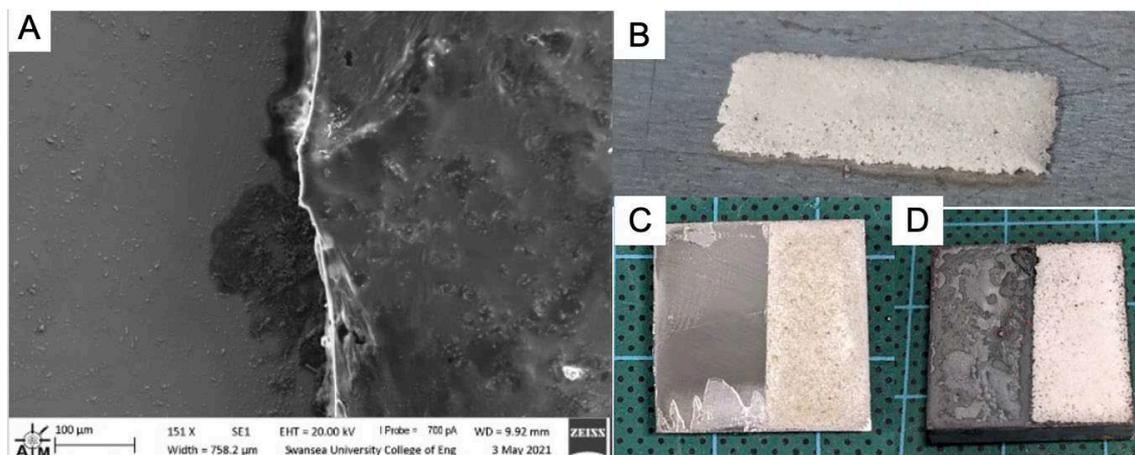
Figure 5.20 – Sopac20-HRc-Bo a) SEM image at 150x magnification at the coated/non-coated boundary b) Delaminated 60μm coating matrix mechanically removed from the steel substrate c) pre-normalised coating d) post-normalised coating.

The material selection process and subsequent optimisation generated a definitive coating for advanced testing, and the next section will evaluate the qualitative, mechanical, and thermal properties of the optimised coating, Sopac20-HRc-Bo.

5.4 Qualitative phase analysis, composition layers and mechanical properties of optimised Sopac20-HRc

Finally, the most optimised version of the investigated $Na_5P_3O_{10}$ coatings, Sopac20-HRc-Bo, was qualitatively analysed to understand the elemental presence within the coating after normalisation and any phase changes that occurred at high temperatures in the glasseous layer. The feasibility of the coating was also evaluated by observing key indicators of thermal transfer and surface morphology.

Initial observations of Sopac20-HRc-Bo were conducted through SEM and EDS mapping. For this technique, a higher gauge of coating of ~100μm was utilised to view a better picture of oxide-composite interaction during reheating and discover the behaviour of key elements' precipitation during normalisation.

Figure 5.21 displays a 110x magnification BSD image of the coating Sopac20-HRc-Bo-23's cross-section and its corresponding elemental EDS spectral maps after an STCA2 thermal cycle.

Figure 5.21 - Sopac20-HRc-Bo-23 a) BSD image at 110x magnification of coating cross-section b) EDS Map of elemental Si c) EDS Map of elemental Fe d) EDS Map of elemental O_2 e) EDS Map of elemental P f) EDS Map of elemental Na g) EDS Map of elemental Ca.

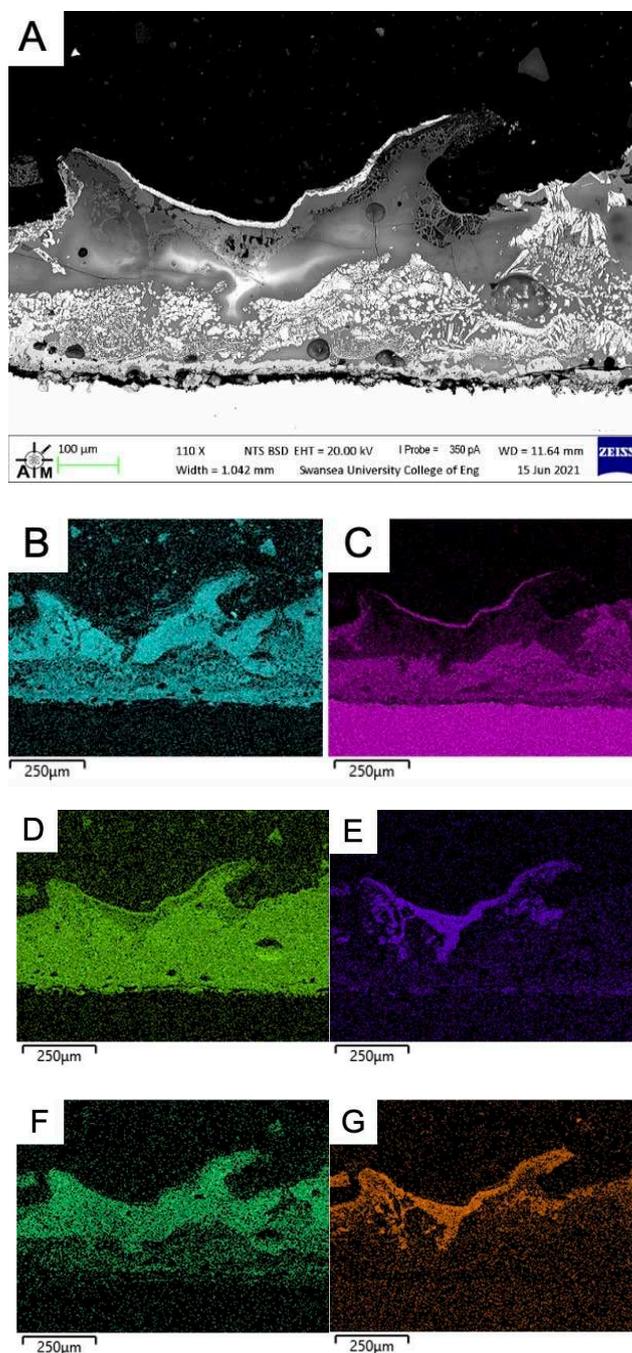This exhibition of elemental species within the coating-oxide matrix is interesting, as it indicates the preferential diffusive nature of the core ingredients of the Sopac20-HRc-Bo while also highlighting how entire regions of oxide (potentially magnetite) spallate away from the bulk oxide. Figure5.21E indicates that phosphate, due to its volatilization, may migrate to cooler regions during reheating due to the poor mobility of its ions within the glass matrix. Na, however, has a higher mobility in glasses due to their single charge and small ionic radius. Which explains why the element appeared to be unaffected by the temperature gradient and remained uniformly distributed in the composite. Finally, the existence of a probable magnetite layer atop the phosphate region is a symptom of poor adhesion between the FeO and Fe_3O_4 during reheating. The two main reasons for this delamination could be from the phosphate preferentially reacting to the magnetite structure, causing changes to its stoichiometry. This may not be favourable for adherence to the underlying material. Also, molten phosphate is known to occur between 800°C - 1000° which has significant implications for the bonds attaching the magnetite to the bulk oxide, especially if it was able to permeate within the interface of the two oxide phases.

Next, the Raman spectra of Sopac20-HRc-Bo was observed for varying isothermal temperatures. Partly to detect the sites of α-Fe_2O_3 ,Fe_3O_4 and FeO within an oxide-coating composite system, the spectra also aimed to reveal key periods during reheating in which certain elemental degradation, such as phosphorus, occurred. Point scans, directed centrally, at the coating material were performed at 0.013mW for 10s using a 531nm radiation. The samples were analysed after normalisations of 400°C, 600°C, 800°C, 1000°C. The resulting spectra is shown in Figure 5.22 in which Savitzky–Golay smoothing of a second order polynomial, was performed to remove accidental peaks and reduce noise. Familiarly, at low temperatures this figure displayed the characteristic wustite

and magnetite peak at around 410cm^{-1} as shown by Figure 4.16 and expected phosphate vibrational peaks between 800cm^{-1} and 1000cm^{-1}. While amorphous, phosphate glasses usually exhibit symmetrical stretching of its PO$_4^{3-}$ tetrahedral units at 900 cm^{-1} -1000 cm^{-1} before being more well defined at its crystalline state. This is in agreement with Fugure 5.23 and it was anticipated sodium would not directly affect the spectra as it does not display molecular vibration compared to the phosphate elements.
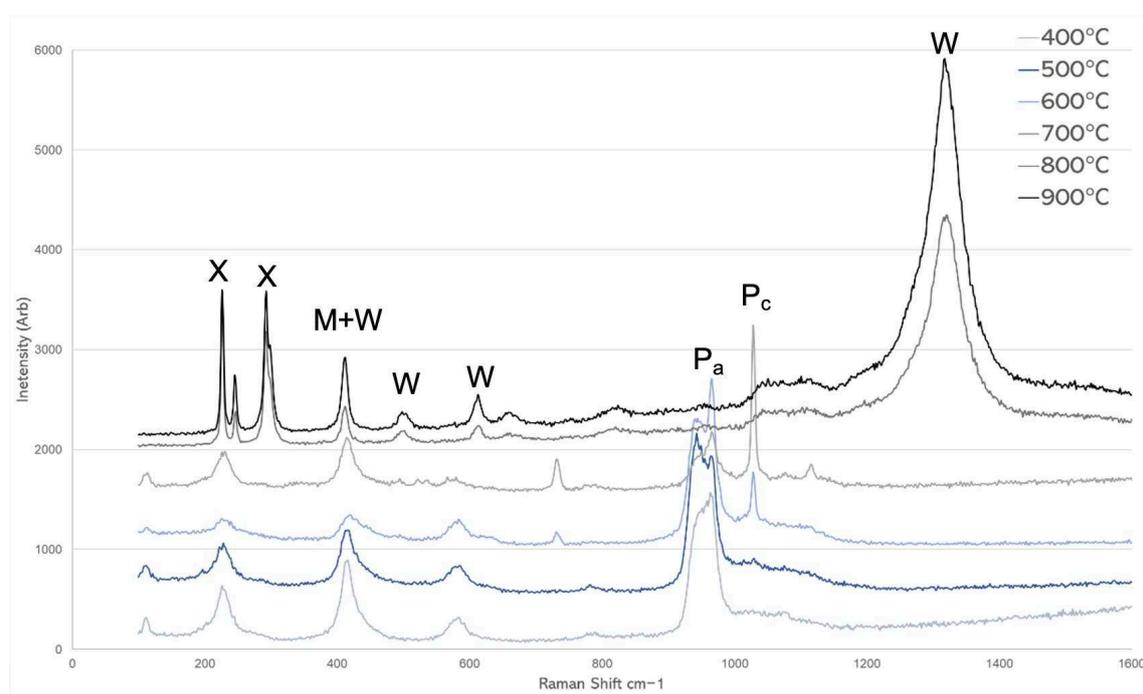
Figure 5.22 - Raman spectra of Sopac20-HRc-Bo' coatings bulk material post-normalisation at varying isothermal temperatures; 400°C, 500°C, 600°C, 700°C, 800°C, 900°C. Savitzky–Golay smoothing was applied to the second-order polynomial. Where P$_a$ is amorphous phosphate and Pc is crystalline phosphate.

At higher temperatures, the dissipation of the phosphate peaks beyond 700°C suggest the thermal decomposition of the phosphate glass and dominance of the oxide matrix due to a known strong wüstite and magnetite peak at 1300cm^{-1} emerging. This is in congruence with a smaller wustite peak being displayed at higher tempertures and the 400cm^{-1} oxide peaks becoming less broad and sharper as the coating layer degrades. Intrestingly, Figure 5.23 may agree with the phase change analysis displayed in Figure 5.18, as phosphate glasses are likely to shift

in peak position after a transtion to a crystalltine state. At 600°C and 700°C, the new peaks at 1000°C indicate a different crystal lattice to the initial phosphate matrix, indicating a change in the crystalline environment.

Further qualitative analysis was conducted in the form of X-ray diffraction. Powder XRD was performed on Sopac20-HRc-Bo samples after 400°C, 600°C, 800°C, 1000°C heat treatments as shown in Figure 5.23. Using 2Θ angles between 0° and 90° in a diffractometer, powdered Sopac20-HRc-Bo was analysed using Co kα radiation (40 kV, 40mA) with a scan speed of 0.03°/s.

Figure 5.23 – XRD diffraction pattern (2Θ) of Sopac20HRc-Bo samples after varying heat treatments.

Usually, increased peak intensity indicates improved crystallinity of a phase as the lattice is able to scatter more x rays from its better-defined structure. As such, the enhanced peak definement at around 35° suggests growth and prominence of wüstite and magnetite in the composite layer. Expectedly, the divergent XRD was unable to pick up typical amorphous phosphate x ray scattering as they

present themselves as broad regions as opposed to distinct peaks. This explains why Figure 5.23 exhibits a crystalline phosphate state between 20° to 30° at 600°C without a pre-existing amorphous state, which degrades at higher temperatures. This result is largely in agreement with the Raman spectra findings, that a crystallization temperature for this material is somewhere around 600°C due to peak intensity significantly increasing in this 2θ region. However, it is possible this peak could have been misconstrued as a phosphate phase (like Na_3PO_4) when actually α-Fe phases are very prevalent in this angle region.

Further divergent XRD scans were performed on the two sides of the delaminated coating structure; the cohesive coated layer and the preserved underlying scale adhered to phosphate-based solutions after normalisation. This established changes in oxide morphology from Figure 4.15 and detected any precipitant coating material in the inhibited scale layer. 2Θ angles between 0° and 90° in a diffractometer, the underlying oxide was analysed using Co k$\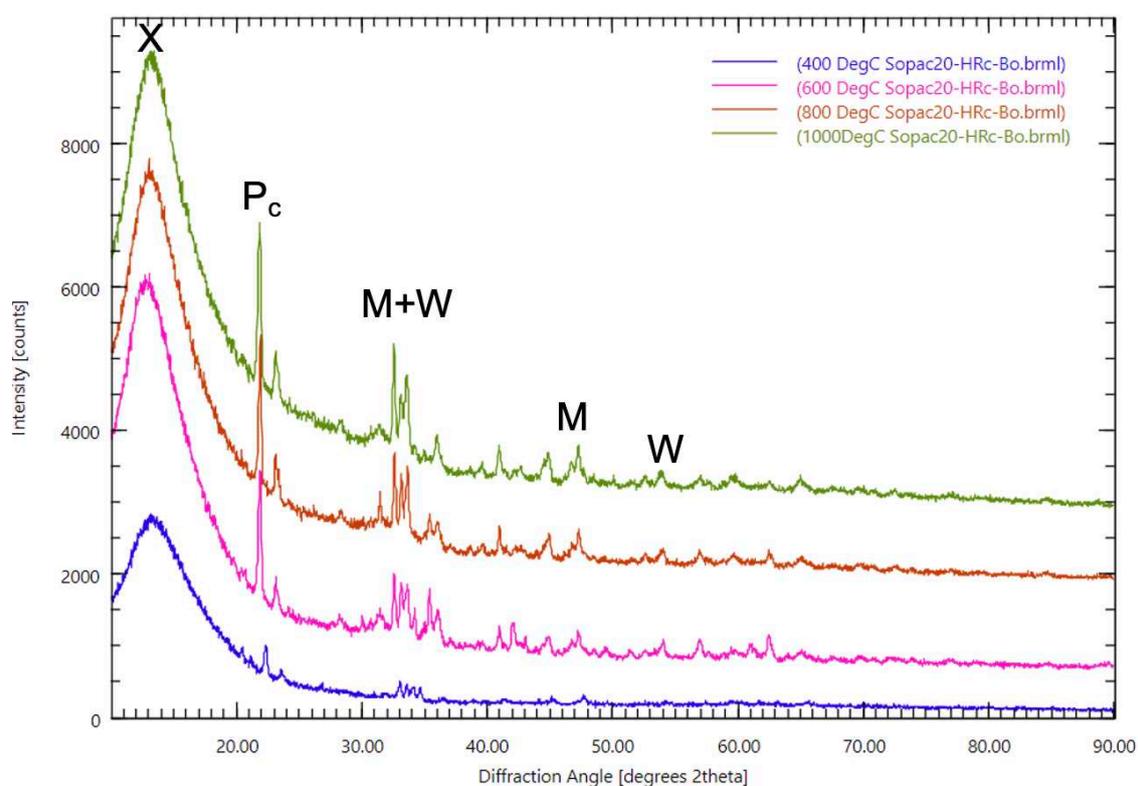alpha$ radiation (40 kV, 40mA) with a scan speed of 0.03°/s. Figure 5.24 displays the XRD scans performed on the phosphate coated scale systems.
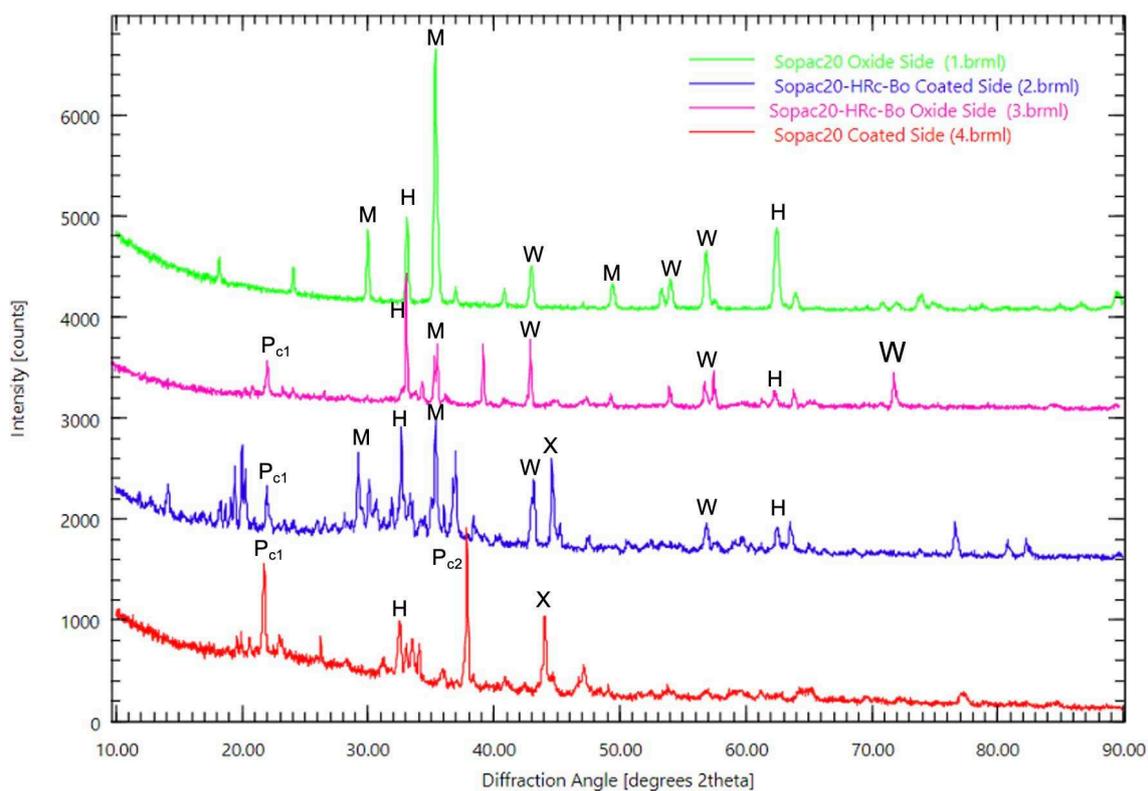
Figure 5.24 – XRD diffraction pattern (2Θ) of underlying oxide layers and the surface layer of coated material of phosphate-based coatings after STCA2 normalisation.

Figure 5.24 builds confidence that the crystalline phosphate phases theorised are not being misrepresented. This is because the XRD pattern only displays strong peaks at around 22° for the Sopac20 Coated side and Sopac20-HRc-Bo Coated side samples and a ferritic α-Fe phase would be present in this region for all samples after reheating. Additionally, the discrepancies in peak clarity and intensity for the magnetite and wüstite peaks between Sopac20 Coated side and Sopac20-HRc-Bo Coated side indicate the improved performance of oxidation reduction, by introducing a glass additive. The higher crystallinity of the Sopac20 sample suggests a strong structure of wüstite while Sopac20-HRc-Bo has either reduced the presence of wüstite or forced a transition to a different oxide form. It's also important to note that the addition of borosilicate glass to the solution may have increased the reactivity of the solution. The sodium polyphosphate phase peaks seen in Sopac20 (coated side) are not present in the oxide matrix for the Sopac20 (oxide side) sample. While this may be due to degradation, there's

also evidence the two compounds maintained a consistent boundary and did not exist in each other's matrix during reheating. However, for Sopac20-HRc, the well-defined 2θ peaks for the phosphate phases and oxide phases appear in both XRD patterns, which were established in Chapter 4. Feasibility studies centred around the thermomechanical properties of Sopac20-HRc-Bo and other coating iterations were conducted to determine effects on yield and normalisation due to the presence of a 40-60μm phosphate-based coating atop the steel substrate. First, hardness tests according to ASTM-E92-17-3-01 were performed along the length of the cross section. The coated samples were subjected to a STC1 thermal cycles prior to metallurgical preparation for testing as detailed in section 3.2. The Vickers hardness variation is illustrated in Figure 5.25 and exhibited an average 14.8% drop in hardness at the mid-cross section and a HV/1 differential of 9.9 between the top and bottom substrates for Sopac20HRc-Bo. High hardness of 152.1HV/1 at the coating-steel interface suggested prominent surface hardening occurred during reheating. These results are indicative of a coating structure which is minimally impacting the thermal conductivity of the steel system. While surface hardening is reduced when compared to Figure 4.1, the drop % is very close to the 12%-14% drop reported form uncoated sample and indicates the hardness mechanical property is somewhat unaffected by the application of Sopac20HRc-Bo.
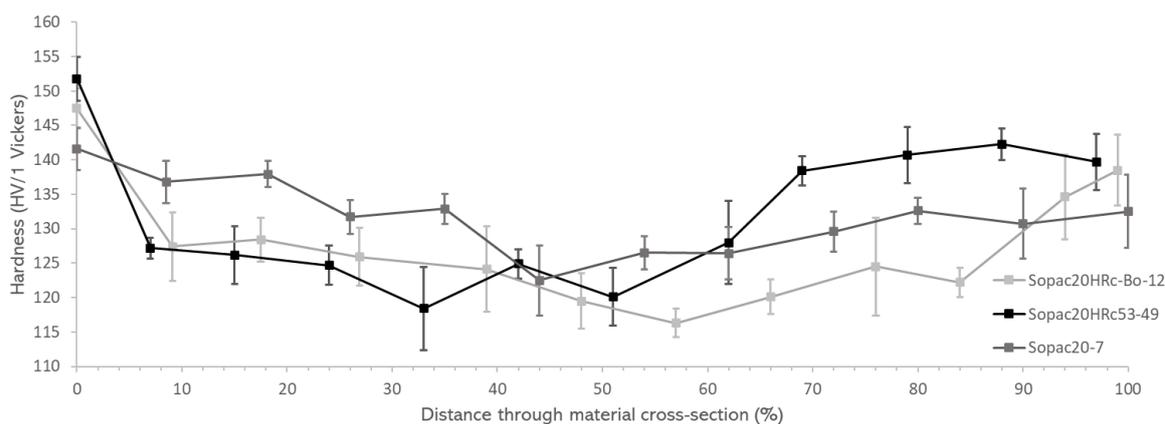
Figure 5.25 - Vickers Hardness (HV/1) variation in various phosphate-based coating samples across the material cross-section. Diamond indentation was applied with a 1Kg load for 10s.

However, the grain size cross-sectional analysis of the phosphate-based coatings was also conducted through measurements in accordance with BS EN ISO 643:2020 by observing grain dimensions with 20x magnification full-length stitches. The results are shown in Figure 5.26. The measurements revealed a 31.7% drop in grain diameter in the 40-60% region compared to the surface boundary grain sizes. While this is around 6% points higher (and therefore more undesirable) than what was observed for uncoated samples, there were specific sample sets, like Sopac20 which remained within the standard 20%-25% drop zone. The results suggest the glass additives increase thermal insulation and may prevent ingress thermal energy, but this trait may be mitigated through the type and concentration of the blend.
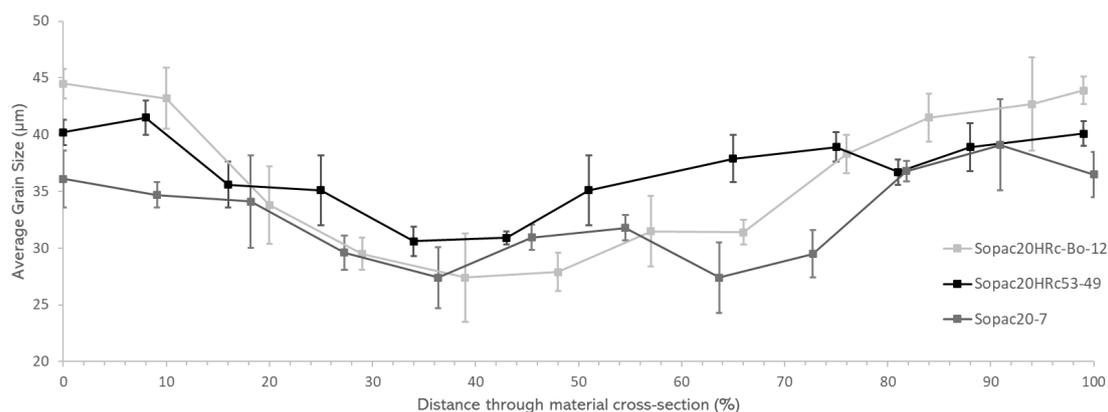
Figure 5.26 - Grain Size (μm) variation in phosphate-based coatings using the mean line intercept method. Calculation of the grain size diameter, 650μm lines were drawn diagonally across intermittent micrographs spaced apart as a function of the total cross-section distance.

In addition to oxide inhibition and mechanical properties, observations of the impact of Sopac20-HRc-Bo application to the steel's surface roughness was a direct method in understanding the commercial viability of the coating. WLI surface roughness maps at 5.1X magnification with a 1.96μm sampling size was performed on Sopac20-HRc-Bo in identification of potential surface cosmetic enhancement as an optimised formulation. The maps examine the Ra and Rz values of the steel substrate for samples at the uncoated substrate, the coated substrate, and the underlying remnant surface after delamination. Figure 5.27 shows examples of the WLI maps utilised to attain the Ra values.
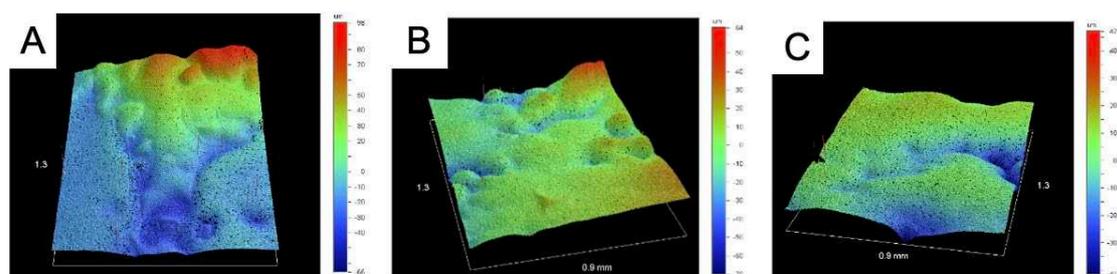
Figure 5.27 – a) Uncoated surface side of Sopac20HRc-Bo b) Coated surface side of Sopac20HRc-Bo c) Underlying surface after Sopac20HRc-Bo delamination.

The Ra and Rz values were averaged over 5 sampling areas for 3 repeat samples and WLI analysis concluded that the uncoated side possessed an average Ra of 16.8(± 4.4)μm and an Rz of 144.1(± 10.7) μm while the coated surface side of Sopac20HRc was discovered to have an average Ra of 20.6μm(±3.1μm) and an Rz

of 129.9 (±8.3μm). However, for steel surfaces with delaminated of remnant Sopac20HRc-Bo, the average Ra and Rz was reduced to 9.89μm (±2.0μm) and 74.21μm(±19.1μm) respectively.

Finally, the thermal properties of the Sopac20HRc-Bo were determined using a combination of LFA and DSC. A cylindrical disk of coating material with diameter 19mm was synthesised and cured ready for laser flash analysis. Using equation 3.9, the thermal conductivity, k, at various temperatures was calculated by observing thermal diffusivity, α, and density, ϱ, from DSC and specific heat capacity, Cp from LFA and the results are shown in Figure 5.28. The results indicate that the optimised phosphate solution, Sopac20-HRc-Bo possessed a thermal conductivity between 0.6W/m*K – 1.0W/m*K. Expectedly, this is vastly lower than the thermal conductivity of the UE1-UE41 samples measured in Chapter 4 and its respective oxide. This is one reason why grain size changes were dampened with a phosphate coating due to the poor thermal transfer from the atmosphere interface to the steel boundary. There are two reasons why this coating may have particularly poor conductivity. First, the use of sodium as a network modifier often leads to poor thermal conductivity due to the disruption of the phosphate network and its inability to efficiently vibrate the lattice structure. Second, evidence of thermal degradation in Figure 5.23 suggests a change in the materials composition or an influx of porosity; both of which can lead to lower thermal k.
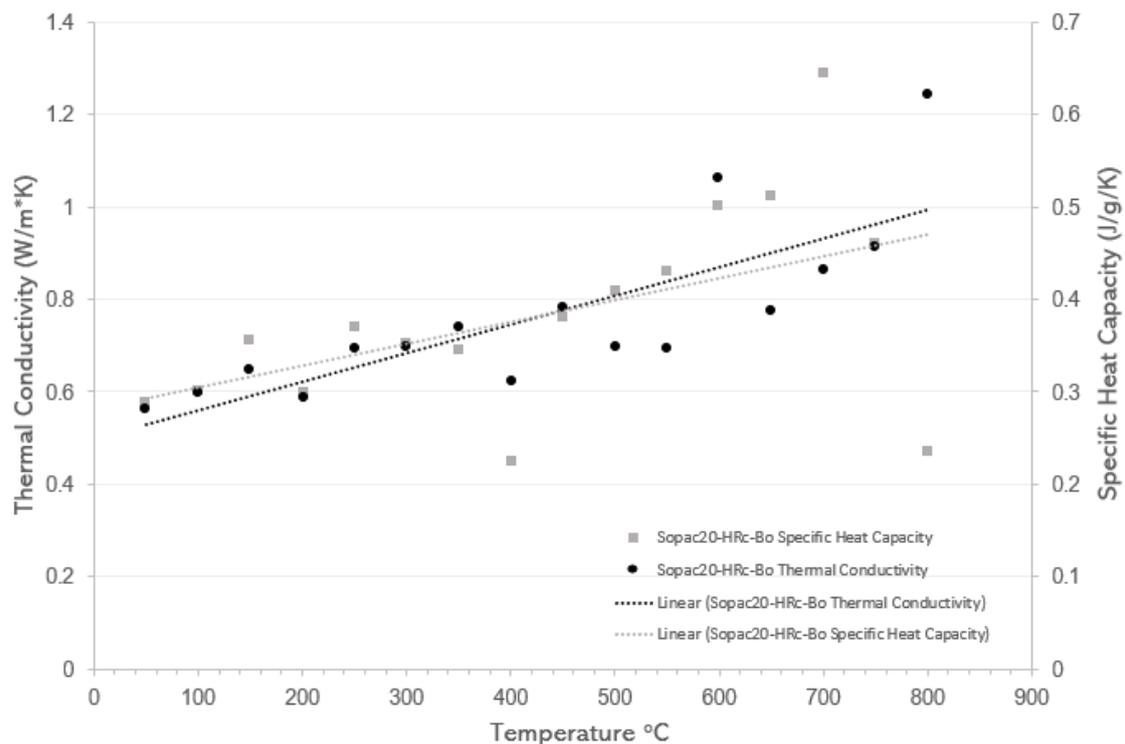
Figure 5.28 – Sopac20-HRc-Bo's calculated Thermal Conductivity from DSC and LFA measurements up to 900°C. Equation 3.9 was utilised, and density measurements were associated with the weight % measurements from the STA and a fixed pre-measured volume.

Additional investigations in financial feasibility and application viability are discussed at length in Chapter 6 as Sopac20-HRc was trialled in an air-spray system as shown in Figure 5.29. Furthermore, the cost analysis of application and yield savings are evaluated whereby simulations of cost and processing calculations determined the profitability of the coating products dependent on several various economic and technical factors.

Figure 5.29 a) Air-spray nozzle utilised for initial viability application trials b) Spray system's pump and coating reservoir c) Application of Sopac20-HRc-HBo to sheet steel.

Following the completed optimisation of a phosphate-based coating solution, Sopac20-HRc-Bo, the project now evaluated the potential of a silicate-based solution for application to Install 235 to improve their processing characteristics. Section 4.3's investigations again utilised the benchmarking performed in Chapter 4 to evaluate solution performance, but direct comparisons of phosphate and silicate coatings are discussed at length in Chapter 6.

Conclusion

Chapter 5 has examined a novel coating matrix which combines the technology of phosphate glasses with a glass reinforcement agent. The solution was optimised by observing its mechanical, thermal and oxidation properties and was the ideal phosphate solution based on the following:

1. Sopac20-HRc-HBo was proven to be the best solution for high temperature oxidation inhibition due to favourable features of consistency, effectiveness, and resistance to mechanical failures. The sol-gel synthesis of $Na_5P_3O_{10}$ with cross-linking agents facilitated a desirable self-healing affect and helped to reduce oxidation by up to 82.1% under certain synthesis and atmospheric conditions. Alternative solutions trialled with chitosan and PVA were unable to provide unform coating coverage and were highly susceptible to localised oxide initiation and defects as a result.

2. The introduction of borosilicate glass additives provided to be crucial with enhanced coating coverage and reversing a previously troublesome surface roughness characteristic. The additives improved the surface roughness Ra values by 78.8% and ensured the ASTM D3359-22 measurement was consistently between 3 and 4. This was partly due to the success of an investigation into the effects of reducing the glass particle size on the cosmetic properties of the steel substrate.

3. The phase morphology and elemental behaviour of the Sopac20-HRc-HBo suggested the coating matrix underwent chemical and crystallographic

changes. The qualitative techniques used, such as XRD or Raman, indicated that the coating changed from an amorphous structure to a crystalline lattice at around 600°C. This was in agreement with a DSC measurement of the coating. Research into the reactions occurring during reheating between the Sopac20-HRc-HBo and the iron oxides theorised that the bonds between the wüstite and magnetite were being affected by coating-substrate reactions causing Fe_3O_4 to delaminate from the bulk oxide.

Chapter 6

Silicate Based Coating Solutions

Introduction

Chapter 6 similarly reviews the synthesis and performance of silicate-based solutions to inhibit oxide growth during reheating. An in-depth analysis of a plain mullite coating was performed prior to subsequent investigations into the impact of various reinforcement agents on the oxidation resistance and mechanical properties of the coated steel systems.

This chapter evaluates the second branch of coating type for the EngD project; silicate-based inhibitors. Section 6.1 will investigate the synthesis routes taken to produce potential coating formulations before initial experimentation prior to the optimisation stage including oxidation-reduction characteristics. Then, section 6.2 reviews the most promising coating formulation's inhibition and its secondary influence on surface cosmetics as well as observing adhesion and porosity performance. The investigation then performs a full optimisation to further improve these factors by trialling various reinforcement media before observing their phase morphology during reheating through qualitative analysis in section 6.3.

This section also reviews the mechanical and thermal properties of Install 235 steel grades after application of the optimised silicate-based solution to directly compare with normalised uncoated samples from Chapter 4 to understand the yield effects of the added coating film.

6.1 Initial silicate formulation trials, their synthesis and application and normalisation.

This section focuses on the wide scope of formulations initially trialled for silicate-based solutions. The criteria used to select these coatings was based on

the "semi-active" silicate coating subgroup shown in Figure 2.12 as more active solutions, like inorganic silicon oxide solutions, were deemed unfeasible for trials. This is because of the impact of chemical changes on the substrate and coating material, as well as the environmental sensitivity during coating formation. Utilising this group of potential formulations, the trialled coatings ranged from pure SiO_2 films to advanced sol-gel composites. The most researched materials in this section are iterations of the ceramic $3Al_2O_3 \cdot 2SiO_2$ or "Mullite". The Mullite precursor was produced with a sol-gel process and the sol was comprised of a Chamotte powder, H_2O, fumed SiO_2, Carboxylic acid, Aluminium powder, and synthetic mica. Known as a type I precursor, this is a single-phase gel which can transform to mullite at 950ºC despite slow diffusion and poor densification.

The initial Mullite precursor, was pre-prepared and provided by Prince Materials Ltd (PML) who had previously produced kaolinite materials for coatings of multiple applications and were heavily collaborative in producing iterative mullite formulations for this project. These precursors mixed together, producing a water-retaining colloidal gel wherein the H_2O acted as transport medium to hydrolyse the solution. In addition, the $C_nH_{2n+1}COOH$ acid was used as a catalyst for the reactions of metal alkoxide by subjecting a chemical change in the suspension through a pH change. This reaction, as explained in section 2.5, was conducted at room temperature and allowed the formation of a microscopically homogenous coating structure. Due to this high homogeneity in the precursor homogeneity, calcination temperatures used to produce the mullite were much lower (950ºC-1300ºC) than conventional synthesis routes which is advantageous for the Install 235 application.

Initially, however, silicate solutions containing either pure SiO_2 , Mullite precursors or other silicate materials were synthesised for application and oxidation trials. Formulations were synthesised in line with target compositions

and the weight % of each component was weighed manually and mixed with a magnetic stirrer unless stated as a pre-prepared formulation made by PML. As an example, Pu-Mull50 is a standard pre-cursor from PML which was both adapted in-house and externally through changes to the hydrolysing agent or water content. Most compositions in-house varied from intended targets set out in methodology by a maximum of 2.0% and coating thicknesses ranged between 25-60µm. Around 5-10 samples of each coating type were trialled and heated to 950ºC using STCA1 thermal cycles after successful adhesion to the sample substrate. Visual inspection was performed to decide which formulations were to be further researched as well as ImageJ analysis in determination of coating coverage. For this coating branch, up to 100 samples were analysed from initial material selection and experimentation concluded with a definitive optimised silicate solution which was viable for use in the Install product application. Table 6.1 outlines the categories of coating technologies for the silicate solutions and their corresponding application success. Their specific synthesis %s were created specific to this investigation, having been inspired by the promising coatings denoted in Chapter 2.

Table 6.1 – Silicate coating groups trialled for initial analysis with formulation details, application technique and adhesion success.

Sample Name	Formula Mol %	Coating Material	Reinforcing Material	Viscosity Modifier	Application Method	Curing Time	Adhesion Success Boolean
Pu-Silica10	$4.0C_2H_4O - 96.0SiO_2$	Silica	N/A	PVB	Bar	1-2 hours	YES
SodSil10	$7.5 C_2H_4O - 92.5 Na_2SiO_3$	Sodium Silicate	N/A	PVB	Bar	1-2 hours	NO
PVBVer20	$3.2C_2H_4O - 96.8 (Mg,Fe^{2+},Fe^{3+})_3[(Al,Si)_4O_{10}](OH)_2 \cdot 4H_2O$	Vermiculite	N/A	PVB	Bar	3-4 hours	YES
PVBPer20	$3.9 C_2H_4O - 96.1 Al_2CaFe_2K_2MgNa12Si$	Perlite	N/A	PVB	Bar	3-4 hours	YES
Pu-Bo15	$21.6C_2H_4O - 88.4SiO_2B_2O_3$	Borosilicate glass	N/A	PVB	Pipette + Spin	1-2 hours	YES
MagSil10	$8.9C_2H_4O - 91.1MgO{:}XSiO_2 \cdot H_2O$	Magnesium Silicate	N/A	PVB	Bar	2-3 hours	NO
Mul50	$50.3SiO_2Al_2O_3 - 49.7H_2O$	Mullite	N/A	H_2O	Pipette + Spin	3-4 hours	YES
Mul-Al50	$9.9Al_2O_3 - 45.2SiO_2Al_2O_3 - 44.9H_2O$	Mullite	Al_2O_3	H_2O	Pipette + Spin	3-4 hours	YES
Mul-Zir50	$9.1ZrO_2 - 45.5SiO_2Al_2O_3 - 45.4H_2O$	Mullite	ZrO_2	H_2O	Pipette + Spin	3-4 hours	YES
Mul-Mag50	$10.3MgO - 45.7SiO_2Al_2O_3 - 45.0H_2O$	Mullite	MgO	H_2O	Pipette + Spin	3-4 hours	YES
Mul-Zin50	$10.1ZnO - 45.1SiO_2Al_2O_3 - 44.8H_2O$	Mullite	ZnO	H_2O	Pipette + Spin	3-4 hours	YES
ZirSil10	$7.0C_2H_4O - 93.0ZrSiO_4$	Zirconium Silicate	N/A	PVB	Bar	2-3 hours	NO
Mul-Ti50	$10.4TiO_2 - 45.7SiO_2Al_2O_3 - 43.9H_2O$	Mullite	TiO_2	H_2O	Pipette + Spin	3-4 hours	YES

Coating coverage, viscosity and adhesion were observed for initial formulations' coating method. The Mullite precursor solutions exhibited a viscosity between 0.8-1.7MPa·S enabling pipette and spin application while silicate solutions such as MagSil10 displayed a poor coverage of 61% and non-uniform adhesion which was associated due poor particulate dispersion and clumping during the PVB suspension. While PVBVer20 and PVBPer20 displayed high viscosities of 5.8MPa·S and 5.7MPa·S respectively and utilised the bar-coated technique for their application, unlike phosphate solutions, they exhibited improved coverage before normalisation between 96.0 and 99.9% as shown in Figure 6.1a and Figure 6.1b. In addition, the solutions both scored 4 in ASTM D3359-22 testing and similar performance was observed for Mullite solutions such as Mul50 shown in Figure 6.1c which was favourable to pipette and spin application based. However

adhesive strength tests on MagSil10 and Sosil10 scored between 0-2 which agreed with visual inspection observations of partial delamination after curing and included signs of checking, cratering, and flaking. This, combined with non-uniformity in coating and complexity in achieving good coverage across the steel substrate, led to these solutions being removed from future testing in the oxidation trials and optimisation stage. Additionally, while Pu-Silica10 samples did proceed to an oxidation trial, the air pocket development within the coating film shown in Figure 4.15 exacerbated the overall number of defects during reheating and so the approach to utilise pure SiO_2 films was discontinued.
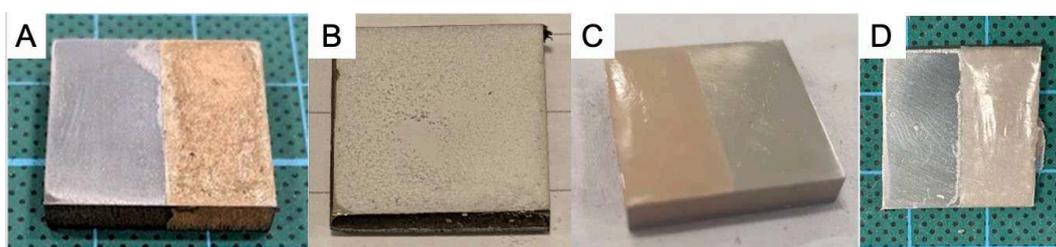
Figure 6.1 – Initial E1 silicate coatings prior to normalisation a) PVBVer20 b) PVBPer20 c) Mul50 d) Pu-Silica10.

Solutions that exhibited coating coverage over 90%, such as PVBVer20 and Mul50, and that also possessed ASTM D3359-22 tests over 3 were selected for further testing. These promising solutions then proceeded to oxidation trials, where they were subjected to STCA1 thermal cycles at 950ºC, and observations were made for their thermal stress degradation and surface coverage characteristics. Examples of the post-normalised silicate coatings are shown in Figure 6.2.
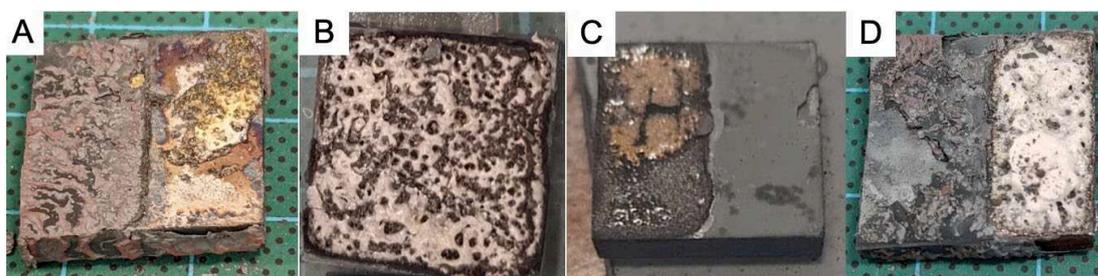

Figure 6.2 – Initial E1 silicate coatings after normalisation a) PVBVer20 b) PVBPer20 c) Mul50 d) Pu-Silica10.

Despite marked improvements in the application, PVBVer20 and PVBPer20 displayed post-normalised coating coverage of 44.7% and 58.2% respectively. Optical observations of sample cross-sections for PVBVer20 displayed only a 19.4% drop in oxidation thickness from 240.1µm to 193.6µm and no improved performance was noted by PVBPer20. While Mul50's surface coverage after normalisation was reported to be 41.5%, the underlying surface condition exhibited a very low Ra of 8.75µm as shown in Figure 6.3c and Figure 6.3d and was able to generate a continuous and uniform film layer during STCA1.
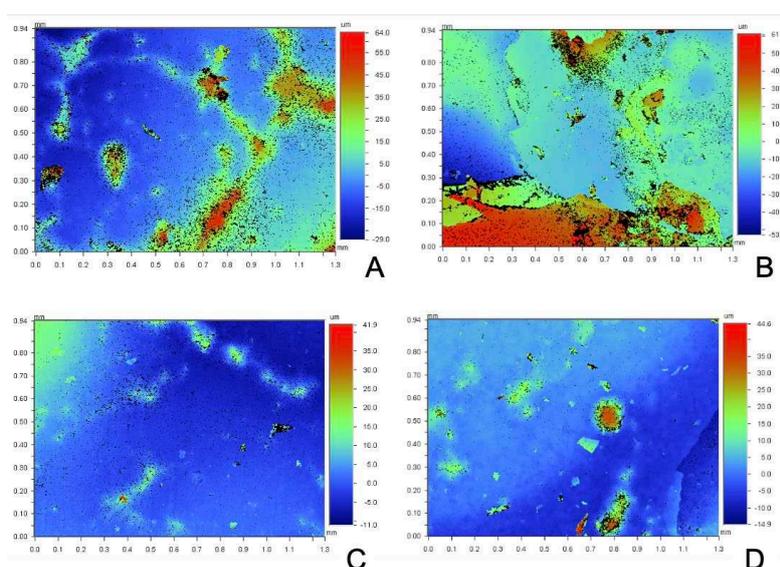
Figure 6.3 – WLI Surface Maps of Mul50 sample a) Oxide side b) Coated side before delamination c) Coated side after delamination d) Coated side after delamination.

This contrasts with the average Ra for the uncoated oxide and non-delaminated coated sides, which was 16.7µm and 20.9µm respectively shown in Figure 6.3a and 6.3b. This, combined with the coating's low thermal expansion during reheating, highlighted Mul50's desirable surface cosmetic characteristics.

Furthermore, Mul50's surface porosity of 0.04 was around 5-10x less than other silicate solutions such as Pu-Bo15 which displayed a high porosity of 0.29 as shown in Figure 6.4.
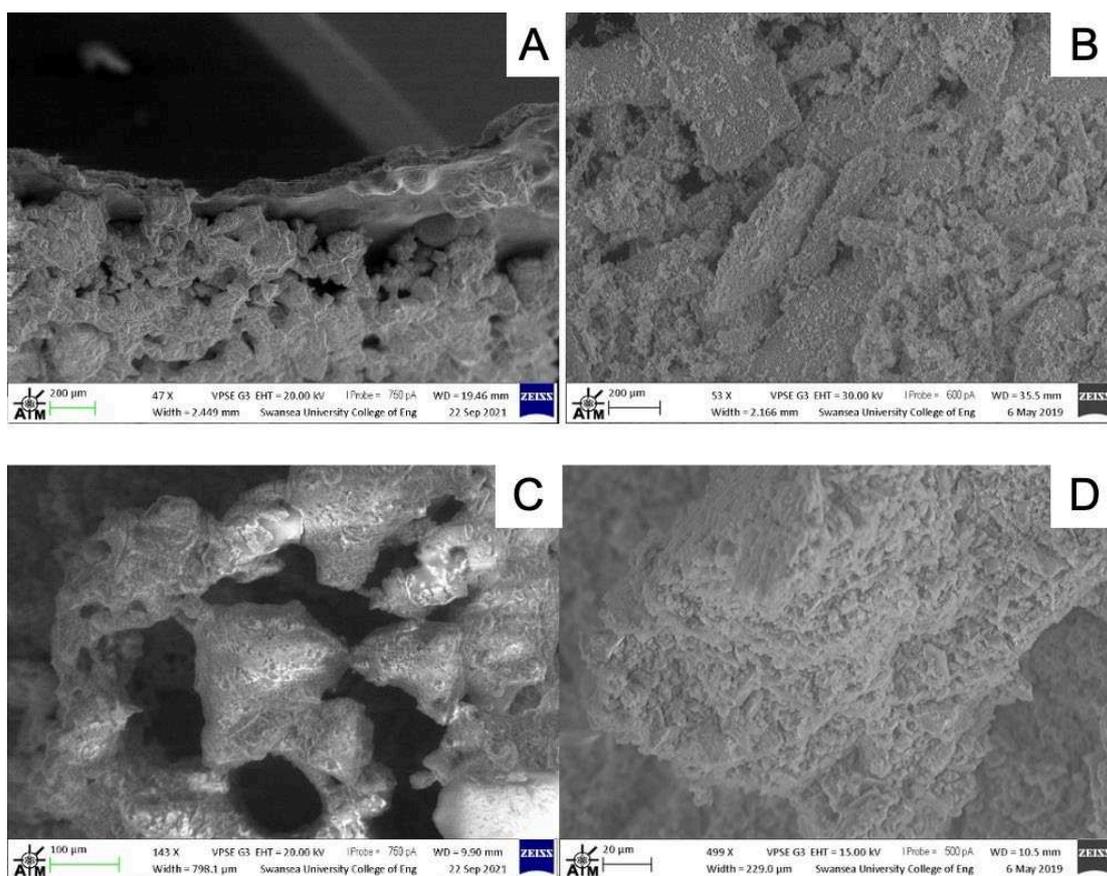
Figure 6.4 - SEM images of post-normalised coatings a) Pu-Bo15 at 50x Magnification b) Mul50 at 50x Magnification c) Pu-Bo15 at 150x Magnification d) Mul50 at 500x Magnification.

In areas where Mul50 was successfully adhered, the oxidation inhibition was found to be ~98% as shown in the cross-sectional overview of a Mul50 coating in Figure 6.5a. This solution also experienced high levels of delamination during reheating and these failures were localised outside the central zone of the $3Al_2O_3 \cdot 2SiO_2$ samples as exhibited in the Smartzoom overview in Figure 6.5b.
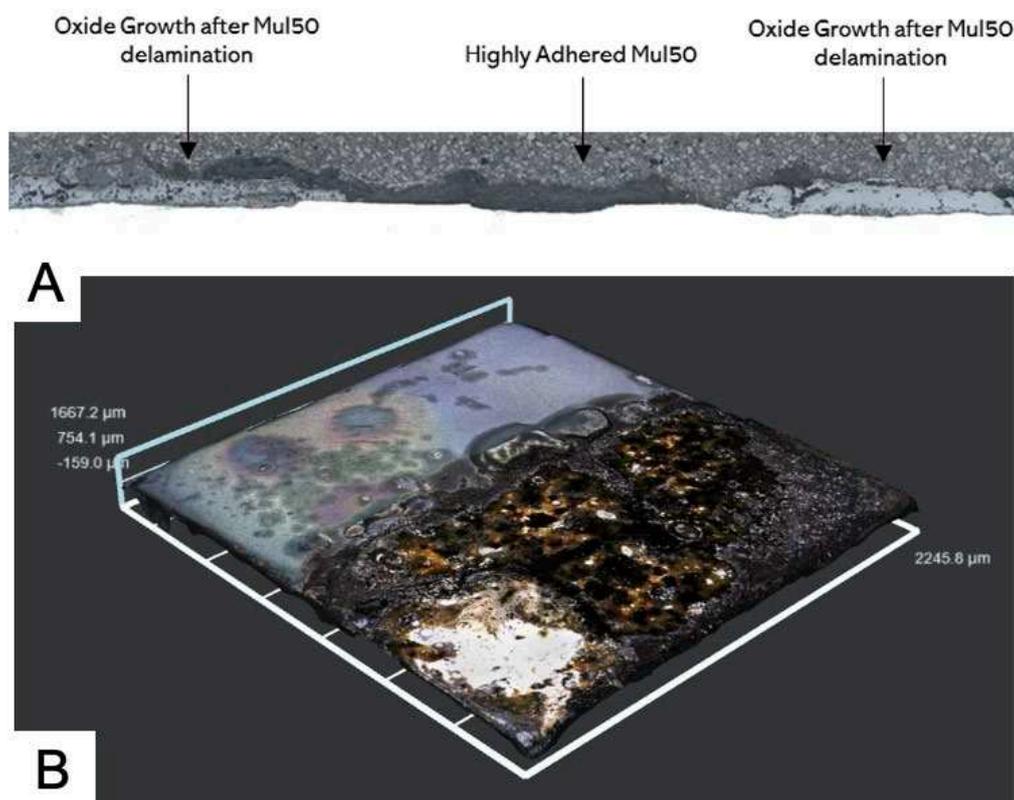
Figure 6.5 – Optical Microscopy of Mul50 a) Observer stitched image at 20x magnification b) Smartzoom Mul50-4 overview image.

Therefore, despite these delamination occurrences, Mul50 was the most promising coating solution from the initial materials selection due to excellent oxidation inhibition during adhesion, significantly improved surface cosmetics and an ability to provide uniform coverage across the steel substrate. Further improvement of the Mul50 formulation was conducted in section 6.2 in which the $3Al_2O_3 \cdot 2SiO_2$ concentration, coating weight, particle size and reinforcement material was optimised.

Prior to optimisation, further observations of Mul50 samples through EDS mapping were conducted of a very high coating weight $3Al_2O_3 \cdot 2SiO_2$ sample, known as Mul50-21, to understand the spallation behaviour. EDS detected high levels of O2 throughout the silicate-scale system and reported silicon precipitation in the underlying Wüstite layer as shown in Figure 6.6. The EDS was conducted as a map scan as described in methodology section 3.6. The top-

most silicon-rich layer (at the atmosphere-oxide boundary) resisted reaction with the iron oxide and preserved a consisted coverage over the sample despite excessive scale growth.
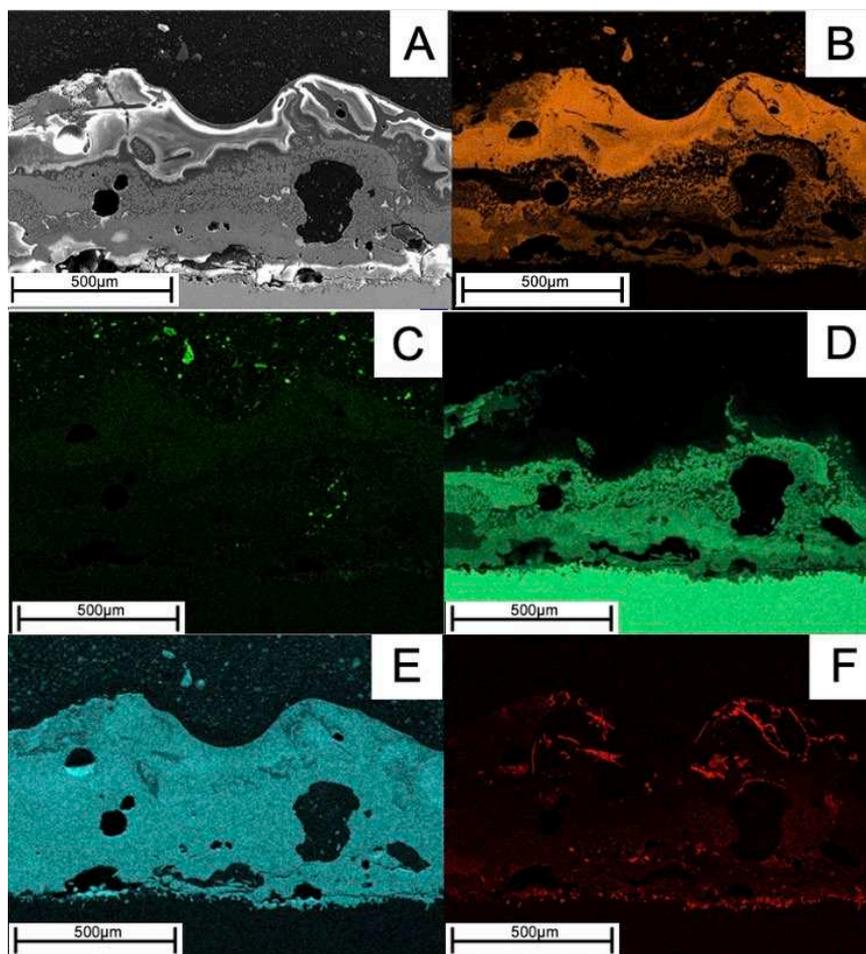
Figure 6.6 – EDS mapping of Mul50-21 a) SEM Image at 100x magnification, b) Si, c) Al, d) Fe, e) O, f) P.

Expectedly, low levels of Al or Alumina was observed with the EDS technique. Mostly due to its' low atomic number, Aluminium produce fewer x-rays for detection and are typically at a lower energy than the other composite elements. In addition, the EDS calibration may not have been specific for lighter elements, and the bulk oxide masked Al presence due to strong signals of Fe or Si. In addition, increased iron content in the coated-scale system layer was detected as

well as Fayalite compositions at the lower steel-oxide interface. High levels of O_2 were present throughout the coated structure.

6.2 Optimisation of $3Al_2O_3 \cdot 2SiO_2$ solutions and introduction of a Mullite reinforcement agent

Based on the performance results shown in section 6.1, initial optimisation of the $3Al_2O_3 \cdot 2SiO_2$ solutions began with an investigation of the impact of coating weight on oxide inhibition. Utilising differing spin speeds after material deposition, 35 E1 steel samples with varying coating weights were subjected to STCA1 thermal cycles to discover their oxide inhibition characteristics and adhesion properties. The T_x was measured at each weight while ASTM D3359-22 methodology was performed on the pre-normalised coated surface as shown by the results in Figure 6.7.
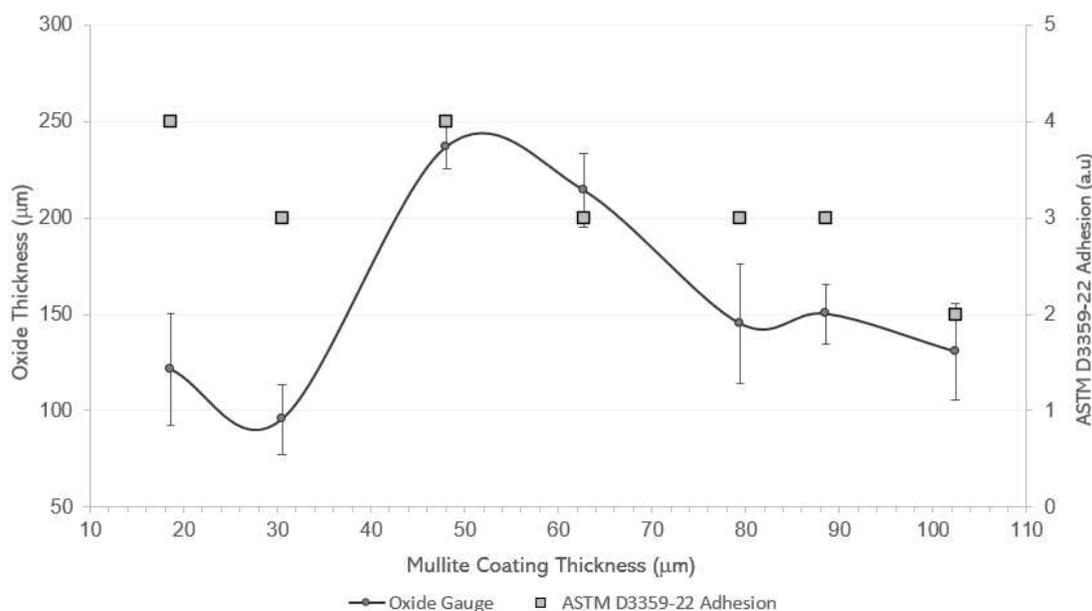
Figure 6.7 - Variation in oxide thickness for $3Al_2O_3 \cdot 2SiO_2$ samples due to applied coating thickness. Elcometer readings taken from 5 predetermined points on the coating substrate prior to normalisation. ASTM D3359-2 Adhesion was concurrently recorded for each coating gauge.

Observations on mullite coatings with a gauge of 50µm or more, displayed spallation of the coated layer and magnetite delamination from the core layer, as shown in cross-sectional observer images in Figure 6.8. High levels of porosity persisted in most coated thicknesses and exhibited an inability to prevent 50% or

more of oxide growth during reheating. Unlike phosphate solution degradation, the oxidation was caused through permeation of O^{2-} ions in the persevered mullite layer.
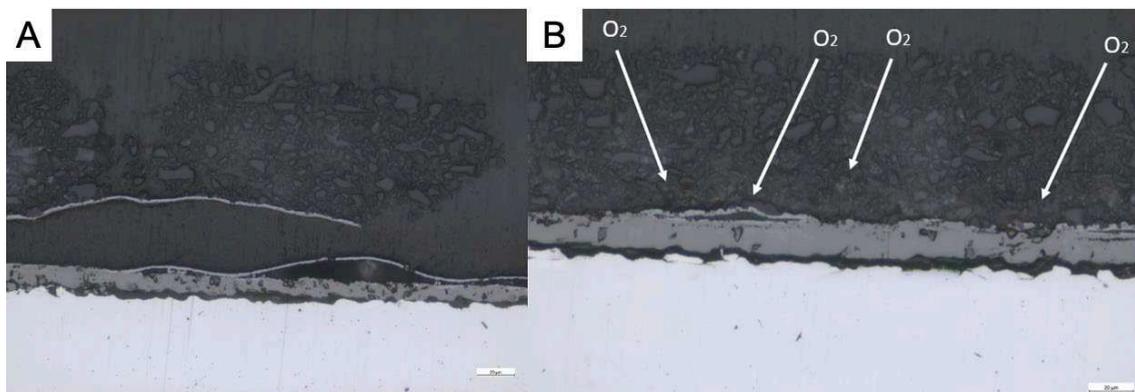
Figure 6.8 – Observer light microscope images of the oxide boundary at 20X magnification of a) Mul50-4 delaminated Fe_3O_4 causing removal of the $3Al_2O_3 \cdot 2SiO_2$ matrix b) Mul50-6; adhered mullite coating system enabling the permeation of O^{2-} to the steel surface.

Improvement of coating porosity was attempted through the reduction of mullite precursor particle size. Conducted by Prince Ltd, the average particle size distribution of the mullite particulates were reduced from 5000nm to 500nm through high-speed jet milling as analysed by their on-site Zetasizer. Small particle mullite solutions or 'Mul50-Sm' were applied to steel coupons using the same methodology as Mul50 and a coating thickness of around 20μm was recorded after curing. The solution was subjected to a STCA1 thermal cycle, before being metallographically prepared and its oxide characteristics recorded. Mul50-Sm achieved a 68.0(±6.2)% reduction in oxide thickness and an average post-normalised surface roughness Ra of 22.3 (±3.1)μm. Poor coating uniformity was associated with the Mul50-Sm solutions due to the initially undesirable coverage during application as shown in Figure 6.9b. Scoring either 3 or 2 during ASTM D3359-2 testing, overall high fragility was an attribute of this solution, a trait which may explain the high levels of delamination occurring during reheating. In addition, areas of coating which had not delaminated from the steel surface had either precipitated into the bulk oxide layer or caused severe iron

whisker formation at the coating oxide interface as shown in Figure 6.9a. This 1-dimensional growth is theorised to be a result of the vapor-solid mechanism, in which thin and fibrous material is generated due to iron atoms from the gas phase depositing on existing iron surfaces. The fibres could also be a symptom of high humidity during cycling, as high temperature and water vapour availability can produce complex iron oxyhydroxides such as α-FeOOH and typically form in needle-like structures. Alternatively, this "whisker-like" formation in the oxide layer is a result of a coating reaction with the oxide layer. Iron silicates can form at high temperatures if the bulk steel was able to react preferentially to the silicon in the mullite layer and while these silicates, like fayalite, usually present as an intermediary layer underneath the scale, they can also develop into independent sharp crystals. This phenomenon is linked to rapid cooling, a characteristic of the utilised STCA1 thermal cycle. Similarly, it's possible the alumina present in the Mul50 solution reaction with the FeO to form an iron aluminate, like hercynite, $FeAl_2O_4$. This is more prospective, due to certain aluminates remaining stable at high temperatures which would preserve their fibrous crystallization during the isothermal stage and in cooling. Despite Figure 7.6 and Figure 6.9a suggesting that the mullite solution is inhibiting oxide growth, the oxidation of silicate material in the matrix would be detrimental to overall coating integrity.
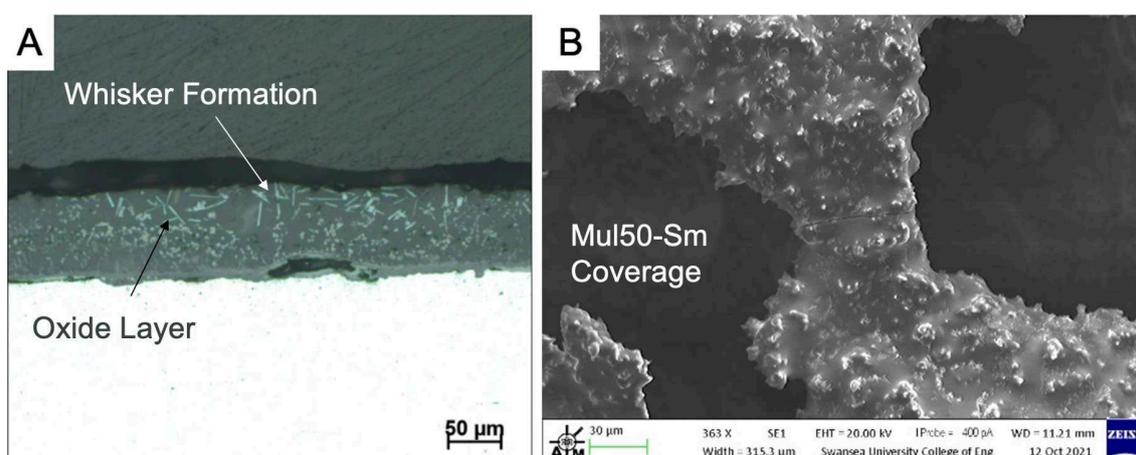

Figure 6.9 – a) 20X Magnification cross-sectional observer image of Mul50-Sm-4 displaying splintered composite fragments in the bulk oxide layer beneath the applied $3Al_2O_3{\cdot}2SiO_2$

coating. b) SEM Image at 360X magnification of pre-normalised Mul50-Sm exhibiting poor coating coverage.

Due to these reactionary and splinter issues, the trial concluded that smaller mullite precursor particle sizes provided a poor coating coverage and inability to withstand low-level mechanical stress. As reported in the literature explored in section 2.5, failures in the ceramic matrix due to the aforementioned thermomechanical properties can be remedied through the introduction of a reinforcement phase. While Mul50 and Mul50-Sm achieved optimum oxidation reductions of 57.1% and 68.0% during testing, their inconsistency in coating application, mostly poor adhesion characteristics and deteriorating surface roughness after normalisation ultimately led to the project seeking a suitable reinforcement agent to enhance the silicate solutions. The main metals and oxides trialled for combination with Mul50 are detailed in Table 6.1.

Synthesis of the reinforcement material candidates initialised with an addition of 30mol% concentration of Al_2O_3, MgO, ZrO_2, TiO2 and ZnO to standard $3Al_2O_3 \cdot 2SiO_2$ solutions. The preparatory method of uniformly mixing mullite powder with reinforcement phase particles and performing a high temperature sinter was utilised. The composite powders were hydrolysed and produced into a gel just as pure mullite had been, as described in section 6.1. The application of these reinforcement candidates is shown in Figure 6.11 with each reinforcement solution having between 5-10 steel samples for oxidation analysis.
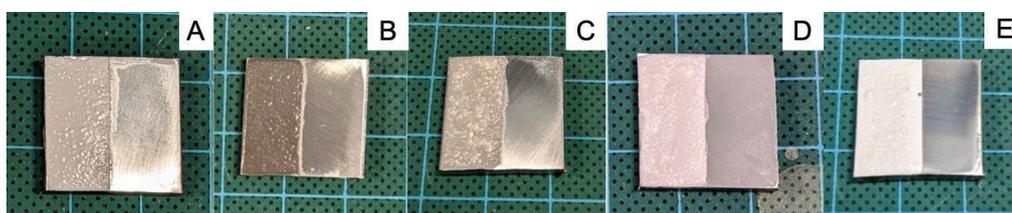
Figure 6.11 – Pre-normalised Reinforced Mullite Solutions a) ZrO_2-$3Al_2O_3 \cdot 2SiO_2$ b) Al_2O_3 - $3Al_2O_3 \cdot 2SiO_2$ c) MgO -$3Al_2O_3 \cdot 2SiO_2$ d) ZnO-$3Al_2O_3 \cdot 2SiO_2$ e) TiO_2-$3Al_2O_3 \cdot 2SiO_2$.

The solutions were subsequently subjected to a STCA1 thermal cycle at 950°C prior to being metallographically prepared for T_x analysis. Figure 6.12 depicts the

reinforcement material candidates' post-normalisation images, revealing clear adhesion failures from visual inspection.
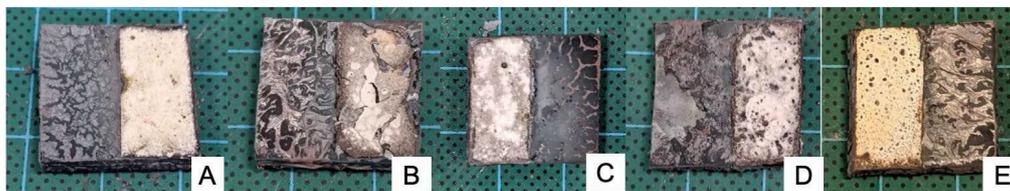
Figure 6.12 - Post-normalised Reinforced Mullite Solutions a) ZrO_2-$3Al_2O_3 \cdot 2SiO_2$ b) Al_2O_3 - $3Al_2O_3 \cdot 2SiO_2$ c) MgO -$3Al_2O_3 \cdot 2SiO_2$ d) ZnO-$3Al_2O_3 \cdot 2SiO_2$ e) TiO_2-$3Al_2O_3 \cdot 2SiO_2$.

In addition, an observation of the oxide inhibition performance of the reinforced candidates is shown in Figure 6.13.
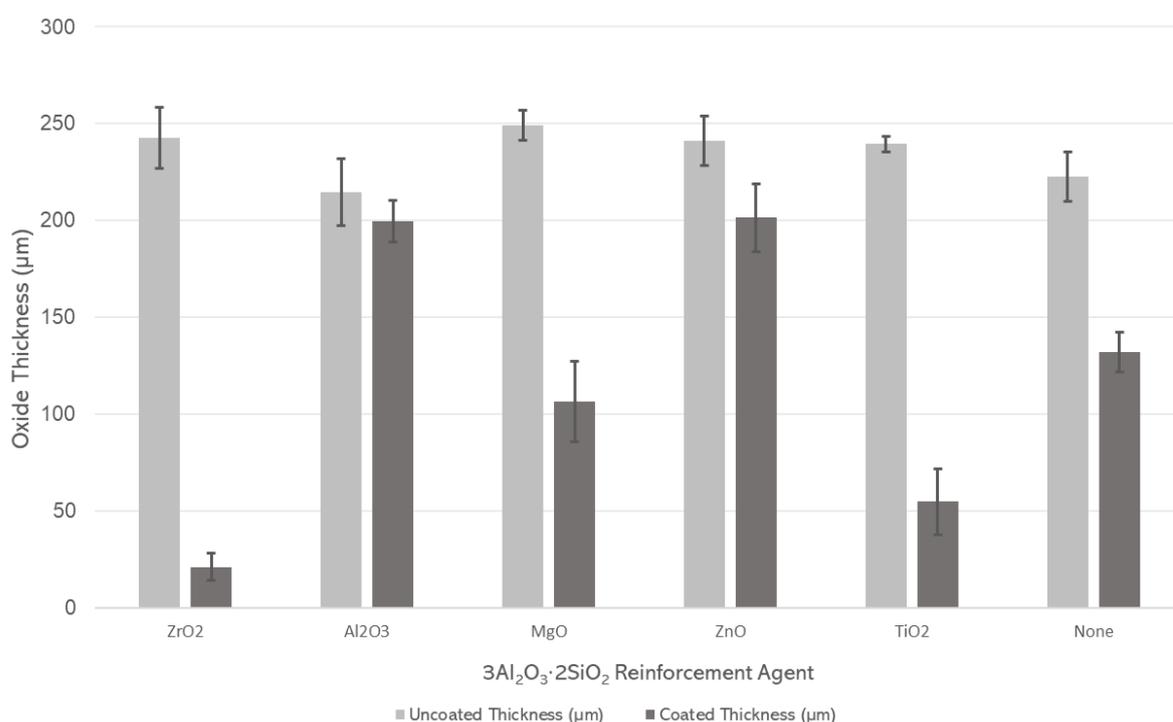
Figure 6.13 – Oxidation inhibition due to the addition of varying reinforcement agents for $3Al_2O_3 \cdot 2SiO_2$ samples.

With an average oxide reduction of 79.5%, an investigation into a particularly promising reinforcement candidate, TiO_2-$3Al_2O_3 \cdot 2SiO_2$, was undertaken. While initial application coverage and adhesion was recorded at <99% and 5 respectively, post-normalisation surface porosity was found to be 0.16 and partial oxidation occurred amongst a localised region of 5-10µm craters as well as other surface defects being discovered. Smartzoom examination of the 5 titania

reinforced samples revealed an inconsistent and rough surface as shown in Figure 6.14a and WLI analysis measured an average Ra value of $32.9 \pm 5.3 \mu m$ as shown in Figure 6.14b.
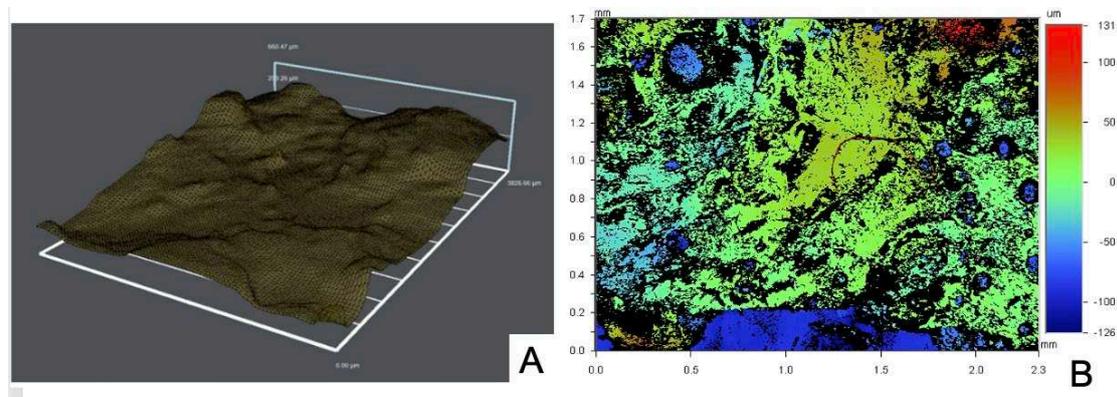
Figure 6.14 - TiO_2-$3Al_2O_3 \cdot 2SiO_2$ a) Smartzoom optical surface profile map at 50X magnification b) WLI surface roughness analysis.

In addition, a qualitative look at the elemental make-up of the TiO_2-$3Al_2O_3 \cdot 2SiO_2$ samples was conducted through SEM-EDS as detailed in section 3.6 revealed poor layer consistency and is shown in Figure 6.15. However, precipitation of Ti, Al, or Si from the coated layer to the bulk oxide did not occur and no detection of O_2 in the TiO_2-$3Al_2O_3 \cdot 2SiO_2$ was observed. The spectral map indicated no composite or dual-phase layers at the boundary interface. (reactivity).
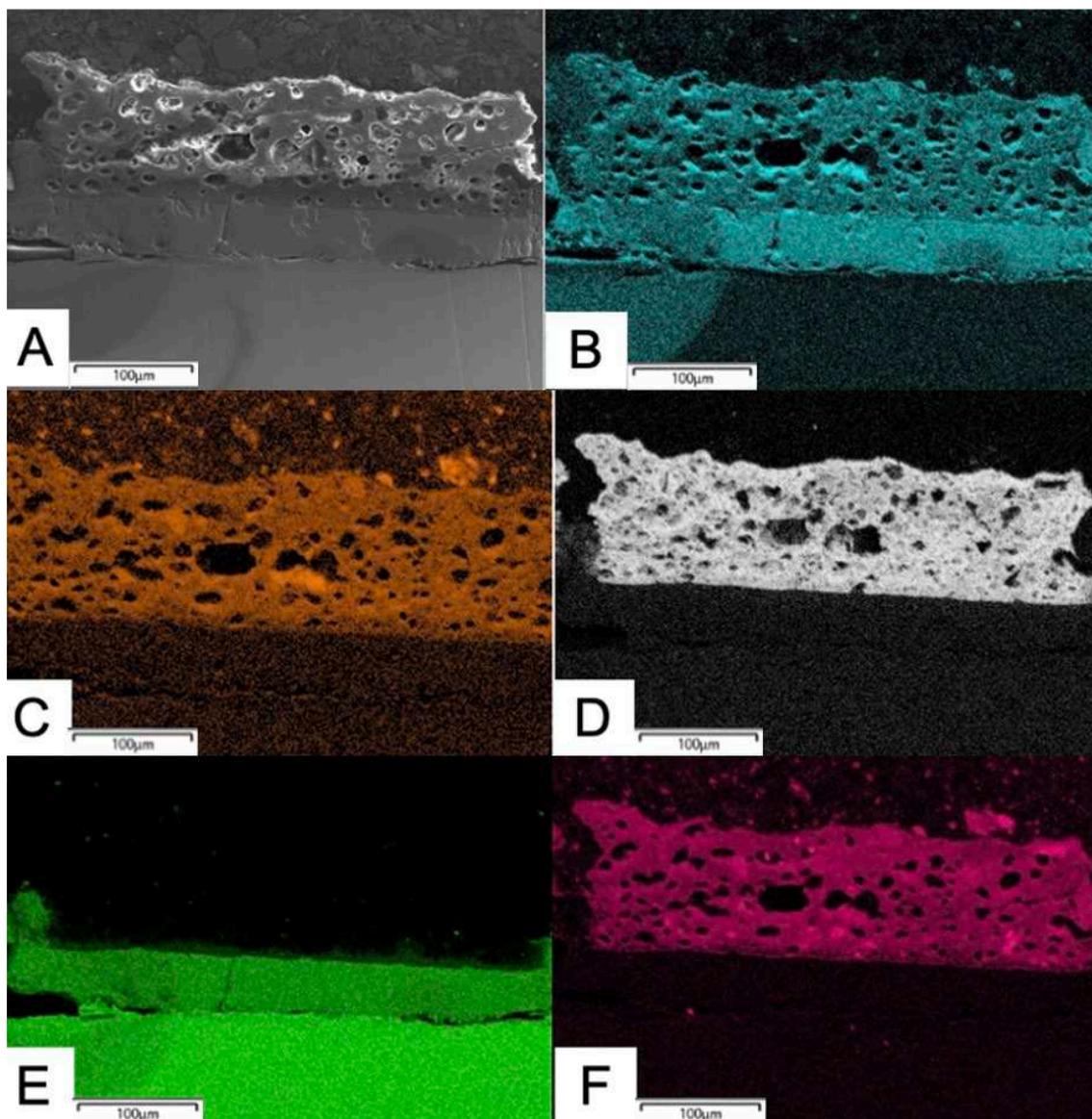
Figure 6.15 – EDS mapping of TiO_2-$3Al_2O_3 \cdot 2SiO_2$ coated cross-sections a) SEM image b) O c) Al d) Ti e) Fe f) Si.

Similar coating failures were attributed to MgO-$3Al_2O_3 \cdot 2SiO_2$ solutions due to high porosity measurements (between 0.19-0.29) and poor adhesion characteristics. With an average oxidation-reduction of 90.5%, further qualitative examination of ZrO_2-$3Al_2O_3 \cdot 2SiO_2$ coated properties was performed in section 6.3. Quantitively, however, initial observations of the composite's post-normalised layer displayed a coverage and porosity of 98.1% and 0.02 respectively. An illustration of this ZrO_2-$3Al_2O_3 \cdot 2SiO_2$'s enhanced coverage is displayed in Figure 6.16.
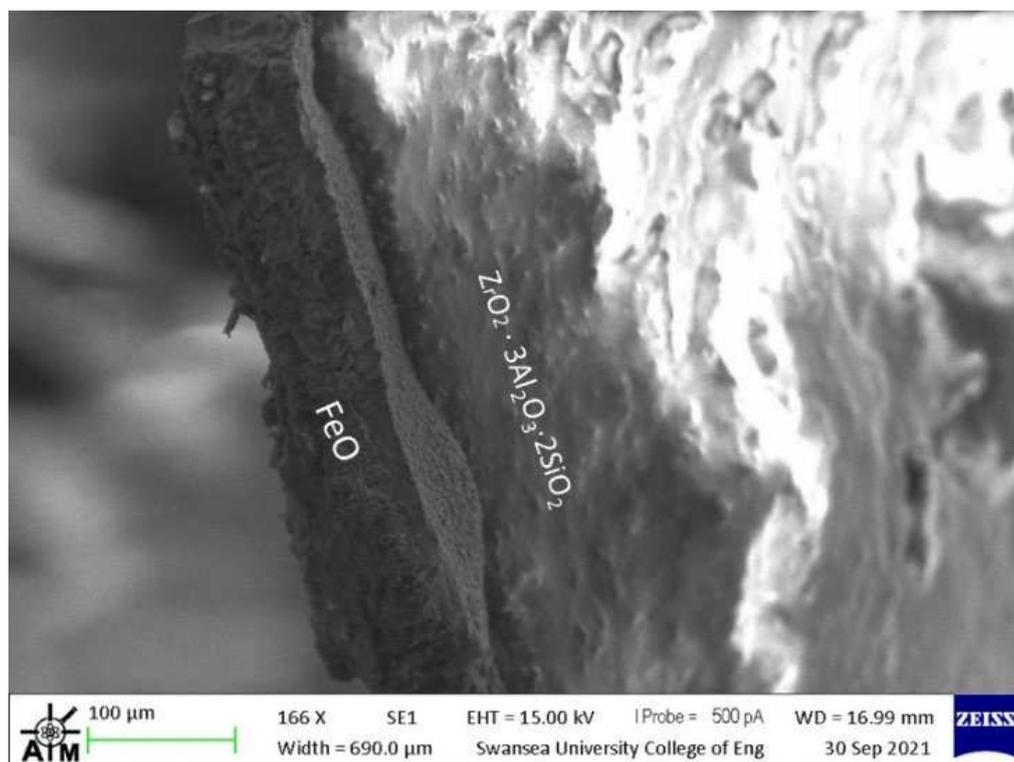
Figure 6.16 – SEM image at 170X magnification depicting ZrO_2-$3Al_2O_3 \cdot 2SiO_2$ coating adhered to a detached scale layer post-normalisation.

Additionally, average ASTM D3359-22 adhesion scores of 3 or 4 were recorded for the solution. The ZrO_2-$3Al_2O_3 \cdot 2SiO_2$ surface possessed a poor average roughness, Ra, of 29.4($\pm$3.3)μm which is depicted by a Smartzoom high-depth of field image in Figure 6.17. The ZrO_2-$3Al_2O_3 \cdot 2SiO_2$ coated film, however, detached as a single continuous layer after normalisation. This highly dimpled, non-uniform surface is likely harming overall coating integrity. Its high roughness is linked to the matrix possessing multiple stress concentration points which is an initiation point for cracking during reheating. More worryingly, ZrO_2-$3Al_2O_3 \cdot 2SiO_2$ is likely to possess a reduced thermal conductivity compared to standard mullite, due to the pores trapping air and creating a thermally insulating layer. This is in agreement with the thermal impact investigations presented in section 6.3.
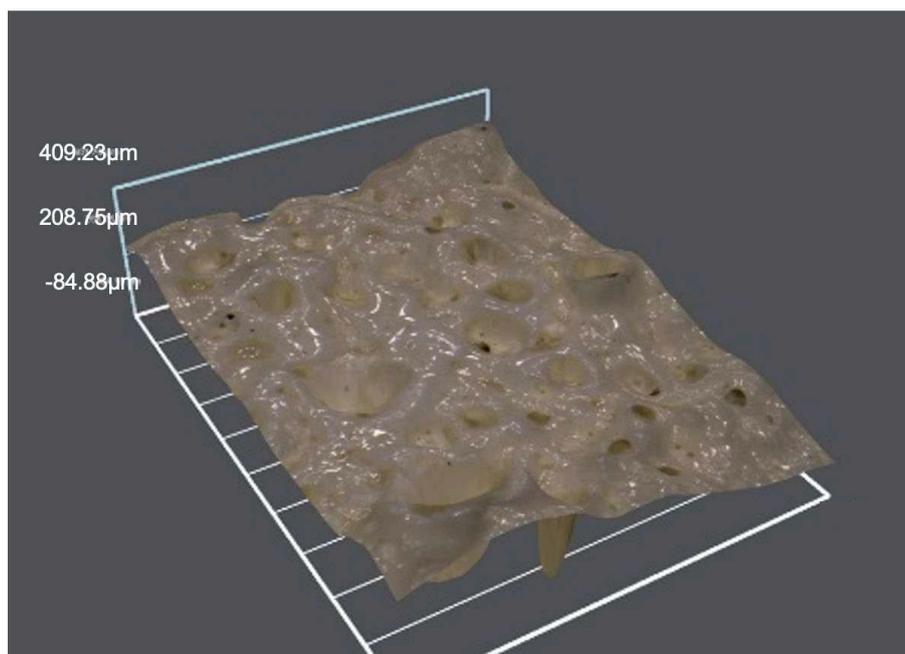
Figure 6.17 – Smartzoom high depth of field optical image at 50X Magnification of ZrO_2-$3Al_2O_3 \cdot 2SiO_2$.

Despite this, and due to these favourable oxide-reduction characteristics, zirconia-reinforced mullite outperformed the alternative silicate solutions and consistently inhibited oxidation with successful adhesion as shown by the overview stitch in Figure 6.18. The left-hand side depicts the prevention of any oxide and it's smooth, unaltered steel surface suggests that there's been no loss of iron material from the bulk substrate. This is in complete contrast to the right-hand side; the topography of its surface indicates that oxidation has "eaten away" at the steel material and a significant portion of scale growth atop the substrate highlight this further.
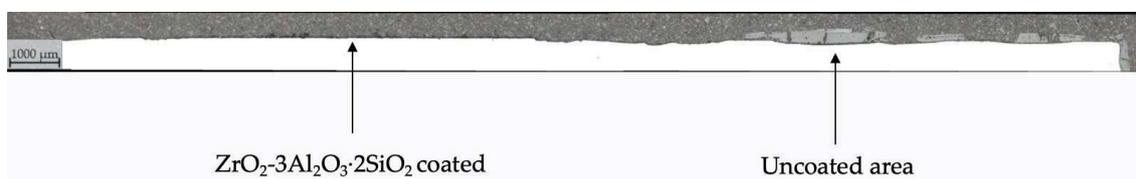
Figure 6.18 – 20X magnification cross-sectional overview stitch of ZrO_2-$3Al_2O_3 \cdot 2SiO_2$

Therefore, due to this successful mitigation of oxidation, ZrO_2-$3Al_2O_3$·$2SiO_2$ was selected as the optimised silicate solution to be analysed for qualitative phase analysis and mechanical properties in section 6.3.

6.3 Qualitative phase analysis, composition layers and mechanical properties of reinforced $3Al_2O_3$·$2SiO_2$ solutions.

An initial examination of the mechanical properties of the ZrO_2-$3Al_2O_3$·$2SiO_2$ solution was conducted to evaluate yield loss or gain due to coating application atop the steel substrate. Hardness tests according to ASTM-E92-17-3-01 were performed along the length of the cross-section of 5 ZrO_2-$3Al_2O_3$·$2SiO_2$ coated samples and 5 Mul50 samples for comparison. The samples were subjected to STCA1 thermal cycles prior to metallurgical preparation for testing as detailed in section 3.1. The Vickers hardness variation is illustrated in Figure 6.19 and displayed a 46.3% drop in hardness at the mid-cross section and an HV/1 differential of 9.9 between the top and bottom substrates for ZrO_2-$3Al_2O_3$·$2SiO_2$.
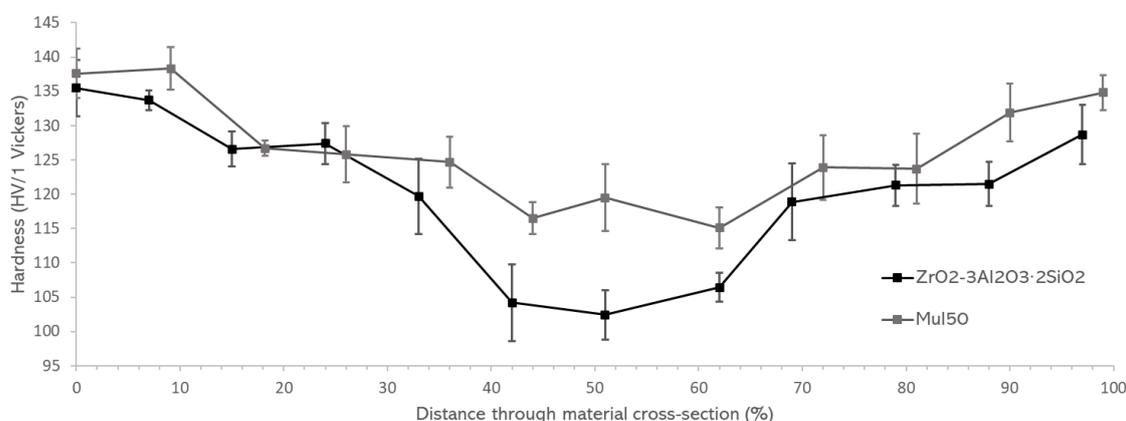
Figure 6.19 - Vickers Hardness (HV/1) variation in various silicate-based coating samples across the material cross-section. Diamond indentation was applied with a 1Kg load for 10s.

The results indicate that ZrO_2-$3Al_2O_3$·$2SiO_2$ is inhibiting the expected hardness increase due to the normalisation. This is an issue, as lower hardness suggests the heat treatment would be less effective in achieving grain size homogeneity and the removal of internal stresses within the tube profile. The reason for the

inefficiency is obvious, the Zirconia reinforced mullite is preventing the ingress of heat energy into the steel system. The highly reflective white coating is reflecting away the incident thermal radiation and also has a very low thermal conductivity, ensuring the coating acts a thermal insulator that limits heat transfer. Furthermore, the stability and integrity of this coating may cause non-uniform heat distribution across the steel surface, sharply affecting the hardness along the cross-section.

Next, the grain size cross-sectional analysis of the silicate-based coatings was conducted through measurements in accordance with BS EN ISO 643:2020 by observing grain dimensions with 20x magnification full length stitches. The results are shown in Figure 6.20 for Mul50 and ZrO_2-$3Al_2O_3$·$2SiO_2$. The measurements revealed a 49.1% drop in grain diameter in the 40-60% region compared to the surface boundary grain sizes.
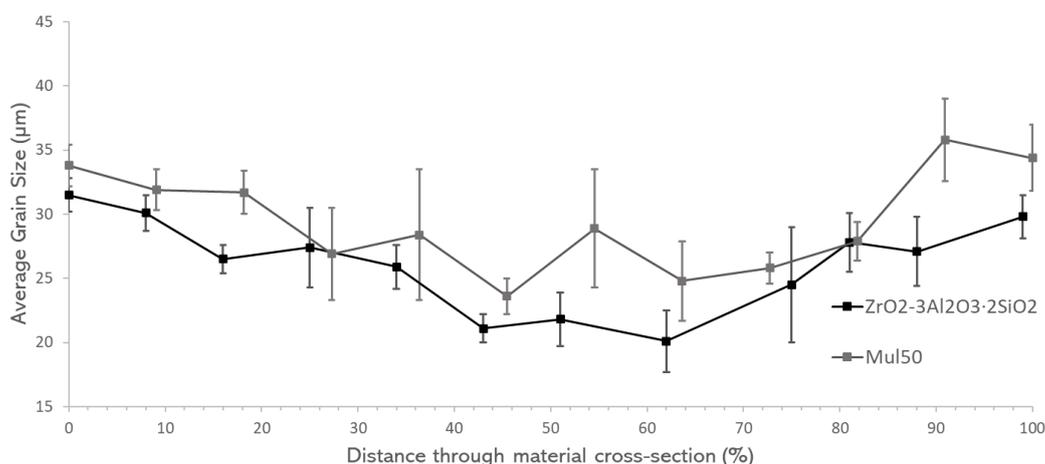
Figure 6.20 - Grain Size (μm) variation in phosphate-based coatings using the mean line intercept method. In calculation of the grain size diameter, 650μm lines were drawn diagonally across intermittent micrographs spaced apart as a function of the total cross-section distance.

In addition, the underlying steel surface was tested for its cosmetic appearance through WLI roughness mapping. The samples were examined in localised regions in which the bulk layer had delaminated but in areas where remnant oxide or coating material may have remained; a suitable imitation of Install 235 SR2 mill products after normalisation. Determination of the average Ra and Rz

values for the silicate solutions were also calculated for adhered using WLI maps as shown in examples in Figure 6.21.
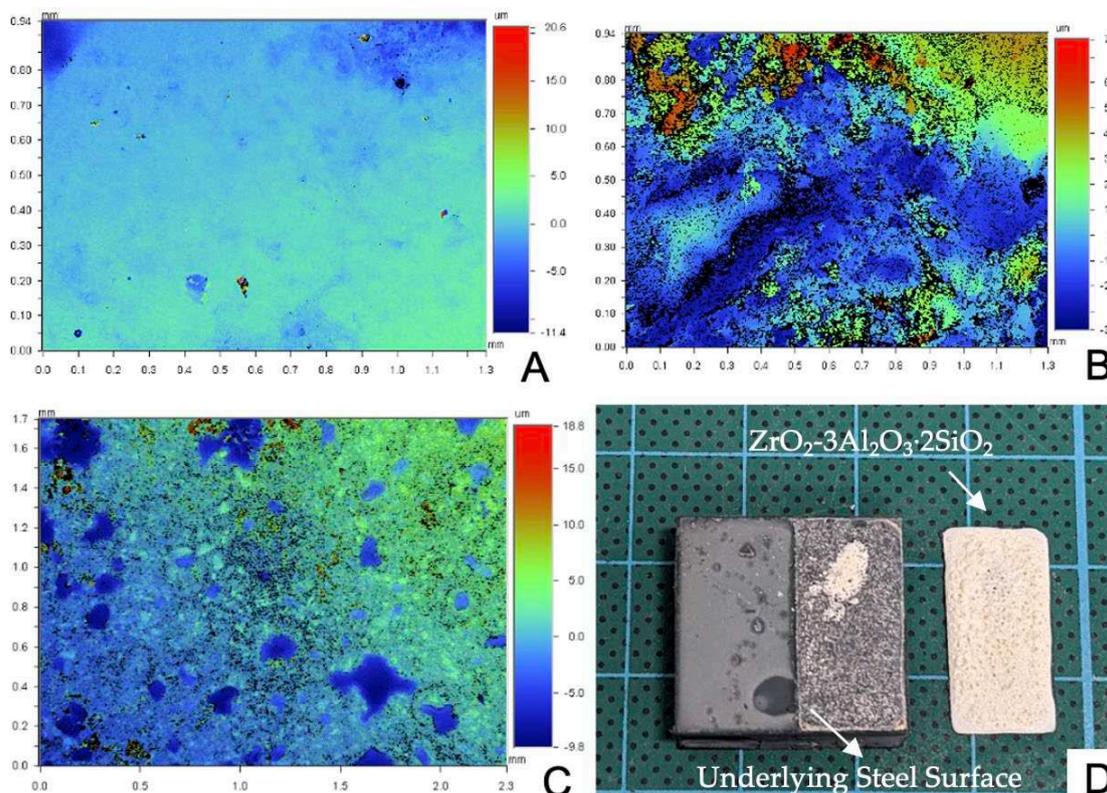
Figure 6.21 – a) Uncoated surface side of ZrO_2-$3Al_2O_3$·$2SiO_2$ b) Coated surface side of ZrO_2-$3Al_2O_3$·$2SiO_2$ c) Underlying surface after delamination of the ZrO_2-$3Al_2O_3$·$2SiO_2$ layer d) Image of the ZrO_2-$3Al_2O_3$·$2SiO_2$ -2 layer uniformly detached from the steel substrate.

WLI analysis determined that the uncoated side possessed an average Ra of 1.4($\pm$0.6)μm and an Rz of 25.8($\pm$ 3.0) μm while the coated surface side of ZrO_2-$3Al_2O_3$·$2SiO_2$ was discovered to have an average Ra of 16.5μm($\pm$2.7μm) and an Rz of 111.8 ($\pm$10.9μm). However, for steel surfaces fully detached from the ZrO_2-$3Al_2O_3$·$2SiO_2$ film, the average Ra and Rz was reduced to 19.5μm ($\pm$1.7μm) and 32.7μm($\pm$7.8μm) respectively.

Next, EDS analysis was conducted in combination with SEM to discover the composition of the coating surface after an STCA1 thermal cycle. Expected detection of Al, Si, and Zr was confirmed. Elemental components of O and Fe indicated precipitation of the underlying α-Fe_2O_3 or cubic γ-Fe_2O_3 into the bulk ZrO_2-$3Al_2O_3$·$2SiO_2$ film with certain regions appeared to be particularly iron rich.

Figure 6.22 displays the EDS spectral maps and indicates the prevalence of 10µm-100µm sized pin-hole defects with this coating formulation. Unexpectedly Figure 6.22D, Ca was detected at localised sites which were coating rich. While Ca was not selected as a modifier during synthesis, it's probable that calcium was an impurity in the raw materials used to produce the mullite solution. Typically, calcium can be used as an additive in mullite generation due to its nature to reduce the overall sintering temperature of the product.
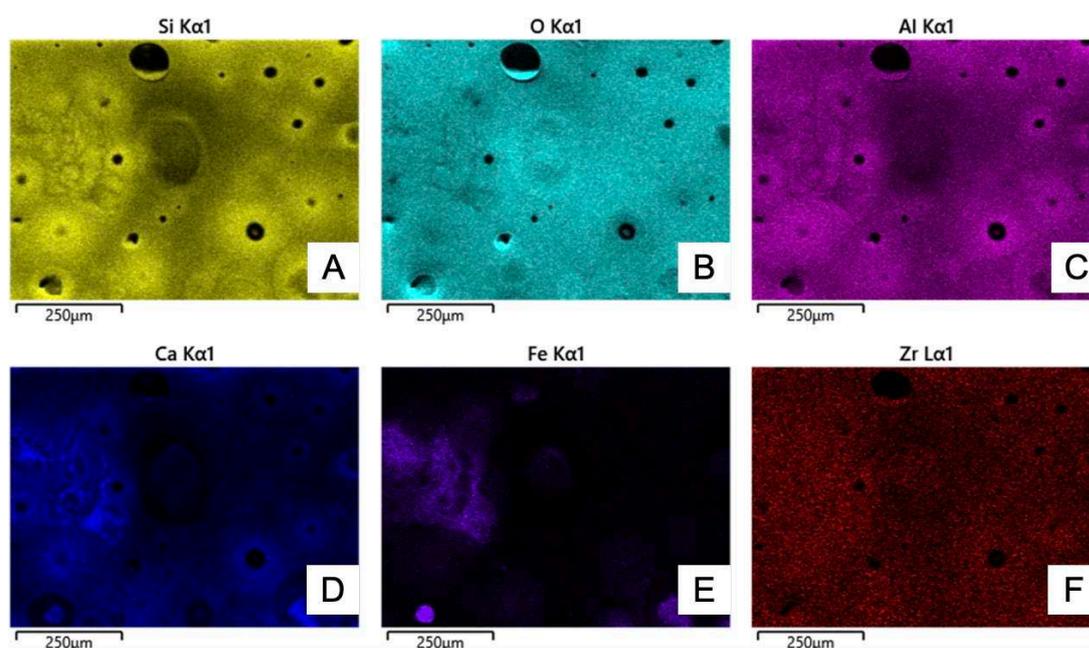
Figure 6.22 - ZrO_2-$3Al_2O_3 \cdot 2SiO_2$ a) EDS Map of elemental Si b) EDS Map of elemental O_2 c) EDS Map of elemental Al d) EDS Map of elemental Ca e) EDS Map of elemental Fe f) EDS Map of elemental Zr.

In further analysis, the Raman spectra of ZrO_2-$3Al_2O_3 \cdot 2SiO_2$ and Mul50 was examined after a 900ºC normalisation to determine crystallinity and phase morphology. Detection of α-Fe_2O_3 ,Fe_3O_4 and FeO within the coated composite film was a secondary aim for these scans and reveal if a compound or element, like Al, had degraded during reheating. Point scans, directed centrally, at the coating material were performed at 0.013mW for 20s using a 531nm radiation. Acquisition occurred as described in methodology section 3.8 and the samples were delaminated from the steel substrate prior to analysis. The resulting spectra

is shown in Figure 6.23 in which Savitzky–Golay smoothing of a second order polynomial, was performed to remove accidental peaks and reduce noise.
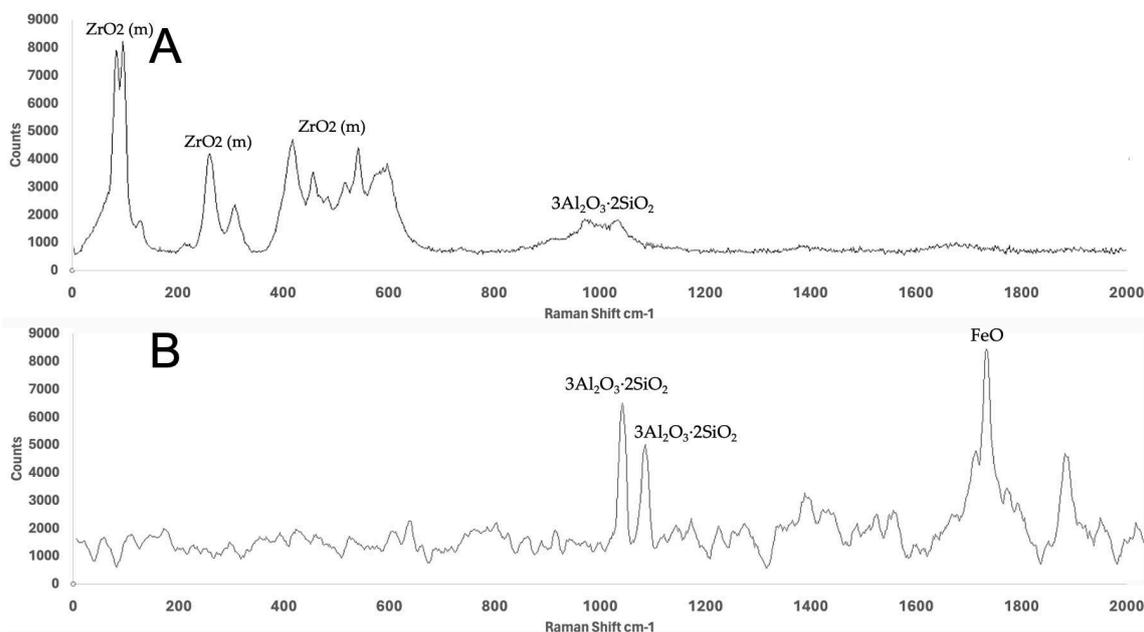
Figure 6.23 - Raman spectra of the bulk coating film of a a) ZrO_2-$3Al_2O_3 \cdot 2SiO_2$ sample. Savitzky–Golay smoothing was applied of the second order polynomial b) Mul50 sample.

Raman shifts of $982cm^{-1}$, $1049cm^{-1}$ and $1611cm^{-1}$ in Figure 6.23b are characteristic peaks of orthorhombic mullite with Al_2O_3 which had undergone no crystalline phase transition as described in literature. Additional peaks above $1600\ cm^{-1}$ indicated some wüstite presence within the coating matrix. While shifts of $171cm^{-1}$, $178cm^{-1}$, $327cm^{-1}$, $466cm^{-1}$, $587cm^{-1}$, and $957cm^{-1}$ in Figure 6.23a are indicative of monoclinic zirconia phase and some remnant mullite presence.

Finally, detection of rhombohedral α-Fe_2O_3 or cubic FeO within the coated film and determination of phase morphology was conducted through X-ray diffraction. As described in methodology section 3.7, powder XRD was performed on Mul50 and of ZrO_2-$3Al_2O_3 \cdot 2SiO_2$ which had been subjected to temperatures of 25ºC, 450ºC and 900ºC. Using 2Θ angles between 0° and 90° in a diffractometer, powdered ZrO_2-$3Al_2O_3 \cdot 2SiO_2$ was analysed using Co kα radiation (40 kV, 40mA) with a scan speed of 0.03°/s as shown in Figure 6.24.
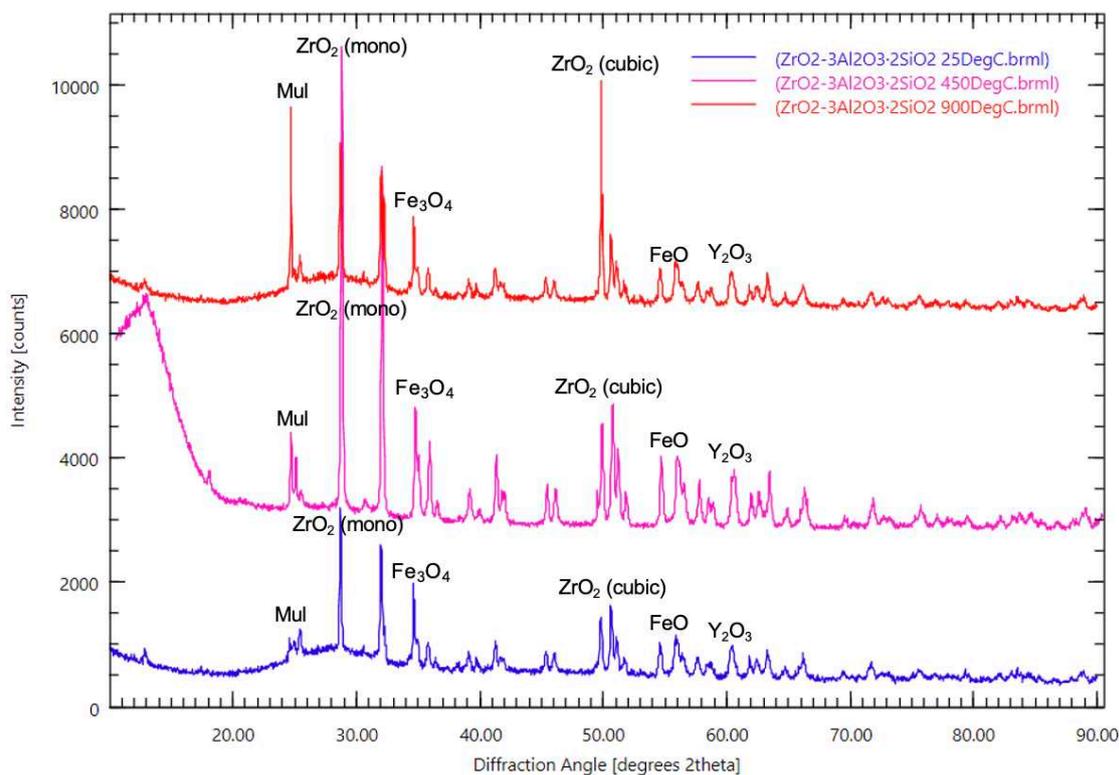
Figure 6.24 - XRD diffraction pattern (2Θ) of ZrO_2-$3Al_2O_3$·$2SiO_2$ coated steel samples after varying heat treatments.

The strongest indicators of monoclinic zirconia are typically found at 28° and 32° 2θ which Figure 6.24 displays. However, a deficit of tetragonal zirconia seems apparent, due to only a tiny peak at 30° and this signal usually appears as a very intense peak for this crystal structure. This is in association with the Raman findings and is expected, as tetragonal phases occur only at very high temperatures and usually are not retained upon cooling, causing them to revert back to monoclinic. At 50°, the scan exhibits a peak which increases in intensity and definition at higher temperatures. This 50° peak is normally found for cubic zirconia and while this phase should similarly revert to monoclinic upon cooling, the phase can be stabilized with yttria additions. The synthesis of ZrO_2-$3Al_2O_3$·$2SiO_2$ by Prince Materials may have utilised this prior to its sintering and explains the presence of Y_2O_3 peaks at around 60°. Expectedly, the solution displayed the most prominent signal of Mullite at 26° which likely became more crystalline between 450°C and 900°C due to a stronger and well-defined peak.

Theoretically, the XRD could have displayed evidence of a crystalline silica phase such as cristobalite, but this was not detected in the expected 2θ positions. The scan also suggests that FeO and Fe_3O_4 phases were present within the composite matrix at 2θ angles of $54°$ and $36°$ respectively but it's possible other common peaks for these phases were shifted by the many compounds in the matrix or were overwhelmed from a silicate signal.

Using the same scan settings, the X-ray diffraction pattern of Mul50 was determined as shown in Figure 6.25. The diffractions patterns were characterised using Reitweld technique as described in methodology section 3.7.
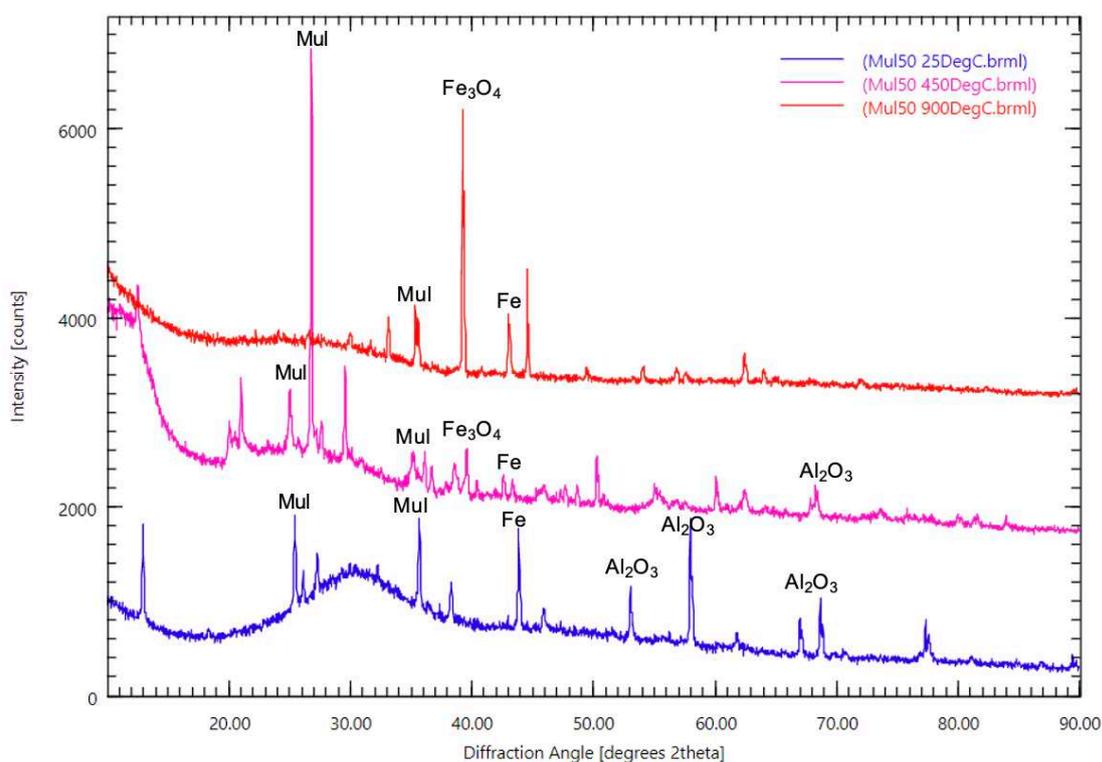
Figure 6.25- XRD diffraction pattern (2Θ) of Mul50 coated E1 steel samples after varying heat treatments.

Mul50 exhibited Al_2O_3 peaks at $52.5°$ and $57.8°$ at $25°C$ but no oxide phases (like FeO) were characterised in any of the diffraction patterns and were considered when performing Reitweld analysis. The core reason behind alumina disappearing from the XRD scan beyond $450°C$ was likely due to the dissolution of alumina into the mullite solution due to the higher temperatures. Amorphous

$3Al_2O_3 \cdot 2SiO_2$ peaks at 27.5° for $25^{\circ}C$ samples were determined and peaks consistent with crystalline $3Al_2O_3 \cdot 2SiO_2$ were found for all temperature samples between 35° and 39.5°. Additionally, some Fe peaks were determined at around 44° but these signals may be from the underlying steel surface as opposed to iron spindles suspended within the coating composite. The fact the most defined peak is at $25^{\circ}C$ supports this. The implication of these results is that both the Mul50 and ZrO_2-$3Al_2O_3 \cdot 2SiO_2$ are both displaying characteristics of crystallization from their core coating mechanisms. Well defined and stronger peaks at $900^{\circ}C$ confirm the stability of these coatings in their crystalline state and reduced the prominence of the troublesome FeO phase within the bulk layer.

Following the research conducted in section 6.3; the synthesis, optimisation and qualitative analysis were completed for silicate and phosphate solutions. Section 6.4 further discusses the presented results and evaluates the feasibility of both optimised coating candidates in the silicate and phosphate domains. This section is an additional piece of analysis which discusses the comparative performance of the most promising and optimised solutions presented in Chapter 5 and Chapter 6. Furthermore, the feasibility and practicality of implementing these solutions on site in the SR2 Mill at Corby are evaluated and determines the economic profitability of each coating through a simulated appraisal.

6.4 Feasibility Studies and Economic Appraisal

In this project, the main scoping and optimisation routes focussed on semi-active or passive coatings to perform oxidation inhibition. While partly due to the application requirements and timeframe for protection, the use of active coatings was mainly unfeasible because of incompatibility when considering safe implementation. As an example, prior to the full investigations of silicate-based

and phosphate-based solutions, a theoretical carbon-based coating solution was assessed by a previous EngD student as described in section 2.4.

While synthesis utilising a combination of a polyether compound and charcoal powder was relatively safe to synthesise at PMRC and on the SR2 Mill, it became apparent from the corresponding COSSH and Risk Assessments that the level of sacrificial coating required during reheating was unviable for use on the mill. This was due to the carbothermal reaction taking place within the furnace which removed oxygen from the surface and creating an artificial reducing atmosphere with insufficient O_2. This insufficient O_2 with the presence of Carbon would likely lead to the generation of carbon monoxide as shown in equations 6.1 and 6.2 below.

$$(\text{Desired reaction to remove } O_2) \qquad C + O_2 = CO_2 \qquad (6.1)$$

$$(\text{Insufficient } O_2 \text{ in the atmosphere}) \qquad 2C + O_2 = CO \qquad (6.2)$$

This immediately presented a health and safety feasibility issue with implementation in a working mill if large amounts of CO were being released into the atmosphere during reheating and led to this solution being scrapped. Similarly, other coatings with particular elements had to be discounted due to the compounds generated with O_2 after coating burn-off. A high volume of Sulphur from VOCs released during normalisation could lead to the release of sulphur dioxide which is highly unsafe to the workers in close proximity to the furnace.

For the two fully optimised coatings presented in this project, a number of implementation factors need to be considered when assessing the viability of each coating for scale-up into productions or even pilot line trials.

As this project proposes a scalable coating technology for utilisation in the SR2 mill, a final and important aspect of each solution must be evaluated, the economic viability. Naturally, the application and effectiveness of each optimised

coating would be obsolete if the synthesis materials cost more than the original steel lost from oxidation. In the calculation of final profitability, the total expense of the coating was determined by analysing the volume of material required to produce the desired coating thickness discovered in sections 4.2 and 4.3 and determining the corresponding costs for synthesis and application. Other costs include maintenance, labour, initial equipment expenditures, energy, quality assurance and efficiency development. The value of the quality grade steel saved from coated protection was computed by reviewing the price per tonne of hot rolled coil, the total scale growth each cycle per conveyance tube and the effectiveness of the coating, including delamination rates. Weighting the outgoing expenditures against the gain in quality grade steel from protection was an obvious metric in determining if the solutions would be profitable. Table 6.2 provides details of some of the factors utilised in this calculation. An initial determination found that, per day, total costs of the coating for Sopac20-HRc would amount to £36,951 and the value of steel saved would be £47,218, providing a daily profit of £10,267 and an annualised profit of £2,6669,502. While ZrO_2-$3Al_2O_3 \cdot 2SiO_2$ provides a daily profit of £12,113 and an annualised profit £3,149,380. These calculations were performed using data from TATA Steel, but the analytical software was provided by Swansea University.

Table 6.2 – Examples of factors included within the simulation with their corresponding standard deviation utilised for the NORMDIST() function in excel required for the 'What If' Analysis.

Examples of Simulation Factors	Sopac20 – HRc Input Value	Sopac20 – HRc Value Standard Deviation (σ)	ZrO_2-$3Al_2O_3$·$2SiO_2$ Input Value	ZrO_2-$3Al_2O_3$·$2SiO_2$ Value Standard Deviation (σ)
Price per Tonne of Steel (£)	£655	£45	£655	£45
Thickness of Scale (µm)	6000	1000	6000	1000
Coating Effectiveness (%)	82.1%	15.1%	94.9%	4.4%
Delamination rate (%)	20.7%	5.8%	38.0%	7.3%
Conveyance tubes made per day	275	0	275	0
Total Cost of 1L of Material	£7.61	£1.87	£10.89	£2.33
Total Cost to coat 1m2	£8.01	£2.01	£12.04	£2.52
Conveyance tube surface area	16m²	0m²	16m²	0m²
Fe – O2 Composition Ratio	66%	3.0%	66%	3.0%
Energy Costs (£) per day	£68.66	+£10.00	£41.19	+£10.00

However, fluctuations in costs for generating and applying the coating must be considered, and additional factors should be integrated to determine risk of loss, such as inflation and wastage. To observe this, a Monte Carlo simulation was performed. The simulation utilises random sampling to generate a range of possible profits achievable for a set of circumstances and can be used to predict the likelihood of a loss should the project be implemented. The simulation ran 10,000 iterations of potential increases or decreases in costs, through Excel's 'What If' analysis. The factors considered for changeability included maintenance costs, labour, raw materials, energy, the price per tonne of steel, coating effectiveness and the delamination rate. The simulation generated a profit/loss for each iteration and was deposited into histogram buckets to observe the most likely range of profit achievable for each solution for a given day. Figure 6.26 stipulates a histogram of all the iterations ran in the simulation for Sopac20-HRc and highlights the most likely profit achieved on an average day. The probability distribution indicates that the standard deviation of profitability is around £17.75K suggesting that this coating will be unable to generate significantly high

profits each day (>£50K+) but has a narrow range of potential profit margins and only generated a loss in 16.1% of iterations in the 1st year.

Figure 6.26 – Probability distribution histogram depicting the most likely profits to occur per day for given factors in synthesis, application, and processing for Sopac20-HRc.

In addition, these predictions account for the initial SR2 set-up costs by subtracting a pro-rata fixed value from the achievable profits each day. This simulation is programmed as if it were the 1st year of implementation, and so the mean or most likely profits achieved per day for years 2 and over would increase by around 3% due to no equipment costs (not including maintenance). It is worth noting that the simulation did not consider the overall impact on costs of ingress thermal energy to which more or less energy may be required due to the emissivity of the coated layer during reheating.

On the other hand, ZrO_2-$3Al_2O_3$·$2SiO_2$ displayed a greater variation in profitability, most likely due to increased standard deviation factors shown in Table 6.2. Figure 6.27 displays the histogram of all the Monte Carlo iterations

generated for this coating's economic appraisal and it was found that the risk of daily loss was 27.9% in the 1st year. However, improved coating effectiveness allowed some iterations to generate a daily profit of <£90K. The incongruent nature of the normal distribution was attributed to the high energy costs reducing the mean profit per day below the median and mode for this simulation to produce a negatively skewed distribution. While this could also be caused by a prediction of high levels of delamination during reheating, the challenge of Zirconia integration though very high temperatures for this coating's synthesis may have led to inflated loss margins not seen in the previous simulation. The standard deviation of profitability was around £44.3K for ZrO_2-$3Al_2O_3$·$2SiO_2$.

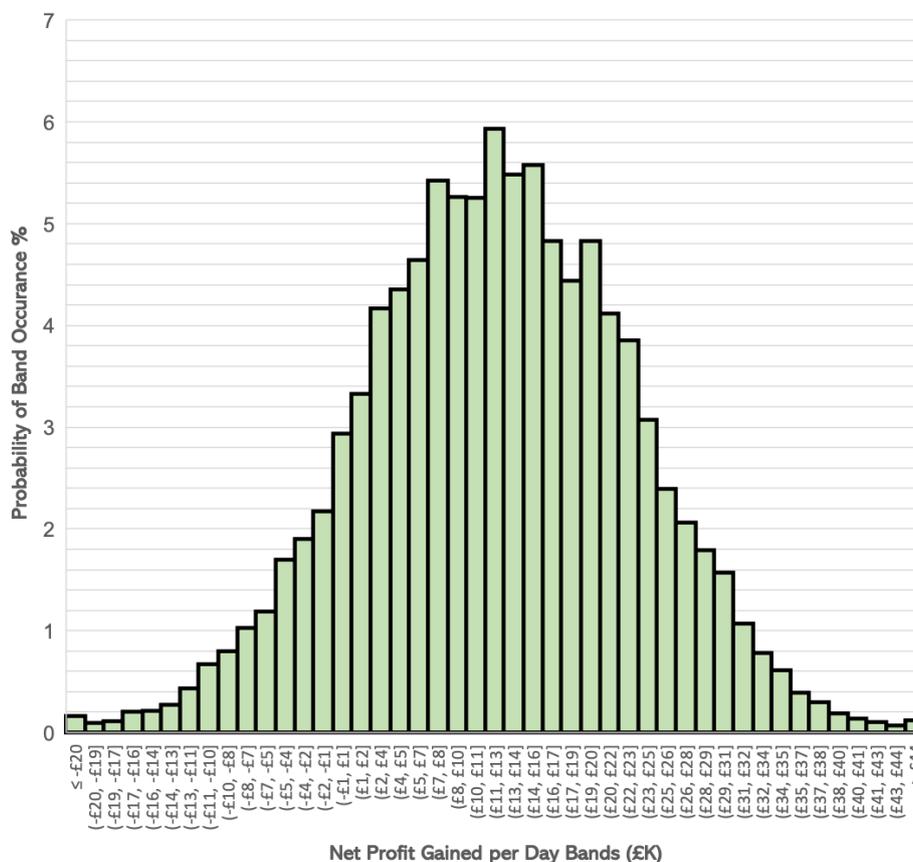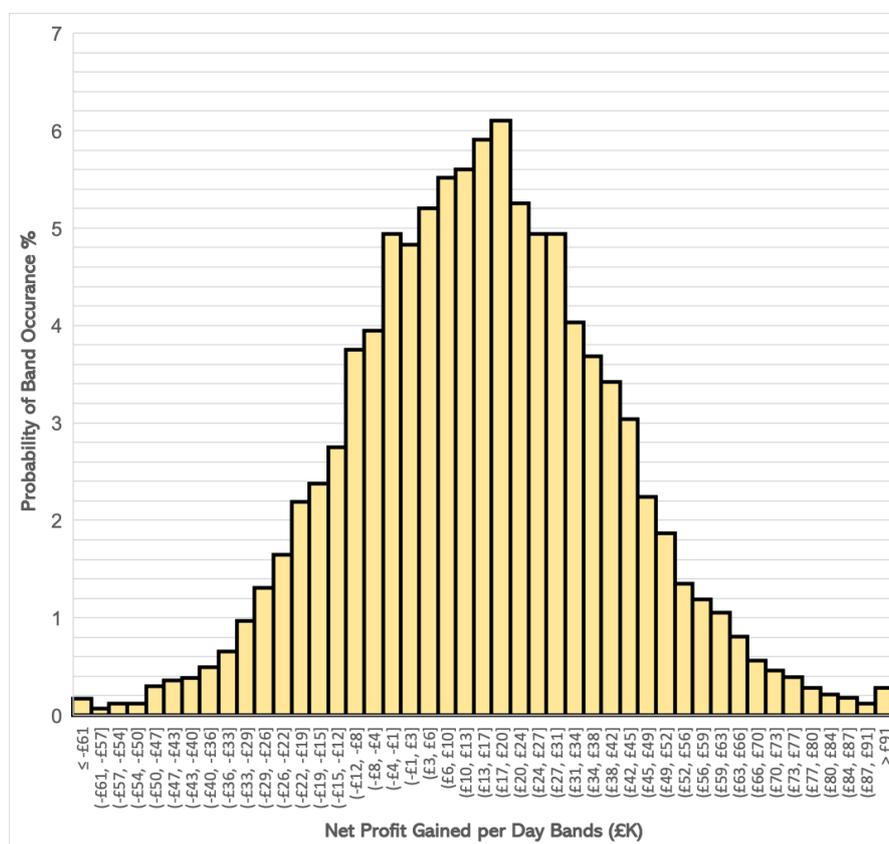**Figure 6.27** – Probability distribution histogram depicting the most likely profits to occur per day for given factors in synthesis, application, and processing for ZrO_2-$3Al_2O_3$·$2SiO_2$.

In summary, an economic appraisal was conducted on the two most optimised coated solutions. It was found that through variations in synthesis materials and application costs, there were a number of conclusions about the profitability of

the two coatings. Firstly, while ZrO_2-$3Al_2O_3 \cdot 2SiO_2$ generated a greater mean profit than Sopac20-HRc but was a riskier choice for implementation financially due to the high variance and losses in some of the iterations. Both coatings overall generated a profit in the majority of the simulations but ZrO_2-$3Al_2O_3 \cdot 2SiO_2$ had a negatively skewed correlation, suggesting a low-level loss was more likely than a medium-high level profit unlike Sopac20-HRc. While the appraisal confirmed that the coatings were economically viable, the non-associated factors, such as thermal energy ingress and surface cosmetic improvements or detriments should be evaluated in future work to encapsulate the profitability of the conveyance tubes from uncoiling up to installation.

Conclusion

Chapter 6 further explored oxidation preventing coatings by investigating various types of silicate-based solutions. From synthesis, trialling, and analysis the resulting summary highlights the determination of the optimised:

- Mullite precursors were synthesized using a sol-gel process involving Chamotte powder, H_2O, fumed SiO_2, carboxylic acid, aluminium powder, and synthetic mica, transforming into mullite at around 950°C. An optimal silicate solution was sought based on adhesion, coverage, and oxidation resistance. The standout coating, Mul50, demonstrated excellent oxidation inhibition, uniform coverage, and improved surface cosmetics. It had a viscosity suitable for pipette and spin application, adhered well, and significantly reduced oxidation thickness.
- Different reinforcement agents were trialled, with ZrO_2 emerging as the best option for improving mechanical properties and oxidation resistance, outperforming other candidates like TiO_2, MgO, and Al_2O_3. Zirconia was found to be the most effective reinforcement agent due to its high

oxidation reduction, good adhesion characteristics, and consistent performance even after thermal cycling. With ZrO_2-$3Al_2O_3$·$2SiO_2$, the oxide layer was reduced by 94.9% although the surface roughness increased by 14.7%.

- Vickers hardness tests revealed a 46.3% reduction in hardness at the mid-cross section compared to uncoated samples, suggesting an insulating effect of the coating against thermal treatment. Grain size analysis indicated a significant reduction in grain diameter by 49.1% in the central region of the coating, highlighting the impact of the coating on the steel's microstructure. Surface roughness measurements showed a marked difference between coated and uncoated sides, with the uncoated side having an average roughness (Ra) of 1.4 μm compared to 16.5 μm for the coated side.

- EDS analysis after thermal cycling confirmed the presence of key elements like Al, Si, and Zr, and the diffusion of iron oxides into the coating, indicating complex interactions at high temperatures. XRD analysis showed strong peaks at 28° and 32° 2θ, with characteristics of monoclinic zirconia, and a peak at 50° associated with cubic zirconia. Raman spectroscopy corroborated the XRD findings, with shifts indicating the presence of orthorhombic mullite and monoclinic zirconia. As intended, this qualitative analysis indicated the coatings had become more crystalline beyond 450°C and were stable at the high isothermal temperature. The economic analysis projected a potential annual profit of £2.7mil for Sopac20 coating and £3.1mil for the ZrO_2-$3Al_2O_3$·$2SiO_2$ coating, considering factors like production costs and the value of the steel saved from oxidation.

Chapter 7

Conclusion

In conclusion, this project aimed to produce a viable coating solution to inhibit the growth of oxide during the normalisation process which removes the HAZ from low carbon steel conveyance tubes at the SR2 mill in TATA Steel Corby. Initially the project observed the oxidation kinetics of three key steel grades before examining the impact on surface quality and mechanical properties due to reheating as well as the phase morphology of the generated oxide compounds. From this technical benchmarking, two passive solutions from the phosphate and silicate branches were selected to be fully optimised to reduce scale and improve product characteristics. Their effect on phase morphology and overall oxidation performance was recorded and compared to the oxidation of untreated steel, from which the following observations were found:

- Oxidation trials were performed on TATA Steel samples using a custom-built atmospheric furnace with a standard thermal cycle before layer analysis on an Observer microscope. The normalised samples were then analysed through various qualitative and quantitative techniques such as SEM, EDS, XRD, Raman and WLI for their kinetic and thermomechanical properties.

- Initial benchmarking assigned a standard oxide thickness value of around 240µm for untreated E41 Steel for STCA1 thermal cycles. E1-E41 all experienced a 12-14% drop in hardness across their mid-section and a 20-25% drop in grain size. The surface roughness of those samples was found to be between 6.1µm-8.8µm. The thermal conductivity ranged between

~45W/mK -51W/mK when observing the steel above 800°C. The project also discovered the wüstite domination switch point during reheating and the ratio of wüstite-magnetite present under the specific atmosphere of the SR2.

- A wide array of phosphate-based coatings was trialled prior to determination of a suitable candidate – a sodium polyphosphate solution with an acrylic addition and a recycled glass additive. Through the application of this optimised Sopac20-HRc at, the oxide layer was reduced by 82.1% and surface roughness improved by 41.1%. Adhesion and delamination prevention factors were improved by reducing porosity by controlling the recycled glass particle size to <80μm. Efforts were made to adapt the T_g through additive blends of borosilicate glass, but this proved ineffective, as shown by the consistent phases described in the XRD Diffraction patterns. The mechanical properties seem unaffected by the coating application stating a within error drop of 14.8% in hardness in the midsection and a drop of 31.7% in grain size across the midsection. Economically, the coating has a potential daily profitability of £10,267.

- A number of silicate solutions were also trialled for implementation into the SR2 Mill. The determined coating was a reinforced mullite technology which incorporated zirconia to improve resistance against internal stresses when oxidation occurs. With ZrO_2-$3Al_2O_3 \cdot 2SiO_2$, the oxide layer was reduced by 94.9% and surface roughness increased by 14.7%. The reinforcement agent was required due to significant oxygen precipitation through the bulk mullite layer during reheating. The mechanical properties were undesirably affected by the coating application in which a 46.3% in hardness in the midsection and a drop of 49.1% in grain size

across the midsection which were significantly higher than the uncoated steel comparison. Economically, the coating has a potential daily profitability of £12,113.

Future work

The project has already undertaken a new EngD student who will make deeper observations into the surface cosmetic issues caused by normalisation and scale and has ambitions to fully model the heat transfer to the tube profile using Thermo-Calc software. As such, there is a technical cross-over with the emissivity and thermal diffusivity characteristics of the coatings presented which can then be integrated into these models.

While the two coated solutions were optimised, the synthesis was largely based on equipment available at PMRC and full batches of coating material were generated through laboratory processes. It would be necessary to scope out and construct a pilot line to enable a scaled-up version of the synthesis and perform Quality Analysis checks to ensure no loss in oxidation inhibition performance when producing at high volumes.

While coatings were discounted because of an inability for surface spraying, and as both coatings were able to be air sprayed, the project did consider the application stage of large-scale implementation. However, a separate project should be performed to fully determine the spray settings required (and which nozzle fitting to utilise) to achieve a uniform, defect-less coating with desired thickness. This project would consider properties such as surface tension, viscosity, fluid dynamics and drying phenomena of the optimised coatings.

Finally, future observations should concentrate on the financial impact of coating implementation from a cosmetic perspective. Once a scaled-up trial of the coatings has been performed, the surface appearance could have a positive or negative affect on the price point of the Install 235 products. In short, conveyance tubes which suffered greatly from scale damage and were unable to be sold as were not "visibly acceptable for the general public" could be marketed as such and would have value added. However, if the coating is remnant on the surface

after normalisation, then it may lead to the removal of paints and protective coatings, reducing the service life of the conveyance tube and leads to financial clawback from the customer. These economic factors should be added to the current appraisal once a suitable large-scale trail has been performed and the Install 235 products examined.

References

[1]   TATA Steel Europe, TATA Construction. The Complete Solution
        Brochure, 2015
        https://www.tatasteeleurope.com/sites/default/files/Complete-Solution-
        Brochure.pdf (accessed Jan 2024)

[2]   Pei Y. *High Frequency Induction Welding & Post-Welding Heat Treatment of
        Steel Pipes*. University of Cambridge, http://www.msm.cam.ac.uk/phase-
        trans/2011/thesis_c.pdf (2011).

[3]   Zinn S, Semiatin L. Theory of Induction Heating. In: *Elements of induction
        heating: Design, Control, and Applications*. Ohio: ASM International, 1998,
        pp. 9–16.

[4]   Davis JR. Basic Understanding of Weld Corrosion. In: *Corrosion of
        Weldments*. ASM International, 2006, pp. 2–3.

[5]   Messler Jr R. *Principles of Welding*. 1st ed. Wiley VCH. Epub ahead of print
        1999. DOI: 10.1002/9783527617487.

[6]   Eroglu M, Aksoy M. Effect of initial grain size on microstructure and
        toughness of intercritical heat-affected zone of a low carbon steel. *Mater
        Sci Eng* 2000; 286: 289–297.

[7]   Güngör OE, Yan P, Thibaux P, et al. Investigations into microstructure-
        toughness relation in high frequency induction welded pipes. In:
        Proceedings of the 8th International Pipeline Conference. Calgary, 2010, pp. 1–
        9.

[8]   Zhao L, Park N, Tian Y, et al. Combination of dynamic transformation
        and dynamic recrystallization for realizing ultrafine-grained steels with
        superior mechanical properties. *Nature* 2016; 6: 1–11.

[9]   Li X, Li K, Cai Z, et al. A review of austenite memory effect in HAZ of B
        containing 9% Cr martensitic heat resistant steel. *Metals (Basel)* 2019; 9: 1–
        21.

[10]   Çöl M, Yılmaz M. The determination of heat treatment parameters of X52
        microalloyed steel after high frequency induction welding. In: *Materials &
        Design*. Elsevier, pp. 507–512.

[11]   K. Esterling. *Introduction to the Physical Metallurgy of Welding*. 2nd ed.
        Oxford: Butterworth, https://www.elsevier.com/books/introduction-to-
        the-physical-metallurgy-of-welding/easterling/978-0-7506-0394-2 (1992).

[12]   Thelning K-E. *Heat Treatment-General*. 2nd ed. Colorado: ASM
        International, 1984.

[13]   Pitakkorraras S, Tangroekwarasakul P. Effect of Normalizing
        Temperature and Time on Microstructures and Mechanical Properties of
        Hot Rolled Steel Strip for Gas Cylinder Production. 2010; 20: 37–41.

[14]   Mcfarlane A. *Corrosion Performance of Welded and Seamless Steel Conveyance*

Tubes. Cranfield, 2013.

[15] Birks N, Meier GH, Pettit FS. *Introduction to the High Temperature Oxidation of Metals*. 2nd ed. Cambridge University Press. Epub ahead of print 2006. DOI: 10.2277/0521480426.

[16] Krauss G. *Heat Treatments to produce Ferrite and Pearlite*. 2nd ed. Butterworth, 1989.

[17] Yánez A, Narváez E, Salinas L, et al. Annealing and Normalizing of AISI 1045 Steel: A Lamellae Analysis. *Int J Metall Met Phys*; 5. Epub ahead of print 2020. DOI: 10.35840/2631-5076/9253.

[18] Zhang XZ, Liu S, Zhao MS, et al. Comparative experimental study of hot-formed, hot-finished and cold-formed rectangular hollow sections. *Case Stud Struct Eng* 2016; 6: 115–129.

[19] Abuluwefa H. *Scale formation in a walking-beam steel reheat furnace*. McGill University, 1992.

[20] ENDO R, HAYASHI H, LI M, et al. Determination of thermal diffusivity/conductivity of oxide scale formed on steel plate by laser flash method through thermal effusivity measurement by transient hot-strip method. *ISIJ Int* 2020; 60: 2773–2779.

[21] Schütze M, Tortorelli PF, Wright IG. Development of a comprehensive oxide scale failure diagram. *Oxid Met* 2010; 73: 389–418.

[22] Sun W, Tieu AK, Jiang Z, et al. Oxide scales growth of low-carbon steel at high temperatures. *J Mater Process Technol* 2004; 155–156: 1300–1306.

[23] Abuluwefa HT. *Characterization of Oxides (Scale) Growth of Low Carbon Steel during Reheating*. McGill University, 1996.

[24] Jang JH, Lee DE, Kim MY, et al. Investigation of the slab heating characteristics in a reheating furnace with the formation and growth of scale on the slab surface. *Int J Heat Mass Transf* 2010; 53: 4326–4332.

[25] Turkdogan ET, McKewan WM, Zwell L. Rate of oxidation of iron to wustite in water-hydrogen gas mixtures. *J Phys Chem* 1965; 69: 327–334.

[26] Birosca S, West GD, Higginson RL. Microstructural investigation of the oxide scale on low carbon steel. *Metal* 2005; 24: 1–8.

[27] Birosca S, Higginson RL. Phase identification of oxide scale on low carbon steel. 2005; 22: Proceedings of the sixth international conference.

[28] Dai J, Zhu J, Chen C, et al. High temperature oxidation behavior and research status of modifications on improving high temperature oxidation resistance of titanium alloys and titanium aluminides: A review. *J Alloys Compd* 2016; 685: 784–798.

[29] Mancheno VVB. *Scale formation and descaling in hot rolling of low carbon steel*. McGill, http://digitool.library.mcgill.ca/R/-?func=dbin-jump-full&object_id=115671&silo_library=GEN01 (2008).

[30] Khanna AS. High-temperature oxidation. *Handb Environ Degrad Mater*

Third Ed 2018; 2: 117–132.

[31] Kofstad P. Oxidation of metals: Determination of activation energies. *Nature* 1957; 179: 1362–1363.

[32] Hao M, Sun B, Wang H. High-Temperature oxidation behavior of Fe-1Cr-0.2Si steel. *Materials (Basel)*; 13. Epub ahead of print 2020. DOI: 10.3390/ma13030509.

[33] Larouk Z, Bouhalais H. Recrystallization behavior of a low carbon steel wire. *Phys Procedia* 2009; 2: 1223–1229.

[34] Dutta S, Panda AK, Mitra A, et al. Microstructural evolution, recovery and recrystallization kinetics of isothermally annealed ultra low carbon steel. *Mater Res Express*; 7. Epub ahead of print 2020. DOI: 10.1088/2053-1591/ab657c.

[35] Materials Thermal Properties Database. *Thermtest Instruments*, https://thermtest.com/thermal-resources/materials-database (accessed 8 December 2021).

[36] Takeda M, Onishi T, Nakakubo S, et al. Physical properties of iron-oxide scales on Si-containing steels at high temperature. *Mater Trans* 2009; 50: 2242–2246.

[37] Wood GC, Stringer J. The adhesion of growing oxide scales to the substrate. *Le J Phys IV* 1993; 03: C9-65-C9-74.

[38] Schütze M, Malessa M, Renusch D, et al. Mechanical Properties and Adherence of Oxide Scales. *Mater Sci Forum* 2006; 522–523: 393–400.

[39] Melfo W, Bolt H, Rijnders M, et al. Experimental study on primary scale formation and descalability on steels containing Ni and Ni+Si. *ISIJ Int* 2013; 53: 866–873.

[40] Kim S-R, Lee S, Park JW, et al. Oxide scale on stainless steels and its effect on sticking during hot-rolling. *Corros Sci* 2020; 164: 10.

[41] Zambrano OA, Coronado JJ, Rodríguez SA. Mechanical properties and phases determination of low carbon steel oxide scales formed at 1200°C in air. *Surf Coatings Technol* 2015; 282: 155–162.

[42] Chen RY, Yuen WYD. Review of the high-temperature oxidation of iron and carbon steels in air or oxygen. *Oxid Met* 2003; 59: 433–468.

[43] Skin H-K. *Iron Oxide Reduction with Flux Additions*. Imperial COllege London, 1984.

[44] Chen Z, Chou KC, Morita K. Mechanism of metastable Wüstite formation in the reduction process of iron oxide below 570°C. *Mater Trans* 2016; 57: 1660–1663.

[45] Raman RKS, Gleeson B, Young DJ. Laser Raman spectroscopy: a technique for rapid characterisation of oxide scale layers. *Mater Sci Technol* 1998; 14: 373–376.

[46] Chen RY, Yuen WYD. Effects of the presence of water vapour on the

oxidation behaviour of low carbon-low silicon steel in 1 %O2-N2 at 1073 K. *Oxid Met* 2013; 79: 655–678.

[47] Rahmel A, Tobolski J. Einfluss Von Wasserdampf Und Kohlend:oxyd Auf Die Oxidation Von Eisen in Sauerstoff Dei Hohen Temperaturen. *Corros Sci* 1965; 5: 333–346.

[48] Kondo Y, Tanei H, Suzuki N, et al. Blistering behavior during oxide scale formation on steel surface. *ISIJ Int* 2011; 51: 1696–1702.

[49] Spreitzer D, Schenk J. Reduction of Iron Oxides with Hydrogen—A Review. *Steel Res Int*; 90. Epub ahead of print 2019. DOI: 10.1002/srin.201900108.

[50] El-Rahaiby SK, Rao YK. The kinetics of reduction of iron oxides at moderate temperatures. *Metall Trans B* 1979; 10: 257–269.

[51] Bonalde A, Henriquez A, Manrique M. Kinetic analysis of the iron oxide reduction using hydrogen-carbon monoxide mixtures as reducing agent. *ISIJ Int* 2005; 45: 1255–1260.

[52] Graf M, Kawalla R. Scale behaviour and deformation properties of oxide scale during hot rolling of steel. *Key Eng Mater* 2012; 504–506: 199–204.

[53] Evans H, Mitchell GP, Lobb RC, et al. A numerical analysis of oxide spallation. *Proc R Soc London Ser A Math Phys Sci* 1993; 440: 1–22.

[54] Melorose J, Perroy R, Careas S. *Modeling and Simulation of Stress-Induced Non-Uniform Oxide Scale Growth During High-Temperature Oxidation of Metallic Alloys*. 2015.

[55] Melfo W, Barabino E. European Oxide Scale Conference. In: *Experimental determination of the critical strain of fracture of oxide scale in hot finishing mill conditions using the sigma test*. 2018.

[56] F. Matsuno. Blistering and Hydraulic Removal of Scale Films of Rimmed Steel at High Temperature. *Trans Iron Steel Inst Japan* 1980; 20: 413.

[57] Kondo Y, Tanei H, Ushioda K, et al. Role of hematite formation on blister generation during high temperature oxidation of steel. *Tetsu-To-Hagane/Journal Iron Steel Inst Japan* 2014; 100: 352–358.

[58] Dewfall R. Blistering Formation in High Strength Steels (HSS) During Hot Rolling. In: *Materials Processing Institute - Postgraduate Research Symposium*. 2021.

[59] Bidmus H, Chau J, Dechant K. Absolute roughness of pipes from different manufacturing and treatment methods and impact on pipeline design. *PSIG Annu Meet PSIG 2019* 2019; 1–11.

[60] Riaz S, Bugdol M, Farrugia D, et al. *Oxidation management in hot rolling processes*. Brussels, 2013.

[61] Pound G. *High-Temperature Oxidation-Resistant Coatings*. 1970. Epub ahead of print 1970. DOI: 10.17226/20603.

[62] Guglielmi M. Sol-gel coatings on metals. *J Sol-Gel Sci Technol* 1997; 8: 443–

449.

[63] Curry N, Leitner M, Körner K. High Porosity Thermal Barrier Coatings from High-Power Plasma Spray Equipment-Processing Performance and Economics. *Coatings* 2020; 10: 957.

[64] Hakam M, Wang CJ, Wardono H, et al. High temperature oxidation of low carbon steel with and without an Al coating in an atmosphere containing burning ethanol. *AIP Conf Proc*; 1983. Epub ahead of print 2018. DOI: 10.1063/1.5046275.

[65] Cao XQ, Vassen R, Stoever D. Ceramic materials for thermal barrier coatings. 2004; 24: 1–10.

[66] Durán A, Castro Y, Aparicio M, et al. Protection and surface modification of metals with sol–gel coatings. *Int Mater Rev* 2007; 52: 175–192.

[67] de Lima Neto P, Atik M, Avaca LA, et al. Sol-gel coatings for chemical protection of stainless steel - Code: EP7. *J Sol-Gel Sci Technol* 1994; 2: 529–534.

[68] Guglielmi M, Festa D, Innocenzi PC, et al. Borosilicate coatings on mild steel. *J Non Cryst Solids* 1992; 147–148: 474–477.

[69] Karthik A, Arunmetha S, Srither SR, et al. High temperature corrosion resistance of silicate based nanostructured thermal barrier coatings using Al2O3-(Y2O3) ZrO2/SiO2 nanocomposite. *Surf Coatings Technol* 2016; 292: 110–120.

[70] Odashima H, Ki Ta Yama M, Maeda S. Oxidation a New Inhibition Protective Mechanism Coating for and Slab Performance Reheating. *Trans Iron Steel Inst Japan* 1987; 27: 110–119.

[71] Odashima H, Kitayama M. Oxidation Inhibition Mechanism and Performance of a New Protective Coating for Slab Reheating of 3% Si-steel. 1990; 30: 255–264.

[72] Torkar M, Glogovac B, Kaučič F, et al. Diminution of scaling by the application of a protective coating. *J Mater Process Technol* 1996; 58: 217–222.

[73] Aramaki S, Roy R. Revised Phase Diagram for the System Al2O3-SiO2. *J Am Ceram Soc* 1962; 45: 229–242.

[74] Davis R, Pask J. Diffusion and Reaction Studies in the Alumina - Silica System. *J Am Ceram Soc* 1972; 2: 35–43.

[75] Toropov NA, Galakhov FI. Solid solutions in the system Al2O3-SiO2. *Acad Sci USSR Div Chem Sci* 1958; 7: 5–9.

[76] Anggono J. Mullite Ceramics: Its Properties Structure and Synthesis. *Mullite Ceram Its Prop Struct Synth* 2005; 7: 1–10.

[77] Davis RF, Pask JA. 3 - Mullite. In: *Refractory Materials, Volume 5 Part 4*. 1971, pp. 37–76.

[78] Hou P, Basu SN, Sarin VK. Nucleation mechanisms in chemically vapor-

deposited mullite coatings on SiC. *J Mater Res* 1999; 14: 2952–2958.

[79] Kubong V. *Processing and properties of alumina reinforced mullite ceramics*. 2013.

[80] Takada H, Nakahira A, Ueda S. Improvement of Mechanical properties of Natural Mullite and SiC nanocomposites. *J Japan Soc Powder Powder Metall* 1991; 348–351.

[81] Marple BR, Green DJ. Mullite/Alumina Particulate Composites by Infiltration Processing: III, Mechanical Properties. *J Am Ceram Soc* 1991; 74: 2453–2459.

[82] Medvedovski E. Alumina-mullite ceramics for structural applications. *Ceram Int* 2006; 32: 369–375.

[83] Aksel C. Mechanical properties and thermal shock behaviour of alumina-mullite-zirconia and alumina-mullite refractory materials by slip casting. *Ceram Int* 2003; 29: 311–316.

[84] Wahsh MMS, Khattab RM, Awaad M. Thermo-mechanical properties of mullite/zirconia reinforced alumina ceramic composites. *Mater Des* 2012; 41: 31–36.

[85] Cui K, Zhang Y, Fu T, et al. Toughening mechanism of mullite matrix composites: A review. *Coatings*; 10. Epub ahead of print 2020. DOI: 10.3390/coatings10070672.

[86] Abdallah AI, Sayed M, Awaad M, et al. Characterization of in-situ zirconia/mullite composites prepared by sol-gel technique. *J Asian Ceram Soc* 2021; 9: 940–946.

[87] Sarraf F, Abbatinali E, Gorjan L, et al. Effect of MgO sintering additive on mullite structures manufactured by fused deposition modeling (FDM) technology. *J Eur Ceram Soc* 2021; 41: 6677–6686.

[88] Kovalenko V, Kotok V. Optimization of the Formation Technology of Tripolyphosphate Coating on Mild Steel. *Eastern-European J Enterp Technol* 2021; 5: 73–78.

[89] Liu B, Zhang X, Xiao GY, et al. Phosphate chemical conversion coatings on metallic substrates for biomedical application: A review. *Mater Sci Eng C* 2015; 47: 97–104.

[90] Asadi V, Danaee I, Eskandari H. The effect of immersion time and immersion temperature on the corrosion behavior of Zinc phosphate conversion coatings on carbon steel. *Mater Res* 2015; 18: 706–713.

[91] Wragg J., Chamberlain J., Chann L, et al. Characterization of polyacrylic acid modified zinc phosphate crystal conversion coatings. *J Appl Polym Sci* 1993; 917–928.

[92] Muñoz F, Rocherullé J, Ahmed I, et al. *Phosphate Glasses*. 2019. Epub ahead of print 2019. DOI: 10.1007/978-3-319-93728-1_16.

[93] Foroutan F. Sol-Gel Synthesis of Phosphate-Based Glasses for Biomedical

Applications. *Div Biomater Tissue Eng UCL Eastman Dent Institute, Univ Coll London* 2015; 202.

[94] Ma LN. Dissolution behavior of phosphate glasses. *Dr Diss*; Missouri S, http://scholarsmine.mst.edu/doctoral_dissertations (2014).

[95] Poluektov PP, Schmidt O V., Kascheev VA, et al. Modelling aqueous corrosion of nuclear waste phosphate glass. *J Nucl Mater* 2017; 484: 357–366.

[96] Bunker BC, Arnold GW, Wilder JA. Phosphate glass dissolution in aqueous solutions. *J Non Cryst Solids* 1984; 64: 291–316.

[97] Delahaye F, Montagne L, Palavit G, et al. Acid dissolution of sodium–calcium metaphosphate glasses. *J Non Cryst Solids* 1998; 242: 25–32.

[98] Szumera M, Wacławska I, Sułowska J. Thermal properties of MnO2 and SiO2 containing phosphate glasses. *J Therm Anal Calorim* 2016; 123: 1083–1089.

[99] Goj P, Ciecińska M, Szumera M, et al. Thermal properties of Na2O–P2O5–Fe2O3 polyphosphate glasses. *J Therm Anal Calorim* 2020; 142: 203–209.

[100] Stoch P, Ciecinska M, Stoch A. Thermal properties of phosphate glasses for salt waste immobilization. *J Therm Anal Calorim* 2014; 117: 197–204.

[101] Yu X, Wang C, Liu L. Properties and structure of nitrogen-doped phosphate glasses. *J Non Cryst Solids* 1989; 215: 21–31.

[102] Ahmed I, Collins CA, Lewis MP, et al. Processing , characterisation and biocompatibility of iron-phosphate glass fibres for tissue engineering. 2004; 25: 3223–3232.

[103] Hu P, Ying L, Li Y, et al. Journal of Materials Processing Technology Effect of oxide scale on temperature-dependent interfacial heat transfer in hot stamping process. 2013; 213: 1475–1483.

[104] Yukawa N, Nakashima Y, Ishiguro T, et al. Modeling of heat transfer coefficient of oxide scale in hot forging. *Procedia Eng* 2014; 81: 492–497.

[105] Jo HJ, King JL, Blomstrand K, et al. Spectral emissivity of oxidized and roughened metal surfaces. *Int J Heat Mass Transf* 2017; 115: 1065–1071.

[106] Optotherm. Emissivity Values, https://www.optotherm.com/emiss-table.htm (2018, accessed 8 April 2022).

[107] Shao G, Wu X, Cui S, et al. High emissivity MoSi2–TaSi2–borosilicate glass porous coating for fibrous ZrO2ceramic by a rapid sintering method. *J Alloys Compd* 2017; 690: 63–71.

[108] SPS. Anti Scale Prevemtion Coatings, https://steelplantspecialities.com/anti-scale-protective-coatings/ (2018).

[109] Rao BG, Mukherjee D, Reddy BM. Novel approaches for preparation of nanoparticles. In: *Nanostructures for Novel Therapy*. Elsevier Inc., pp. 5–17.

[110] Pathak SS, Khanna AS. *Sol-gel nanocoatings for corrosion protection*. Woodhead Publishing Limited. Epub ahead of print 2012. DOI:

10.1016/B978-1-84569-949-9.50012-5.

[111] Bersani D, Lottici PP, Montenero A. Micro-Raman Investigation of Iron Oxide Films and Powders Produced by Sol – Gel Syntheses. *J Raman Spectrosc* 1999; 30: 355–360.

[112] Li H, Liang K, Mei L, et al. Oxidation resistance of mild steel by zirconia sol-gel coatings. *Mater Sci* 2003; 341: 87–90.

[113] Mennig M, Schelle C, Duran A. Investigation of glass-like sol-gel coatings for corrosion protection of stainless steel against liquid and gaseous attack. *J sol-gel* 1998; 722: 717–722.

[114] Watanawanyoo P, Mochida H, Teruyuki F, et al. Experimental Study on the Spray Characteristics of an Air Assisted Atomizer with Internal Mixing Chamber. *Eur J Sci Res* 2012; 84: 505–521.

[115] Lee DW, Hwang JG, Kwon YD, et al. A study on the air knife flow with Coanda effect. *J Mech Sci Technol* 2007; 21: 2214–2220.

[116] Gilbert-Kawai E, Wittenberg M. Dalton's law of partial pressures. In: *Essential Equations for Anaesthesia*. 2014, pp. 11–12.

[117] TATA-Steel. *Install® Plus 235 & Inline ™ Technical Specification*. Corby, 2018.

[118] Liu S, Hua H. Extended depth-of-field microscopic imaging with a variable focus microscope objective. *Opt Express* 2011; 19: 353.

[119] ASTM International. Standard Test Methods for Determining Average Grain Size. *Astm E112-10* 2010; 96: 1–27.

[120] ASTM International. D3359-17 Standard test methods for rating adhesion by tape test. In: *Annual Book of ASTM Standards*, pp. 1–7.

[121] Meuwese Stefan. *Cross-Cut Test Report According to ISO-2409 (ASTM 3359)*. 2020.

[122] Astuti NH, Wibowo NA, Ayub MRSSN. The Porosity Calculation of Various Types of Paper Using Image Analysis. *J Pendidik Fis Indones* 2018; 14: 46–51.

[123] Devia DM, Rodriguez-Restrepo L V, Restrepo-Parra E. Methods Employed in Optical Emission Spectroscopy Analysis: a Review. *Ing y Cienc* 2015; 11: 239–267.

[124] Goldstein J, Newbury D, Joy D, et al. The SEM and Its Modes of Operation. In: *Scanning Electron Microscopy and X-Ray Microanalysis*. 1975, pp. 21–61.

[125] Anjam Khursheed. Conventional SEM Design. In: *Scanning Electron Microscope Optics and Spectrometers*. World Scientific Publishing, pp. 1–69.

[126] Dante R. *Handbook of Friction Materials and their Applications*. Elsevier Ltd, 2016. Epub ahead of print 2016. DOI: 10.3726/978-3-653-00413-7/2.

[127] Pavlicek P. Measurement Uncertainty of White-Light Interferometry on Optically Rough Surfaces. In: *Numerical Simulations of Physical and*

Engineering Processes, p. 491.

[128] Wyant JC. White Light Interferometry. *Fibre Opt* 1990; 1314: 307.

Declarations

This work has not previously been accepted in substance for any degree and is not being concurrently submitted in candidature for any degree.

Signed.....................James Grant..

Date........................31/12/2022..
.

This thesis is the result of my own investigations, except where otherwise stated. Other sources are acknowledged by footnotes giving explicit references. A bibliography is appended.

Signed....................James Grant..

Date.....................31/12/2022...
.

I hereby give consent for my thesis, if accepted, to be available for electronic sharing.

Signed....................James Grant..

Date......................31/12/2022...
.

The University's ethical procedures have been followed and, where appropriate, that ethical approval has been granted.

Signed....................James Grant..

Date......................31/12/2022...